Analytical Study On Compound Planetary Gear Dynamics

DISSERTATION

Presented in Partial Fulfillment of the Requirements for the Degree Doctor of Philosophy in the Graduate School of The Ohio State University

By

Yichao Guo, B.S., M.S.

Graduate Program in Mechanical Engineering

The Ohio State University

2011

Dissertation Committee:

Prof. Robert G. Parker, Advisor

Prof. Daniel A. Mendelsohn, Co-advisor

Prof. Stephen E. Bechtel

Dr. Sandeep M. Vijayakar

Abstract

Noise and vibration are major concerns in applications of compound planetary gears, and dynamic analysis is essential to their reduction. This work conducts a series of analytical investigations on several problems in compound planetary gear dynamics.

A purely rotational model for compound planetary gear is developed, and the unique modal properties for the natural frequency spectra and vibration modes are presented and analytically proved. This model aims to simplify subsequent analyses on compound planetary gear dynamics while keeping the main dynamic behavior generated by tooth mesh forces.

A systematic study on general compound planetary gear eigensensitivities is performed by utilizing the rotational-translational model in [53]. The eigensensitivities are derived in compact, closed-form expressions for all parameter variations in both tuned (each stage in the system retains cyclic symmetry) and mistuned systems. The resultant formulae also suggest that modal strain and kinetic energy distribution plots are effective and straightforward means to identify the system parameters that have the greatest impact on adjusting the related natural frequency.

Compound planetary gear natural frequency veering and crossing phenomena are also systematically examined. By grouping all system parameters into tuned and mistuned parameters, the veering/crossing patterns with respect to each system parameter are determined. These patterns provide critical information on dramatic mode shape changes when tuning a compound planetary gear during the design stage.

Gear mesh phases that are critical for analytical or computational study on compound planetary gear dynamics are defined and calculated analytically. All the mesh phases are grouped into a hierarchical structure of system-level, stage-level, and train-level mesh phases to simplify the subsequent analytical investigations. In addition to providing a complete procedure to determine all the necessary relative phases, the specific relations between train-level relative phases are derived by applying the assembly conditions of compound planetary gears. Such relations, together with the systematically defined mesh phases, provide the foundation for the general rules to suppress selected dynamic responses of a general compound planetary gear through proper mesh phasing. The resultant mesh phasing rules are crucial for the troubleshooting of the vibration and noise problems in compound planetary gear applications.

Compound planetary gear parametric instabilities caused by mesh stiffness variations are analytically explored. Systems with single or multiple mesh frequencies are investigated. The instability boundaries are derived for different cases depending on the degeneracy of the natural frequencies. Application of the well-defined modal properties yields simple, closed-form expressions for instability boundaries. Some instability boundaries vanish under specific mesh phasing conditions.

The back-side mesh stiffness variation is inspected in this work to address the needs for gear vibration models that consider the gear tooth contacts on the back

side. The results reveal the inherent relationship between the back-side and drive-side mesh stiffnesses. The impact of backlash on the back-side mesh stiffness variation function is also quantified.

Dedicated to my wife, Zongcui Mu

to my son, Kevin Guo

and to my mother, Jinmei Wang

Acknowledgments

I would like to express my sincere thanks to my advisor, Robert G. Parker, for the opportunity to pursue this Ph.D. degree, his generous academic guidance, the precious opportunities to explore the academic world through numerous conferences, and the chance to understand the engineering world through practical projects and trainings. In addition, his invaluable suggestions during manuscript preparations has helped me greatly improve my academic/technical writing skills.

I want to express my sincere thanks to Prof. Mendelsohn for being my co-advisor. Without his help, the defense is not possible to happen.

I sincerely thank Prof. Bechtel for his kindness of being the committee member of my Ph.D. dissertation.

I am thankful to Dr. Vijayakar for providing exceptional finite element analysis capability that is used extensively in this work and for being the committee member of my Ph.D. dissertation.

I also want to thank Ms. Sands for her kind help throughout my graduation and my lab mates in the Dynamics and Vibrations Lab for their help during my study in The Ohio State University.

I owe my thanks to my wife and my son for their support and, particularly, I want to thank my mother, who recently injuried in a car accident while still supporting me to finalize my Ph.D. study.

Vita

July, 1999	B.S., Mechanical Engineering, Shanghai Jiao Tong University, Shanghai, China
July, 2002	M.S., Vehicle Engineering, Shanghai Jiao Tong University, Shanghai, China
May, 2004	M.S., Mechanical Engineering, State University of New York at Stony Brook, NY, USA
September 2004 - September 2008	University/Graduate Fellowship, The Ohio State University
September 2008 - Present	Powertrain System Engineer, Delphi

Publications

Research Publications

Guo, Y., and Parker, R. G. "Natural Frequency Veering and Crossing Patterns for General Compound Planetary Gears". *In preparation*, 2011.

Guo, Y., and Parker, R. G. "Suppression of Various Modal Responses in General Compound Planetary Gears through Mesh Phasing". *In preparation*, 2011.

Guo, Y., and Parker, R. G. "Parametric Instabilities of General Compound Planetary Gear Caused by Mesh Stiffness Variations". *In preparation*, 2011.

Guo, Y., and Parker, R. G. "Back-side Contact Gear Mesh Stiffness". *11th International ASME Power Transmission and Gearing Conference (DETC2011/PTG-48055)*, accepted, Washington, DC.

Guo, Y., and Parker, R. G. "Analytical Determination of Mesh Phase Relations in General Compound Planetary Gears". *Mechanism and Machine Theory*, accepted.

Guo, Y., and Parker, R. G. "Sensitivity of General Compound Planetary Gear Natural Frequencies and Vibration Modes to Model Parameters". *Journal of Vibration and Acoustics*, 132(1):1–13, 2010.

Guo, Y., and Parker, R. G. "Purely Rotational Model and Vibration Modes of Compound Planetary Gears". *Mechanism and Machine Theory*, 45:365–377, 2010.

Guo, Y., and Parker, R. G. "Mesh Phase Relations of General Compound Planetary Gears". *Proceedings of 10th International ASME Power Transmission and Gearing Conference (IDETC2007-35799)*, Las Vegas, NV.

Guo, Y., and Parker, R. G. "Sensitivity of General Compound Planetary Gear's Natural Frequencies and Vibration Modes to Model Parameters". *Proceedings of 10th International ASME Power Transmission and Gearing Conference (IDETC2007-35802*, Las Vegas, NV.

Guo, Y., and Parker, R. G. "Sensitivity of Tuned General Compound Planetary Gear's Natural Frequencies and Vibration Modes to Model Parameter". *Proceedings of 2006 International Mechanical Engineering Congress and Exposition (IMECE2006-14978)*, Chicago, IL.

Fields of Study

Major Field: Mechanical Engineering

Table of Contents

Page

List of Tables

List of Figures

Nomenclature

Variables

I Moment of inertia

a Number of carriers

b Number of central gears

c^i Number of planet trains in planet set i

d^i Number of planets per train in planet set i

$k^{jn}_{gg,\theta\theta}$ Torsional shaft stiffness between central gears j and n

$k^{jn}_{gg,xx}$, $k^{jn}_{gg,yy}$ Translational shaft stiffness between central gears j and n. When $k^{jn}_{gg,xx} = k^{jn}_{gg,yy}$, k^{jn}_{gg} represents both translational shaft stiffness.

$k^{ih}_{cc,\theta\theta}$ Torsional shaft stiffness between carriers i and h

$k^{ih}_{cc,xx}$, $k^{ih}_{cc,yy}$ Translational shaft stiffness between carriers j and n. When $k^{ih}_{cc,xx} = k^{ih}_{cc,yy}$, k^{ih}_{cc} represents both translational shaft stiffnesses.

$k^{ij}_{cg,\theta\theta}$ Torsional shaft stiffness between carrier i and central gear j

$k^{ij}_{cg,xx}$, $k^{ij}_{cg,yy}$ Translational shaft stiffness between carrier i and central gear j. When $k^{ij}_{cg,xx} = k^{ij}_{cg,yy}$, k^{ij}_{cg} represents both translational shaft stiffnesses.

$k^{ilmq}_{p-p,\theta\theta}$ Torsional shaft stiffness between planet m and q in planet train l of planet set i

$k^{ilmq}_{p-p,\zeta\zeta}$, $k^{ilmq}_{p-p,\eta\eta}$ Translational shaft stiffness between planet m and q in planet train l of planet set i. When $k^{ilmq}_{p-p,\zeta\zeta} = k_{p-p,\eta\eta}$, k^{ilmq}_{p-p} represents both translational shaft stiffnesses.

$k^{i}_{cb,\theta\theta}$ Torsional bearing stiffness of carrier i

$k^{i}_{cb,xx}$, $k^{i}_{cb,yy}$ Translational bearing stiffness of carrier. When $k^{i}_{cb,xx} = k^{i}_{cb,yy}$, k^{i}_{cb} represents both translational support stiffnesses.

$k^{j}_{gb,xx}$, $k^{j}_{gb,yy}$ Translational bearing stiffness of carrier. When $k^{j}_{gb,xx} = k^{j}_{gb,yy}$, k^{j}_{gb} represents both translational support stiffnesses.

$k^{j}_{gb,\theta\theta}$ Torsional bearing stiffness of central gear j

$k^{jilm}_{gp}(t)$ Mesh stiffness between central gear j and planet m in train l of set i

$k^{ilmq}_{pp}(t)$ Mesh stiffness between planet m and q in train l of set i

m Mass

r Radius

S^{jilm}_{gp} Sign variable for the planet-planet mesh deflection between planet m and q in planet train l of set i

u Rotational coordinate,$u = r\theta$.

S^{ilmq}_{pp} Sign variable for the planet-planet mesh deflection between planet m and q in planet train l of set i

δ_{gp}^{jilm} Mesh spring deflection between central gear j and planet m in train l of set i

δ_{pp}^{ilmq} Mesh spring deflection between central gear j and planet m in train l of set i

σ^{j} Equals -1 when the central gear j is a sun gear. Equals 1 when the central gear j is a ring gear.

θ Rotational coordinate

T_u Modal kinetic energy of vibration mode u

U_u Modal strain energy of vibration mode u

$x,\ y$ Translational coordinates

α_{g}^{jilm} Pressure angle at the mesh between gear j and planet m in train l of set i

α_{p}^{ilmq} Pressure angle at the mesh between planet m and planet q in train l of set i

β_{p}^{ilmq} The angle (for meshes planets) between positive ζ direction of planet m to the line connecting planets m and q in train l of set i

$\delta_{g,u}^{jilm}$ Mesh deflection between central gear j and planet m in train l of set i

$\delta_{\zeta,u}^{ilm},\ \delta_{\eta,u}^{ilm}$ Bearing deflection of planet m in train l of set i in ζ and η directions

$\delta_{p,u}^{ilmq}$ Bearing deflection of planet m in train l of set i in ζ and η directions

ψ^{ilm} Angular position of planet m in planet train l of set i

ψ_{g}^{jilm} $\psi_{g}^{jilm} = \psi^{ilm} + \sigma^{j}\alpha_{g}^{jilm}$

$Z_{g}^{s^i}$ Tooth number of the sun gear associated with stage i

$Z_g^{r^i}$ Tooth number of the ring gear associated with stage i

Z_p^{ilm} Tooth number of planet m in train l of planet set i

$\theta_g^{s^i}$ The angle that central gear s^i rotates relative to a fixed reference frame

$\theta_g^{r^i}$ The angle that central gear r^i rotates relative to a fixed reference frame

θ_c^i The angle that carrier i rotates relative to a fixed reference frame

$\hat{\theta}_p^{ilm}$ The angle that planet m needs to rotate relative to carrier i such that the gear teeth positions for the gear mesh between planets m and $m+1$ in train 1 after the rotation are equivalent to those in train l before the rotation

T_{gp}^{jilm} and T_{pp}^{ilmq} Mesh periods of k_{gp}^{ji1m} and k_{pp}^{i1mq}

$k_{gp}^{jilm}(t)$ Actual mesh tooth variation function of the mesh between central gear j and planet m in train l of planet set i

$k_{pp}^{ilmq}(t)$ Actual mesh tooth variation function of the mesh between planet m and planet q in train l of planet set i

$\kappa_{gp}^{jilm}(\tau)$ Mesh tooth variation function mesh between central gear j and planet m in train l of planet set i with its pitch point in contact at $\tau = 0$

$\kappa_{pp}^{ilmq}(\tau)$ Mesh tooth variation function of the mesh between planet m and planet q in train 1 of planet set i with its pitch point in contact at $\tau = 0$

t_1 Referring time of system-level relative phases. It is the time when the pitch point of the *base referred mesh* is in contact.

t_1^i Referring time of stage-level relative phases of stage i. It is the time when the pitch point of the *stage i referred mesh* ($k_{gp}^{s^i i11}$) is in contact for the first time after t_1.

$t_1^{ji1m,gp}$ and $t_1^{i1mq,pp}$ Referring times for train-level relative phases. They are the referring times when the pitch points of the *base-train referred meshes* k_{gp}^{ji1m} and k_{pp}^{i1mq} are in contact for the first time after t_1^i, respectively.

$\hat{\gamma}^{jilm,gp}(t_1)$ Relative phase of k_{gp}^{ji1m} referring to the base referred mesh with referring time t_1

$\hat{\gamma}^{ilmq,pp}(t_1)$ Relative phase of k_{pp}^{i1mq} referring to the base referred mesh with referring time t_1

$\bar{\gamma}^{jilm,gp}$ Relative phase of k_{gp}^{ji1m} referring to its matching base-train referred mesh. No referring time is needed.

$\tilde{\gamma}^{jilm,gp}(t_1^i)$ Relative phase of k_{gp}^{ji1m} referring to stage i referred mesh with referring time t_1^i

$\bar{\gamma}^{ilmq,pp}$ Relative phase of k_{pp}^{i1mq} referring to its matching base-train referred mesh. No referring time is needed.

$\tilde{\gamma}^{ilmq,pp}(t_1^i)$ Relative phase of k_{pp}^{i1mq} referring to stage i referred mesh with referring time t_1^i

Subscripts

b bearings(to ground)

c carrier

g central gear

p planet

ps planet set

pt planet train

$-$ shaft connection between two components

u vibration mode u

ζ in ζ direction

η in η direction

xx in x direction of the fixed reference frame

yy in y direction of the fixed reference frame

Superscripts

i, h carrier

j, n central gear

l planet train

m, q planet

$*$ any planet train

Chapter 1: INTRODUCTION

1.1 Motivation and Objectives

Planetary gears are widely used in all kinds of transmission systems, such as wind turbines, aircraft engines, automobiles, and machine tools, and they are classified into two categories: simple and compound planetary gears [31–33, 35, 36, 38, 47, 53]. Simple planetary gears have one sun, one ring, one carrier, and one planet set (i.e., single-stage). There is only one planet in each planet train (i.e., simple) (Figure 1.1). Compound planetary gears involve one or more of the following three types of structures: meshed-planet (as shown in Figure 1.2, there are at least two more more planets in mesh with each other in each planet train), stepped-planet (as shown in Figure 1.3, there exists a shaft connection between two planets in each planet train), and multi-stage structures (as shown in Figure 1.4, the system contains two or more planet sets) [53]. Compared to simple planetary gears, compound planetary gears have the advantages of larger reduction ratio, higher torque-to-weight ratio, and more flexible configurations.

In spite of these advantages, vibration remains a major concern in planetary gear applications. Vibration creates undesirable noise, reduces fatigue life of the whole system, and decreases durability and reliability. Vibration reduction, therefore, is a key to the applications of compound planetary gears. This requires analytical study

Figure 1.1: A typical simple planetary gear: OH-58D planetary gear.

on compound planetary gear dynamics to provide fundamental understanding of the dynamics and guide vibration reduction.

Most research on gear dynamics focuses on single gear pairs [30, 40, 51, 52, 78] or multi-mesh gear systems [24, 60, 62–64]. Recently, considerable progress has been made in the modeling and analysis of simple planetary gears [6, 9, 34, 43–46, 48, 56–59, 75, 77, 90, 97, 98]. Studies on compound planetary gears, however, are limited. Many fundamental analyses that are proved to be essential in other systems and studies have not been performed, including the purely rotational system modeling and the associated modal properties [43, 45, 47, 53, 56, 58, 97], the impact of system parameter changes on natural frequencies and vibration modes (eigensensitivity analysis) [57], the natural frequency veering and crossing patterns [59], the clarification of mesh phase relations [48, 77], the suppression of selected dynamic responses through mesh

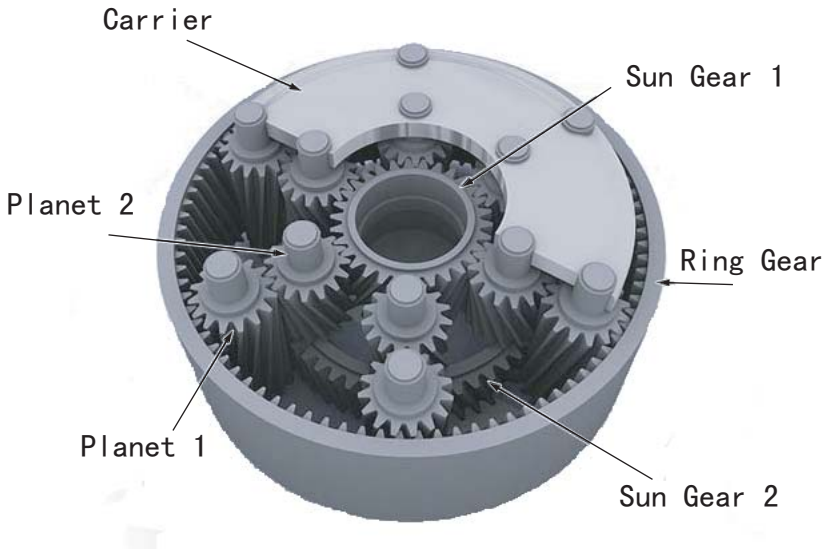

Figure 1.2: A typical meshed-planet structure.

phasing [5, 75], and the parametric instability caused by mesh stiffness variations [61, 98], are not performed.

This study aims at these research gaps and the main objectives are

1. To develop a purely rotational model for general compound planetary gears that can clarify the confusion in previous rotational planetary gear models and analytically prove the associated modal properties,

2. To perform an eigensensitivity analysis based on Kiracofe and Parker's rotational-translational model [53] and derive the eigensensitivities in compact formulae,

3. To inspect the natural frequency veering/crossing phenomena and identify any patterns or general rules,

4. To find a way to analytically describe and calculate all the relative mesh phases in a compound planetary gear,

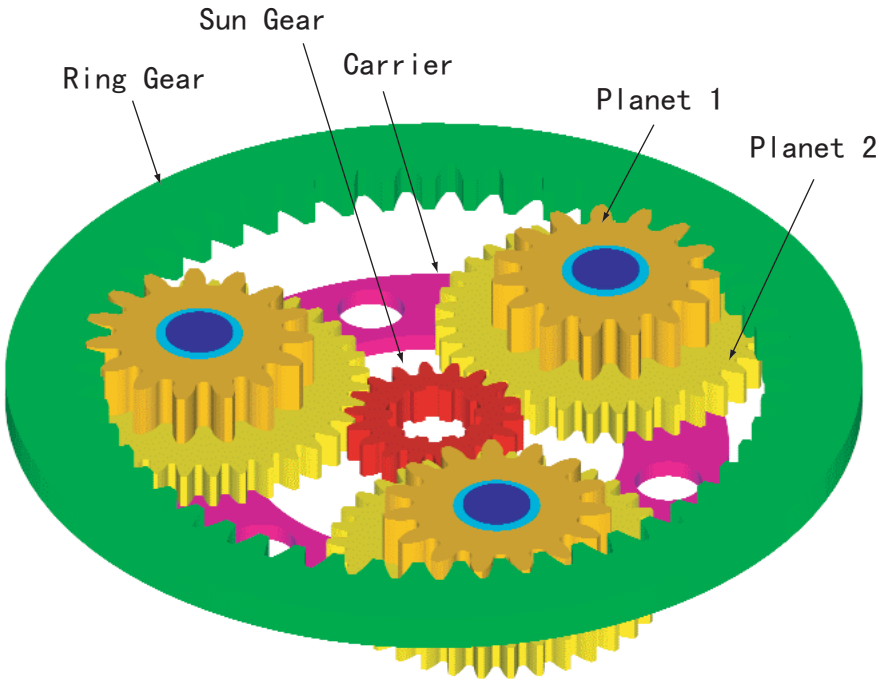

Figure 1.3: A typical stepped-planet structure.

5. To investigate the existence of mesh phasing rules for different compound planetary gear models that can suppress certain vibration,

6. To study the parametric instability caused by mesh stiffness variations and to analytically determine the boundaries for instability regions,

7. To examine the back-side mesh stiffness and to quantify the impact of backlash on the back-side mesh stiffness.

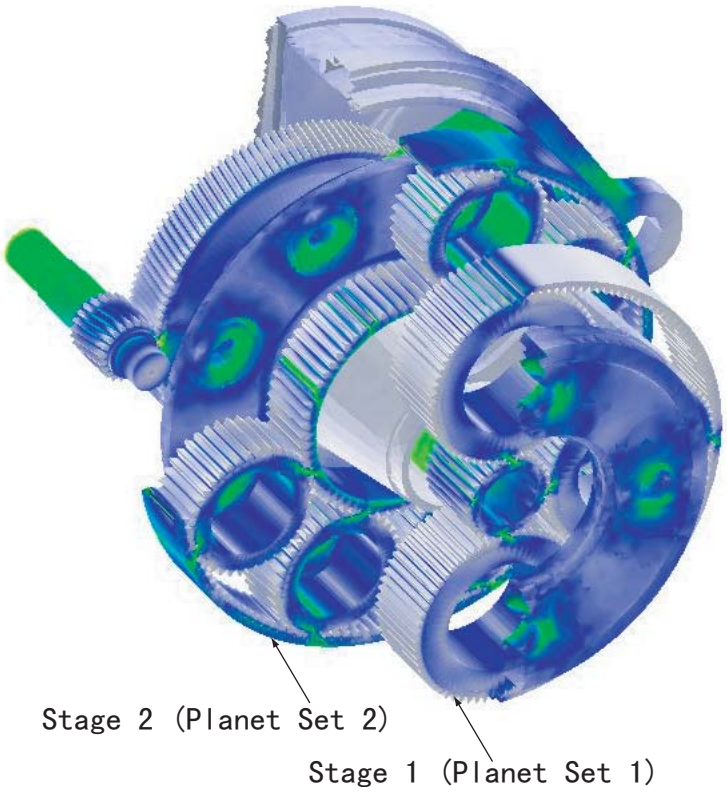

Figure 1.4: A typical multi-stage structure. This picture is courtesy of Chris Cooley using Calyx [96] to generate a 3D FEM example system at the Dynamics and Vibrations Laboratory of The Ohio State University Mechanical and Aerospace Engineering Department.

1.2 Literature Review

Planetary gear dynamics have been extensively studied since 1970. Most of the studies, however, focus only on simple planetary gears. In the area of system modeling and modal properties, Cunliffe et al. [22] developed a free vibration model for an epicyclic gearbox and studied the eigenvalue problem of this specific system. Botman [15] studied the natural frequencies and vibration modes of a simple planetary gear with eighteen degrees of freedom and measured the responses of planetary gears

in aircraft turbine engines [17]. Kahraman [43, 44] developed a simple single-stage planetary gear model with time varying nonlinearity, and carried out a series of researches. He also reduced his model to a purely rotational one, and investigated the eigenvalue problem of the purely rotational model [45]. Lin and Parker used a two-dimensional (2-D), lumped-parameter model for simple planetary gears to analytically examine the vibration properties of equally-spaced [58] and unequally-spaced [56] systems. Wu and Parker inspected the modal properties of simple planetary gears when ring gear deformations are included [79, 97]. Eritenel and Parker [25] extended the investigation scope to helical planetary gears. They set up a three-dimensional (3-D) model, and provided the mathematical proof of the modal properties that generalize the previous findings on 2-D planetary gear models.

No research on the modeling and modal properties of compound planetary gears was conducted until Kahraman [47] proposed a purely rotational model for compound planetary gears. Purely rotational models greatly simplify the analytical study of parametric instabilities and nonlinear dynamic responses while still capturing the main dynamic behavior [5, 6, 9, 61]. Kahraman's compound planetary gear model addresses limited configurations of single-stage planetary gears, and the associated modal properties are not analytically proved. In addition, there are inconsistencies between this model and the purely rotational models for simple planetary gears used by other researchers. In particular, the formulae for gear mesh deflections that are important for the correctness of the model contain mismatches. It is necessary to clarify the confusion in planetary gear modeling and to develop a purely rotational model that it is suitable for general compound planetary gears. In addition, the free vibration properties for this new model should be analytically proved. This model

along with the associated modal properties are crucial for further analytical studies, such as the study on parametric instabilities.

Recently Kiracofe and Parker [53] developed a rotational-translational lumped-parameter model for general compound planetary gears and analytically proved that tuned compound planetary gears (all planet trains within the same planet set are identical in system parameters) have structured modal properties. This model provides a better mathematical description of the system than the purely rotational one. This model is briefly introduced in this work due to the demands of a refined model from some later investigations.

Sensitivity of natural frequencies and vibration modes to system parameters is important for gear design because it shows crucial information on how to tune resonances away from system operating speeds and how to identify the parameters that have the greatest impact on a certain natural frequency. In addition, veering phenomena occur and obstruct the tracing of eigenvalue loci when some system parameter varies [59, 80]. It is desirable to understand the veering and crossing characters of planetary gear natural frequencies in order to complete the understanding on the free vibration properties for planetary gears. Few studies, however, address these topics. The influence of design parameters on planetary gear natural frequencies was merely touched in a few papers, such as Botman's investigation on the change of natural frequencies caused by planet support stiffness [15], Ma and his colleague's study on the impact of errors and misalignment on load sharing [66], the study on unequal planet stiffness by Frater et al. [28], and Saada and Velex's work on the impact of ring gear support stiffness on natural frequencies. General conclusions, however, were not presented. The first analytical inspection on eigensensitivity of planetary gears

was performed by Lin and Parker [57]. They analyzed the eigensensitivities for both tuned and mistuned simple planetary gears using a rotational-translational model. Later, Lin and Parker [59] examined the natural frequency veering and crossing phenomena and discovered the veering/crossing patterns for simple planetary gears. All these studies are limited to simple planetary gears and no work is done for compound planetary gears. To fill the research gap, it is essential to perform a thorough eigensensitivity analysis of the natural frequencies and vibration modes to key compound planetary gear parameters, especially the parameters associated with meshed-planet, stepped-planet, and multi-stage structures. In addition, the examinations on natural frequency veering/crossing phenomena in general compound planetary gears is wanted to complete the understandings on compound planetary gear free vibration problem.

Mesh phase refers to the phase lag between gear meshes and it is unique to multi-mesh gear systems. Proper incorporation of mesh phases into analytical models is a key for the correctness of planetary gear models. The importance of mesh phase to planetary gear dynamics has been recognized in past researches. Hidaka et al. [41] explored the influence of mesh phase on the dynamic behavior of simple planetary gears. Lots of other studies [8, 43, 44, 48, 94] considered mesh phases in the planetary gear dynamic models. But there are discrepancies between these studies on the understanding of mesh phases. Parker and Lin [77] clarified the confusions on simple planetary gear mesh phases and provided an analytical description of mesh phase relations in terms of fundamental gear parameters. The mesh phasing relations in [77], however, are only for simple planetary gears and do not apply to compound planetary gears, because the meshed-planet, stepped-planet, and multi-stage structures

that are unique to compound planetary gears add the complexity of mesh phase relations, and make some key assumptions that are necessary for the derivation of mesh phases relations in [77], such as the assumption of one mesh frequency, be invalid for compound planetary gears. It is, hence, critical to have a clear understanding of compound planetary gear mesh phases and to analytically determine the mesh phases that are needed for any analytical studies on static or dynamic responses.

Previous investigations on gear dynamics show that proper mesh phasing can suppress selected dynamic responses and help minimize noise and vibration in the operating range of transmission systems. Schlegel and Mard [86], Palmer and Fuehrer [74], Hidaka et al. [41], Platt and Leopold [83], Kahraman [48], and Kahraman and Blankenship [48] experimentally or numerically illustrated the effectiveness of simple planetary gear mesh phasing in reducing noise and vibration. Parker [75] analytically explained the suppression of selected translational and rotational mode responses through mesh phasing in simple planetary gears. As an extension to [75], Ambarisha and Parker [5] derived the rules to suppress planet mode responses in a 2-D simple planetary model through mesh phasing and proposed the mesh phasing rules for a purely rotational simple planetary gear model. Eritenel and Parker [26] inspected the elimination of the net force and moment fluctuations at certain harmonics on the central components (sun, ring, and carrier) of a 3-D planetary gear model under different mesh phasing conditions. In order to utilize mesh phasing to reduce noise and vibration in real compound planetary gear applications, it is important to analytically investigate and drive the mesh phasing rules which provide the guidance to suppress selected responses by minor adjustments in fundamental system parameters.

A number of studies suggest that gear mesh stiffness variation has a dramatic impact on the static and dynamic behavior of gear systems and mesh stiffness variations combines with geometric errors and tooth micro-geometry modifications are the main source of parametric instability for gear systems. The parametric instabilities of single-pair gears are extensively examined in [3, 11, 13, 70]. For multi-mesh gears, Tordion and Gauvin [92] and Benton and Seireg [11] analyzed the instabilities of two-stage gear systems but gave contradictory conclusions. The confusion was clarified by Lin and Parker [60]. Only a few studies explore the parametric instabilities for planetary gears and most of them are computational investigations whose scopes are limited to simple planetary gears. For example, August and Kasuba [8] numerically calculated the dynamic responses of a simple planetary gear with three sequentially-phased planets when the mesh stiffnesses are time-varying. Velex and Flamand [94] did a similar work. The analytical inspection on planetary gear parametric instability was not addressed until Lin and Parker [61] investigated the parametric instability of simple planetary gears caused by mesh stiffness variation and analytically determined the instability boundaries. Wu and Parker [98] expanded the investigative scope to simple planetary gears with elastic continuum ring gears. Similar analytical studies on compound planetary gears are yet to be performed. Because meshed-planet, stepped-planet, and multi-stage structures distinguish compound planetary gears from simple planetary gears, the parametric instability that is related to these three types of structures is the focus of this study, and the key problems that are unique to compound planetary gears, such as how multiple mesh frequencies affect the instability boundaries, are addressed in this work.

Recent investigations on gear dynamics [34,39,54,84] indicates that tooth wedging (or tight mesh), the simultaneous drive-side and back-side contacts in certain gear meshes, is possible and such phenomena are observed in planetary gear applications [34]. In order to fully understand the impact of back-side contact on compound planetary gear failures, it is important to set up a model that includes the accurate description of the back-side contact mesh stiffness. In addition, the study on anti-backlash gear dynamics requires the analytical description of back-side mesh stiffness. In spite of these needs, the analytical determination of the back-side mesh stiffness is not addressed in any published literature. This work analytically determines back-side mesh stiffnesses and clarifies the relation between drive-side and back-side mesh stiffnesses.

1.3 Scope of Investigation

The scope of this project is to advance the modeling and understanding of compound planetary gear dynamics and analytically examine certain critical factors affecting noise and vibration of compound planetary gear. A purely rotational compound planetary gear model and the associated modal properties are presented in Chapter 2. These models provide the foundation for the subsequent analyses in this work. Sensitivity of natural frequencies and vibration modes to system parameters and natural frequency veering/crossing patterns of general compound planetary gears are investigated in Chapter 3 and 4. The systematical studies on the mesh phasing relations of compound planetary gears present in Chapter 5, and the suppression of selected compound planetary gear dynamic responses through mesh phasing are studied in chapter 6. In Chapter 7, the parametric instability of general compound planetary

gears caused by mesh stiffness variation is analytically investigated. Chapter 8 examines the time-varying back-side mesh stiffness and its relation with the drive-side one. The detailed scope of each chapter is as follows.

Chapter 2 develops a purely rotational for general compound planetary gears that involves any combination of meshed-planet, stepped-planet, and multi-stage configurations. In addition to clarify the discrepancies in gear mesh deflection expressions and correcting errors in previously published models, this chapter presents and analytically proves the structured modal properties that are associated with the purely rotational model. The rotational-translational model by Kiracofe and Parker [53] and the well-defined modal properties are also briefly introduced in this chapter.

In Chapter 3, the systematic investigation on general compound planetary gear eigensensitivities are performed. The method to determine the eigensensitivities in a general compound planetary gear is first introduced. By applying the well-defined modal properties of general compound planetary gears, the eigensensitivity expressions for both tuned and mistuned systems are simplified and expressed in compact form. The relationships between eigensensitivities and modal strain/kinetic energies are studied and the results indicate that the modal strain/kinetic energy distribution plots are effective tools to identify which system parameters have the greatest impact on tuning the related natural frequency.

Chapter 4 examines the natural frequency veering and crossing phenomena in compound planetary gears. By calculating the coupling factors between two frequency loci and applying the well-defined modal properties and eigensensitivies, the veering/crossing patterns for general compound planetary gears are derived for rotational, translational, and planet tuned parameters, as well as mistuned parameters.

Compound planetary gear mesh phase relationships that are critical for the correctness of models involving mesh stiffness variations are analytically investigated in Chapter 5. This chapter defines and calculates all the mesh phases for general compound planetary gears. In addition to derive a complete and simple procedure to determine all the necessary relative phases, the specific relationships between train-level relative phases are also derived by applying the assembly conditions of compound planetary gears. The results are numerically verified by Calyx [96] that precisely tracks gear tooth contacts without any predefined relations.

In Chapter 6, the rules to suppress selected dynamic responses and resonances through mesh phasing are analytically investigated for both purely rotational and rotational-translational models of general compound planetary gears.

Chapter 7 studies the parametric instability of general compound planetary gears that are caused by mesh stiffness variations. Parametric instability boundaries are analytically derived in closed-form expressions in terms of gear parameters for different modal and phasing conditions. Both individual and mutual (unique to compound planetary gears with multiple mesh frequencies) excitations are inspected in this chapter.

As the expansion of the scope for this work, chapter 8 investigates the phenomenon of back-side gear mesh contact, analytically derives the relationship between the drive-side and back-side mesh stiffnesses, and quantitatively evaluates the impacts of backlash on the phase lag of the back-side mesh stiffness. The resultant analytical formulae are confirmed by the simulation results from Calyx [96].

Chapter 2: COMPOUND PLANETARY GEAR MODELS AND ASSOCIATED MODAL PROPERTIES

The lumped parameter models of compound planetary gears are the bases for further dynamic analysis, and the associated modal properties are critical to understand the dynamic behavior of such systems. In this chapter, a purely rotational model for general compound planetary gears that greatly simplifies further analytical work is first developed. This model clarifies the conflicting gear mesh deflection expressions in prior research. In addition, the structured vibration properties are analytically proven.

A rotational-translational compound planetary model developed by Kiracofe and Parker [53] is briefly introduced in the later part of this chapter. This model provides more accurate description of compound planetary gears than the purely rotational one. The well-defined modal properties are essential for further analysis on general compound planetary gear dynamics in this work.

2.1 Purely Rotational Model and Vibration Modes of Compound Planetary Gears

Compared to planetary gear models with three or more degrees of freedom per component [22, 36, 43, 53, 56–59, 85, 94], purely rotational degree of freedom models

simplify the analytical investigation of gear vibration and nonlinear response while keeping the main dynamic behavior generated by tooth mesh forces. Such models have proven useful in studies of simple (no meshed or stepped planet structures), single-stage planetary gears [6,8,9,61]. Kahraman [47] built purely rotational models for single-stage compound planetary gears. He derived equations of motion for each configuration and summarized the vibration properties from numerical results. The results apply only to the specific configurations in [47].

The present work examines compound planetary gears that involve one or more of stepped-planet, meshed-planet, and multi-stage configurations. The objectives are to develop a purely rotational model that is suitable for compound planetary gears with general configurations, to demonstrate the natural frequency and vibration mode properties, and to analytically prove these structured vibration properties.

In addition, this study clarifies discrepancies in past planetary gear rotational models that appear inconsistent in some places [6,9,45,47,61]. For example, the gear mesh deflection expressions are different in compound [47] and simple planetary gear rotational models [6,45,61]. Some of these models are incorrect in handling gear mesh deflections. Others are correct but do not provide enough detail to expose the source of differences with other models. This study clarifies the confusion.

2.1.1 Purely Rotational Model of Compound Planetary Gears

The purely rotational model of an example two-stage compound planetary gear is shown in Figure 2.1 (no bearing/shaft stiffnesses are shown). Each carrier, central gear (i.e., sun gear or ring gear), and planet has a single rotational degree of freedom.

All external supports and shaft connections are modeled as linear torsional stiffnesses. The gear meshes are represented by stiffness elements, which could be time-varying or nonlinear depending on the research needs.

Figure 2.1 also illustrates the concepts of planet train and planet set. A planet set is all the planets associated with a particular carrier. Each planet set is divided into several planet trains. Two planets are considered to be in the same planet train if they are in mesh with each other (meshed planets) or connected to each other by a shaft (stepped planets) [53].

Choice of Coordinates

The absolute rotations of central gear j and carrier i are $\hat{\theta}_g^j$ and $\hat{\theta}_c^i$. $\bar{\theta}_g^j$ and $\bar{\theta}_c^i$ are the rotations incurred by the nominal constant rotation speeds of central gear j and carrier i, respectively. The system coordinates for central gear j and carrier i are

$$\theta_g^j = \hat{\theta}_g^j - \bar{\theta}_g^j \tag{2.1}$$

$$\theta_c^i = \hat{\theta}_c^i - \bar{\theta}_c^i \tag{2.2}$$

The coordinate for planet m in train l of planet set i (θ_p^{ilm}) is the rotational vibration of this planet *relative to* its associated carrier i, that is,

$$\theta_p^{ilm} = (\hat{\theta}_p^{ilm} - \bar{\theta}_p^{ilm}) - (\hat{\theta}_c^i - \bar{\theta}_c^i) \tag{2.3}$$

where $\hat{\theta}_p^{ilm}$ is the absolute rotation and $\bar{\theta}_p^{ilm}$ is the rotation caused by the nominal constant speed of this planet.

Researchers studying previous purely rotational planetary gear models [6,9,45,47, 61] have chosen other coordinates. In order to compare different models, in the rest

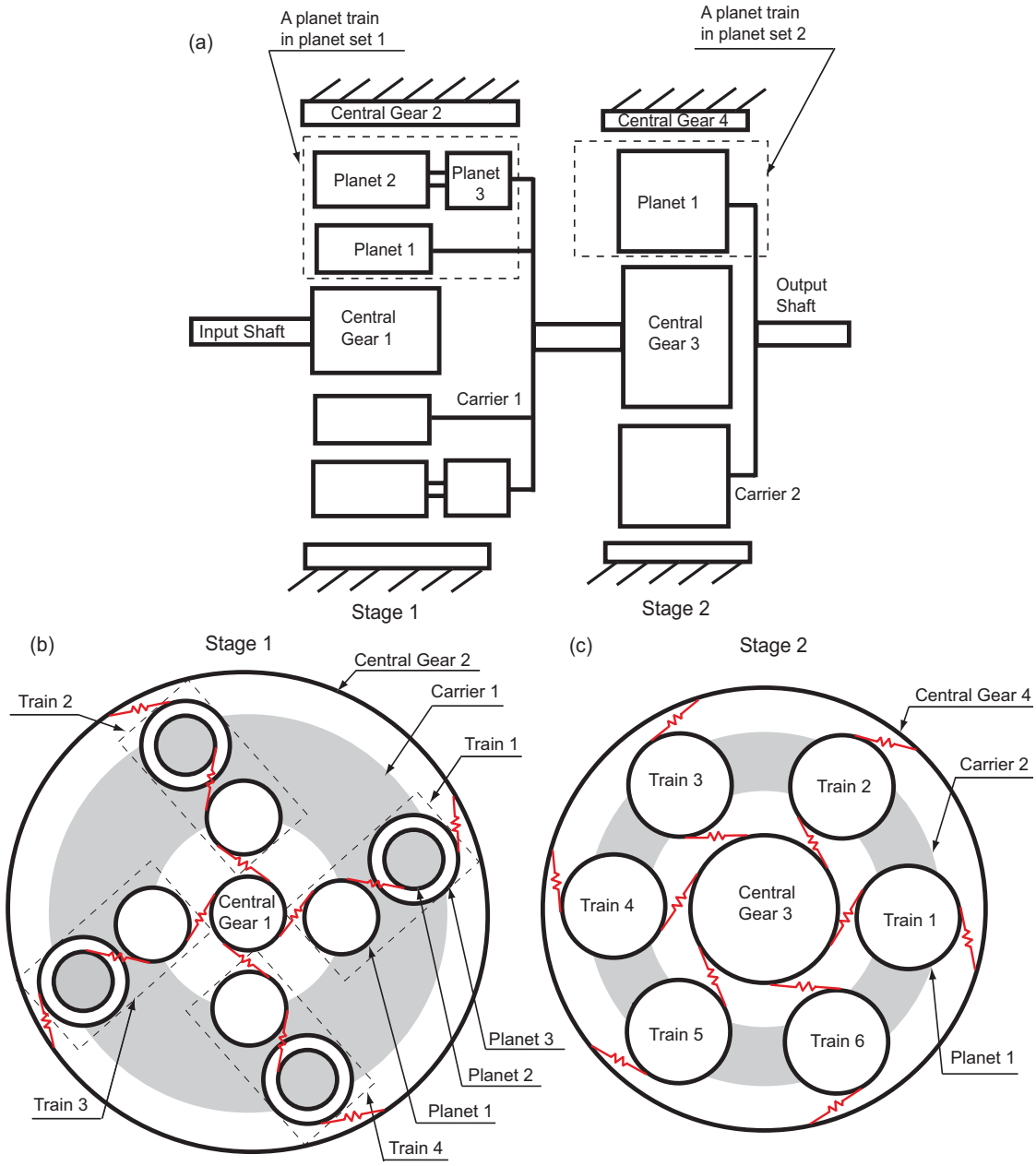

Figure 2.1: The example system. All gear meshes are represented by the springs in red color.

of this study the coordinates and variables of previous studies are cast in the notation defined in this study.

Clarification of Gear Mesh Deflections

The expression for deflection of a gear mesh depends on the gear mesh model, coordinate definition, choice of positive rotation directions, and the components involved in the gear mesh. In this study, gear mesh deflections are calculated along the line of action tangent to the base circles of the meshing gears. Compressive deflection along the line of action between two gears is chosen to be positive deflection. Furthermore, counterclockwise rotation is the positive direction for all components. The two types of gear meshes in compound planetary gears are planet-planet meshes and central gear-planet meshes (i.e., sun-planet and ring-planet meshes).

Figure 2.2 shows the two possible cases of the planet-planet mesh between planet m and planet q in train l of planet set i. For case (1), the points A and B are the ends of the mesh spring that are hinged on planet m and planet q, respectively. The gear mesh deflection is actually the change of the length of line AB that is caused by the vibratory motions of points A and B. Considering the length of line AB is independent of the choice of reference frames and the points A and B are moving with carrier i, it is convenient to calculate the mesh deflection in the reference frame rotating together with carrier i.

Figure 2.3 illustrates the deflection of the gear mesh spring in the moving reference frame that is fixed to carrier i. The points A_1 and B_1 are the ends of the mesh spring when planets m and q rotate θ_p^{ilm} and θ_p^{ilq} in the reference frame. Because θ_p^{ilm} and θ_p^{ilq} are small, the length of A_1B_1 (the deformed mesh spring) is approximated by A_2B_2,

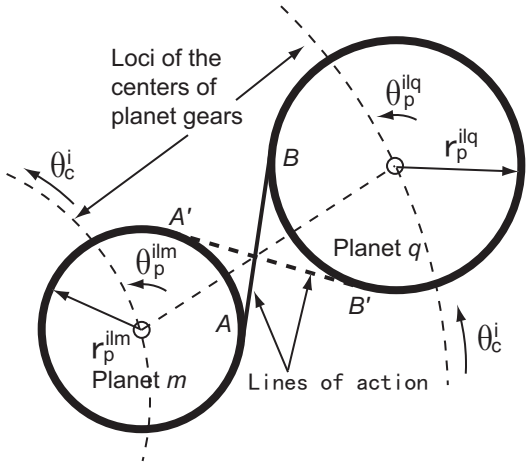

Figure 2.2: The two cases of a planet-planet mesh: (1) along the line of action of the solid line from A to B, and (2) along the line of action of the dashed line from A' to B'.

the projection of line A_1B_1 on line AB. Thus, the gear mesh deflection is approximately the difference in length between the two lines AB and A_2B_2. Let $\mathbf{e_1}$ be the positive unit vector along line AB. $\overrightarrow{AA_2} = \delta A\mathbf{e_1}$ and $\overrightarrow{BB_2} = \delta B\mathbf{e_1}$ ($\delta B < 0$ for positive θ_p^{ilq}) are the displacements of points A and B. Application of geometric and trigonometric relations in Figure 2.3 yields $\delta A = r_p^{ilm}\tan\theta_p^{ilm} - r_p^{ilm}(1/\cos\theta_p^{ilm} - 1)\sin\theta_p^{ilm} \approx \theta_p^{ilm}r_p^{ilm}$ and $\delta B = r_p^{ilq}\tan\theta_p^{ilq} - r_p^{ilq}(1/\cos\theta_p^{ilq} - 1)\sin\theta_p^{ilq} \approx -\theta_p^{ilq}r_p^{ilq}$, where r_p^{ilm} and r_p^{ilq} are the base radii of planets m and q. The mesh deflection in this case is

$$\delta_{pp}^{ilmq} = \delta A - \delta B = \theta_p^{ilm}r_p^{ilm} + \theta_p^{ilq}r_p^{ilq} \tag{2.4}$$

In case (2), the approximate displacements of points A' and B' in Figure 2.2 along the line of action are $\delta A' = -\theta_p^{ilm}r_p^{ilm}$ and $\delta B' = \theta_p^{ilq}r_p^{ilq}$. The mesh deflection is

$$\delta_{pp}^{ilmq} = \delta A' - \delta B' = -(\theta_p^{ilm}r_p^{ilm} + \theta_p^{ilq}r_p^{ilq}) \tag{2.5}$$

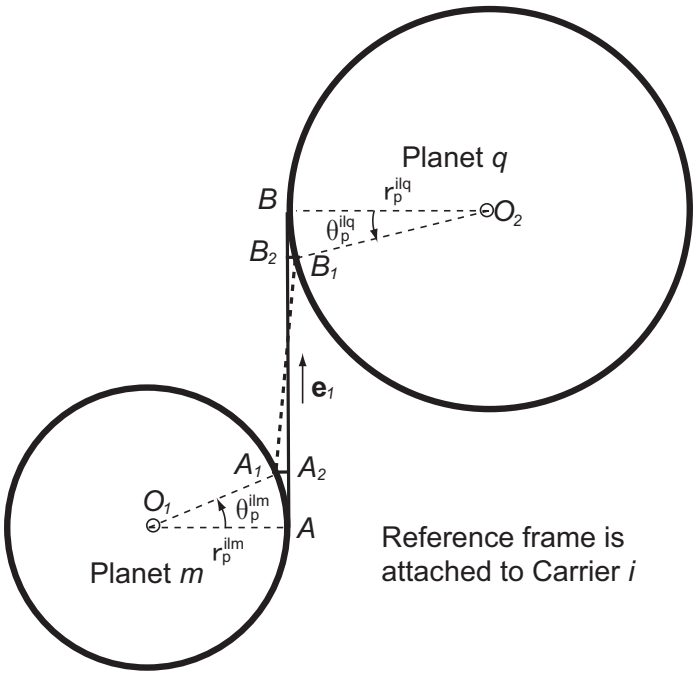

Figure 2.3: The calculation of the gear mesh deflection of Case 1 in Figure 2.

Equations (2.4) and (2.5) differ by a minus sign. They are merged as

$$\begin{aligned} \delta_{pp}^{ilmq} &= S_{pp}^{ilmq}(\theta_p^{ilm} r_p^{ilm} + \theta_p^{ilq} r_p^{ilq}) \\ S_{pp}^{ilmq} &= \begin{cases} 1 & \text{case (1) in Figure 2.2} \\ \text{-1} & \text{case (2) in Figure 2.2} \end{cases} \end{aligned} \tag{2.6}$$

Similarly, Figure 2.4 shows the two cases of an external gear-planet (sun-planet) mesh between central gear j and planet m in train l of planet set i. By the above process, the sun-planet mesh deflection is

$$\begin{aligned} \delta_{gp}^{jilm} &= S_{gp}^{jilm}(\theta_g^j r_g^j - \theta_c^i r_g^j + \theta_p^{ilm} r_p^{ilm}) \\ S_{gp}^{jilm} &= \begin{cases} 1 & \text{case (1) in Figure 2.4} \\ \text{-1} & \text{case (2) in Figure 2.4} \end{cases} \end{aligned} \tag{2.7}$$

For an internal gear-planet mesh (ring-planet mesh, shown in Figure 2.5), the same process yields the mesh deflection

$$\delta_{gp}^{jilm} = S_{gp}^{jilm}(\theta_g^j r_g^j - \theta_c^i r_g^j - \theta_p^{ilm} r_p^{ilm}) \tag{2.8}$$

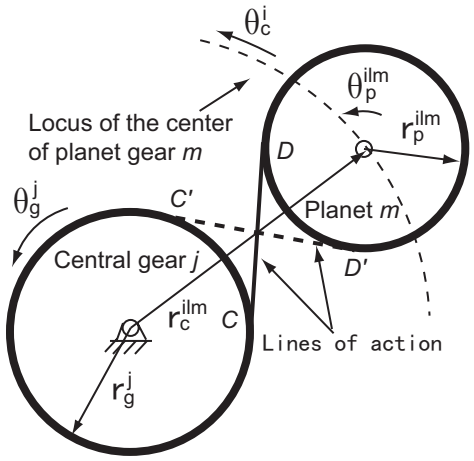

Figure 2.4: The two cases of a sun gear-planet mesh: (1) along the line of action of the solid line from C to D, and (2) along the line of action of the dashed line from C' to D'.

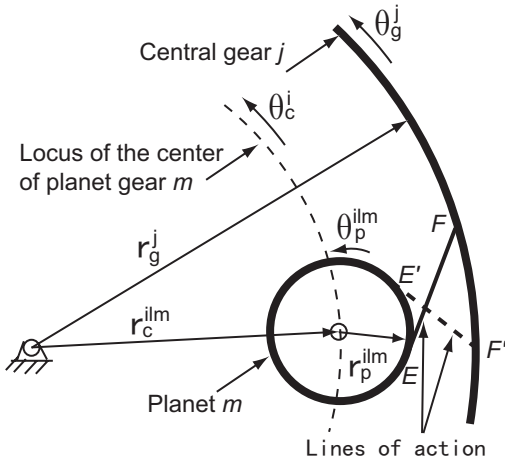

Figure 2.5: The two cases of a ring gear-planet mesh: (1) along the line of action of the solid line from E to F, and (2) along the line of action of the dashed line from E' to F'.

where S_{gp}^{jilm} is +1 for case (1) of Figure 2.5, and -1 for case (2).

By introducing the variable σ_j that equals +1 for an external mesh and -1 for an internal mesh, equations (2.7) and (2.8) are merged into a general expression for central gear-planet mesh deflections as

$$\delta_{gp}^{jilm} = S_{gp}^{jilm}\left(\theta_g^j r_g^j - \sigma^j \theta_p^{ilm} r_p^{ilm} - \theta_c^i r_g^j\right) \tag{2.9}$$

Equations (2.6) and (2.9) are the general formulae for any mesh deflection in general compound planetary gears. Comparisons between these general formulae and the gear mesh deflections in previous studies [6,9,45,47,61] show differences in some cases. Some of these studies derived incorrect gear mesh deflection formulae, such as [61]. Others [6,9,45,47] are correct only under certain circumstances because they did not fully consider the sign of gear mesh deflections. The differences with prior papers are discussed below.

The gear-planet mesh deflection formulae in [6, 9, 45] are the same. The mesh deflection between central gear j and planet m in train l of planet set i from these studies is called $\delta_A\left|_{gp}^{jilm}\right.$ here. In the notation of this study,

$$\begin{aligned}\delta_A\left|_{gp}^{jilm}\right. &= \theta_g^j r_g^j - \sigma^j(\theta_p^{ilm} + \theta_c^i) r_p^{ilm} - \theta_c^i r_c^{ilm}\cos\alpha_{gp}^{jilm} \\ &= \theta_g^j r_g^j - \sigma^j \theta_p^{ilm} r_p^{ilm} - \theta_c^i r_g^j\end{aligned} \tag{2.10}$$

where r_c^{ilm} is the distance between the centers of carrier i and planet m, and α_{gp}^{jilm} is the pressure angle of this gear-planet mesh. Equation (2.10) agrees with equation (2.9) except that it lacks the sign variable S_{gp}^{jilm}. It applies only to case (1) in Figure 2.4. Equation (2.9) is the general form for both cases in Figure 2.4.

The same gear-planet mesh deflection from [61] is called $\delta_B\left|_{gp}^{jilm}\right.$ here. In the notation of this study, this is

$$\delta_B\left|_{gp}^{jilm}\right. = u_g^j - \sigma^j u_p^{ilm} - u_c^i = \theta_g^j r_g^j - \sigma^j \theta_p^{ilm} r_p^{ilm} - \theta_c^i(\sigma^j r_p^{ilm} + r_c^{ilm}) \tag{2.11}$$

Comparing with (2.9), equation (2.11) is incorrect. In addition to missing S_{gp}^{jilm}, the last term in (2.11) does not equal the matching term in (2.9), that is, $-\theta_c^i(\sigma^j r_p^{ilm} + r_c^{ilm}) \neq -\theta_c^i r_g^j$.

Because simple planetary gears have no planet-planet meshes, no comparisons of planet-planet mesh deflection expressions can be made to previous simple planetary gear models.

Comparisons of gear-planet and planet-planet mesh deflections with the compound planetary gear models in [47] are possible. The gear-planet mesh deflection in [47] is called $\delta_C \left|_{gp}^{jilm}\right.$ here. The planet-planet mesh deflection between planet m and planet q in train l of planet set i from [47] is called $\delta_D \left|_{pp}^{ilmq}\right.$. In the notation of this study, these are

$$\begin{aligned} \delta_C \left|_{gp}^{jilm}\right. &= \hat{\theta}_g^j \bar{r}_g^j - \sigma^j \hat{\theta}_p^{ilm} \bar{r}_p^{ilm} - \hat{\theta}_c^i r_c^{ilm} \\ &= \theta_g^j \bar{r}_g^j - \sigma^j \theta_p^{ilm} \bar{r}_p^{ilm} - \theta_c^i \bar{r}_g^j \end{aligned} \tag{2.12}$$

$$\begin{aligned} \delta_D \left|_{pp}^{ilmq}\right. &= (\hat{\theta}_p^{ilm} - \hat{\theta}_c^i)\bar{r}_p^{ilm} + (\hat{\theta}_p^{iln} - \hat{\theta}_c^i)\bar{r}_p^{iln} \\ &= (\theta_p^{ilm} + \bar{\theta}_p^{ilm} - \bar{\theta}_c^i)\bar{r}_p^{ilm} + (\theta_p^{iln} + \bar{\theta}_p^{iln} - \bar{\theta}_c^i)\bar{r}_p^{iln} \\ &= \theta_p^{ilm}\bar{r}_p^{ilm} + \theta_p^{iln}\bar{r}_p^{iln} \end{aligned} \tag{2.13}$$

where $\bar{r}_g^j$ and $\bar{r}_p^{ilm}$ are the pitch radii. Equations (2.12) and (2.13) agree with the general formulae (2.6) and (2.9) except that all the sign variables S_{gp}^{jilm} and S_{pp}^{ilmq} are missing and all the base radii are replaced by their matching pitch radii. The presence of pitch radii in equations (2.12) and (2.13) is as expected considering the use of pitch radius gear mesh model in [47]. The missing sign variables, however, limit equations (2.12) and (2.13) to case (1) in Figures 2.2, 2.4, and 2.5.

Equations of Motion and Eigenvalue Problem

The general system has a carriers and b central gears. A certain stage i has c^i planet trains, and each planet train in stage i has d^i planets.

The Lagrangian of a general compound planetary gear is

$$\begin{aligned}
L = \tfrac{1}{2}\sum_{i=1}^{a}\Bigg\{\Bigg\{I_c^i + \sum_{l=1}^{c^i}\sum_{m=1}^{d^i}[I_p^{ilm} + m_p^{ilm}(r_c^{ilm})^2]\Bigg\}(\dot\theta_c^i + \bar{\dot\theta}_c^i)^2 + \\
2\sum_{l=1}^{c^i}\sum_{m=1}^{d^i} I_p^{ilm}(\dot\theta_p^{ilm} + \bar{\dot\theta}_p^{ilm} - \bar{\dot\theta}_c^i)(\dot\theta_c^i + \bar{\dot\theta}_c^i) + \\
\sum_{l=1}^{c^i}\sum_{m=1}^{d^i} I_p^{ilm}(\dot\theta_p^{ilm} + \bar{\dot\theta}_p^{ilm} - \bar{\dot\theta}_c^i)^2\Bigg\} + \\
\tfrac{1}{2}\sum_{j=1}^{b} I_g^j(\dot\theta_g^j + \bar{\dot\theta}_g^j)^2 - \tfrac{1}{2}\sum_{j=1}^{b}\sum_{i=1}^{a}\sum_{l=1}^{c^i}\sum_{m=1}^{d^i} k_{gp}^{jilm}(\delta_{gp}^{jilm})^2 - \\
\tfrac{1}{2}\sum_{i=1}^{a}\sum_{l=1}^{c^i}\sum_{m=1}^{d^i}\sum_{q=m+1}^{d^i}\Big[k_{pp}^{ilmq}(\delta_{pp}^{ilmq})^2 + k_{p-p,\theta\theta}^{ilmq}(\theta_p^{ilm} - \theta_p^{ilq})^2\Big] - \\
\tfrac{1}{2}\sum_{i=1}^{a} k_{cb}^{i}(\theta_c^i)^2 - \tfrac{1}{2}\sum_{j=1}^{b} k_{gb}^{j}(\theta_g^j)^2 - \tfrac{1}{2}\sum_{i=1}^{a}\sum_{n=i+1}^{a} k_{cc,\theta\theta}^{in}(\theta_c^i - \theta_c^n)^2 - \\
\tfrac{1}{2}\sum_{i=1}^{a}\sum_{j=i}^{b} k_{cg,\theta\theta}^{ij}(\theta_c^i - \theta_g^j)^2 - \tfrac{1}{2}\sum_{j=1}^{a}\sum_{h=j+1}^{b} k_{gg,\theta\theta}^{jh}(\theta_g^j - \theta_g^h)^2
\end{aligned} \tag{2.14}$$

where θ_c^i and θ_g^j are the rotational vibrations of carrier i and central gear j, θ_p^{ilm} is the rotational vibration of planet m in train l of planet set i relative to its associated carrier i, $\bar{\dot\theta}_c^i$ and $\bar{\dot\theta}_g^j$ are the nominal constant rotation speeds of carrier i and central gear j, $\bar{\dot\theta}_p^{ilm}$ is the nominal constant rotation speed of planet m in train l of planet set i, $\dot\theta_c^i$ and $\dot\theta_g^j$ are the rotational vibration speeds of carrier i and central gear j, and $\dot\theta_p^{ilm}$ is the rotational vibration speed of planet m in train l of planet set i relative to its associated carrier i.

Lagrange's equation yields the $a + b + \sum_{i=1}^{a} c^i d^i$ equations of motion. For the a carriers, these are

$$\begin{aligned}
&I^i_{ce}\ddot{\theta}^i_c + \sum_{l=1}^{c^i}\sum_{m=1}^{d^i} I^{ilm}_p \ddot{\theta}^{ilm}_p + k^i_{cb}\theta^i_c + \\
&\sum_{j=1}^{b}\sum_{l=1}^{c^i}\sum_{m=1}^{d^i} \frac{\partial \delta^{jilm}_{gp}}{\partial \theta^i_c} k^{jilm}_{gp}\delta^{jilm}_{gp} + \\
&\sum_{n=i+1}^{a} k^{in}_{cc,\theta\theta}(\theta^i_c - \theta^n_c) + \sum_{j=1}^{b} k^{ij}_{cg,\theta\theta}(\theta^i_c - \theta^j_g) = \tau^i_c \qquad i = 1, \cdots, a \\
&I^i_{ce} = I^i_c + \sum_{l=1}^{c^i}\sum_{m=1}^{d^i} I^{ilm}_p + \sum_{l=1}^{c^i}\sum_{m=1}^{d^i} m^{ilm}_p (r^{ilm}_c)^2
\end{aligned} \tag{2.15}$$

where $\ddot{\theta}^i_c$ is the rotational acceleration of carrier i, and τ^i_c is the externally applied torque on carrier i. The b equations of motion for the central gears are

$$\begin{aligned}
&I^j_g \ddot{\theta}^j_g + k^j_{gb}\theta^j_g + \sum_{i=1}^{a}\sum_{l=1}^{c^i}\sum_{m=1}^{d^i} \frac{\partial \delta^{jilm}_{gp}}{\partial \theta^j_g} k^{jilm}_{gp}\delta^{jilm}_{gp} + \\
&\sum_{h=j+1}^{a} k^{jh}_{gg,\theta\theta}(\theta^j_g - \theta^h_g) + \sum_{i=1}^{a} k^{ij}_{cg,\theta\theta}(\theta^j_g - \theta^i_c) = \tau^j_g \qquad j = 1, \cdots, b
\end{aligned} \tag{2.16}$$

where $\ddot{\theta}^j_g$ is the rotational acceleration of central gear j, and τ^j_g is the externally applied torque on central gear j. The $\sum_{i=1}^{a} c^i d^i$ planet equations of motion are

$$\begin{aligned}
&I^{ilm}_p \ddot{\theta}^{ilm}_p + I^{ilm}_p \ddot{\theta}^i_c + \sum_{j=1}^{b} \frac{\partial \delta^{jilm}_{gp}}{\partial \theta^{ilm}_p} k^{jilm}_{gp}\delta^{jilm}_{gp} \\
&+ \sum_{q=1, q\neq m}^{d^i} \left[\frac{\partial \delta^{ilmq}_{pp}}{\partial \theta^{ilm}_p} k^{ilmq}_{pp}\delta^{ilmq}_{pp} + k^{ilmq}_{p-p,,\theta\theta}(\theta^{ilm}_p - \theta^{ilq}_p) \right] = 0 \\
&i = 1, \cdots, a;\ l = 1, \cdots, c^i;\ m = 1, \cdots, d^i
\end{aligned} \tag{2.17}$$

where $\ddot{\theta}^{ilm}_p$ is the rotational acceleration of planet m in train l of planet set i relative to its associated carrier i.

When all gear meshes are modeled as constant stiffnesses, the eigenvalue problem is

$$\omega^2 \mathbf{M}\boldsymbol{\theta} = \mathbf{K_{iv}}\boldsymbol{\theta} \tag{2.18}$$

$$\boldsymbol{\theta} = [\underbrace{\theta^1_c \cdots \theta^a_c}_{\text{Carriers}} \mid \underbrace{\theta^1_g \cdots \theta^b_g}_{\text{Central gears}} \mid \underbrace{\boldsymbol{\theta}^1_{ps} \cdots \boldsymbol{\theta}^a_{ps}}_{\text{Planet sets}}]^T \tag{2.19}$$

$$\boldsymbol{\theta}_{ps}^{i} = [\theta_{pt}^{i1} \cdots \theta_{pt}^{ic^i}]^T \quad i = 1, \cdots, a \tag{2.20}$$

$$\theta_{pt}^{il} = [\theta_{p}^{il1} \cdots \theta_{p}^{ild^i}]^T \quad i = 1, \cdots, a;\ l = 1, \cdots, c^i \tag{2.21}$$

$$\mathbf{M} = \begin{bmatrix} \mathbf{I}_c & \mathbf{0} & \mathbf{I}_{c,ps} \\ & \mathbf{I}_g & \mathbf{0} \\ symm. & & \mathbf{I}_{ps} \end{bmatrix} \tag{2.22}$$

$$\mathbf{K}_{iv} = \mathbf{K}_b + \mathbf{K}_m \tag{2.23}$$

$$\mathbf{K}_b = diag(k_{cb}^1, \ \cdots, k_{cb}^a, \ k_{gb}^1, \ \cdots, k_{gb}^b, \ 0, \ \cdots, 0) \tag{2.24}$$

$$\mathbf{K}_m = \begin{bmatrix} \mathbf{K}_c & \mathbf{K}_{c,g} & \mathbf{K}_{c,ps} \\ & \mathbf{K}_g & \mathbf{K}_{g,ps} \\ symm. & & \mathbf{K}_{ps} \end{bmatrix} \tag{2.25}$$

$\mathbf{K}_{iv}$ is the time-invariant stiffness matrix. Details of the sub-matrices in $\mathbf{M}$ and $\mathbf{K}_m$ are given in Appendix A.

In contrast to previous simple planetary gear models [6,9,45,61], the mass matrix here is non-diagonal. This is caused by choosing of the rotational planet vibrations *relative to* their associated carriers as the planet coordinates. As a result of this choice of planet coordinates, the left hand side of equation (2.15) contains the term $\sum_{l=1}^{c^i} \sum_{m=1}^{d^i} I_p^{ilm} \ddot{\theta}_p^{ilm}$ that causes the non-diagonal elements I_p^{ilm} in the mass matrix.

Equation (2.18) is expanded into three groups of equations for the carriers, central gears, and planet sets, respectively,

$$\begin{aligned} &(k_{cb}^i - \omega^2 I_c^i)\theta_c^i - \omega^2 \sum_{l=1}^{c^i} \sum_{m=1}^{d^i} I_p^{ilm} \theta_p^{ilm} + \sum_{h=1}^{a} k_c^{ih} \theta_c^i + \\ &\sum_{j=1}^{b} k_{c,g}^{ij} \theta_g^j + \left(\mathbf{k}_{c,ps}^i\right)^T \boldsymbol{\theta}_{ps}^i = 0 \end{aligned} \qquad i = 1, \cdots, a \tag{2.26}$$

$$(k_{gb}^j - \omega^2 I_g^j)\theta_g^j + \sum_{n=1}^{b} k_g^{jn} \theta_g^j + \sum_{i=1}^{a} k_{c,g}^{ij} \theta_c^i + \sum_{i=1}^{a} \left(\mathbf{k}_{g,ps}^{ji}\right)^T \boldsymbol{\theta}_{ps}^i = 0 \quad j = 1, \cdots, b \tag{2.27}$$

$$(\mathbf{K}_{ps}^i - \omega^2 \mathbf{I}_{ps}^i)\boldsymbol{\theta}_{ps}^i - \omega^2 \theta_c^i \mathbf{I}_{c,ps}^i + \theta_c^i \mathbf{k}_{c,ps}^i + \sum_{j=1}^{b} \theta_g^j \mathbf{k}_{g,ps}^{ji} = 0 \quad i = 1, \cdots, a \tag{2.28}$$

where $\mathbf{k}_{c,ps}^i$, $\mathbf{k}_{g,ps}^{ji}$, $\mathbf{I}_{c,ps}^i$, and $\boldsymbol{\theta}_{ps}^i$ are all $c^i d^i \times 1$ column vectors given in Appendix A.

2.1.2 Characteristics of Natural Frequencies and Vibration Modes

Numerical results from (2.18) show that the natural frequencies and vibration modes have distinctive properties when all planet trains within the same planet set are identical and equally spaced. All vibration modes can be classified into two types: overall modes and planet modes.

In an overall mode, all planet trains in the same planet set have identical motions. There are exactly $a + b + \sum_{i=1}^{a} d^i$ overall modes. Each mode is associated with a distinct natural frequency. Figure 2.6 shows a typical overall mode for the compound planetary gear in Figure 2.1 with the system parameters in Table 2.1.

Planet modes exist when the system has a stage with two or more planet trains. In planet modes, only the planets in one stage have motion, and all other components have no motion. Stage i has d^i sets of degenerate (for $c^i \geqslant 3$) planet modes, with each having natural frequency multiplicity $c^i - 1$. The total number of planet modes of stage i is $(c^i - 1)d^i$. In addition, any planet train's motion in this stage is a scalar multiple of an arbitrarily chosen planet train's motion. Figure 2.7 shows a set of planet modes of stage 1 for the system in Figure 2.1 and Table 2.1. The complete list of natural frequencies is collected in Table 2.2.

The above properties differ from the summary of vibration properties in [47] in two ways. Firstly, [47] separates a "rigid body" mode from the above two types. Secondly, the number of overall modes is $a + b + \sum_{i=1}^{a} d^i - 2$ in [47], instead of $a + b + \sum_{i=1}^{a} d^i$.

The rigid body mode that [47] separates from all other modes is actually an overall mode. In the rigid body mode all planet trains in the same planet set have identical motions, which is the characteristic of an overall mode. The rigid body modes exist

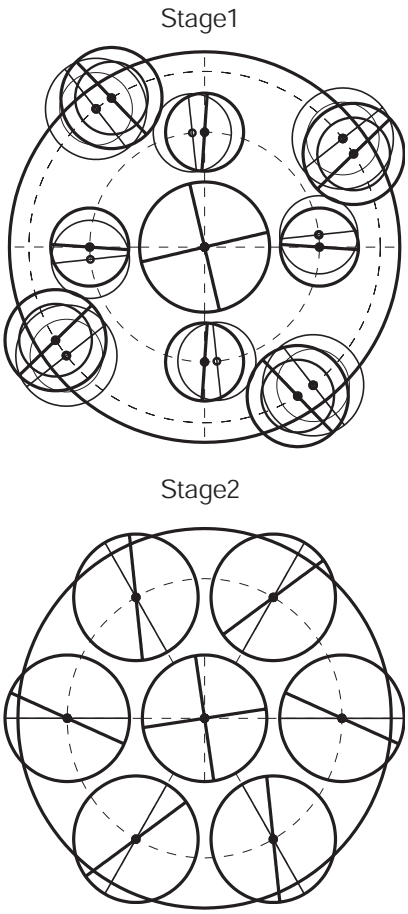

Figure 2.6: The overall mode (associated with ω_5=902 Hz) of the example system in Figure 2.1 and Table 2.1. The deflections of carriers are not shown.

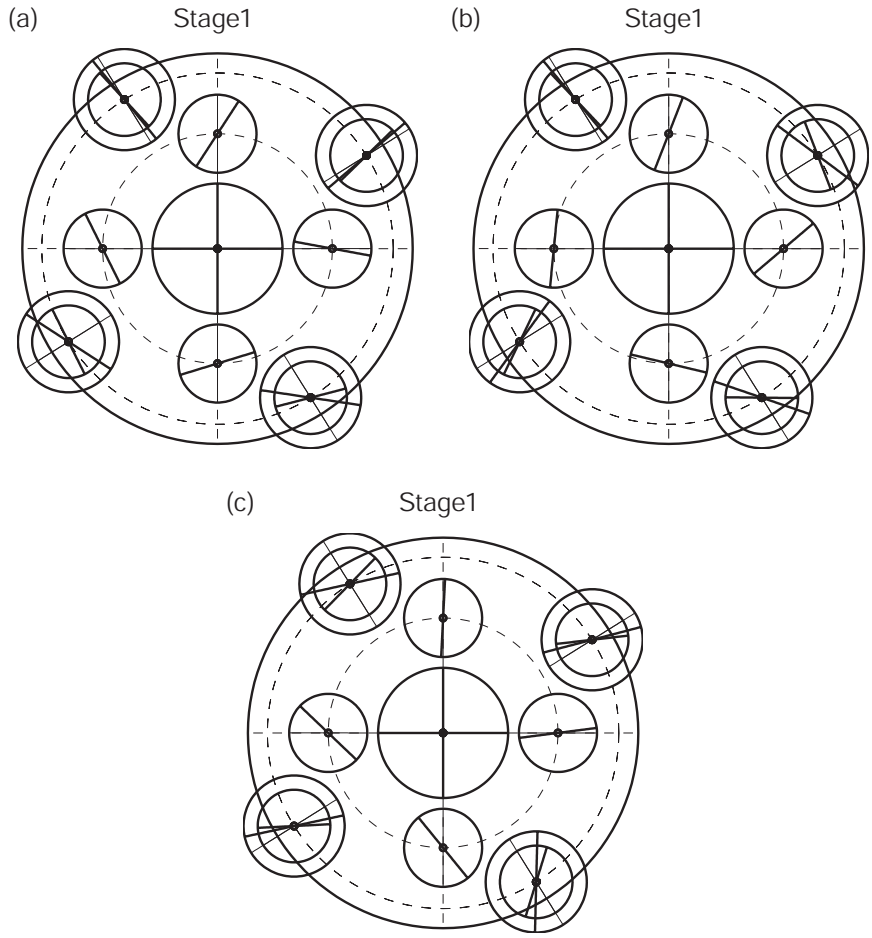

Figure 2.7: The three planet modes (associated with $\omega_{14,15,16}$=3067 Hz) of the example system in Figure 2.1 and Table 2.1. The mode shapes of stage 2 are not shown here, because no component in stage 2 has motion.

in [47] because all configurations discussed therein have unconstrained input and output components. If one or both of the input/output components are constrained or spring-mounted to ground, no rigid body mode exists.

The second difference with the summary of modal properties in [47] is because [47] is based on a restricted set of configurations. All the configurations in [47] have a fixed central gear or carrier, so the number of degrees of freedom are reduced by one due to that fixed component.

In what follows, the above vibration mode properties are proved mathematically. Proposed candidate modes for each type of mode based on the above properties are shown to satisfy the eigenvalue problem. By showing that the total number of eigenvalues obtained in this way equals the total number of degrees of freedom of the system, the two mode types are proven to be an exhaustive list of the possible mode types.

Overall Modes

A candidate overall mode from (2.19)-(2.21) is

$$\begin{array}{l} \boldsymbol{\theta} = [\theta_c^1 \cdots \theta_c^a | \theta_g^1 \cdots \theta_g^b | \boldsymbol{\theta}_{ps}^1 \cdots \boldsymbol{\theta}_{ps}^a]^T \\ \boldsymbol{\theta}_{ps}^i = [\boldsymbol{\theta}_{pt}^{i1} \cdots \boldsymbol{\theta}_{pt}^{i1}]^T \qquad\qquad i = 1, \cdots, a \\ \boldsymbol{\theta}_{pt}^{i1} = [\theta_p^{i11} \cdots \theta_p^{i1d^i}]^T \end{array} \tag{2.29}$$

Note that all d^i planet trains in planet set i have the same deflection. Insertion of (2.29) into (2.26)-(2.28) yields

$$\begin{array}{l} (k_{cb}^i - \omega^2 I_c^i)\theta_c^i - \omega^2 c^i \sum_{m=1}^{d^i} I_p^{i1m}\theta_p^{i1m} + \\ \sum_{h=1}^{a} k_c^{ih}\theta_c^i + \sum_{j=1}^{b} k_{c,g}^{ij}\theta_g^j + c^i \left(k_{c,pt}^{i1}\right)^T \theta_{pt}^{i1} = 0 \end{array} \qquad i = 1, \cdots, a \tag{2.30}$$

$$\begin{array}{l} (k_{gb}^j - \omega^2 I_g^j)\theta_g^j + \sum_{n=1}^{b} k_g^{jn}\theta_g^j + \\ \sum_{i=1}^{a} k_{c,g}^{ij}\theta_c^i + c^i \sum_{i=1}^{a} \left(k_{g,pt}^{ji1}\right)^T \theta_{pt}^{i1} = 0 \end{array} \qquad j = 1, \cdots, b \tag{2.31}$$

$$\left\{ \begin{bmatrix} k_p^{i111} & \dots & k_p^{i11d^i} \\ \vdots & \ddots & \vdots \\ k_p^{i1d^i1} & \dots & k_p^{i1d^id^i} \end{bmatrix} - \omega^2 \begin{bmatrix} I_p^{i11} & & 0 \\ & \ddots & \\ 0 & & I_p^{i1d^i} \end{bmatrix} \right\} \begin{bmatrix} \theta_p^{i11} \\ \vdots \\ \theta_p^{i1d^i} \end{bmatrix}$$
$$-\omega^2\theta_c^i \begin{bmatrix} I_p^{i11} \\ \vdots \\ I_p^{i1d^i} \end{bmatrix} + \theta_c^i \begin{bmatrix} k_{c,p}^{i11} \\ \vdots \\ k_{c,p}^{i1d^i} \end{bmatrix} + \sum_{j=1}^{b} \theta_g^j \begin{bmatrix} -\sigma^j k_{gp}^{ji11} r_g^j r_p^{i11} \\ \vdots \\ -\sigma^j k_{gp}^{ji1d^i} r_g^j r_p^{i1d^i} \end{bmatrix} = 0 \qquad (2.32)$$
$$i = 1, \cdots, a$$

Equations (2.30) and (2.31) give a and b independent equations, respectively. For each i, the matrix equation (2.32) contains d^i independent component equations. Thus, equations (2.30)-(2.32) yield $a + b + \sum_{i=1}^{a} d^i$ linear, homogeneous equations with $a + b + \sum_{i=1}^{a} d^i$ unknowns from equation (2.29) and the undetermined eigenvalue ω^2. This forms a reduced eigenvalue problem. From the $a + b + \sum_{i=1}^{a} d^i$ solutions of this reduced eigenvalue problem, overall modes for the whole system are constructed from (2.29).

Planet Modes

A candidate planet mode associated with stage i is

$$\begin{aligned} \boldsymbol{\theta} &= [0 \cdots 0 | 0 \cdots 0 | \mathbf{0} \cdots, \boldsymbol{\theta}_{ps}^i, \cdots \mathbf{0}]^T \\ \theta_{ps}^i &= [v^1 \theta_{pt}^{i1}, v^2 \theta_{pt}^{i1}, \cdots, v^{c^i} \theta_{pt}^{i1}]^T \\ \theta_{pt}^{i1} &= [\theta_p^{i11} \cdots \theta_p^{i1d^i}]^T \end{aligned} \qquad (2.33)$$

where the v^l ($l = 1, \cdots, c^i$) are as yet unknown scalars. All motion is confined to the ith planet set. Substitution of (2.33) into (2.26)-(2.28) and use of the cyclical symmetry of planet trains in stage i ($\mathbf{k}_{c,pt}^{il} = \mathbf{k}_{c,pt}^{i1}$, $\mathbf{k}_{g,pt}^{jil} = \mathbf{k}_{g,pt}^{ji1}$, and $\mathbf{I}_{pt}^{il} = \mathbf{I}_{pt}^{i1}$) give

$$\sum_{l=1}^{c^i} v^l \left(\mathbf{k}_{c,pt}^{i1}\right)^T \boldsymbol{\theta}_{pt}^{i1} = \sum_{l=1}^{c^i} v^l \sum_{j=1}^{b} \sum_{m=1}^{d^i} \sigma^j k_{gp}^{ji1m} r_g^j r_p^{i1m} \theta_p^{i1m} = 0 \qquad (2.34)$$

$$\sum_{l=1}^{c^i} v^l \left(\mathbf{k}_{g,pt}^{ji1}\right)^T \boldsymbol{\theta}_{pt}^{i1} = \sum_{l=1}^{c^i} v^l \sum_{m=1}^{d^i} (-\sigma^j k_{gp}^{ji1m} r_g^j r_p^{i1m} \theta_p^{i1m}) = 0 \quad j = 1, \cdots, b \qquad (2.35)$$

$$(\mathbf{K}_{pt}^{i1} - \omega^2 \mathbf{I}_{pt}^{i1}) \boldsymbol{\theta}_{pt}^{i1} = 0 \qquad (2.36)$$

Equation (2.34) represents the moment exerted on carrier i by the planets. This equation requires either $\sum_{l=1}^{c^i} v^l = 0$ or $\sum_{j=1}^{b}\sum_{m=1}^{d^i} \sigma^j k_{gp}^{ji1m} r_g^j r_p^{i1m} \theta_p^{i1m} = 0$. The quantity $\sum_{j=1}^{b}\sum_{m=1}^{d^i} \sigma^j k_{gp}^{ji1m} r_g^j r_p^{i1m} \theta_p^{i1m}$ is nonzero, in general, because θ_p^{i1m} $(m = 1, \cdots, d^i)$ are independently determined by (2.36). Hence, equation (2.34) yields

$$\sum_{l=1}^{c^i} v^l = 0 \tag{2.37}$$

The same analysis applies to equation (2.35) and yields the same equation as (2.37), which has $c^i - 1$ independent, non-trivial solutions.

Equation (2.36) is a reduced eigenvalue problem with d^i eigensolutions. For each such eigensolution of (2.36), $c^i - 1$ independent planet modes, each having the same natural frequency, can be constructed for the full system eigenvalue problem (2.18) using (2.33) and the independent solutions of (2.37). Therefore, stage i has $(c^i - 1)d^i$ planet modes. For the whole system, the total number of planet modes is $\sum_{i=1}^{a} (c^i - 1)d^i$.

Completeness of the Modes

Summing the total number of overall and planet modes gives $a+b+\sum_{i=1}^{a} c^i d^i$ modes, which equals the total system degrees of freedom. Therefore, the overall and planet modes discussed above form a complete set of vibration modes of a general compound planetary gear.

2.1.3 Summary for Purely Rotational Compound Planetary Gear Model

A purely rotational degree of freedom model is constructed for general compound planetary gears involving any combination of meshed-planet, stepped-planet, and multi-stage configurations. By providing the modeling details and comparisons with

previous planetary gear models, this study clarifies discrepancies in gear mesh deflection expressions and corrects errors in previously published models. All vibration modes of the system fall into the categories of overall and planet modes. The properties of these mode types are presented and proved.

Table 2.1: Parameters of the compound planetary gear in Figure 2.1.

Number of Carriers	2
Number of Central Gears	4
Number of Planet Trains	c^1=4, c^2=6
Number of Planets per Train	d^1=3, d^2=1
Planet Location	$\psi^{1l1} = \frac{2\pi(l-1)}{4};\ l = 1, \cdots, 4$ $\psi^{2l1} = \frac{2\pi(l-1)}{6};\ l = 1, \cdots, 6$ $\psi^{1l2} = \psi^{1l3} = \psi^{1l1} + 32^\circ$ $\beta^{1l12} = 70^\circ, \beta^{1l21} = 218^\circ$
Mesh Stiffnesses (N/m)	$k_{gp}^{jilm} = \begin{cases} 500 \times 10^6 & \text{If } j=1, i=1, m=1 \\ & j=2, i=1, m=3 \\ & j=3, i=2, m=1 \\ & j=4, i=2, m=1 \\ 0 & \text{Otherwise} \end{cases}$ $k_{pp}^{ilmq} = \begin{cases} 500 \times 10^6 & \text{If } i=1, m=1, q=2 \\ & i=1, m=2, q=1 \\ 0 & \text{Otherwise} \end{cases}$
Torsional Bearing Stiffness (*N-m/rad*)	$k_{cb,\theta\theta}^{i} = 0,\ k_{gb,\theta\theta}^{1} = k_{gb,\theta\theta}^{3} = 0$ $k_{gb,\theta\theta}^{2} = k_{gb,\theta\theta}^{4} = 500 \times 10^6$
Torsional Shaft Stiffnesses (*N-m/rad*)	$k_{g,\theta\theta}^{jn} = k_{c,\theta\theta}^{ih} = 0$ $k_{cg,\theta\theta}^{ij} = \begin{cases} 200 \times 10^6 & \text{If } i=1, j=3 \\ 0 & \text{Otherwise} \end{cases}$ $k_{p-p,\theta\theta}^{ilmq} = \begin{cases} 100 \times 10^6 & \text{If } i=1, m=2, q=3 \\ & i=1, m=3, q=2 \\ 0 & \text{Otherwise} \end{cases}$
Mass (*kg*)	$m_p^{1l1} = m_p^{1l2} = m_p^{1l3} = 0.75,\ m_p^{2l1} = 2.00$

Continued on next page

Table 2.1 – *Continued from previous page*

Moment of Inertia (kg-m^2)	$I_g^1 = 0.05,\ I_g^2 = 0.5$ $I_g^3 = 0.05,\ I_g^4 = 0.5$ $I_c^1 = 1.00,\ I_c^2 = 1.20$ $I_p^{1l1} = I_p^{1l2} = 0.01,\ I_p^{1l3} = 0.09\ I_p^{2l1} = 0.20$
Radii (mm)	$r_g^1 = 100.0,\ r_g^2 = 320.6$ $r_g^3 = 100.0,\ r_g^4 = 300.0$ $r_c^{1l1} = 176.5,\ r_c^{1l2} = r_c^{1l3} = 270.0,\ r_c^{2l1} = 220.7$ $r_p^{1l1} = 60.0,\ r_p^{1l2} = 77.7,\ r_p^{1l3} = 55.8\ r_c^{2l1} = 100.0$
Gear Type	$\sigma^1 = \sigma^3 = -1$ (sun gear) $\sigma^2 = \sigma^4 = 1$ (ring gear)

Table 2.2: Natural frequencies for the example system of Figure 2.1 with parameters listed in Table 2.1. O means overall mode, $P1$ means planet mode of planet set 1, and $P2$ means planet mode of planet set 2.

Natural Frequency Number	Natural Frequency (Hz)	Vibration Mode Type
1	0	O
2, 3, 4	860	$P1$
5	902	O
6, 7, 8, 9, 10	1125	$P2$
11	1241	O
12	1746	O
13	1899	O
14, 15, 16	3067	$P1$
17	4226	O
18	5926	O
19	6314	O
20	10945	O
21, 22, 23	16985	$P1$
24	16986	O

2.2 Rotational-translational Model of Compound Planetary Gears and the Associated Modal Properties

Compared to the purely rotational model in previous section, the rotational-translational model for general compound planetary gears developed by Kiracofe and Parker [53] provides a better mathematical description of compound planetary gear systems. Because this model and the associated modal properties are extensively used and cited in the subsequent investigations, this section briefly introduces this model and the findings by Kiracofe and Parker to prevent redundancy in the following chapters.

2.2.1 Rotational-translational Model of Compound Planetary Gears

Similar to the rotational-translational model for simple planetary gear by Lin and Parker [58], each carrier, planet, and central gear in Kiracofe and Parker's model [53] has three degrees of freedom: two translational and one rotational, bearings are modeled as two translational springs, shaft connections are modeled as one torsional and two translational springs, and gear meshes are modeled as springs.

Different from the simple planetary gear model in [58], a single fixed basis is used for all central components coordinates(carriers and central gears)in order to be compatible with multi-stage structures, the meshed-planet orientation angle (e.g., β^{ilmn} the orientation angle between planets m and n in train l of planet set i in Figure 2.8) and the planet-planet mesh stiffnesses (e.g., κ_{pp}^{ilmn} the mesh stiffness between planets m and n in train l of planet set i in Figure 2.8) are introduced to include meshed-planet structures, and two translational shaft connection stiffnesses (e.g., $k_{p-p,\zeta\zeta}^{ilmq}$ and $k_{p-p,\eta\eta}^{ilmq}$ the translational shaft stiffnesses between planet m and q in planet train l of

planet set i) and one torsional shaft connection stiffness (e.g., $k^{ilmq}_{p-p,uu}$ the torsional shaft stiffnesses between planet m and q in planet train l of planet set i) are introduced to incorporate stepped-planet structures.

Figure 2.8 illustrates the model of a planet-planet mesh between planets m and n in train l of planet set i in [58], where k_p^{ilm} and k_p^{iln} are the bearing stiffnesses of planets m and n in train l of planet set i, ψ^{ilm} and ψ^{iln} are the angular positions of these two planets, (ζ_p^{ilm}, η_p^{ilm}) and (ζ_p^{iln}, η_p^{iln}) are their radial and tangential coordinates which are fixed at each planet's equilibrium position and do not translate with the vibration of the associated carrier, $u_p^{ilm} = r_p^{ilm}\theta_p^{ilm}$ and $u_p^{iln} = r_p^{iln}\theta_p^{iln}$ are the their rotational coordinates, and (r_p^{ilm}, θ_p^{ilm}) and (r_p^{iln}, θ_p^{iln}) are the rotations and base radii of these two planets, respectively. Figure 2.9 shows the model of an external central gear-planet (i.e, sun-planet) mesh between central gear j and planet m in train l of planet set i in [58], where κ_{gp}^{jilm} is the mesh stiffness for this this central gear-planet mesh, α_g^{jilm} is the associated pressure angle, (x_g^j, y_g^j) are the translational coordinates for central gear j, r_g^j and θ_g^j are the rotation and base radius of central gear j, and $k_{g,xx}^j$ and $k_{g,yy}^j$ are the translational bearing stiffnesses central gear j.

The equations of motion for each component in a general compound planetary gear system are given in [53]. Putting all equations of motion into matrix form yields

$$\mathbf{M}\ddot{\boldsymbol{\phi}}(t) + \mathbf{K}\boldsymbol{\phi}(t) = \mathbf{F}(t) \tag{2.38}$$

where $\mathbf{K} = \mathbf{K}_b + \mathbf{K}_m(t)$, $\mathbf{K}_b$ is the diagonal bearing stiffness matrix, $\mathbf{K}_m(t)$ is the symmetric stiffness matrix from coupling between elements (both tooth meshes and shaft couplings), and $\mathbf{F}(t)$ is the vector of applied forces and torques. For details of $\mathbf{M}$ and $\mathbf{K}$, please refer to the Appendix of [53].

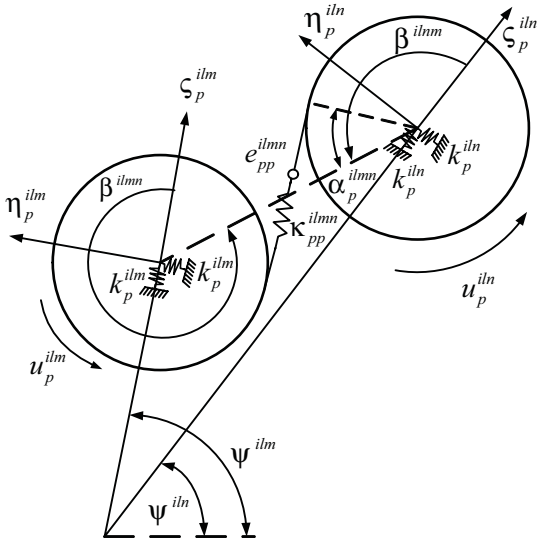

Figure 2.8: The planet-planet gear mesh between planet m and q in planet train l of planet set i) is modeled by a spring with stiffness κ_{pp}^{ilmn} and the static transmission error e_{pp}^{ilmn} in [53].

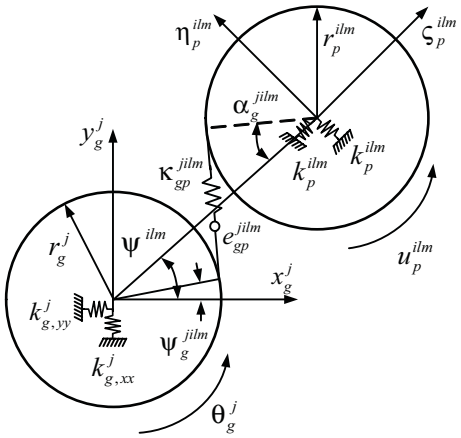

Figure 2.9: The sun-planet gear mesh between central gear j and planet m in train l of planet set i is modeled by spring with stiffness κ_{gp}^{jilm} and the static transmission error e_{gp}^{jilm} in [53].

2.2.2 Modal Properties of General Compound Planetary Gears

For eigenvalue analysis the linear time-invariant form of the above rotational-translational model is considered, where the mesh stiffnesses are averages over a mesh cycle. The imposed assumptions are that all planet trains are equally spaced around their associated carrier, each planet set has three or more planet trains, and all bearing and shaft stiffnesses are isotropic. Thus, the eigenvalue problem for a general compound planetary gear is

$$
\begin{aligned}
&(\mathbf{K}-\lambda\mathbf{M})\boldsymbol{\phi}=(\mathbf{K}_b+\mathbf{K}_m-\omega^2\mathbf{M})\boldsymbol{\phi}=\mathbf{0}\\
&\boldsymbol{\phi}=(\underbrace{\boldsymbol{\phi}_c^1,\cdots,\boldsymbol{\phi}_c^a}_{\text{carriers}},\underbrace{\boldsymbol{\phi}_g^1,\cdots,\boldsymbol{\phi}_g^b}_{\text{central gears}},\underbrace{\boldsymbol{\phi}_{ps}^1,\cdots,\boldsymbol{\phi}_{ps}^a}_{\text{planet sets}})^T\\
&\text{Carrier } i\text{: } \boldsymbol{\phi}_c^i=[x_c^i,y_c^i,\theta_c^i]^T\\
&\text{Central gear } j\text{: } \boldsymbol{\phi}_g^j=[x_g^j,y_g^j,\theta_g^j]^T\\
&\text{Planet set } i\text{: } \boldsymbol{\phi}_{ps}^i=(\boldsymbol{\phi}_{pt}^{i1},\cdots,\boldsymbol{\phi}_{pt}^{ic^i})^T\\
&\text{Planet train } l \text{ of set } i\text{: } \boldsymbol{\phi}_{pt}^{il}=(\boldsymbol{\phi}_p^{il1},\cdots,\boldsymbol{\phi}_p^{ild^i})^T\\
&\text{Planet } m \text{ in train } l \text{ of set } i\text{ : } \boldsymbol{\phi}_p^{ilm}=(\zeta_p^{ilm},\eta_p^{ilm},u_p^{ilm})^T
\end{aligned}
\tag{2.39}
$$

where throughout this study $1\le i\le a$, $1\le j\le b$, $1\le l\le c^i$, $1\le m\le d^i$, a is the number of carriers, b is the number of central gears, c^i is the number of planet trains of planet set i, and d^i is the number of planets per train of planet set i. The eigenvalue $\lambda=\omega^2$, where ω is the natural frequency. The translational coordinates for carrier i are x_c^i and y_c^i, and the rotation of carrier i is θ_c^i. The total degrees of freedom is $\Lambda=3\left(a+b+\sum_{i=1}^{a}c^id^i\right)$.

If all planet trains in a planet set are equally spaced and have identical model parameters, the planet set is *tuned*. Otherwise, the planet set is *mistuned*. If all the planet sets in a system are tuned, then the whole system is tuned, otherwise it is mistuned. For tuned systems, all modes fall into one of the following classes [53]

(A) Rotational Modes

The natural frequencies of rotational modes are distinct. All central gears and

carriers have rotational motion only. All planet trains within a planet set have the same motion. Thus, a rotational mode has the form

$$\boldsymbol{\phi}_c^i = (0, 0, \theta_c^i)^T \ , \quad i = 1, 2,...,a \tag{2.40}$$

$$\boldsymbol{\phi}_g^j = (0, 0, \theta_g^j)^T \ , \quad j = 1, 2,..., \mathrm{b} \tag{2.41}$$

$$\boldsymbol{\phi}_{ps}^i = (\underbrace{\boldsymbol{\phi}_{pt}^{i1}, \boldsymbol{\phi}_{pt}^{i1}, \ \cdots, \boldsymbol{\phi}_{pt}^{i1}}_{c^i \quad trains})^T \ , \quad i = 1, 2,...,a \tag{2.42}$$

(B) Translational Modes

The natural frequencies of translational modes have multiplicity two when all planet sets have three or more planet trains. All central gears and carriers have translational motion only. The pair of degenerate translational modes ($\boldsymbol{\phi}$ and $\hat{\boldsymbol{\phi}}$ are chosen such that $\hat{\boldsymbol{\phi}}^T \mathbf{M} \boldsymbol{\phi} = 0$) has the form

$$\boldsymbol{\phi} = (\boldsymbol{\phi}_c^1, \cdots, \boldsymbol{\phi}_c^a, \boldsymbol{\phi}_g^1, \cdots, \boldsymbol{\phi}_g^b, \boldsymbol{\phi}_{ps}^1, \cdots, \boldsymbol{\phi}_{ps}^a)^T \tag{2.43}$$

$$\hat{\boldsymbol{\phi}} = (\hat{\boldsymbol{\phi}}_c^1, \cdots, \hat{\boldsymbol{\phi}}_c^a, \hat{\boldsymbol{\phi}}_g^1, \cdots, \hat{\boldsymbol{\phi}}_g^b, \hat{\boldsymbol{\phi}}_{ps}^1, \cdots, \hat{\boldsymbol{\phi}}_{ps}^a)^T \tag{2.44}$$

$$\boldsymbol{\phi}_c^i = (x_c^i, y_c^i, 0)^T \hat{\boldsymbol{\phi}}_c^i = (y_c^i, -x_c^i, 0)^T \tag{2.45}$$

$$\boldsymbol{\phi}_g^j = (x_g^j, y_g^j, 0)^T \hat{\boldsymbol{\phi}}_g^j = (y_g^j, -x_g^j, 0)^T \tag{2.46}$$

$$\begin{bmatrix} \boldsymbol{\phi}_p^{ilm} \\ \hat{\boldsymbol{\phi}}_p^{ilm} \end{bmatrix} = \begin{bmatrix} \mathbf{I} \cos \hat{\psi}^{ilm} & \mathbf{I} \sin \hat{\psi}^{ilm} \\ -\mathbf{I} \sin \hat{\psi}^{ilm} & \mathbf{I} \cos \hat{\psi}^{ilm} \end{bmatrix} \begin{bmatrix} \boldsymbol{\phi}_p^{il1} \\ \hat{\boldsymbol{\phi}}_p^{il1} \end{bmatrix} \tag{2.47}$$

where $1 \le i \le a$, $1 \le j \le b$, $1 \le l \le c^i$, $1 \le m \le d^i$, $\boldsymbol{I}$ is an identity matrix, and $\hat{\psi}^{ilm} = \psi^{ilm} - \psi^{i1m}$ is the planet position angle difference between planet m of train l and planet m of train l in planet set i.

(C) Planet Modes

In planet modes, only one planet set deflects. With planet set h being the planet

set having motion in a certain planet mode, the planet mode associated with planet set h has the form

$$\boldsymbol{\phi} = (\underbrace{0, \cdots, 0}_{carriers}, \underbrace{0, \cdots, 0}_{central\ \ gears}, \underbrace{0, \cdots, \boldsymbol{\phi}^h_{ps}, 0, \cdots 0}_{planet\ \ sets})^T \tag{2.48}$$

In addition, the motion of each planet train in planet set h is a scalar multiple of any chosen planet train in this planet set, that is,

$$\boldsymbol{\phi}^h_{ps} = (w^1 \boldsymbol{\phi}^{h1}_{pt}, w^2 \boldsymbol{\phi}^{h1}_{pt}, \cdots, w^{c^h} \boldsymbol{\phi}^{h1}_{pt})^T \tag{2.49}$$

$$\boldsymbol{\phi}^{h1}_{pt} = (\boldsymbol{\phi}^{h11}_{p}, \boldsymbol{\phi}^{h12}_{p}, \cdots, \boldsymbol{\phi}^{h1d^h}_{p})^T \tag{2.50}$$

$$\boldsymbol{\phi}^{h1m}_{p} = (\zeta^{h1m}_{p}, \eta^{h1m}_{p}, u^{h1m}_{p})^T, \quad m = 1, \cdots, d^i \tag{2.51}$$

where the scalar multipliers w^l ($l = 1, \cdots, c^h$) satisfy

$$\sum_{l=1}^{c^h} w^l \sum_{m=1}^{d^h} \sin \psi^{hlm} = 0 \qquad \sum_{l=1}^{c^h} w^l \sum_{m=1}^{d^h} \cos \psi^{hlm} = 0 \qquad \sum_{l=1}^{c^h} w^l = 0 \tag{2.52}$$

The planet mode frequencies for planet set h have multiplicity $c^h - 3$.

2.3 Conclusion

A purely rotational model for general compound planetary gears is developed in the first section of this Chapter's study. This model clarifies discrepancies in gear mesh deflection expressions and corrects errors in previously published models. The distinct modal properties for this purely rotational model are presented and analytically proved. This model aims to greatly simplify further analysis on compound planetary gear dynamics, such as the parametric instability caused by mesh stiffness variations, while keeping the main dynamic behavior generated by tooth mesh forces.

The rotational-translational model by Kirocofe and Parker [53] is also briefly introduced in this Chapter. This model, together with the associated well-defined modal properties, are critical to the parametric analysis of compound planetary gears, such as the sensitivity of natural frequencies and vibration modes to system parameters and the natural frequency veering and crossing patterns, which require a refined mathematical description of the system.

Chapter 3: SENSITIVITY OF GENERAL COMPOUND PLANETARY GEAR NATURAL FREQUENCIES AND VIBRATION MODES TO MODEL PARAMETERS

3.1 Introduction

Simple planetary gears have only one stage and only one planet in each load path. Compound planetary gears involve stepped-planet, meshed-planet or multi-stage structures [53]. Compared to simple planetary gears, compound planetary gears provide larger reduction ratios and more flexible configurations [53, 65], but they create more noise and vibration problems [47]. Sensitivity of the natural frequencies and vibration modes to system parameters, such as mesh stiffnesses and mases of the components, provides important information for tuning resonances away from operating speeds and minimizing dynamic response. The study in this chapter derives the eigensensitivities of general compound planetary gears to system parameters with the purpose of providing guidance for system design.

The variations of planetary gear natural frequencies to selected parameters have been examined previously. Botman [16] plotted the natural frequencies versus planet support stiffness and studied the effect of carrier rotation through a numerical example. Saada and Velex [85] studied the influence of ring gear support stiffness on the natural frequencies. These and similar works present only numerical results. Lin and

Parker used a two-dimensional, lumped-parameter model to systematically analyze planetary gear eigensensitivities [57, 58]. All of these analyses are restricted to simple planetary gears. No systematic analysis of general compound planetary gear eigensensitivities exists. In addition, the eigensensitivities to the system parameters that are unique to compound planetary gears (e.g., planet-planet mesh stiffness, planet-planet shaft stiffness, and the coupling stiffness between stages) have not been considered numerically or analytically.

One barrier for the eigensensivity analysis of compound planetary gears is to choose the proper model for this analysis. Kahraman [47] developed a purely rotational models for limited configurations of single-stage compound planetary gears. The purely rotational model that is introduced in Chapter 2 of this work applies to general compound planetary gears. These purely rotational models, however, are not suitable for eigensensivity analysis because eigensensivity analysis requires the model to have an accurate description of the real system such that the eigensensitivity results are accurate enough to predict the changes of natural frequencies and vibration modes for real applications. For lumped-parameter models, a model with three or more degrees of freedom for each component is preferred, because more degrees of freedom indicate better description of the motions for each component, and the resultant natural frequencies, vibration modes, and eigensensitivities are closer to real systems. Purely rotational models ignores all translational motions of the components and assign just one rotational degree of freedom to each component. The total degrees of freedom for purely rotational models is much less than those rotational-translational models which have three degrees of freedom for each component. Thus,

it is preferred to choose the rotational-translational compound planetary gear model for the eigensensivity analysis in this chapter.

In previous chapter a rotational-translational model by Kiracofe and Parker [53] is briefly introduced. In that model each gear or carrier has one rotational and two translational degrees of freedom. All bearings and shaft connections are modeled as one torsional and two translational springs. All gear meshes are modeled as springs. The results of [53] show that tuned (that is, axisymmetric) compound planetary gears with three or more planet trains in each planet set have structured modal properties that are similar to those of simple planetary gears [58]. The vibration modes of such compound planetary gears are classified as rotational, translational and planet modes, with each having well-defined properties. The investigation in this chapter uses the model by Kiracofe and Parker [53] to analytically investigate the sensitivities of natural frequencies and vibration modes to all stiffness and inertia parameters of general compound planetary gears. Both tuned and mistuned compound planetary gears are studied in this chapter.

3.2 Eigensensitivity Calculation

The eigensensitivities of interest in this study are the first and second eigenvalue derivatives and the first order eigenvector derivative with respect to a system parameter: λ_u', λ_u'', and $\boldsymbol{\phi}_u'$. The analytical procedures to calculate these eigensensitivities [21, 27, 57] are introduced briefly as follows.

When λ_u is a distinct eigenvalue of (2.39), the associated eigensensitivities are found by differentiating (2.39) to obtain

$$\lambda_u' = \boldsymbol{\phi}_u^T(\mathbf{K}' - \lambda_u \mathbf{M}')\boldsymbol{\phi}_u \tag{3.1}$$

$$\boldsymbol{\phi}'_u = -\frac{1}{2}(\boldsymbol{\phi}_u^T \mathbf{M}' \boldsymbol{\phi}_u)\boldsymbol{\phi}_u + \sum_{v=1, v\neq u}^{\Lambda} \frac{\boldsymbol{\phi}_v^T(\mathbf{K}' - \lambda_u \mathbf{M}')\boldsymbol{\phi}_u}{\lambda_u - \lambda_v}\boldsymbol{\phi}_v \tag{3.2}$$

$$\lambda''_u = 2\boldsymbol{\phi}_u^T(\mathbf{K}' - \lambda_u \mathbf{M}')\boldsymbol{\phi}'_u + \boldsymbol{\phi}_u^T(\mathbf{K}'' - \lambda_u \mathbf{M}'' - \lambda'_u \mathbf{M}')\boldsymbol{\phi}_u \tag{3.3}$$

The form of (3.2) results from series expansion of $\boldsymbol{\phi}'_u$ in the basis of the eigenvectors $\boldsymbol{\phi}_v$, $v = 1,\ 2, \cdots,\ u-1,\ u+1, \cdots,\ \Lambda$.

For the case of a degenerate eigenvalue of (2.39), suppose the eigenvalue has multiplicity w such that $\lambda_1 = \cdots = \lambda_w$. $\mathbf{N} = [\boldsymbol{\eta}_1,\ \cdots \boldsymbol{\eta}_w]$ is an arbitrary set of independent eigenvectors normalized such that $\mathbf{N}^T\mathbf{M}\mathbf{N} = \mathbf{I}$. The eigenvectors $[\boldsymbol{\eta}_1,\ \cdots \boldsymbol{\eta}_w]$ have the translational or planet mode properties in (2.43)-(2.52). Let $\boldsymbol{\Phi} = \mathbf{N}\mathbf{B}$ produce a preferred set of eigenvectors $\boldsymbol{\Phi} = [\boldsymbol{\phi}_1,\ \cdots, \boldsymbol{\phi}_w]$, where the $w \times w$ matrix $\mathbf{B}$ is to be determined, $\mathbf{B} = [\boldsymbol{\beta}_1,\ \cdots,\ \boldsymbol{\beta}_w]_{w\times w}$, and $\boldsymbol{\phi}_f = \mathbf{N}\boldsymbol{\beta}_f$ $(f = 1,\ \cdots,\ w)$. Differentiation of (2.39) gives

$$(\mathbf{K} - \lambda_f \mathbf{M})\boldsymbol{\phi}'_f = (\lambda'_f \mathbf{M} + \lambda_f \mathbf{M}' - \mathbf{K}')\mathbf{N}\boldsymbol{\beta}_f = \mathbf{f} \tag{3.4}$$

The w solvability conditions of (3.4) are $\boldsymbol{\eta}_1^T\mathbf{f} = \boldsymbol{\eta}_2^T\boldsymbol{f} = \cdots = \boldsymbol{\eta}_t^T\mathbf{f} = \mathbf{0}$, and these yield the eigenvalue problem

$$\mathbf{D}\boldsymbol{\beta}_f = \lambda'_f \boldsymbol{\beta}_f \qquad \mathbf{D} = \mathbf{N}^T(\mathbf{K}' - \lambda_f \mathbf{M}')\mathbf{N} \tag{3.5}$$

Thus, the first order eigenvalue derivatives of the w degenerate eigenvalues of (2.39) are the eigenvalues of $\mathbf{D}$ in (3.5). For the case when all the eigenvalues of $\mathbf{D}$ are distinct, $\boldsymbol{\beta}_f$ is uniquely determined from (3.5) with normalization $\boldsymbol{\beta}_f^T\boldsymbol{\beta}_f = 1$. Thus, $\boldsymbol{\phi}_f = \mathbf{N}\boldsymbol{\beta}_f$ is also determined. Like $\boldsymbol{\eta}_f$, the w eigenvectors $\boldsymbol{\phi}_f$ also have the translational or planet mode properties in (2.43)-(2.52). The set $\boldsymbol{\Phi}$ is the preferred set compared to $\mathbf{N}$, because $\boldsymbol{\Phi}$ yields a diagonal form of $\mathbf{D}$ in (3.5) and leads to simpler eigenvector derivative expressions.

The first order eigenvector derivative for a distinct λ'_f in (16) is

$$\boldsymbol{\phi}'_f = \mathbf{j}_f + \boldsymbol{\Phi}\boldsymbol{\pi}_f \tag{3.6}$$

where $\boldsymbol{\Phi}\boldsymbol{\pi}_f$ is the general solution of the homogeneous form of (3.4), and $\mathbf{j}_f$ is a particular solution of (3.4) such that $(\mathbf{K} - \lambda_f \mathbf{M})\mathbf{j}_f = \mathbf{f}$. According to Nelson [73], $\mathbf{j}_f = \sum_{k=w+1}^{\Lambda} g_{kf}\boldsymbol{\phi}_k$, where $g_{kf} = \frac{\boldsymbol{\phi}_k^T(\lambda_f \mathbf{M}' - \mathbf{K}')\boldsymbol{\phi}_f}{\lambda_k - \lambda_f}$, and $k = w+1,\ \cdots,\ \Lambda$.

The $\boldsymbol{\pi}_f$ in (17) are determined collectively by first forming the $w \times w$ matrix $\boldsymbol{\Pi} = [\boldsymbol{\pi}_1,\ \cdots \boldsymbol{\pi}_w]$. The diagonal and off-diagonal elements of $\boldsymbol{\Pi}$ are given as [29, 57, 67, 73]

$$\Pi_{ff} = -\frac{1}{2}\boldsymbol{\phi}_f^T \mathbf{M}' \boldsymbol{\phi}_f,\ f = 1,\ \cdots,\ w \tag{3.7}$$

$$\Pi_{ef} = \frac{2\boldsymbol{\phi}_e^T(\mathbf{K}' - \lambda_f \mathbf{M}')\mathbf{j}_f}{2(\lambda'_f - \lambda'_e)} - \frac{\boldsymbol{\phi}_e^T(2\lambda'_f \mathbf{M}' - \mathbf{K} + \lambda_f \mathbf{M})\boldsymbol{\phi}_f}{2(\lambda'_f - \lambda'_e)} \qquad e = 1,\ \cdots,\ w \quad f = 1,\ \cdots,\ w \quad e \neq f \tag{3.8}$$

By taking the second order derivative of (2.39) [29, 57, 67, 73], the second order eigenvalue derivatives λ''_f are calculated as

$$\lambda''_f = 2\boldsymbol{\phi}_f^T(\mathbf{K}' - \lambda_f \mathbf{M}')\mathbf{j}_f + \boldsymbol{\phi}_f^T(\mathbf{K} - \lambda_f \mathbf{M} - \lambda'_f \mathbf{M}')\boldsymbol{\phi}_f \tag{3.9}$$

When the matrix $\mathbf{D}$ has degenerate eigenvalues, the eigenvectors of $\mathbf{D}$ that are associated with these degenerate eigenvalues are not unique. Therefore, the associated first order eigenvector derivatives of (2.39) can not be determined. Nevertheless, the w second order eigenvalue derivatives are derived as the eigenvalues of [29, 57]

$$\mathbf{E} = 2\boldsymbol{\Phi}^T(\mathbf{K}' - \lambda_f \mathbf{M}')\mathbf{J} + \boldsymbol{\Phi}^T(\mathbf{K} - \lambda_f \mathbf{M} - \lambda'_f \mathbf{M}')\boldsymbol{\Phi} \tag{3.10}$$

where $\mathbf{J} = [\mathbf{j}_1,\ \cdots,\ \mathbf{j}_w]$consists of $\mathbf{j}_f$ ($f = 1,\ \cdots,\ w$), which is calculated during the derivation of $\boldsymbol{\phi}_f$ in (3.6).

With these closed-form eigensensitivity expressions, the approximate uth eigenvalue $\tilde{\lambda}_u$ and its associated eigenvector $\tilde{\boldsymbol{\phi}}_u$ of the perturbed system are

$$\tilde{\lambda}_u = \lambda_u + \sum_{\rho} \lambda'_u \,|_{\rho=\rho_0} \, (\rho - \rho_0) + \frac{1}{2} \sum_{\rho} \lambda''_u \,|_{\rho=\rho_0} \, (\rho - \rho_0)^2 \tag{3.11}$$

$$\tilde{\boldsymbol{\phi}}_u = \boldsymbol{\phi}_u + \sum_{\rho} \boldsymbol{\phi}'_u \,|_{\rho=\rho_0} \, (\rho - \rho_0) \tag{3.12}$$

3.3 Eigensensitivity of Tuned Systems

For the case when the perturbed system remains tuned, the structured modal properties for compound planetary gears [53] are retained. The possible changing stiffness parameters considered are the mesh stiffnesses between planets and central gears/other planets (k_{gp}^{ji*m}, k_{pp}^{i*mq}), the translational support (bearing) stiffnesses of carriers/central gears/planet (k_{cb}^{i}, k_{gb}^{i}, k_{p}^{i*m}), the torsional support stiffnesses of carriers/central gears ($k_{cb,\theta\theta}^{i}$, $k_{gb,\theta\theta}^{i}$), and the shaft stiffnesses connecting any two components . The changing inertia parameters are the mass and moment of inertia of each component (m_c^i, I_c^i, m_g^j, I_g^j, m_p^{ilm}, I_p^{ilm}). The nomenclature section states the meaning of all variables, superscripts, and subscripts (the same nomenclature as in [53] is used).

3.3.1 Calculation of Eigensensitivity of Tuned Systems

Because the eigensensitivity calculation procedures are similar for all parameters, explanation of one calculation for a certain stiffness parameter is sufficient. The eigensensitivities to k_{gp}^{ji*m} are a representative example. In order to use equations (2.39)-(2.52) and (3.1)-(3.12) to calculate the eigensensitivities, the derivatives of the mass and stiffness matrix with respect to the perturbed parameter are needed. These

are

$$\frac{\partial \mathbf{M}}{\partial k_{gp}^{ji*m}} = \mathbf{0} \tag{3.13}$$

$$\frac{\partial \mathbf{K}}{\partial k_{gp}^{ji*m}} = \begin{bmatrix} \ddots & & \\ & \frac{\partial \sum_{l=1}^{c^i} \mathbf{K}_{g1}^{jilm}}{\partial k_{gp}^{ji*m}} & \cdots & \frac{\partial \sum_{l=1}^{c^i} \mathbf{K}_{gp}^{jilm}}{\partial k_{gp}^{ji*m}} \\ & \vdots & & \vdots \\ & \frac{\partial \sum_{l=1}^{c^i} \left(\mathbf{K}_{gp}^{jilm}\right)^T}{\partial k_{gp}^{ji*m}} & \cdots & \frac{\partial \sum_{l=1}^{c^i} \mathbf{K}_{g3}^{jilm}}{\partial k_{gp}^{ji*m}} \\ & & & \ddots \end{bmatrix} \tag{3.14}$$

where all sub-matrices of $\partial \mathbf{K}/\partial k_{gp}^{ji*m}$ are zero except the four sub-matrices indicated in (3.13), which are coupling terms between central gear j and planet m in any train of stage i. These sub-matrices are linearly dependent on k_{gp}^{ji*m} as shown below.

$$\mathbf{K}_{g1}^{jilm} = k_{gp}^{jilm} \begin{bmatrix} \sin^2 \psi_g^{jilm} & -\cos \psi_g^{jilm} \sin \psi_g^{jilm} & -r_g^j \sin \psi_g^{jilm} \\ & \cos^2 \psi_g^{jilm} & r_g^j \cos \psi_g^{jilm} \\ symmetric & & \left(r_g^j\right)^2 \end{bmatrix} \tag{3.15}$$

$$\mathbf{K}_{g3}^{jilm} = k_{gp}^{jilm} \begin{bmatrix} \sin^2 \alpha_g^{jilm} & -\sigma^j \cos \alpha_g^{jilm} \sin \alpha_g^{jilm} & -\sin \alpha_g^{jilm} \\ & \cos^2 \alpha_g^{jilm} & \sigma_g^j \cos \alpha_g^{jilm} \\ symmetric & & 1 \end{bmatrix} \tag{3.16}$$

$$\mathbf{K}_{gp}^{jilm} = k_{gp}^{jilm} \begin{bmatrix} -\sigma^j \sin \psi_g^{jilm} \sin \alpha_g^{jilm} & \sin \psi_g^{jilm} \cos \alpha_g^{jilm} & \sigma^j \sin \psi_g^{jilm} \\ -\sigma^j \cos \psi_g^{jilm} \sin \alpha_g^{jilm} & -\cos \psi_g^{jilm} \cos \alpha_g^{jilm} & -\sigma^j \cos \psi_g^{jilm} \\ r_g^j \sigma^j \sin \alpha_g^{jilm} & -r_g^j \cos \alpha_g^{jilm} & r_g^j \sigma^j \end{bmatrix} \tag{3.17}$$

where α_g^{jilm} is the pressure angle of gear mesh k_{gp}^{jilm}, σ^j equals 1 (or -1) when central gear j is a ring gear (or a sun gear), and $\psi_g^{jilm} = \psi^{ilm} + \sigma^j \alpha_g^{jilm}$.

Because rotational, translational and planet modes have different multiplicity of eigenvalues, one must consider their eigensensitivities separately.

For the case of rotational modes, one can apply (2.40)-(2.42) directly because all rotational mode eigenvalues are distinct. The expressions for the eigensensitivities simplify further by applying the relationships

$$\boldsymbol{\phi}_u^T \frac{\partial \mathbf{K}}{\partial k_{gp}^{ji*m}} \boldsymbol{\phi}_v = \delta_{g,u}^{jilm} \delta_{g,v}^{jilm} \tag{3.18}$$

$$\delta_{g,u}^{jilm} = y_{g,u}^{j}\cos\psi_{g,u}^{jilm} - x_{g,u}^{i}\sin\psi_{g,u}^{jilm} + r_g^i\theta_{g,u}^{i} + \xi_{p,u}^{ilm}\sigma^i\sin\alpha_{g,u}^{jilm} - \eta_{p,u}^{ilm}\cos\alpha_{g,u}^{jilm} - \sigma^j u_{p,u}^{ilm} \tag{3.19}$$

where $\delta_{g,u}^{jilm}$ is the mesh deflection between gear j and planet m in train l of planet set i for vibration mode u. Rotational mode properties indicate $\delta_{g,u}^{jilm}$ is the same for all the trains in planet set i. Therefore, the mesh deflection between gear j and planet m in any train of planet set i in a rotational mode u is expressed as $\delta_{g,u}^{ji*m}$, where * implies any planet train.

The simplified eigensensitivities for a rotational mode are

$$\frac{\partial\lambda_u}{\partial k_{gp}^{ji*m}} = \sum_{l=1}^{c^i}(\delta_{g,u}^{jilm})^2 = c^i(\delta_{g,u}^{ji*m})^2 \tag{3.20}$$

$$\frac{\partial\boldsymbol{\phi}_u}{\partial k_{gp}^{ji*m}} = \sum_{v=1,v\neq u}^{\Lambda}\sum_{l=1}^{c^i}\frac{\delta_{g,u}^{ji*m}\delta_{g,v}^{jilm}}{\lambda_u-\lambda_v}\boldsymbol{\phi}_v \tag{3.21}$$

$$\frac{\partial^2\lambda_u}{(\partial k_{gp}^{ji*m})^2} = \sum_{v=1,v\neq u}^{\Lambda}\frac{2}{\lambda_u-\lambda_v}(\sum_{l=1}^{c^i}\delta_{g,u}^{ji*m}\delta_{g,v}^{jilm})^2 \tag{3.22}$$

Equation (3.20) expresses the eigenvector derivative $\frac{\partial\boldsymbol{\phi}_u}{\partial k_{gp}^{ji*m}}$ as a modal expansion of all other eigenvectors. The eigenvector $\boldsymbol{\phi}_v$ ($v \neq u$) has dominant impact on $\frac{\partial\boldsymbol{\phi}_u}{\partial k_{gp}^{ji*m}}$ if its associated eigenvalue (λ_v) is close to λ_u, and if the sum of the mesh deflections of gear j and planet m in all the trains of planet set i for vibration mode v ($\sum_{l=1}^{c^i}\delta_{g,v}^{jilm}$) is large compared to those for other modes. In addition, if $\sum_{l=1}^{c^i}\delta_{g,v}^{jilm} = 0$ (e.g., when $\boldsymbol{\phi}_v$ is a planet mode of stages other than stage i), the eigenvector $\boldsymbol{\phi}_v$ has no contribution to $\boldsymbol{\phi}_u'$. While the first derivative in (3.20) depends only on $\boldsymbol{\phi}_u$ (the mode associated with λ_u), the second order derivative in (3.22) depends on all modes other than $\boldsymbol{\phi}_u$, with the greatest contribution coming from modes with eigenvalues close to λ_u.

If all planet sets have three or more planet trains, there are $a+b+3\sum_{i=1}^{a} d^i$ different translational eigenvalues, each with multiplicity two [53]. Suppose $\lambda_1 = \lambda_2$ is a degenerate translational eigenvalue, and $\boldsymbol{\phi}_1$ and $\boldsymbol{\phi}_2$ are the associated pair of orthonormal (with respect to $\mathbf{M}$) translational modes of the unperturbed system. The matrix $\mathbf{D}$ is derived from equation (3.5) as

$$\begin{aligned}\mathbf{D} &= \boldsymbol{\Phi}^T[\frac{\partial \mathbf{K}}{\partial k_{gp}^{ji*m}} - \lambda_u \frac{\partial \mathbf{M}}{\partial k_{gp}^{ji*m}}]\boldsymbol{\Phi} \\ &= \boldsymbol{\Phi}^T[\frac{\partial \mathbf{K}}{\partial k_{gp}^{ji*m}}]\boldsymbol{\Phi} = \sum_{l=1}^{c^i} \begin{bmatrix} (\delta_{g,1}^{jilm})^2 & \delta_{g,1}^{jilm}\delta_{g,2}^{jilm} \\ \delta_{g,1}^{jilm}\delta_{g,2}^{jilm} & (\delta_{g,2}^{jilm})^2 \end{bmatrix}\end{aligned} \tag{3.23}$$

The properties of translational modes indicate the equalities $\sum_{l=1}^{c^i} (\delta_{g,1}^{jilm})^2 = \sum_{l=1}^{c^i} (\delta_{g,2}^{jilm})^2$ and $\sum_{l=1}^{c^i} \delta_{g,1}^{jilm}\delta_{g,2}^{jilm} = 0$. Because $\mathbf{D}$ is diagonalized by $[\boldsymbol{\phi}_1,\ \boldsymbol{\phi}_2]$, these two eigenvectors form a preferred pair of translational modes. From the eigenvalues of $\mathbf{D}$, the first order eigenvalue derivatives are

$$\frac{\partial \lambda_1}{\partial k_{gp}^{ji*m}} = \frac{\partial \lambda_2}{\partial k_{gp}^{ji*m}} = \sum_{l=1}^{c^i} (\delta_{g,1}^{jilm})^2 \tag{3.24}$$

Because $\mathbf{D}$ has a degenerate eigenvalue, the first order eigenvector derivatives can not be determined. The second order eigenvalue derivatives are calculated from the eigenvalues of $\mathbf{E}$ in (3.10), where

$$\mathbf{E} = \begin{bmatrix} \sum_{v=3}^{\Lambda}\sum_{l=1}^{c^i} \frac{2(\delta_{g,v}^{jilm})^2}{\lambda_1-\lambda_v}\delta_{g,1}^{jilm}\delta_{g,1}^{jilm} & \sum_{v=3}^{\Lambda}\sum_{l=1}^{c^i} \frac{2(\delta_{g,v}^{jilm})^2}{\lambda_2-\lambda_v}\delta_{g,1}^{jilm}\delta_{g,2}^{jilm} \\ \sum_{v=3}^{\Lambda}\sum_{l=1}^{c^i} \frac{2(\delta_{g,v}^{jilm})^2}{\lambda_1-\lambda_v}\delta_{g,1}^{jilm}\delta_{g,2}^{jilm} & \sum_{v=3}^{\Lambda}\sum_{l=1}^{c^i} \frac{2(\delta_{g,v}^{jilm})^2}{\lambda_2-\lambda_v}\delta_{g,2}^{jilm}\delta_{g,2}^{jilm} \end{bmatrix} \tag{3.25}$$

The translational mode properties give $E_{11} = E_{22}$ and $E_{12} = E_{21}$. Thus, $\mathbf{E}$ is also diagonal and the second order eigenvalue derivatives are

$$\begin{aligned}\frac{\partial^2 \lambda_1}{(\partial k_{gp}^{ji*m})^2} &= \sum_{v=3}^{\Lambda}\sum_{l=1}^{c^i} \frac{2(\delta_{g,v}^{jilm}\delta_{g,1}^{jilm})^2}{\lambda_1-\lambda_v} \\ \frac{\partial^2 \lambda_2}{(\partial k_{gp}^{ji*m})^2} &= \sum_{v=3}^{\Lambda}\sum_{l=1}^{c^i} \frac{2(\delta_{g,v}^{jilm}\delta_{g,2}^{jilm})^2}{\lambda_2-\lambda_v}\end{aligned} \tag{3.26}$$

For a given planet set, planet modes of stage i exist only for $c^i \geq 4$, where c^i is the number of planet trains in stage i. For $c^i = 4$, the planet mode natural frequencies for planet set i are distinct, and the procedure to calculate the eigensensitivities is the same as that for rotational modes. The results are as (3.20)-(3.22).

For $c^i > 4$, the planet mode frequencies for planet set i are degenerate with multiplicity $w = c^i - 3$. Suppose this degenerate eigenvalue and its associated modes are $\lambda_{1,\ \cdots,\ w} = \lambda_u$ and $\boldsymbol{\phi}_1,\ \cdots,\ \boldsymbol{\phi}_w$. The eigenvectors $\boldsymbol{\phi}_1,\ \cdots,\ \boldsymbol{\phi}_w$ are an arbitrary set of planet modes, which forms the matrix $\boldsymbol{\Phi} = [\boldsymbol{\phi}_1,\ \cdots,\ \boldsymbol{\phi}_w]$. The elements in $\mathbf{D}$ are calculated using (3.5), and the results are $D_{ef} = \sum_{l=1}^{c^i} \delta_{g,e}^{jilm} \delta_{g,f}^{jilm}$, where $e,\ f = 1,\ \cdots,\ w$. Application of the planet mode properties shows that $\mathbf{D}$ is diagonal for any choice of independent planet modes $\boldsymbol{\phi}_1,\ \cdots,\ \boldsymbol{\phi}_w$. In addition, all the diagonal elements of are equal. Thus, the first order eigenvalue derivatives are

$$\frac{\partial \lambda_1}{\partial k_{gp}^{ji*m}} = \cdots = \frac{\partial \lambda_w}{\partial k_{gp}^{ji*m}} = D_{11} = \sum_{l=1}^{c^i} (\delta_{g,1}^{jilm})^2 \tag{3.27}$$

Because $\mathbf{D}$ has a single degenerate eigenvalue, the first order eigenvector derivatives of the set of planet modes can not be determined. The second order eigenvalue derivatives are derived by calculating the eigenvalues of $\mathbf{E}$ in (3.10), and the results are

$$\frac{\partial^2 \lambda_f}{(\partial k_{gp}^{ji*m})^2} = \sum_{v=w+1}^{\Lambda} \sum_{l=1}^{c^i} \frac{2(\delta_{g,v}^{ijlm} \delta_{g,f}^{ijlm})^2}{\lambda_f - \lambda_v} \qquad f = 1,\ \cdots,\ w \tag{3.28}$$

The expressions (3.20), (3.24), and (3.27) suggest that the eigenvalue derivatives are proportional to modal strain energies in the associated stiffness elements. Similar expressions for changing inertia parameters relate these eigenvalue derivatives to modal kinetic energies of the component with changing inertia. The relations between eigenvalue sensitivities and modal strain/kinetic energies are below, where the modal

strain and kinetic energies are defined in Table 3.1 and Table 3.2, respectively. These relations apply to all three types of vibration modes of compound planetary gears. The expressions for $\boldsymbol{\phi}_i'$ and λ'' are collected in Appendix B.1. The following notation is used: $i, h = 1, \ \cdots, \ a$; $j, n = 1, \ \cdots, \ b$; $l = 1, \ \cdots, \ c^i$; $m, q = 1, \ \cdots, \ d^i$.

Table 3.1: The expressions of modal strain energies in vibration mode $\boldsymbol{\phi}_u$. All other subscripts and superscripts for modal strain energies have the same meanings as for stiffness parameters. For example, $U^i_{cb,u}$ means the modal strain energy in the translational bearing stiffness of carrier i.

$U^i_{cb,u} = \frac{1}{2}k^i_{cb}[(x^i_{c,u})^2 + (y^i_{c,u})^2]$
$U^i_{cb,,\theta\theta,u} = \frac{1}{2}k^i_{cb,\theta\theta}(\theta^i_{c,u})^2$
$U^{ij}_{cg,u} = \frac{1}{2}k^{ij}_{cg}[(x^i_{c,u} - x^j_{g,u})^2 + (y^i_{c,u} - y^j_{g,u})^2]$
$U^{ij}_{cg,\theta\theta,u} = \frac{1}{2}k^{ij}_{cg,\theta\theta}(\theta^i_{c,u} - \theta^j_{g,u})^2$
$U^{ih}_{cc,u} = \frac{1}{2}k^{ip}_{cc}[(x^i_{c,u} - x^h_{c,u})^2 + (y^i_{c,u} - y^h_{c,u})^2]$
$U^{ih}_{cc,\theta\theta,u} = \frac{1}{2}k^{ih}_{cc,\theta\theta}(\theta^i_{c,u} - \theta^h_{c,u})^2$
$U^j_{gb,u} = \frac{1}{2}k^j_{gb}[(x^j_{g,u})^2 + (y^j_{g,u})^2]$
$U^{jn}_{gg,u} = \frac{1}{2}k^{jn}_{gg}[(x^j_{g,u} - x^n_{g,u})^2 + (y^j_{g,u} - y^n_{g,u})^2]$
$U^{jn}_{gg,\theta\theta,u} = \frac{1}{2}k^{jn}_{gg,\theta\theta}(\theta^j_{g,u} - \theta^n_{g,u})^2$
$U^{jilm}_{gp,u} = \frac{1}{2}k^{jilm}_{gp}(\delta^{jilm}_{g,u})^2 U^{ji*m}_{gp,u} = \sum_{l=1}^{c^i} U^{ji1m}_{gp,u}$ where $\delta^{jilm}_{g,u} = y^j_{g,u}\cos\psi^{jilm}_{g,u} - x^i_g \sin\psi^{jilm}_{g,u} + r^i_{g,u}\theta^i_{g,u} +$ $\xi^{ilm}_{p,u}\sigma^i \sin\alpha^{jilm}_{g,u} - \eta^{ilm}_{p,u}\cos\alpha^{jilm}_{g,u} - \sigma^j u^{ilm}_{p,u}$.
$U^{ilmq}_{pp,u} = \frac{1}{2}k^{ilmq}_{pp}(\delta^{ilmq}_{p,u})^2 U^{i*mq}_{pp,u} = \sum_{l=1}^{c^i} U^{ilmq}_{pp,u}$ where $\delta^{ilmq}_{p,u} = -\sin(\gamma^{ilmq}_u)\zeta^{ilm}_{p,u} - \sin(\gamma^{ilqm}_u)\zeta^{ilq}_{p,u} +$ $\cos(\gamma^{ilmq}_u)\eta^{ilm}_{p,u} + \cos(\gamma^{ilqm}_u)\eta^{ilq}_{p,u} + u^{ilm}_{p,u} + u^{ilq}_{p,u}$.
$U^{ilm}_{pb,u} = \frac{1}{2}k^{ilm}_p[(\delta^{ilm}_{\zeta,u})^2 + (\delta^{ilm}_{\eta,u})^2]U^{i*m}_{pb,u} = \sum_{l=1}^{c^i} U^{ilm}_{pb,u}$ where $\delta^{ilm}_{\xi,u} = x^i_{c,u}\cos\psi^{ilm}_u + y^i_{c,u}\sin\psi^{ilm}_u - \zeta^{ilm}_{p,u}$, $\delta^{ilm}_{\eta,u} = -x^i_{c,u}\sin\psi^{ilm}_u + y^i_{c,u}\cos\psi^{ilm}_u + r^{ilm}_c\theta^i_{c,u} - \eta^{ilm}_{p,u}$.
$U^{ilmq}_{p-p,u} = \frac{1}{2}k^{ilmq}_{p-p}[(\zeta^{ilm}_{p,u} - \zeta^{ilp}_{p,u})^2 + (\eta^{ilm}_{p,u} - \eta^{ilp}_{p,u})^2]$ $U^{i*mq}_{p-p,u} = \sum_{l=1}^{c^i} U^{ilmq}_{p-p,u}$
$U^{ilmq}_{p-p,\theta\theta,u} = \frac{1}{2}k^{ilmq}_{p-p,\theta\theta}(\frac{u^{ilm}_{p,u}}{r^{ilm}_p} - \frac{u^{ilq}_{p,u}}{r^{ilq}_p})^2$ $U^{i*mq}_{p-p,\theta\theta,u} = \sum_{l=1}^{c^i} U^{ilmq}_{p-p,\theta\theta,u}$

Table 3.2: The expressions of modal kinetic energies in vibration mode $\boldsymbol{\phi}_u$. The subscript $\theta\theta$ means the modal kinetic energy is associated with a certain moment of inertia. All other subscripts and superscripts for modal kinetic energies have the same meaning as for mass/inertia parameters. For example, $T^i_{c,\theta\theta,u}$ is the modal kinetic energy associated with the moment of inertia of carrier i.

$T^i_{c,u} = \frac{1}{2}\lambda_u m^i_c[(x^i_{c,u})^2 + (y^i_{c,u})^2]$
$T^i_{c,\theta\theta,u} = \frac{1}{2}\lambda_u I^i_c(\theta^i_{c,u})^2$
$T^j_{g,u} = \frac{1}{2}\lambda_u m^j_g[(x^j_{g,u})^2 + (y^j_{g,u})^2]$
$T^j_{g,\theta\theta,u} = \frac{1}{2}\lambda_u I^j_g(\theta^j_{g,u})^2$
$T^{ilm}_{p,u} = \frac{1}{2}\lambda_u m^{ilm}_p[(\xi^{ilm}_{p,u})^2 + (\eta^{ilm}_{p,u})^2]$ $T^{i*m}_{p,u} = \sum_{l=1}^{c^i} T^{ilm}_{p,u}$
$T^{ilm}_{p,\theta\theta,u} = \frac{1}{2}\lambda_u I^{ilm}_p(u^{ilm}_p)^2/(r^{ilm}_p)^2$ $T^{i*m}_{p,\theta\theta,u} = \sum_{l=1}^{c^i} T^{ilm}_{p,\theta\theta,u}$

(A) Eigenvalue sensitivities to support (bearing) stiffnesses:

$$\frac{\partial\lambda_u}{\partial k^i_{cb}} = (x^i_{c,u})^2 + (y^i_{c,u})^2 = \frac{2}{k^i_{cb}}U^i_{cb,u} \tag{3.29}$$

$$\frac{\partial\lambda_u}{\partial k^i_{cb,\theta\theta}} = (\theta^i_{c,u})^2 = \frac{2}{k^i_{cb,\theta\theta}}U^i_{cb,\theta\theta,u} \tag{3.30}$$

$$\frac{\partial\lambda_u}{\partial k^j_{gb}} = (x^j_{g,u})^2 + (y^j_{g,u})^2 = \frac{2}{k^j_{gb}}U^j_{gb,u} \tag{3.31}$$

$$\frac{\partial\lambda_u}{\partial k^j_{gb,\theta\theta}} = (\theta^j_{g,u})^2 = \frac{2}{k^j_{gb,\theta\theta}}U^j_{gb,\theta\theta,u} \tag{3.32}$$

$$\frac{\partial\lambda_u}{\partial k^{i*m}_p} = \sum_{l}^{c^i}[(\delta^{ilm}_{\zeta,u})^2 + (\delta^{ilm}_{\eta,u})^2] = \frac{2}{k^{i*m}_p}U^{i*m}_{pb,u} \tag{3.33}$$

(B) Eigenvalue sensitivities to shaft stiffnesses between carriers/central gears and between coaxial planets:

$$\frac{\partial\lambda_u}{\partial k^{ij}_{cg}} = (x^i_{c,u} - x^j_{g,u})^2 + (y^i_{c,u} - y^j_{g,u})^2 = \frac{2}{k^{ij}_{cg}}U^{ij}_{cg,u} \tag{3.34}$$

$$\frac{\partial \lambda_u}{\partial k_{cg,\theta\theta}^{ij}} = (\theta_{c,u}^i - \theta_{g,u}^j)^2 = \frac{2}{k_{cg,\theta\theta}^{ij}} U_{cg,\theta\theta,u}^{ij} \tag{3.35}$$

$$\frac{\partial \lambda_u}{\partial k_{cc}^{ih}} = (x_{c,u}^i - x_{c,u}^h)^2 + (y_{c,u}^i - y_{c,u}^h)^2 = \frac{2}{k_{cc}^{ih}} U_{cc,u}^{ih} \tag{3.36}$$

$$\frac{\partial \lambda_u}{\partial k_{cc,\theta\theta}^{ih}} = (\theta_{c,u}^i - \theta_{c,u}^h)^2 = \frac{2}{k_{cc,\theta\theta}^{ih}} U_{cc,\theta\theta,u}^{ih} \tag{3.37}$$

$$\frac{\partial \lambda_u}{\partial k_{gg}^{jn}} = (x_{g,u}^j - x_{g,u}^n)^2 + (y_{g,u}^j - y_{g,u}^n)^2 = \frac{2}{k_{gg}^{jn}} U_{gg,u}^{jn} \tag{3.38}$$

$$\frac{\partial \lambda_u}{\partial k_{gg,\theta\theta}^{jn}} = (\theta_{g,u}^j - \theta_{g,u}^n)^2 = \frac{2}{k_{gg,\theta\theta}^{jn}} U_{gg,\theta\theta,u}^{jn} \tag{3.39}$$

$$\frac{\partial \lambda_u}{\partial k_{p-p}^{i*mq}} = \sum_l^{c^i} [(\zeta_{p,u}^{ilm} - \zeta_{p,u}^{ilq})^2 + (\eta_{p,u}^{ilm} - \eta_{p,u}^{ilq})^2] = \frac{2}{k_{p-p}^{i*mq}} U_{p-p,u}^{i*mq} \tag{3.40}$$

$$\frac{\partial \lambda_u}{\partial k_{p-p,\theta\theta}^{i*mq}} = \sum_l^{c^i} (\frac{u_{p,u}^{ilm}}{r_p^{ilm}} - \frac{u_{p,u}^{ilq}}{r_p^{ilq}})^2 = \frac{2}{k_{p-p,\theta\theta}^{i*mq}} U_{p-p,\theta\theta,u}^{i*mq} \tag{3.41}$$

(C) Eigenvalue sensitivities to mesh stiffnesses:

$$\frac{\partial \lambda_u}{\partial k_{gp}^{ji*m}} = \sum_l^{c^i} (\delta_{gp,u}^{jilm})^2 = \frac{2}{k_{gp}^{ji*m}} U_{gp,u}^{ji*m} \tag{3.42}$$

$$\frac{\partial \lambda_u}{\partial k_{pp}^{i*mq}} = \sum_l^{c^i} (\delta_{p,u}^{ilmq})^2 = \frac{2}{k_{pp}^{i*mq}} U_{pp,u}^{i*m,q} \tag{3.43}$$

(D) Eigenvalue sensitivities to masses and moments of inertia:

$$\frac{\partial \lambda_u}{\partial m_c^i} = -\lambda_u[(x_{c,u}^i)^2 + (y_{c,u}^i)^2] = -\frac{2}{m_c^i} T_{c,u}^i \tag{3.44}$$

$$\frac{\partial \lambda_u}{\partial I_{c,u}^i} = -\lambda_u(\theta_{c,u}^i)^2 = -\frac{2}{I_{c,u}^i} T_{c,\theta\theta,u}^i \tag{3.45}$$

$$\frac{\partial \lambda_u}{\partial m_g^j} = -\lambda_u[(x_{g,u}^j)^2 + (y_{g,u}^j)^2] = -\frac{2}{m_g^j} T_{g,u}^j \tag{3.46}$$

$$\frac{\partial \lambda_u}{\partial I_{g,u}^j} = -\lambda_u(\theta_{g,u}^j)^2 = -\frac{2}{I_{g,u}^j} T_{g,\theta\theta,u}^j \tag{3.47}$$

$$\frac{\partial \lambda_u}{\partial m_p^{i*m}} = -\lambda_u \sum_{l=1}^{c^i} [(\xi_{p,u}^{ilm})^2 + (\eta_{p,u}^{ilm})^2] = -\frac{2}{m_p^{i*m}} T_{p,u}^{i*m} \tag{3.48}$$

$$\frac{\partial \lambda_u}{\partial I_p^{i*m}} = -\lambda_u \sum_{l=1}^{c^i} \frac{(u_p^{ilm})^2}{(r_p^{ilm})^2} = -\frac{2}{I_p^{i*m}} T_{p,\theta\theta,u}^{i*m} \tag{3.49}$$

Application of the well-defined modal properties (2.40)-(2.48) to the derived eigensensitivities in (3.29)-(3.49) and (B.1)-(B.30) yields some immediate results. The rotational mode property that central gears and carriers have no translational motion leads to the independence of all rotational modes to the masses of all central gears and carriers, and the translational support/shaft stiffnesses of these components. Due to the translational mode property that all central gears and carriers have no rotational motion, all translational modes are independent of the moments of inertia of central gears and carriers, and the rotational support/shaft stiffnesses of these components. Similarly, planet mode properties ensure that all planet modes for a given planet set are independent of all inertia and stiffness parameters except for those associated with this given planet set.

3.3.2 Application of the Modal Strain/Kinetic Energy Distribution Plots

The formulae (3.29)-(3.49) show that the modal strain/kinetic energies of compound planetary gears determine the eigenvalue sensitivities to stiffness/inertia parameters. As a result, the modal strain/kinetic energy distribution plots of a certain mode qualitatively and quantitatively give the sensitivity of the natural frequency associated with this mode to all system parameters.

Consider the two-stage compound planetary gear system shown in Figure 3.1, where for clarity only the mesh stiffnesses (no bearing and shaft stiffnesses) are shown

as solid lines. The nominal system parameters are listed in Table 3.3, and the lowest fourteen natural frequencies are listed in Table 3.4. Consider the case where practical design or troubleshooting needs require the fourth natural frequency (ω_4) to be greater than 900 Hz, where it is ω_4=871Hz with nominal parameters values. The mode associated with ω_4 is a rotational mode, and its mode shape is shown in Figure 3.2.

Table 3.3: Nominal parameters of the example system shown in Figure 3.1.

Number of Carriers	2
Number of Central Gears	4
Number of Planet Trains	c^1=4, c^2=6
Number of Planets per Train	d^1=2, d^2=1
Planet Location	$\psi^{1l1}(0) = \frac{2\pi(l-1)}{4};\ l = 1,\ \cdots,\ 4$ $\psi^{2l1}(0) = \frac{2\pi(l-1)}{6};\ l = 1,\ \cdots,\ 6$ $\psi^{1l2}(0) = \psi^{1l1}(0) + 32^\circ$ $\beta^{1l12} = 70^\circ, \beta^{1l21} = 218^\circ$
Mesh Stiffnesses (N/m)	$k_{gp}^{jilm} = \begin{cases} 500\times10^6 & \text{If } j=1,i=1,m=1 \\ & \text{or } j=2,i=1,m=2 \\ & \text{or } j=3,i=2,m=1 \\ & \text{or } j=4,i=2,m=1 \\ 0 & \text{Otherwise} \end{cases}$ $k_{pp}^{ilmq} = \begin{cases} 500\times10^6 & \text{If } i=1 \\ 0 & \text{Otherwise} \end{cases}$
Translational Support Stiffness (N/m)	$k_{cb,xx}^{i} = k_{cb,yy}^{i} = 1\times10^9$ $k_{gb,xx}^{j} = k_{gb,yy}^{j} = 1\times10^9$ $k_{p}^{ilm} = 1\times10^9$
Torsional Support Stiffness (N-m/rad)	$k_{cb,\theta\theta}^{i} = 0,\ k_{gb,\theta\theta}^{1} = k_{gb,\theta\theta}^{3} = 0$ $k_{gb,\theta\theta}^{2} = k_{gb,\theta\theta}^{4} = 500\times10^6$
Torsional Shaft Stiffnesses (N-m/rad)	$k_{g,xx}^{jn} = k_{g,yy}^{jn} = 0,\ k_{c,xx}^{ih} = k_{c,yy}^{ih} = 0$ $k_{cg,xx}^{ij} = k_{cg,yy}^{ij} = \begin{cases} 800\times10^6 & \text{If } i=1,j=3 \\ 0 & \text{Otherwise} \end{cases}$
Torsional Shaft Stiffnesses (N-m/rad)	$k_{g,\theta\theta}^{jn} = k_{c,\theta\theta}^{ih} = 0$ $k_{cg,\theta\theta}^{ij} = \begin{cases} 200\times10^6 & \text{If } i=1,j=3 \\ 0 & \text{Otherwise} \end{cases}$

Continued on next page

Table 3.3 – *Continued from previous page*

Mass (kg)	$m_g^1 = 1,\ m_g^2 = 5,\ m_g^3 = 1,\ m_g^4 = 5$ $m_c^1 = 10,\ m_c^2 = 10$ $m_p^{1l1} = m_p^{1l2} = 0.75,\ m_p^{2l1} = 2.00$
Moment of Inertia (kg-m^2)	$I_g^1 = 0.05,\ I_g^2 = 0.5$ $I_g^3 = 0.05,\ I_g^4 = 0.5$ $I_c^1 = 1.00,\ I_c^2 = 1.20$ $I_p^{1l1} = I_p^{1l2} = 0.01,\ I_9^{2l1} = 0.20$
Radii (mm)	$r_g^1 = 100.0,\ r_g^2 = 320.6$ $r_g^3 = 100.0,\ r_g^4 = 300.0$ $r_c^{1l1} = 176.5,\ r_c^{1l2} = 270.0,\ r_c^{2l1} = 220.7$ $r_p^{1l1} = 60.0,\ r_p^{1l2} = 77.7,\ r_c^{2l1} = 100.0$
Gear Type	$\sigma^1 = \sigma^3 = -1$ (sun gear) $\sigma^2 = \sigma^4 = 1$ (ring gear)

Table 3.4: The lowest fourteen natural frequencies for the example system of Figure 3.1 with nominal parameters listed in Table 3.3. R means Rotational mode, T means Translational mode, $P1$ means Planet mode of planet set 1, and $P2$ means Planet mode of planet set 2.

Natural Frequency Number	Natural Frequency (Hz)	Vibration Mode Type
1	0	R
2, 3	657	T
4	871	R
5, 6, 7	1030	$P2$
8	1134	R
9, 10	1152	T
11	1535	R
12, 13	1554	T
14	1854	$P1$
15, 16	1946	T
17, 18	2421	T
19	2944	R
20, 21	3190	T
...	...	...
55, 56	9083	T
57	9148	R
58, 59	9408	T
60	11073	R

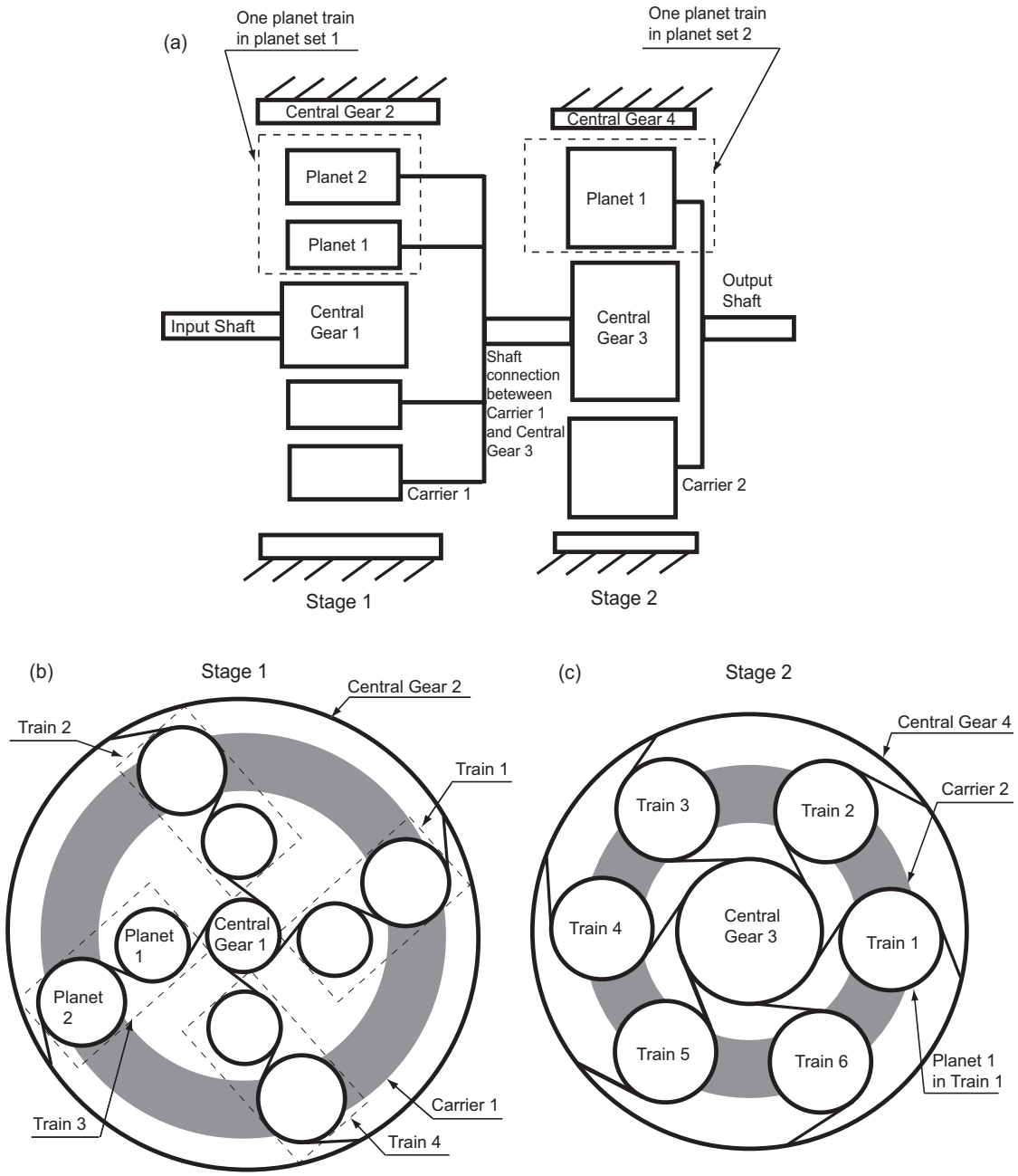

Figure 3.1: The example system for the eigensensitivity analysis in this chapter.

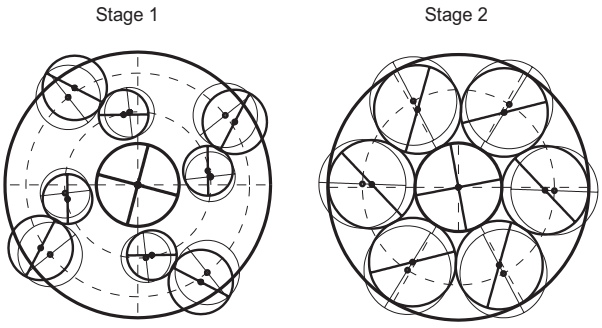

Figure 3.2: Mode shape of vibration mode 4 ($\omega_4 = 871Hz$) for the example system with nominal parameter values.

The modal strain and kinetic energy distribution plots for this mode are shown in Figure 3.3. The strain energies in k_{gp}^{32*1} and k_{gp}^{42*1} (the mesh stiffnesses of the sun-planet and ring-planet meshes in the second stage of the example system) are the highest modal strain energies, and the modal kinetic energy associated with I_p^{2*1} (the moment of inertia of the planets in stage 2) is the largest modal kinetic energy. Thus, k_{gp}^{32*1}, k_{gp}^{42*1} and I_p^{2*1} are the most effective parameters in tuning ω_4.

Figure 3.4 shows ω_4 versus the variation of k_{gp}^{32*1} and k_{gp}^{42*1}, and the change of I_p^{2*1}. When both k_{gp}^{32*1} and k_{gp}^{42*1} increase 16% from their nominal values, or I_p^{2*1} is reduced by 8.2% from its nominal value, ω_4 is tuned to be larger than 900 Hz, which achieves the design goal.

3.4 Eigensensitivity of Mistuned Compound Planetary Gears

The candidate mistuned parameters are k_{gp}^{jilm}, k_{pp}^{ilmq}, k_p^{ilm}, k_{p-p}^{ilmq}, $k_{p-p,\theta\theta}^{ilmq}$, m_p^{ilm}, and I_p^{ilm}, because these perturbed parameters are the only ones that break the symmetry of planet sets to create mistuning. This study focuses on the case of one mistuned parameter because equations (3.11)-(3.13) show that the impact of multiple mistuned

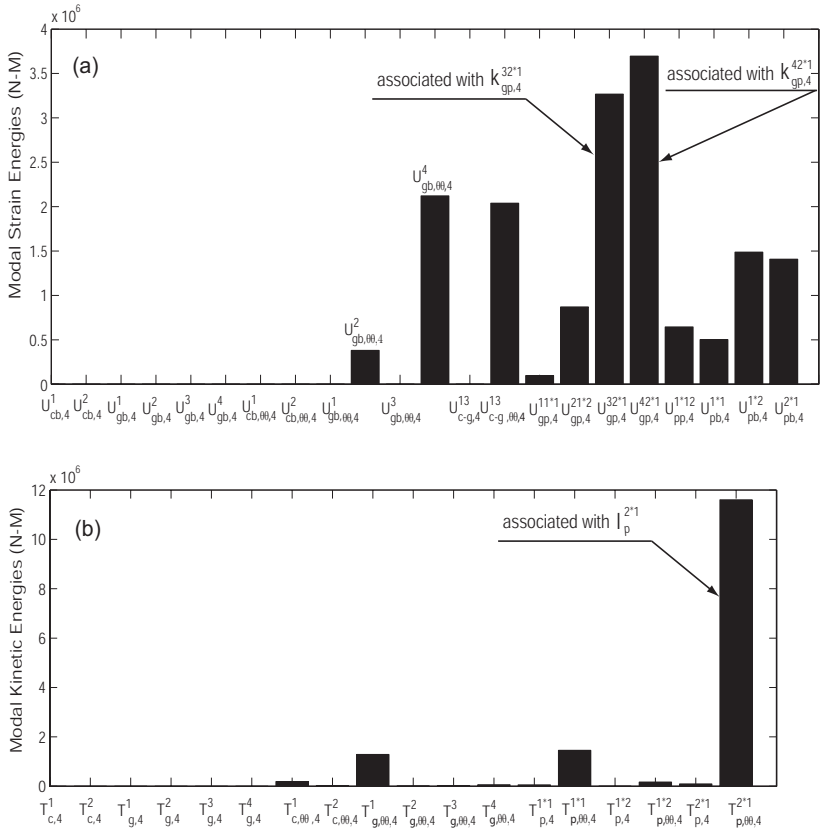

Figure 3.3: Modal (a) strain, and (b) kinetic energy distributions associated with mode 4 ($\omega_4 = 871Hz$).

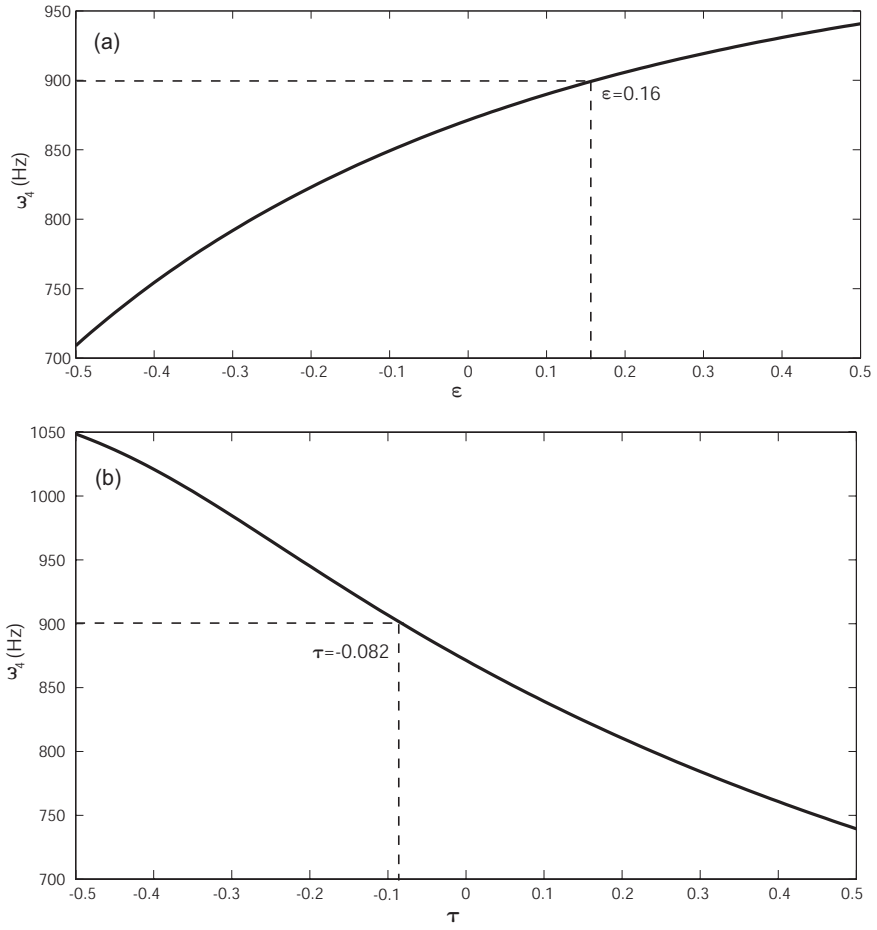

Figure 3.4: (a) ω_4 versus $\varepsilon = \frac{k_{gp}^{32*1} - \bar{k}_{gp}^{32*1}}{\bar{k}_{gp}^{32*1}} = \frac{k_{gp}^{42*1} - \bar{k}_{gp}^{42*1}}{\bar{k}_{gp}^{42*1}}$, and (b) ω_4 versus $\tau = \frac{I_p^{2*1} - \bar{I}_p^{2*1}}{\bar{I}_p^{2*1}}$. $\bar{k}_{gp}^{32*1}$ and k_{gp}^{32*1} are the nominal and perturbed values of the mesh stiffness between the sun gear in stage 2 (central gear 3) and planet 1 in any planet train of planet set 2. $\bar{k}_{gp}^{42*1}$ and k_{gp}^{42*1} are the nominal and perturbed values of the mesh stiffness between the ring gear in stage 2 (central gear 4) and planet 1 in any planet train of planet set 2. $\bar{I}_p^{2*1}$ and I_p^{2*1} are the nominal and perturbed values of moment of inertia of planet 1 in any planet train of planet set 2.

parameters on natural frequencies and vibration modes is the superposition of the impacts from each mistuned parameter.

As a representative example, the derivation of eigensensitivities to a mistuned mesh stiffness parameter is illustrated. Consider the case that k_{gp}^{ji1m} (the mesh stiffness between central gear j and planet m in train 1 of planet set i) is the only varying parameter, and its nominal value is $\bar{k}_{gp}^{ji1m}$. In order to apply equations (3.1)-(3.10, the derivatives of the mass and stiffness matrices are

$$\frac{\partial \mathbf{M}}{\partial k_{gp}^{ji1m}} = \mathbf{0} \qquad \frac{\partial^2 \mathbf{M}}{(\partial k_{gp}^{ji1m})^2} = \mathbf{0} \tag{3.50}$$

$$\frac{\partial \mathbf{K}}{\partial k_{gp}^{ji1m}} = \begin{bmatrix} \ddots & & \\ & \frac{\partial \mathbf{K}_{g1}^{ji1m}}{\partial k_{gp}^{ji1m}} \quad \cdots \quad \frac{\partial \mathbf{K}_{gp}^{ji1m}}{\partial k_{gp}^{ji1m}} & \\ & \vdots \qquad\qquad \vdots & \\ & \frac{\partial \left(\mathbf{K}_{gp}^{ji1m}\right)^T}{\partial k_{gp}^{ji1m}} \quad \cdots \quad \frac{\partial \mathbf{K}_{g3}^{ji1m}}{\partial k_{gp}^{ji1m}} & \\ & & \ddots \end{bmatrix} \qquad \frac{\partial^2 \mathbf{K}}{(\partial k_{gp}^{ji1m})^2} = \mathbf{0} \tag{3.51}$$

where all sub-matrices of $\partial \mathbf{K}/\partial k_{gp}^{ji1m}$ are zero except the four sub-matrices shown in (3.51), which are coupling terms between central gear j and planet m in the first train of stage i. Substitution of $l = 1$ (for the first train) into equations (3.15)-(3.17) shows that these four sub-matrices depend linearly on k_{gp}^{ji1m}.

By applying equations (3.1)-(3.3), the sensitivities of a rotational mode to k_{gp}^{ji1m} are

$$\frac{\partial \lambda_u}{\partial k_{gp}^{ji1m}} = (\delta_{g,u}^{ji1m})^2 = \frac{2}{k_{gp}^{ji1m}} U_{gp,u}^{ji1m} \tag{3.52}$$

$$\frac{\partial \boldsymbol{\phi}_u}{\partial k_{gp}^{ji1m}} = \sum_{v=1, v\neq u}^{\Lambda} \frac{\delta_{g,u}^{ji1m} \delta_{g,v}^{ji1m}}{\lambda_u - \lambda_v} \boldsymbol{\phi}_v \tag{3.53}$$

$$\frac{\partial^2 \lambda_u}{(\partial k_{gp}^{ji1m})^2} = \sum_{v=1, v\neq u}^{\Lambda} \frac{2}{\lambda_u - \lambda_v} (\delta_{g,u}^{ji1m} \delta_{g,v}^{ji1m})^2 \tag{3.54}$$

where $U_{gp,u}^{ji1m}$ is the modal strain energy in the stiffness k_{gp}^{ji1m}. The sensitivities of a rotational mode or a distinct planet mode to all other possible mistuned parameters are listed in Appendix B.2.

For a pair of translational modes, the eigensensitivities to k_{gp}^{ji1m} are calculated by following the procedure in (3.4)-(3.10). The degenerate translational eigenvalue is $\lambda_u = \lambda_{u+1}$. Choosing the preferred pair of translational modes $\boldsymbol{\Phi} = [\boldsymbol{\phi}_u, \boldsymbol{\phi}_{u+1}]$ that diagonalizes $\mathbf{D}$ in (2.44) gives

$$\mathbf{D} = \boldsymbol{\Phi}^T \frac{\partial \mathbf{K}}{\partial k_{gp}^{ji1m}} \boldsymbol{\Phi} = \begin{bmatrix} (\delta_{g,u}^{ji1m})^2 & 0 \\ 0 & 0 \end{bmatrix} \tag{3.55}$$

where $\delta_{g,u}^{ji1m}$ is the mesh deflection between gear j and planet m in train 1 of planet set i in vibration mode $\boldsymbol{\phi}_u$. The eigenvalue sensitivities from the eigenvalues of $\mathbf{D}$ are

$$\frac{\partial \lambda_u}{\partial k_{gp}^{ji1m}} = (\delta_{g,u}^{ji1m})^2 = \frac{2}{k_{gp}^{ji1m}} U_{gp,u}^{ji1m} \qquad \frac{\partial \lambda_{u+1}}{\partial k_{gp}^{ji1m}} = 0 \tag{3.56}$$

where $U_{gp,u}^{ji1m}$ is the modal strain energy associated with k_{gp}^{ji1m} in mode $\boldsymbol{\Phi}_u$.

By applying (3.6)-(3.10), the closed-form expressions for the first order eigenvector and second order eigenvalue derivatives are

$$\frac{\partial \boldsymbol{\phi}_u}{\partial k_{gp}^{ji1m}} = \sum_{v=1, v\neq u, u+1}^{\Lambda} \frac{\delta_{g,v}^{ji1m} \delta_{g,u}^{ji1m}}{\lambda_u - \lambda_v} \boldsymbol{\phi}_v \qquad \frac{\partial \boldsymbol{\phi}_{u+1}}{\partial k_{gp}^{ji1m}} = \mathbf{0} \tag{3.57}$$

$$\frac{\partial^2 \lambda_u}{(\partial k_{gp}^{ji1m})^2} = \sum_{v=1, v\neq u, u+1}^{\Lambda} \frac{2(\delta_{g,v}^{ji1m} \delta_{g,u}^{ji1m})}{\lambda_u - \lambda_v} \qquad \frac{\partial^2 \lambda_{u+1}}{(\partial k_{gp}^{ji1m})^2} = 0 \tag{3.58}$$

Equations (3.56)-(3.58) show that one of a pair of translational modes is not affected by the mistuned mesh stiffness k_{gp}^{ji1m}; the translational mode properties are retained in this mode, even though the system symmetry is broken by the mistuning. The other translational mode, however, changes with k_{gp}^{ji1m} and loses its well-defined translational mode properties; the perturbed mode is contaminated by contributions

from all other modes in (3.57). The magnitude of a contaminating mode v is determined by that mode's mesh deflection $\delta_{g,v}^{ji1m}$ and the proximity of the associated eigenvalue value λ_v to λ_u. The eigensensitivities of a pair of translational modes to all other mistuned parameters are derived in the same way, and their expressions are collected in Appendix B.2.

The eigensensitivities in (3.52)-(3.58) and (B.31)-(B.48) show that only a mistuned planet bearing stiffness (k_p^{i1m}), translational shaft stiffness between two coaxial planets of a stepped-planet arrangement (k_{pp}^{i1mq}), or planet mass (m_p^{ilm}) can affect both modes of a pair of degenerate translational modes. In theses cases, the degenerate translational natural frequency of the unperturbed system splits into two distinct natural frequencies, and both associated modes lose their translational mode properties. Any other mistuned parameter affects only one of the pair of translational modes and has no impact on the other mode.

Using the example system of Figure 3.1, Table 3.3, and Table 3.4, Figure 3.5(a) shows the impact of the perturbed mesh stiffness between central gear 3 and planet 1 in train 1 of planet set 2 (k_{gp}^{3211}) on a pair of degenerate translational frequencies (ω_{12} and ω_{13}). ω_{12} is affected by k_{gp}^{3211} dramatically, while ω_{13} remains unchanged. Figure 3.5(b) illustrates how the same pair of translational frequencies is changed by the bearing stiffness of planet 1 in train 1 of planet set 2 (k_p^{211}). The mistuned parameter k_p^{211} splits the loci of ω_{12} and ω_{13} and changes both of them.

For a set of planet modes with a degenerate natural frequency, the procedure in (3.4)-(3.10) is applied to calculate their eigensensitivities. This degenerate eigenvalue with multiplicity $w \geq 2$ is $\lambda_u = \lambda_{u+1} = \cdots = \lambda_{u+w-1}$. The associated eigenvectors are chosen to be the preferred eigenvectors $\boldsymbol{\Phi} = [\boldsymbol{\phi}_u, \cdots, \boldsymbol{\phi}_{u+w-1}]$ that diagonalize

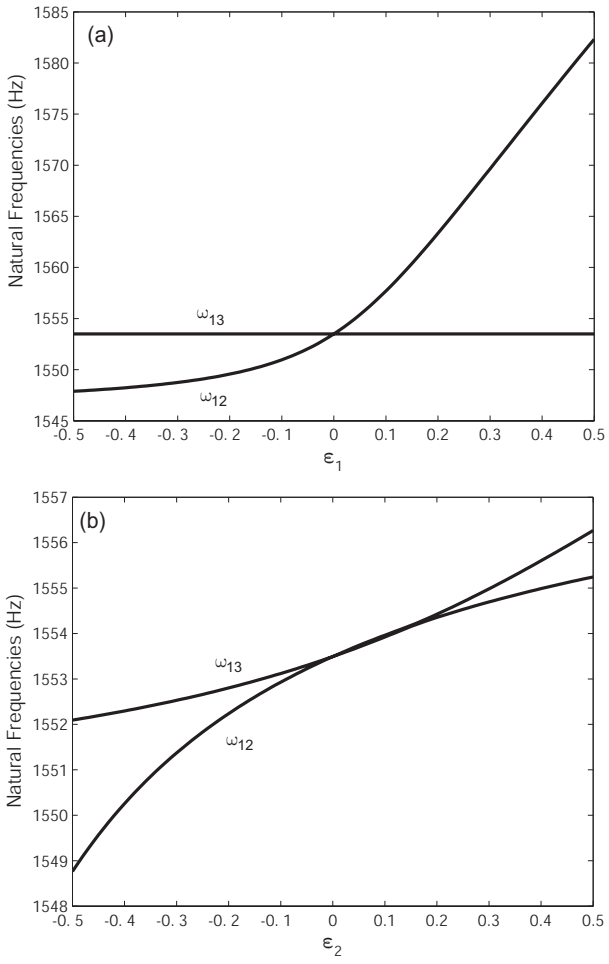

Figure 3.5: (a) ω_{12} and ω_{13} versus $\varepsilon_1 = \frac{k_p^{3211} - \bar{k}_p^{3211}}{k_p^{3211}}$, and (b) ω_{12} and ω_{13} versus $\varepsilon_2 = \frac{k_p^{211} - \bar{k}_p^{211}}{k_p^{211}}$. $\bar{k}_{gp}^{3211}$ and k_{gp}^{3211} are the nominal and perturbed values of the mesh stiffness between the sun gear in stage 2 (central gear 3) and planet 1 in train 1 of planet set 2. $\bar{k}_p^{211}$ and k_p^{211} are the nominal and perturbed values of the bearing stiffness of planet 1 in train 1 of planet set 2.

the matrix $\mathbf{D}$ in (2.49). Thus, the diagonalized $\mathbf{D}$ and its eigenvalues yield

$$\mathbf{D} = \mathbf{\Phi}^T \frac{\partial \mathbf{K}}{\partial k_{gp}^{ji1m}} \mathbf{\Phi} = \begin{bmatrix} (\delta_{g,u}^{ji1m})^2 & 0 & \cdots & 0 \\ & 0 & \cdots & 0 \\ & & \ddots & \vdots \\ symm. & & & 0 \end{bmatrix}_{w \times w} \tag{3.59}$$

$$\begin{array}{l} \frac{\partial \lambda_u}{\partial k_{gp}^{ji1m}} = (\delta_{g,u}^{ji1m})^2 = \frac{2}{k_{gp}^{ji1m}} U_{gp,u}^{ji1m} \\ \frac{\partial \lambda_{u+1}}{\partial k_{gp}^{ji1m}} = \cdots = \frac{\partial \lambda_{u+w-1}}{\partial k_{gp}^{ji1m}} = 0 \end{array} \tag{3.60}$$

where $\delta_{g,u}^{ji1m}$ and $U_{gp,u}^{ji1m}$ are the mesh deflection and modal strain energy associated with k_{gp}^{ji1m} in mode $\boldsymbol{\phi}_u$.

When the multiplicity of a degenerate planet mode frequency is two, $\mathbf{D}$ in (3.59) has distinct eigenvalues. The first order eigenvector derivative and the second order eigenvalue derivative with respect to k_{gp}^{ji1m} are exactly the same as those for translational modes in equations (3.57)-(3.58). Only one of the two natural frequencies is affected. When the planet mode frequency multiplicity is greater than two, $\mathbf{D}$ in (3.59) has a degenerate zero eigenvalue. Therefore, the eigenvector derivatives of these planet modes with respect to the mistuned parameter k_{gp}^{ji1m} can not be determined. By calculating the eigenvalues of $\mathbf{E}$ in (3.10), the second order eigenvalue derivatives are

$$\begin{array}{l} \frac{\partial^2 \lambda_u}{(\partial k_{gp}^{ji1m})^2} = \sum_{v=1, v \neq u, \cdots, u+w-1}^{\Lambda} \frac{2(\delta_{g,v}^{ji1m} \delta_{g,u}^{ji1m})}{\lambda_u - \lambda_v} \\ \frac{\partial^2 \lambda_{u+1}}{(\partial k_{gp}^{ji1m})^2} = \cdots = \frac{\partial^2 \lambda_{u+w-1}}{(\partial k_{gp}^{ji1m})^2} = 0 \end{array} \tag{3.61}$$

The eigensensitivities of planet modes to all other mistuned parameters are collected in Appendix B.2. Equations (3.60)-(3.61) and (88)-(99) reveal that only one of a set of degenerate planet modes is affected by a single mistuned parameter and loses it well-defined modal properties. All other planet modes of the set retain their distinctive modal properties; their natural frequency is unchanged, but its multiplicity is reduced to $w - 1$.

The above analytical results show that the eigenvalue sensitivity of all mode types to a mistuned parameter is proportional to the modal strain/kinetic energy associated with this mistuned parameter. Therefore, as for tuned systems, inspection of the modal strain/kinetic energy distribution for mistuned systems remains an effective way to quantitatively determine the parameters that have the largest impact on a certain mode.

3.5 Conclusion

The major results for the eigensensitivities of general compound planetary gears to all stiffness and inertia parameters are summarized as follows:

(1) All eigenvalue derivatives are proportional to the modal strain/kinetic energies associated with the perturbed parameters. Application of the well-defined modal properties of general compound planetary gears simplifies the eigensensitivity expressions to compact, closed-form formulae for all parameter variations. For both tuned and mistuned systems, the modal strain/kinetic energy distribution plots give effective and straightforward means to identify which system parameters have the greatest impact on tuning the related natural frequency. This process can be done qualitatively and quantitatively by inspection.

(2) For tuned systems, the eigenvector sensitivities of degenerate translational and planet modes can not be determined, although the second order eigenvalue derivatives can be. The first and second order eigenvalue derivatives of degenerate eigenvalues of the original system are such that degenerate eigenvalues remain degenerate for parameter perturbations that preserve the tuned symmetry. Rotational modes are independent of translational support/shaft stiffnesses and masses

of central gears/carriers. Translational modes are independent of torsional support/shaft stiffnesses and moments of inertia of central gears/carriers. Planet modes of a certain planet set are independent of any system parameters associated with other planet sets. They are also independent of the mass/moment of inertia parameters and support/shaft stiffness parameters of all central gears/carriers.

(3) When a system is perturbed by a mistuned parameter, a degenerate translational mode natural frequency of the unperturbed system splits into two distinct frequencies. A mistuned planet bearing stiffness, translational shaft stiffness between two planets in a stepped planet arrangement, or planet mass impacts both modes associated with the two frequencies, while any other mistuned parameter affects only one of the modes despite the apparent disruption of system symmetry. Parameter mistuning always splits degenerate planet mode frequencies of the stage associated with the mistuned parameter into two frequencies. One frequency keeps its original value and its associated modes retain the well-defined planet mode properties; the other frequency is distinct and its associated mode loses the planet mode properties.

Chapter 4: NATURAL FREQUENCY VEERING AND CROSSING PATTERNS FOR GENERAL COMPOUND PLANETARY GEARS

4.1 Introduction

Natural frequency veering is the phenomenon that two eigenvalue loci approach each other and then abruptly veer away when a certain parameter varies, and natural frequency crossing refers to the situation that two eigenvalue loci approach and cross each other with the variation of a parameter. These phenomena are commonly observed in different mechanical systems and investigated in previous studies [42, 72, 80–82, 89]. All these previous studies suggest that the eigenvalue loci veering and crossing patterns are important to the free vibration analysis and further dynamics study of a mechanical system because the vibration modes retain their characteristics in case of crossing and they change dramatically near the vicinity of strongly-coupled veering natural frequencies.

Planetary gear natural frequency veering and crossing phenomena are observed by lots of researchers, such as Cunliffe et al. [22], Botman [16], Saada and Velex [85], Kahraman [43, 45], and Lin and Parker [57]. The systematical investigation on planetary gear natural frequency veering and crossing phenomena, however, was not performed until Lin and Parker's investigation in [59]. By calculating the coupling factors

that approximate the local curvatures of two close eigenvalue loci and applying the structured vibration properties in [56], they derived the veering and crossing patterns for simple planetary gears. The research scopes for all these previous studies are limited to simple planetary gears. Due to the involving of stepped-planet, meshed-planet, and multi-stage structures that are unique to compound planetary gears, the eigensensitivities for compound planetary gears differ from those for simple planetary gears [36], and the results for simple planetary gears in [59] can not be applied to compound planetary gears. In addition, there is no published literature on the veering and crossing patterns for compound planetary gears. It is, hence, necessary to systematically investigate the natural frequency veering and crossing patterns for general compound planetary gears.

4.2 Natural Frequency Veering and Crossing Phenomena in Compound Planetary Gears

Natural frequency veering and crossing phenomena present in compound planetary gears when certain parameter varies. For example, when k_{gb}^2, the bearing stiffness of the ring gear in the first stage of the example system that is shown in Figure 3.1 with the nominal parameters and natural frequencies listed in Tables 3.3 and 3.4, varies, both natural frequency veering and crossing happen in Figure 4.1. The loci of translational frequencies ω_{17} and ω_{18} cross the locus of a rotational frequency ω_{19} at point O when k_{gb}^2 increases to roughly twice of its nominal value. The loci of ω_{17} and ω_{18} veer away from the loci of another pair of translational frequencies ω_{20} and ω_{21} in the vicinity of point O' when k_{gb}^2 is 2.75 times of its nominal value.

Points A and B are on the loci of ω_{17} and ω_{18} in the vicinity of the loci-crossing point O. Figure 4.2 shows the translational mode shapes that associated with ω_{17} and

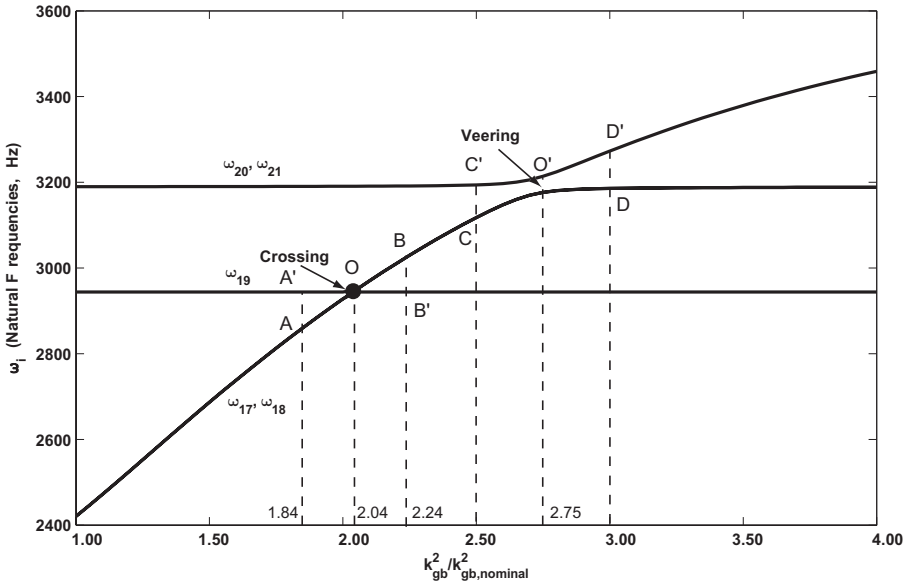

Figure 4.1: Natural frequency crossing and veering phenomena in the example system when k_{gb}^2 varies.

ω_{18} at points A (when k_{gb}^2 is 1.84 times of its nominal value) and B (when k_{gb}^2 is 2.24 times of its nominal value) in Figure 4.1. The mode shapes in Figure 4.2(a) are similar to those in 4.2(b). That is, the translational modes ω_{17} and ω_{18} retain their modal properties when k_{gb}^2 varies in the vicinity of point O. In addition, Figure 4.3 shows the rotational mode shapes at points A' and B' in Figure 4.1. There is no difference between these two mode shapes in Figure 4.3. This matches the eigensensitivity results from previous chapter that k_{gb}^2 has no impact on any rotational mode. Hence, both the rotational frequency ω_{17} and the translational frequencies ω_{17} and ω_{18} retain their mode shapes and modal properties in the vicinity of the loci-crossing point O when k_{gb}^2 varies.

Points C and D around the loci-veering point O' are on the loci of ω_{17} and ω_{18}. Figure 4.4 demonstrates the translational mode shapes that associated with these two

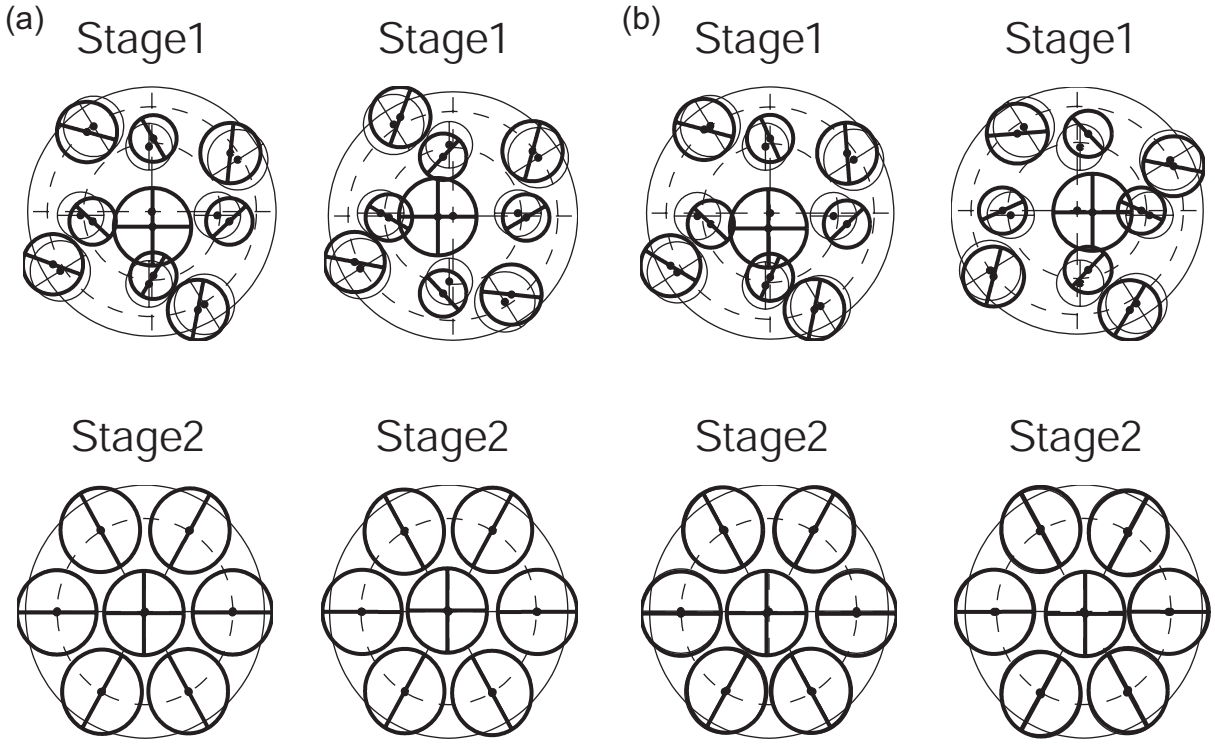

Figure 4.2: Mode shapes of the translational modes associated with ω_{17} and ω_{18} at points A (sub-figure a) and B (sub-figure b) in Figure 4.1.

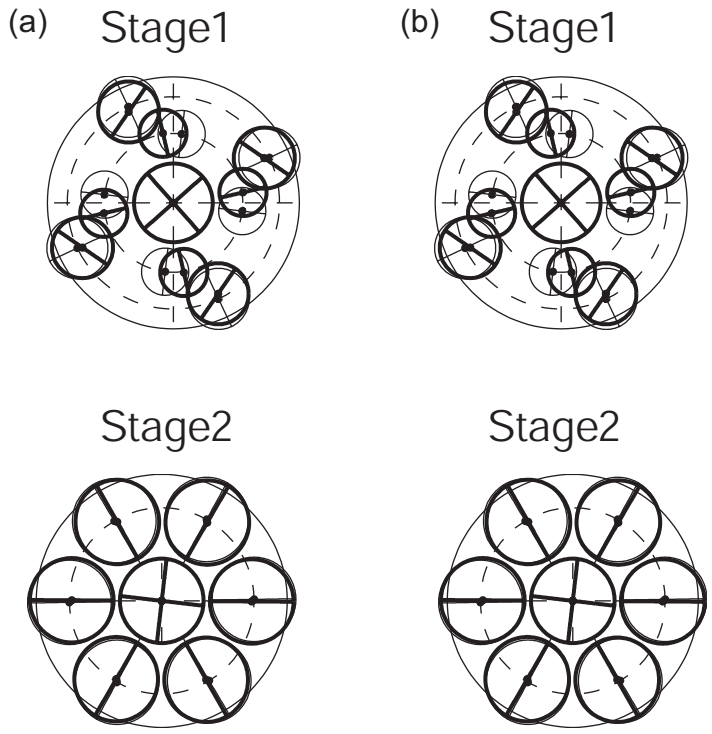

Figure 4.3: Mode shapes of the rotational mode associated with ω_{19} at points A' (sub-figure a) and B' (sub-figure b) in Figure 4.1.

frequencies at points C (when k_{gb}^2 is 1.5 times of its nominal value) and D in Figure 4.1 (when k_{gb}^2 is three times of its nominal value). The mode shapes in Figure 4.4(a) are significantly different from those in 4.4(b). The components in Stage 1 have large amplitudes and Stage 2 components barely moves in Figure 4.4(b). In Figure 4.4(b), however, the components in Stage 2 have large amplitudes and the vibrations of Stage 1 components are insignificant. Hence, the pair of translational modes ω_{17} and ω_{18} experiences dramatic changes in mode shapes and modal properties in the vicinity of loci-veering point O' when k_{gb}^2 varies. Points C' and D' in Figure 4.1 are on the loci of another pair of translational modes ω_{20} and ω_{21}. The mode shapes associated with ω_{20} and ω_{21} at these two points are shown in Figure 4.5. The mode shapes at point C' are significantly different from those at point D'. Therefore, both pairs of translational frequencies $[\omega_{17},\ \omega_{17}]$ and $[\omega_{20},\ \omega_{21}]$ lose their original mode shape and modal properties in the vicinity of the loci-crossing point when k_{gb}^2 varies. Such dramatic change in vibration mode shapes in the vicinity of natural frequency veering is called *mode localization* in several studies [42, 72, 81, 82] or *high mode sensitivity* in some other studies [20, 69]. Taking another look at Figures 4.4 and 4.5, the mode shapes at point C are similar to those in point D', and the mode shapes at point C' are very close to those in point D. That is, the two pair of translational modes $[\omega_{17},\ \omega_{17}]$ and $[\omega_{20},\ \omega_{21}]$ interchange their mode shapes and modal properties during the natural frequency veering caused by the variation of k_{gb}^2.

This example indicates that natural frequency veering and crossing phenomena present in compound planetary gears. Because slight variations in system parameters may cause dramatic changes in the mode shapes and dynamic responses in vicinity of natural frequency veering while mode shapes and dynamic responses have no such

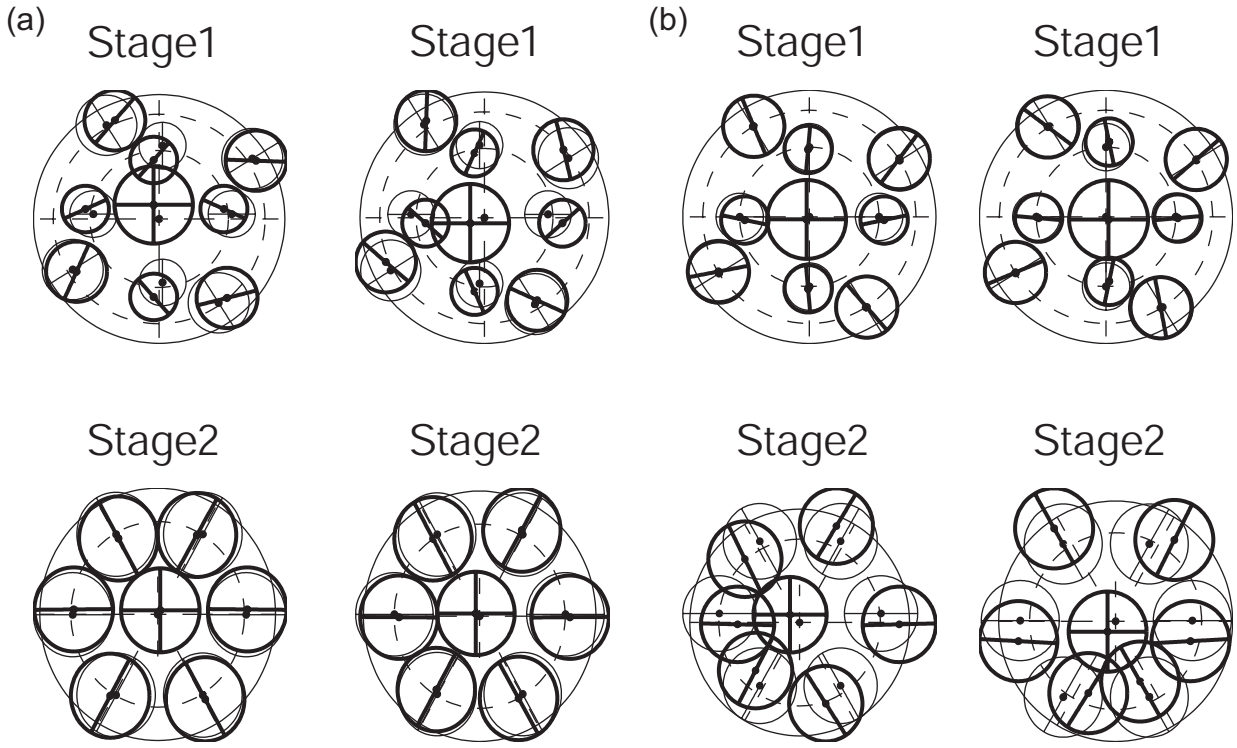

Figure 4.4: Mode shapes of the translational modes associated with ω_{17} and ω_{18} at points C (sub-figure a) and D (sub-figure b) in Figure 4.1.

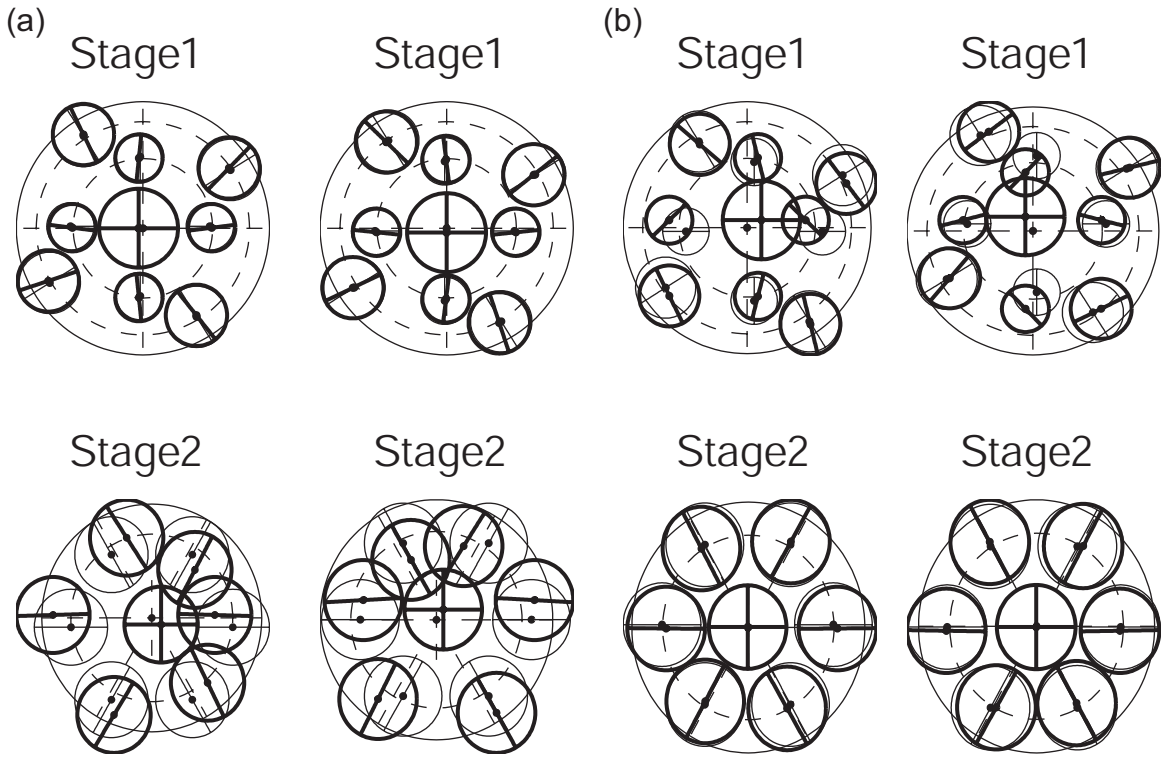

Figure 4.5: Mode shapes of the translational modes associated with ω_{20} and ω_{21} at points C' (sub-figure a) and D' (sub-figure b) in Figure 4.1.

changes in the vicinity of natural frequency crossing, to understand the natural frequency veering and crossing patterns is critical for the design and troubleshooting of compound planetary gears. In the following section, the method to detect eigenvalue veering and crossing in dynamic systems is first introduced. Then all the system parameters for compound planetary gears are divided into two groups: *tuned parameters* (the variation of this group of system parameters does not break the axisymmetry of any planet set) and *mistuned parameters* (the axisymmetry of a certain stage is broken by the variations of this group of system parameters). The natural frequency veering and crossing patterns for each group of parameters are investigated and the general rules of eigenvalue loci veering and crossing for general compound planetary gears are derived.

4.3 Detection of Natural Frequency Veering and Crossing

There are many ways to detect eigenvalue veering/crossing in dynamic systems, such as the methods in [55], [20], and [89]. This study adopts the method by Perkins and Mote [80] because this method is proved to be effective in detecting the natural frequency veering and crossing in lots of studies [72, 81, 82], especially in the natural frequency veering detection for simple planetary gears [59]. The details of this method and its application to compound planetary gears are introduced as follows.

$\lambda_s\,|_{\rho=\rho^0}$ and $\lambda_t\,|_{\rho=\rho^0}$ denote two nearly equal eigenvalues for the eigenvalue problem of a general compound planetary gear in (2.39) when the perturbed parameter ρ is equal to its nominal value ρ^o. ε is the perturbation of ρ such that $\rho = \rho^o + \varepsilon$. Application of Taylor Series Expansion of ε around $\lambda_s\,|_{\rho=\rho^0}$ and $\lambda_t\,|_{\rho=\rho^0}$ yields the approximation of λ_s and λ_t, the perturbed eigenvalues in the vicinities of the

unperturbed ones, as

$$\begin{aligned}\lambda_s &= \lambda_s^o + \varepsilon \frac{\partial \lambda_s}{\partial \rho}\mid_{\rho=\rho^0} + \frac{1}{2}\varepsilon^2 \frac{\partial^2 \lambda_s}{\partial \rho^2}\mid_{\rho=\rho^0} \\ \lambda_t &= \lambda_t^o + \varepsilon \frac{\partial \lambda_t}{\partial \rho}\mid_{\rho=\rho^0} + \frac{1}{2}\varepsilon^2 \frac{\partial^2 \lambda_t}{\partial \rho^2}\mid_{\rho=\rho^0}\end{aligned} \tag{4.1}$$

Both Perkins and Mote [80] and Lin and Parker [59] believe that there exist terms that depends on $\frac{1}{\lambda_s - \lambda_t}$ (i.e., the separation of λ_s and λ_t) in the second order eigenvalue derivatives in equation (4.1). These terms are called the coupling factors in their studies and the evaluation of these coupling factors for the unperturbed eigenvalue problem provides key indications of the veering or crossing of the two eigenvalue loci in the vicinities of $\lambda_s \mid_{\rho=\rho^0}$ and $\lambda_t \mid_{\rho=\rho^0}$. It is because the coupling terms dominate $\frac{\partial^2 \lambda_s}{\partial \rho^2}$ and $\frac{\partial^2 \lambda_t}{\partial \rho^2}$ when λ_s and λ_t are nearly equal. The loci concavities that are determined by the second order eigenvalue derivatives, therefore, strongly rely on these coupling factors. One main task of this study is to locate the coupling factors in the second order eigenvalue derivatives for compound planetary gears.

When λ_s is a distinct eigenvalue for the eigenvalue problem of a general compound planetary gear in (2.39), insertion of (2.2) and (3.2) into (3.3) yields the second order eigenvalue derivative for λ_s in terms of $[\lambda_s,\ \boldsymbol{\phi}_s,\ \lambda_s',\ \mathbf{M}',\ \mathbf{K}']$ as

$$\begin{aligned}\lambda_s'' =& 2\boldsymbol{\phi}_s^T(\mathbf{K}' - \lambda_s\mathbf{M}')\left[-\frac{1}{2}(\boldsymbol{\phi}_s^T\mathbf{M}'\boldsymbol{\phi}_s)\boldsymbol{\phi}_s + \sum_{v=1,v\neq s}^{\Lambda} \frac{\boldsymbol{\phi}_v^T(\mathbf{K}' - \lambda_s\mathbf{M}')\boldsymbol{\phi}_s}{\lambda_s - \lambda_v}\boldsymbol{\phi}_v\right] + \\ & \boldsymbol{\phi}_s^T(\mathbf{K}'' - \lambda_s\mathbf{M}'' - \lambda_s'\mathbf{M}')\boldsymbol{\phi}_s \\ =& -\lambda_s'\boldsymbol{\phi}_s^T\mathbf{M}'\boldsymbol{\phi}_s + \sum_{v=1,v\neq s}^{\Lambda} \frac{2\left[\boldsymbol{\phi}_s^T(\mathbf{K}' - \lambda_s\mathbf{M}')\boldsymbol{\phi}_v\right]^2}{\lambda_s - \lambda_v} + \\ & \boldsymbol{\phi}_s^T(\mathbf{K}'' - \lambda_s\mathbf{M}'' - \lambda_s'\mathbf{M}')\boldsymbol{\phi}_s \\ =& \sum_{v=1,v\neq s}^{\Lambda} \frac{2\left[\boldsymbol{\phi}_s^T(\mathbf{K}' - \lambda_s\mathbf{M}')\boldsymbol{\phi}_v\right]^2}{\lambda_s - \lambda_v} + \boldsymbol{\phi}_s^T(\mathbf{K}'' - \lambda_s\mathbf{M}'' - 2\lambda_s'\mathbf{M}')\boldsymbol{\phi}_s\end{aligned} \tag{4.2}$$

When another distinct eigenvalue λ_t is close to λ_s, the only term in (4.2) that depends on $\frac{1}{\lambda_s-\lambda_t}$ is

$$\chi_{s,t} = \frac{2\left[\boldsymbol{\phi}_s^T(\mathbf{K}' - \lambda_s\mathbf{M}')\boldsymbol{\phi}_t\right]^2}{\lambda_s - \lambda_t} \tag{4.3}$$

where $\chi_{s,t}$ is the coupling factor between λ_s and λ_t and it is for the locus of λ_s. Replacing the subscript s with t in equation (4.2) yields the second order eigenvalue derivative for λ_t as

$$\lambda_t'' = \sum_{v=1,v\neq t}^{\Lambda} \frac{2\left[\boldsymbol{\phi}_t^T(\mathbf{K}' - \lambda_t\mathbf{M}')\boldsymbol{\phi}_v\right]^2}{\lambda_t - \lambda_v} + \boldsymbol{\phi}_t^T(\mathbf{K}'' - \lambda_t\mathbf{M}'' - 2\lambda_t'\mathbf{M}')\boldsymbol{\phi}_t \tag{4.4}$$

The term that depends on $\frac{1}{\lambda_t-\lambda_s}$ in (4.4) is

$$\chi_{t,s} = \frac{2\left[\boldsymbol{\phi}_t^T(\mathbf{K}' - \lambda_t\mathbf{M}')\boldsymbol{\phi}_s\right]^2}{\lambda_t - \lambda_s} \tag{4.5}$$

where $\chi_{t,s}$ is the coupling factor for the locus of λ_t. Because $\lambda_t \approx \lambda_s$ and $\left[\boldsymbol{\phi}_t^T(\mathbf{K}' - \lambda_t\mathbf{M}')\boldsymbol{\phi}_s\right]$ is a scalar, the fact that the transpose of a scalar is equal to itself gives

$$\begin{aligned}\left[\boldsymbol{\phi}_t^T(\mathbf{K}' - \lambda_t\mathbf{M}')\boldsymbol{\phi}_s\right] &= \left[\boldsymbol{\phi}_t^T(\mathbf{K}' - \lambda_t\mathbf{M}')\boldsymbol{\phi}_s\right]^T \\ &= \left[\boldsymbol{\phi}_s^T(\mathbf{K}' - \lambda_t\mathbf{M}')\boldsymbol{\phi}_t\right] \approx \left[\boldsymbol{\phi}_s^T(\mathbf{K}' - \lambda_s\mathbf{M}')\boldsymbol{\phi}_t\right]\end{aligned} \tag{4.6}$$

Application of (4.6) to (4.3) and (4.5) yields

$$\chi_{t,s} \approx -\chi_{s,t} \tag{4.7}$$

Equation (4.7) shows that the coupling factor for λ_t is approximately equal to that for λ_s with the opposite sign. The evaluation of $[\chi_{s,t},\ \chi_{t,s}]$ for the unperturbed system (i.e., $\rho = \rho^0$) quantifies the strength of the veering between the loci of λ_s and λ_t as follows [59, 80]. Larger $|\chi_{s,t}|$ and $|\chi_{t,s}|$ (the absolute values for these coupling factors) indicates sharper changes of the loci and stronger veering. If $\chi_{s,t} = \chi_{t,s} = 0$, the loci of λ_s and λ_t cross each other instead of veering.

Lin and Parker [59] extends the above quantified veering detection method to degenerate eigenvalues of planetary gears. Let $\lambda_s = \lambda_{s+1} = \cdots = \lambda_{s+m-1}$ be a degenerate eigenvalue with multiplicity m. The general form for the second order derivatives of the degenerate eigenvalue is [29, 59]

$$\lambda_i'' = \sum_{v=1, v\neq s,\ \cdots,\ s+m-1}^{\Lambda} \frac{2\left[\boldsymbol{\phi}_i^T(\mathbf{K}' - \lambda_i\mathbf{M}')\boldsymbol{\phi}_v\right]^2}{\lambda_i - \lambda_v} + \boldsymbol{\phi}_i^T(\mathbf{K}'' - \lambda_i\mathbf{M}'' - 2\lambda_i'\mathbf{M}')\boldsymbol{\phi}_i \quad (4.8)$$

where $i = s,\ \cdots,\ s+m-1$. If a distinct eigenvalue λ_t is nearly equal to this degenerate eigenvalue when $\rho = \rho^0$, collecting the terms in (4.8) that depend on $\frac{1}{\lambda_i - \lambda_t}$ yields the coupling factor for the locus of λ_i as

$$\chi_{i,t} = \frac{2\left[\boldsymbol{\phi}_i^T(\mathbf{K}' - \lambda_i\mathbf{M}')\boldsymbol{\phi}_t\right]^2}{\lambda_i - \lambda_t},\ i = s,\ \cdots,\ s+m-1 \quad (4.9)$$

Considering $\lambda_s = \lambda_{s+1} = \cdots = \lambda_{s+m-1}$ and collecting all the terms that depend on $\frac{1}{\lambda_t - \lambda_s}$ in equation (4.4) give the coupling factor for λ_t as

$$\chi_{t,(s,\cdots,s+m-1)} = \sum_{k=s}^{s+m-1} \frac{2\left[\boldsymbol{\phi}_t^T(\mathbf{K}' - \lambda_t\mathbf{M}')\boldsymbol{\phi}_k\right]^2}{\lambda_s - \lambda_t} \quad (4.10)$$

If another degenerate eigenvalue $\lambda_t = \lambda_{t+1} = \cdots = \lambda_{t+n-1}$ with multiplicity n is close to the degenerate eigenvalue $\lambda_s = \lambda_{s+1} = \cdots = \lambda_{s+m-1}$ when $\rho = \rho^0$, the coupling factor for the locus of λ_x ($x = s,\ \cdots,\ s+m-1$) is the sum of all the terms that depend on $\frac{1}{\lambda_s - \lambda_t}$ in equation (4.8) and it is

$$\chi_{x,(t,\cdots,t+n-1)} = \sum_{k=t}^{t+n-1} \frac{2\left[\boldsymbol{\phi}_x^T(\mathbf{K}' - \lambda_x\mathbf{M}')\boldsymbol{\phi}_k\right]^2}{\lambda_s - \lambda_t},\ x = s,\ \cdots,\ s+m-1 \quad (4.11)$$

Replacing x ($x = s,\ \cdots,\ s+m-1$) with y ($y = t,\ \cdots,\ t+n-1$) in equation (4.8) and collecting all the terms that depend on $\frac{1}{\lambda_t - \lambda_s}$ produce the coupling factor for the locus of λ_y as

$$\chi_{y,(s,\cdots,s+m-1)} = \sum_{k=s}^{s+m-1} \frac{2\left[\boldsymbol{\phi}_y^T(\mathbf{K}' - \lambda_y\mathbf{M}')\boldsymbol{\phi}_k\right]^2}{\lambda_s - \lambda_t},\ y = t,\ \cdots,\ t+n-1 \quad (4.12)$$

4.4 Natural Frequency Veering and Crossing Pattern for Tuned Parameters

Tuned parameters refer to the group of system parameters whose variation does not break the axisymmetry of any planet set in a general compound planetary gear. Based on the eigensensitivity analysis results in previous chapter, tuned parameters can be classified into three groups: rotational, translational, and planet tuned parameters. Because any rotational mode is independent of the change of translational stiffness (bearing or shaft connection) and the change of masses in any component. Hence, only the rotational bearing and shaft connection stiffnesses for carriers and central gears ($k^{i}_{cb,\theta\theta}$, $k^{j}_{gb,\theta\theta}$, $k^{jn}_{gg,\theta\theta}$, $k^{ih}_{cc,\theta\theta}$, $k^{ij}_{cg,\theta\theta}$) and the moments of inertia of carriers and central gears have impact on rotational frequency loci. These parameters are *rotational tuned parameters* in this study. All translational bearing and shaft connection stiffnesses for carriers and central gears (k^{i}_{cb}, k^{j}_{gb}, k^{jn}_{gg}, k^{ih}_{cc}, k^{ij}_{cg}) and the masses of carriers and central gears are *translational tuned parameters* in this investigation, because they only impact translational frequencies and their associated modes. k^{jilm}_{gp}, k^{ilmq}_{pp}, k^{ilmq}_{p-p}, k^{ilm}_{p}, m^{ilm}_{p}, and I^{ilm}_{p} are system parameters that associated with certain planet in a specific planet train of stage i. The change of any of these parameters will cause stage i to lose its axisymmetry. There is only one way to change these parameters while keeping stage i tuned. It is to change these parameters in all the trains of stage i instead of just in a specific planet train. Such parameter variations are also considered to be tuned, and these parameters that impact all the trains in the same stage (k^{ji*m}_{gp}, k^{i*mq}_{pp}, k^{i*mq}_{p-p}, k^{i*m}_{p}, m^{i*m}_{p}, and I^{i*m}_{p}) are *planet tuned parameters.*

Because all compound planetary gear natural frequencies and their associated vibration modes are classified into three different types: rotational, translational,

and planet, the veering and crossing of the two approaching natural frequency loci always fall into one of following six cases.

(A) Two rotational frequency loci:

Rotational tuned parameters impact rotational frequencies [36]. Taking $k^j_{gb,\theta\theta}$ as a representative example for rotational tuned parameters, the veer/crossing of two rotational natural frequency loci with respect to the change of $k^j_{gb,\theta\theta}$ is explained as follows.

Let λ_s and λ_t be two rotational eigenvalues. Application of equations (4.3) and (4.5) directly (or extracting the terms depending on $\frac{1}{\lambda_s-\lambda_t}$ in equation (B.3)) gives the coupling factors of λ_s and λ_s with respect to $k^j_{gb,\theta\theta}$ as

$$\chi_{s,t}^{k^j_{gb,\theta\theta}} = \frac{2(\theta^j_{g,t}\theta^j_{g,s})^2}{\lambda_s - \lambda_t} = -\chi_{t,s}^{k^j_{gb,\theta\theta}} \tag{4.13}$$

where $\theta^j_{g,s}$ and $\theta^j_{g,t}$ are the rotations of central gear j in rotational modes s and t, respectively. If $\theta^j_{g,s} = 0$ or $\theta^j_{g,t} = 0$, the coupling factors in equation (4.13) are equal to zero, and the loci of λ_s and λ_t cross each other when $k^j_{gb,\theta\theta}$ varies. The modal properties of rotational mode [53], however, show that the rotation of central gear j is not zero in all rotational modes except the rigid body mode. Therefore, two rotational loci always veer away when $k^j_{gb,\theta\theta}$ is changed. Following the same process, the veering/crossing patterns of two rotational frequency loci with respect to the change of other rotational tuned parameters are determined and the results are the same as that for $k^j_{gb,\theta\theta}$.

The eigensensitivity analysis results in previous chapter indicate that planet tuned parameters have impact on rotational frequencies as well. Use k^{ji*m}_{gp} as the example for planet tuned parameters. Insertion of (3.18) into equations (4.3)

and (4.5) (or collecting the terms depending on $\frac{1}{\lambda_s-\lambda_t}$ in equation (3.22)) and application of the rotational mode properties give the coupling factors of λ_s and λ_s with respect to k_{gp}^{ji*m} as

$$\chi_{s,t}^{k_{gp}^{ji*m}} = \frac{2}{\lambda_s - \lambda_t}(c^i \delta_{g,s}^{ji*m} \delta_{g,t}^{ji*m})^2 = -\chi_{t,s}^{k_{gp}^{ji*m}} \tag{4.14}$$

where $\delta_{g,s}^{ji*m}$ and $\delta_{g,t}^{ji*m}$ are the mesh deflections between central gear j and planet m in all trains of stage i in modes s and t, respectively. Because the modal properties of rotational mode indicate that $\delta_{g,s}^{ji*m}$ and $\delta_{g,t}^{ji*m}$ are not equal to zero except in the rigid body mode, the two rotational loci veer away with the variation of k_{gp}^{ji*m}. The same result applies to other planet tuned parameters.

(B) Two translational frequency loci:

Translational tuned parameters alter translational frequencies. Use k_{gb}^{j} as a representative example for veering/crossing detection of two approaching translational frequency loci. $\lambda_s = \lambda_{s+1}$ and $\lambda_t = \lambda_{t+1}$ are two translational eigenvalue loci. Application of equations (4.11) and (4.12) directly (or collecting the terms depending on $\frac{1}{\lambda_s-\lambda_t}$ in (B.4)) yields

$$\begin{aligned}
\chi_{s,t}^{k_{gb,\theta\theta}^{j}} &= \chi_{s,t+1}^{k_{gb,\theta\theta}^{j}} = \frac{2(x_{g,t}^{j}x_{g,s}^{j}+y_{g,t}^{j}y_{g,s}^{j})^2+2(x_{g,t+1}^{j}x_{g,s}^{j}+y_{g,t+1}^{j}y_{g,s}^{j})^2}{\lambda_s-\lambda_t} \\
\chi_{s+1,t}^{k_{gb,\theta\theta}^{j}} &= \chi_{s+1,t+1}^{k_{gb,\theta\theta}^{j}} = \frac{2(x_{g,t}^{j}x_{g,s+1}^{j}+y_{g,t}^{j}y_{g,s+1}^{j})^2+2(x_{g,t+1}^{j}x_{g,s+1}^{j}+y_{g,t+1}^{j}y_{g,s+1}^{j})^2}{\lambda_{s+1}-\lambda_t} \\
\chi_{t,s}^{k_{gb,\theta\theta}^{j}} &= \chi_{t,s+1}^{k_{gb,\theta\theta}^{j}} = \frac{2(x_{g,t}^{j}x_{g,s}^{j}+y_{g,t}^{j}y_{g,s}^{j})^2+2(x_{g,t}^{j}x_{g,s+1}^{j}+y_{g,t}^{j}y_{g,s+1}^{j})^2}{\lambda_t-\lambda_s} \\
\chi_{t+1,s}^{k_{gb,\theta\theta}^{j}} &= \chi_{t+1,s+1}^{k_{gb,\theta\theta}^{j}} = \frac{2(x_{g,t+1}^{j}x_{g,s}^{j}+y_{g,t+1}^{j}y_{g,s}^{j})^2+2(x_{g,t+1}^{j}x_{g,s+1}^{j}+y_{g,t+1}^{j}y_{g,s+1}^{j})^2}{\lambda_{t+1}-\lambda_s}
\end{aligned} \tag{4.15}$$

where $(x_{g,s},y_{g,s})$, $(x_{g,s+1},y_{g,s+1})$, $(x_{g,t},y_{g,t})$, and $(x_{g,t+1}, y_{g,t+1})$ are the translations of central gear j in translational modes s, $s+1$, t, and $t+1$, respectively. Because the modal properties of translational modes ensure non-zero translations of central gear j in all translational modes, the coupling factors in (4.15) are not

equal to zero. As a result, the loci of two translational frequencies veer away when k_{gb}^{j} varies. It is the same for other translational tuned parameters.

Eigensensitivity analysis in previous chapter shows that planet tuned parameters have impact on translational frequencies. Let k_{gp}^{ji*m} be the representative example. Insertion of (3.18) into equations (4.11) and (4.12) produces

$$\begin{aligned}
\chi_{s,t}^{k_{gp}^{ji*m}} &= \chi_{s,t+1}^{k_{gp}^{ji*m}} = \frac{2(\sum_{l=1}^{c^i} \delta_{g,s}^{jilm}\delta_{g,t}^{jilm})^2+2(\sum_{l=1}^{c^i} \delta_{g,s}^{jilm}\delta_{g,t+1}^{jilm})^2}{\lambda_s-\lambda_t} \\
\chi_{s+1,t}^{k_{gp}^{ji*m}} &= \chi_{s+1,t+1}^{k_{gp}^{ji*m}} = \frac{2(\sum_{l=1}^{c^i} \delta_{g,s+1}^{jilm}\delta_{g,t}^{jilm})^2+2(\sum_{l=1}^{c^i} \delta_{g,s+1}^{jilm}\delta_{g,t+1}^{jilm})^2}{\lambda_{s+1}-\lambda_t} \\
\chi_{t,s}^{k_{gp}^{ji*m}} &= \chi_{t,s+1}^{k_{gp}^{ji*m}} = \frac{2(\sum_{l=1}^{c^i} \delta_{g,s+1}^{jilm}\delta_{g,t}^{jilm})^2+2(\sum_{l=1}^{c^i} \delta_{g,s}^{jilm}\delta_{g,t}^{jilm})^2}{\lambda_t-\lambda_s} \\
\chi_{t+1,s}^{k_{gp}^{ji*m}} &= \chi_{t+1,s+1}^{k_{gp}^{ji*m}} = \frac{2(\sum_{l=1}^{c^i} \delta_{g,s+1}^{jilm}\delta_{g,t+1}^{jilm})^2+2(\sum_{l=1}^{c^i} \delta_{g,s}^{jilm}\delta_{g,t+1}^{jilm})^2}{\lambda_{t+1}-\lambda_s}
\end{aligned} \tag{4.16}$$

To vanish the coupling factors in (4.16), the gear mesh deflections should satisfy $\delta_{g,s}^{jilm} = \delta_{g,s+1}^{jilm} = 0$ or $\delta_{g,t}^{jilm} = \delta_{g,t+1}^{jilm} = 0$, where $\delta_{g,w}^{jilm},\ w = s,\ s+1,\ t,\ t+1$ is the mesh deflection between central gear g and planet m in train l of stage i in vibration mode w. It is, however, impossible according to the modal properties for translational modes. As a result, the loci of translational frequencies always veer away as k_{gp}^{ji*m} is altered and the same conclusion applies to other planet tuned parameters.

(C) Two planet-mode frequency loci:

Because central gears and carriers have no rotational or translational motions in any planet mode, the change of any rotational or translational tuned parameters has no impact on any planet-mode natural frequencies. Planet tuned parameters, hence, are the only parameters that impact planet mode. $\lambda_s = \cdots = \lambda_{s+m-1}$ and $\lambda_t = \cdots = \lambda_{t+n-1}$ are two sets of planet-mode eigenvalues with multiplicity m

and n, respectively. Use k_{gp}^{ji*m} as the example. Insertion of the related eigensensitivities in (3.28) and planet mode properties into equations (4.11) and (4.12) yields

$$\begin{aligned}
\chi_{x,(t,\cdots,t+n-1)}^{k_{gp}^{ji*m}} &= \sum_{k=t}^{t+n-1} \frac{2(\sum_{l=1}^{c^i} \delta_{g,x}^{jilm} \delta_{g,k}^{jilm})^2}{\lambda_s - \lambda_t}, \ x = s, \ \cdots, \ s+m-1 \\
\chi_{y,(s,\cdots,s+m-1)}^{k_{gp}^{ji*m}} &= \sum_{k=s}^{s+m-1} \frac{2(\sum_{l=1}^{c^i} \delta_{g,y}^{jilm} \delta_{g,k}^{jilm})^2}{\lambda_t - \lambda_s}, \ y = t, \ \cdots, \ t+n-1
\end{aligned} \tag{4.17}$$

If the planet modes associated with $\lambda_s = \cdots = \lambda_{s+m-1}$ and $\lambda_t = \cdots = \lambda_{t+n-1}$ belong to different stages, the planet modes associated with $\lambda_s = \cdots = \lambda_{s+m-1}$ are decoupled with those for $\lambda_t = \cdots = \lambda_{t+n-1}$. Therefore, $\delta_{g,k}^{jilm} = 0$ in equation (4.17) and the loci of the two planet-mode frequencies cross each other.

If the modes associated with $\lambda_s = \cdots = \lambda_{s+m-1}$ and $\lambda_t = \cdots = \lambda_{t+n-1}$ are affiliated to the same stage (m has to equal n in this case), the coupling factors in (4.17) are not equal to zero because the planet mode properties guarantee that there are always mesh deflections for k_{gp}^{ji*m}.

The same result applies to other planet tuned parameters with the exception that the planet-mode frequency loci of the same stage may cross each other when the planet-mode frequencies are distinct, the associated modes are decoupled, and the varying parameter is k_p^{ilm}, m_p^{ilm}, or I_p^{ilm}. The details of these exceptions are covered in [59] and this study will not repeat it.

(D) One rotational frequency locus and one translational frequency locus:

λ_s is the rotational eigenvalue and $\lambda_t = \lambda_{t+1}$ is the translational natural frequency. Because rotational tuned parameters have impact on λ_s but not on translational frequencies and translational tuned parameters can change $\lambda_t = \lambda_{t+1}$ while keeping rotational frequencies untouched, this case is separated into two

situations: the change of a rotational tuned parameter and the variation of a translational tuned parameter.

Consider $k^j_{gb,\theta\theta}$ as a representative rotational tuned parameters. Application of equations (4.9) and 4.10 (or collecting the terms depending on $\frac{1}{\lambda_s-\lambda_t}$ in equation (B.3)) gives

$$\begin{aligned}\chi^{k^j_{gb,\theta\theta}}_{s,t} &= \chi^{k^j_{gb,\theta\theta}}_{s,t+1} = \frac{2(\theta^j_{g,t}\theta^j_{g,s})^2+2(\theta^j_{g,t+1}\theta^j_{g,s})^2}{\lambda_s-\lambda_t} \\ \chi^{k^j_{gb,\theta\theta}}_{t,s} &= \frac{2(\theta^j_{g,t}\theta^j_{g,s})^2}{\lambda_t-\lambda_s} \\ \chi^{k^j_{gb,\theta\theta}}_{t+1,s} &= \frac{2(\theta^j_{g,t+1}\theta^j_{g,s})^2}{\lambda_{t+1}-\lambda_s}\end{aligned} \tag{4.18}$$

Because the modal properties of translational mode ensure that $\theta^j_{g,t} = \theta^j_{g,t+1} = 0$, the coupling factors in (4.18) equal zero. The locus of the rotational frequency λ_s, hence, crosses the locus of $\lambda_t = \lambda_{t+1}$ when $k^j_{gb,\theta\theta}$ is changed. It is the same for other rotational tuned parameters.

When $k^j_{gb,}$ is the perturbed parameter, application of equations (4.9) and 4.10 (or collecting the terms depending on $\frac{1}{\lambda_s-\lambda_t}$ in equation (B.3)) yields

$$\begin{aligned}\chi^{k^j_{gb}}_{s,t} &= \chi^{k^j_{gb,\theta\theta}}_{s,t+1} = \frac{2(x^j_{g,t}x^j_{g,s}+y^j_{g,t}y^j_{g,s})^2+2(x^j_{g,t+1}x^j_{g,s}+y^j_{g,t+1}y^j_{g,s})^2}{\lambda_s-\lambda_t} \\ \chi^{k^j_{gb}}_{t,s} &= \frac{2(x^j_{g,t}x^j_{g,s}+y^j_{g,t}y^j_{g,s})^2}{\lambda_t-\lambda_s} \\ \chi^{k^j_{gb}}_{t+1,s} &= \frac{2(x^j_{g,t+1}x^j_{g,s}+y^j_{g,t+1}y^j_{g,s})^2}{\lambda_t-\lambda_s}\end{aligned} \tag{4.19}$$

According to the modal properties of rotational mode, $x^j_{g,s}$ and $y^j_{g,s}$ are all equal to zero. The coupling factors in equation (4.19), hence, are zero and the locus of $\lambda_t = \lambda_{t+1}$ crosses that of λ_s with the change of $k^j_{gb,}$. The same result applies to other translational tuned parameter. Summarizing both situations in this case, one rotational frequency locus always crosses the loci for translational frequencies with the variation of any rotational or translational tuned parameter.

Different from rotational and translational tuned parameters, planet tuned parameters can change both rotational and translational frequencies. Let k^{ji*m}_{gp} be

the perturbed parameter. Insertion of (3.28) into (4.9) and 4.10 produces

$$\begin{aligned}
\chi_{s,t}^{k_{gp}^{ji*m}} &= \chi_{s,t+1}^{k_{gp}^{ji*m}} = \frac{2(\sum_{l=1}^{c^i} \delta_{g,s}^{jilm}\delta_{g,t}^{jilm})^2+2(\sum_{l=1}^{c^i} \delta_{g,s}^{jilm}\delta_{g,t+1}^{jilm})^2}{\lambda_s-\lambda_t} \\
\chi_{t,s}^{k_{gp}^{ji*m}} &= \frac{2(\sum_{l=1}^{c^i} \delta_{g,s}^{jilm}\delta_{g,t}^{jilm})^2}{\lambda_t-\lambda_s} \\
\chi_{t+1,s}^{k_{gp}^{ji*m}} &= \frac{2(\sum_{l=1}^{c^i} \delta_{g,s}^{jilm}\delta_{g,t+1}^{jilm})^2}{\lambda_{t+1}-\lambda_s}
\end{aligned} \tag{4.20}$$

The modal properties of rotational modes ensure

$$\delta_{g,s}^{jilm} = \delta_{g,s}^{ji*m} \tag{4.21}$$

and the translational mode properties yield

$$\begin{bmatrix} \delta_{g,t}^{jilm} \\ \delta_{g,t+1}^{jilm} \end{bmatrix} = \begin{bmatrix} \cos\hat{\psi}^{ilm} & \sin\hat{\psi}^{ilm} \\ -\sin\hat{\psi}^{ilm} & \cos\hat{\psi}^{ilm} \end{bmatrix} \begin{bmatrix} \delta_{g,t}^{ji1m} \\ \delta_{g,t+1}^{ji1m} \end{bmatrix} \tag{4.22}$$

The coupling factors in equation (4.22) vanishes after the insertion of the identities in (4.21) and (4.22) into (4.22). The locus of a rotational frequency, hence, are free to cross the loci of translational frequencies when k_{gp}^{ji*m} varies. The same result applies to other planet tuned parameters.

(E) One rotational frequency locus and one planet-mode frequency locus:

Because translational tuned parameters have no impact to rotational or planet-mode frequencies, rotational and planet tuned parameters are studied in this case. Application of the same analytical process as that in Case D produces the result that rotational natural frequency loci always cross the loci of planet-mode frequencies when any rotational or planet tuned parameter is changed.

(F) One translational frequency locus and one planet-mode frequency locus:

Compound planetary gear modal properties ensure that rotational tuned parameters do not affect translational or planet-mode frequencies. Translational and

planet tuned parameters, hence, are the only impacting parameters in this case. Application of the same analytical process as that in Case D gives the result that translational natural frequency loci are free to cross the loci of planet-mode frequencies as any translational or planet tuned parameter varies.

Table 4.1: Veering (V) and crossing(X) pattern of a general compound planetary gears with respect to the change of any rotational tuned parameter. R means Rotational mode, T means Translational mode, P means Planet mode. $-$ indicates that no veering/crossing is possible.

Mode Types	R	T	P
R	$-$	X	$-$
T	X	V	X
P	$-$	X	$-$

Table 4.2: Veering (V) and crossing(X) pattern of a general compound planetary gears with respect to the change of any translational tuned parameter. R means Rotational mode, T means Translational mode, P means Planet mode. $-$ indicates that no veering/crossing is possible.

Mode Types	R	T	P
R	V	X	X
T	X	$-$	$-$
P	X	$-$	$-$

Table 4.3: Veering (V) and crossing(X) pattern of a general compound planetary gears with respect to the change of any planet tuned parameter. R means Rotational mode, T means Translational mode, P means Planet mode. V/X indicates that both veering and crossing are possible.

Mode Types	R	T	P
R	V	X	X
T	X	V	X
P	X	X	V/X

The veering and crossing pattern of a general compound planetary gear with respect to the change of any rotational, translational, and planet tuned parameter are illustrated in Tables 4.1, 4.2, and 4.3, respectively. The natural frequency veering/crossing phenomena of the example system in Figures 4.1, 4.6, and 4.7 confirm the patterns in these tables. In Figure 4.1, the loci of a pair of translational frequencies ($\omega_{17},\ \omega_{18}$) cross the locus of the rotational frequency (ω_{19}) and veer away from another pair of translational frequencies ($\omega_{20},\ \omega_{21}$) when $k^2_{gb,}$ varies. Figure 4.6 shows that the locus of a rotational frequency (ω_{57}) crosses the loci of a pair of translational frequencies ($\omega_{58},\ \omega_{59}$) and veers away from another rotational frequency (ω_{60}) when $k^2_{gb,\theta\theta}$ is changed. Figure 4.7 illustrates that the loci of a pair of translational frequencies ($\omega_{55},\ \omega_{56}$) cross the locus of a rotational frequency (ω_{57}) and veer away from another pair of translational frequencies ($\omega_{58},\ \omega_{59}$) when k^{11*1}_{gp} is altered.

4.5 Natural Frequency Veering and Crossing Pattern for Mistuned Parameters

k^{jilm}_{gp}, k^{ilmq}_{pp}, k^{ilmq}_{p-p}, k^{ilm}_{p}, m^{ilm}_{p}, and I^{ilm}_{p} are the only parameters that can break the axisymmetry of stage i and they are mistuned parameters. Similar to the previous

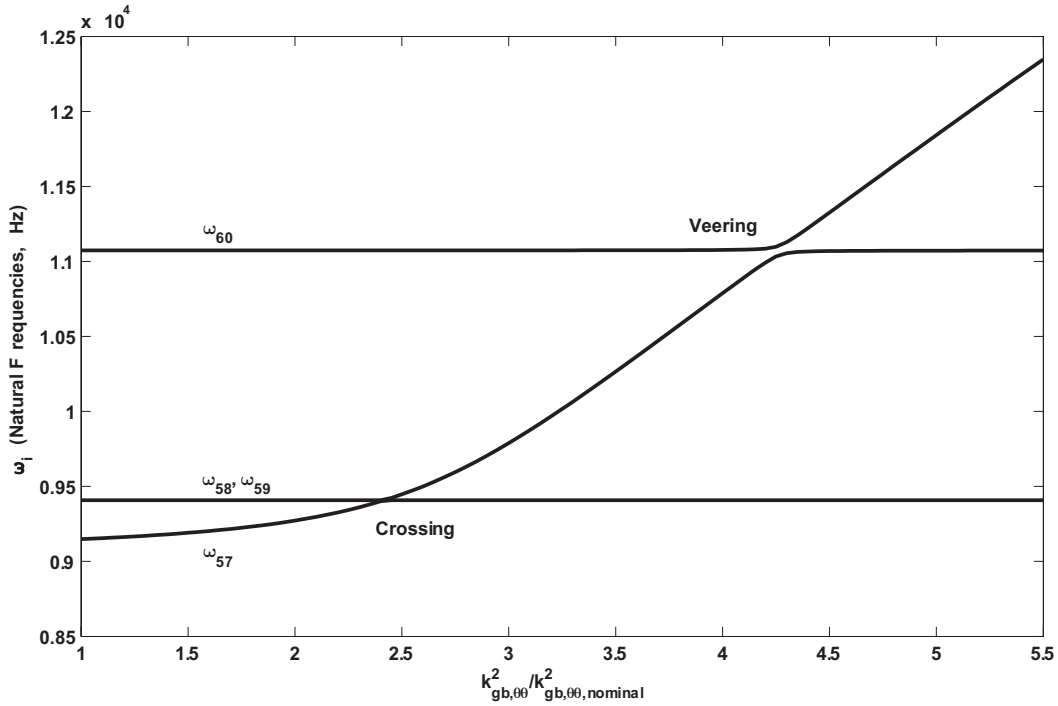

Figure 4.6: Natural frequency crossing and veering phenomena in the example system when $k^2_{gb,\theta\theta}$ changes.

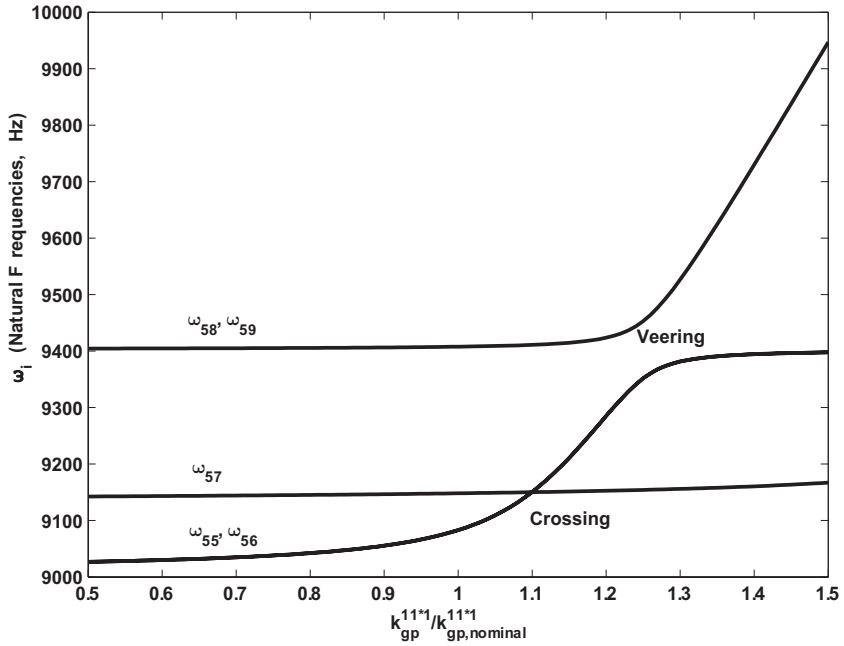

Figure 4.7: Natural frequency crossing and veering phenomena in the example system when k_{gp}^{11*1} changes.

section, six cases are discussed based on the structured modal properties of compound planetary gears.

(A) Two rotational frequency loci:

λ_s and λ_t are two rotational eigenvalues. Take k_{gp}^{ji1m} as the representative example. Insertion of (3.18) into (4.3) yields

$$\chi_{s,t}^{k_{gp}^{ji1m}} = \frac{2}{\lambda_s - \lambda_t}(\delta_{g,s}^{ji1m}\delta_{g,t}^{ji1m})^2 = -\chi_{t,s}^{k_{gp}^{ji1m}} \tag{4.23}$$

According to the rotational modal properties [53], $\delta_{g,s}^{ji1m}$ and $\delta_{g,t}^{ji1m}$ are not zero if neither mode s nor mode t is a rigid body mode. Hence, λ_s and λ_t veer away if k_{gp}^{ji1m} varies and breaks the axisymmetry of stage i. It is the same for other mistuned parameters.

(B) Two translational frequency loci:

λ_s and λ_{s+1} are a pair of translational frequencies. Let k_{gp}^{ji1m} be the perturbed parameter. Due to the break of system symmetry caused by mistuned parameters, the loci of λ_s and λ_{s+1} split as k_{gp}^{ji1m} varies (Figure 3.5). That is, the locus of λ_s crosses that of λ_{s+1}. Such crossing can not be explained by the coupling factors in equations (4.11)and (4.12), because $\frac{1}{\lambda_s-\lambda_{s+1}}\,|_{\rho=\rho^0}$ does not exist. Instead, equation (4.1) provides the answer directly. Insertion of the eigensensitivities in (3.56)-(3.58) into (4.1) gives

$$\begin{aligned}\lambda_s &= \lambda_s^o + \varepsilon(\delta_{g,s}^{ji1m})^2\,|_{\rho=\rho^0} + \tfrac{1}{2}\varepsilon^2 \sum_{v=1,v\neq s,s+1}^{\Lambda} \frac{2(\delta_{g,v}^{ji1m}\delta_{g,s}^{ji1m})}{\lambda_s-\lambda_v}\,|_{\rho=\rho^0} \\ \lambda_{s+1} &= \lambda_{s+1}^o = \lambda_s^o\end{aligned} \tag{4.24}$$

Because $(\delta_{g,s}^{ji1m})^2\,|_{\rho=\rho^0}$ and $\sum_{v=1,v\neq s,s+1}^{\Lambda} \frac{2(\delta_{g,v}^{ji1m}\delta_{g,s}^{ji1m})}{\lambda_s-\lambda_v}\,|_{\rho=\rho^0}$ are not equal to zero in translational modes, the locus of λ_s changes as k_{gp}^{ji1m} varies. λ_{s+1}, however, is not impacted by k_{gp}^{ji1m}. Hence, the locus of changing λ_s naturally crosses the locus of unchanged λ_{s+1}. Now consider two pairs of nearly equal translational frequencies $\lambda_s = \lambda_{s+1}$ and $\lambda_t = \lambda_{t+1}$. Insertion of equation (3.55) into equations (4.11) and (4.12) produces

$$\begin{aligned}\chi_{s,t}^{k_{gp}^{ji1m}} &= \chi_{s,t+1}^{k_{gp}^{ji1m}} = \frac{2(\delta_{g,s}^{ji1m}\delta_{g,t}^{ji1m})^2+2(\delta_{g,s}^{ji1m}\delta_{g,t+1}^{ji1m})^2}{\lambda_s-\lambda_t} \\ \chi_{s+1,t}^{k_{gp}^{ji1m}} &= \chi_{s+1,t+1}^{k_{gp}^{ji1m}} = \frac{2(\delta_{g,s+1}^{ji1m}\delta_{g,t}^{ji1m})^2+2(\delta_{g,s+1}^{ji1m}\delta_{g,t+1}^{ji1m})^2}{\lambda_{s+1}-\lambda_t} \\ \chi_{t,s}^{k_{gp}^{ji1m}} &= \chi_{t,s+1}^{k_{gp}^{ji1m}} = \frac{2(\delta_{g,s+1}^{ji1m}\delta_{g,t}^{ji1m})^2+2(\delta_{g,s}^{ji1m}\delta_{g,t}^{ji1m})^2}{\lambda_t-\lambda_s} \\ \chi_{t+1,s}^{k_{gp}^{ji1m}} &= \chi_{t+1,s+1}^{k_{gp}^{ji1m}} = \frac{2(\delta_{g,s+1}^{ji1m}\delta_{g,t+1}^{ji1m})^2+2(\delta_{g,s}^{ji1m}\delta_{g,t+1}^{ji1m})^2}{\lambda_{t+1}-\lambda_s}\end{aligned} \tag{4.25}$$

Because $\delta_{g,s}^{ji1m}$, $\delta_{g,s+1}^{ji1m}$, $\delta_{g,t}^{ji1m}$ and $\delta_{g,t+1}^{ji1m}$ are not equal to zero in a translational mode, the coupling factors in equation (4.25) are non-zeros. As a result, the loci of λ_s and λ_{s+1} veer away from those for λ_t and λ_{t+1} when k_{gp}^{ji1m} is perturbed and stage i becomes mistuned. Other mistuned parameters impact two pairs of nearly-equal translational frequencies in the same way.

(C) Two planet-mode frequency loci:

$\lambda_s = \cdots = \lambda_{s+m-1}$ are planet-mode frequencies with multiplicity m and k_{gp}^{ji1m} is the perturbed parameter. Insertion of the eigensensitivities in (3.60)-(3.61) into (4.1) yields

$$\begin{aligned} \lambda_s &= \lambda_s^o + \varepsilon(\delta_{g,s}^{ji1m})^2 \mid_{\rho=\rho^0} + \tfrac{1}{2}\varepsilon^2 \sum_{v=1, v\neq s,\cdots,s+m-1}^{\Lambda} \frac{2(\delta_{g,v}^{ji1m}\delta_{g,s}^{ji1m})}{\lambda_s - \lambda_v} \mid_{\rho=\rho^0} \\ \lambda_{s+1} &= \cdots = \lambda_{s+m-1} = \lambda_s^o \end{aligned} \tag{4.26}$$

Because planet mode properties ensure that $(\delta_{g,s}^{ji1m})$ is not zero, the locus of changing λ_s naturally crosses the loci of $\lambda_{s+1},\ \cdots,\ \lambda_{s+m-1}$ which are straight lines. For such frequency loci crossing, coupling factors do not exist. Similar to Case B in this section, insertion of the eigensensitivities into equation (4.1) provides the answer to such crossing phenomenon.

Consider another case that two sets of planet-mode eigenvalues, $\lambda_s = \cdots = \lambda_{s+m-1}$ and $\lambda_t = \cdots = \lambda_{t+n-1}$, are close to each other when k_{gp}^{ji1m} is at its nominal value. If $\lambda_s,\ \cdots,\ \lambda_{s+m-1}$ are completely decoupled with $\lambda_t,\ \cdots,\ \lambda_{t+n-1}$ (i.e., they are planet-mode frequencies of different planet sets, or they are distinct planet-mode frequencies and decoupled with the varying parameter being k_p^{ilm}, m_p^{ilm}, or I_p^{ilm} [59]), direct application of (4.11) and (4.12) gives zero coupling factors. Thus, the loci are free to cross each other in this situation. If the two sets of planet modes are not decoupled, both sets of planet modes have to be for the same stage and their multiplicity should be equal. Insertion of the related eigensensitivities in (3.60)-(3.61) and planet mode properties into equations (4.11) and (4.12) yields

$$\begin{aligned} \chi_{x,(t,\cdots,t+n-1)}^{k_{gp}^{ji1m}} &= \sum_{k=t}^{t+n-1} \frac{2(\delta_{g,x}^{ji1m}\delta_{g,k}^{ji1m})^2}{\lambda_s - \lambda_t},\ x = s,\ \cdots,\ s+m-1 \\ \chi_{y,(s,\cdots,s+m-1)}^{k_{gp}^{ji1m}} &= \sum_{k=s}^{s+m-1} \frac{2(\delta_{g,y}^{ji1m}\delta_{g,k}^{ji1m})^2}{\lambda_t - \lambda_s},\ y = t,\ \cdots,\ t+n-1 \end{aligned} \tag{4.27}$$

The fact that δ_g^{ji1m} is not zero in any planet mode leads to non-zero coupling factors in (4.27). The loci of $\lambda_s,\ \cdots,\ \lambda_{s+m-1}$, hence, always veer away from the loci of $\lambda_t,\ \cdots,\ \lambda_{t+n-1}$ in this case when k_{gp}^{ji1m} is changed. The same results apply to other mistuned parameters.

(D) One rotational frequency locus and one translational frequency locus:

When k_{gp}^{ji1m} is the perturbed parameter, insertion of (3.55) into (4.9) and 4.10 produces

$$\begin{aligned} \chi_{s,t}^{k_{gp}^{ji1m}} &= \chi_{s,t+1}^{k_{gp}^{ji1m}} = \frac{2(\delta_{g,s}^{ji1m}\delta_{g,t}^{ji1m})^2+2(\delta_{g,s}^{ji1m}\delta_{g,t+1}^{ji1m})^2}{\lambda_s-\lambda_t} \\ \chi_{t,s}^{k_{gp}^{ji*m}} &= \frac{2(\delta_{g,s}^{jilm}\delta_{g,t}^{jilm})^2}{\lambda_t-\lambda_s} \\ \chi_{t+1,s}^{k_{gp}^{ji1m}} &= \frac{2(\delta_{g,s}^{jilm}\delta_{g,t+1}^{jilm})^2}{\lambda_{t+1}-\lambda_s} \end{aligned} \tag{4.28}$$

Different from Case D for tuned parameters, the identities in (4.21)-(4.22) can not be applied to (4.28) because only the central gear-planet mesh spring in train 1 deforms. The coupling factors in (4.28), hence, do not vanish and veering occurs when δ_g^{ji1m} changes. It is the same for all other mistuned parameters.

(E) One rotational or translational frequency locus and one planet-mode frequency locus:

Application of the same analytical process as that in Case D in this section yields the result that rotational or translational natural frequency loci always veer away from the loci of planet-mode frequencies as any mistuned parameter changes.

The above results for the veering/crossing patterns for mistuned parameters are summarized Table 4.4. Compared to Tables 4.1-4.3, Table 4.4 shows more occurrences of veering. The natural frequency veering/crossing phenomena of the example system in Figure 4.8 confirm the results in Table 4.4. Figure 4.8 shows that one of the pair of translational frequencies, ω_{55}, crosses the locus of other translational frequency of

the same pair, ω_{56} when k_{gp}^{1111} changes, and similar crossing phenomenon happens to another pair of translational frequencies, ω_{58} and ω_{59}. Such split of translational frequency loci are caused by the break of axisymmetry as analyzed previously. Different from Figures 4.6 and 4.7, the rotational frequency locus (ω_{57}) in Figure 4.8 veers away from the translational frequency locus (ω_{56}) as predicted in Table 4.4.

Table 4.4: Veering (V) and crossing(X) pattern of a general compound planetary gears with respect to the change of any mistuned parameter. R means Rotational mode, T means Translational mode, P means Planet mode. V/X indicates that both veering and crossing are possible.

Mode Types	R	T	P
R	V	V	V
T	V	V/X	V
P	V	V	V/X

4.6 Conclusion

This study thoroughly investigates the natural frequency veering and crossing of general compound planetary gears. By checking whether the axisymmetry in all stages are retained, all system parameters are divided into tuned and mistuned parameters. Tuned parameters are further classified as rotational, translational, and planet tuned parameters based on the eigensensitivity analysis result of previous chapter. Taking advantage of the coupling factors which are effective measurements for the veering of natural frequency loci and utilizing the structured modal properties, the veering/crossing patterns with respect to each group of tuned parameters are determined. The veering/crossing patterns for mistuned parameter are derived in a similar way. Different from the veering/crossing patterns with respect to the

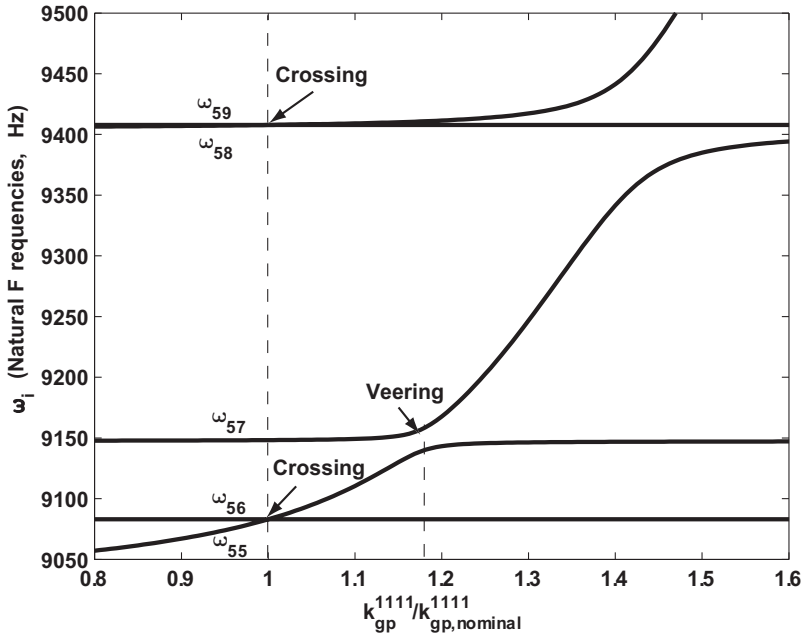

Figure 4.8: Natural frequency crossing and veering phenomena in the example system when k_{gp}^{1111} changes.

change of tuned parameters, the veering/crossing patterns for mistuned parameters have more occurrences of veering due to the break of axisymmetry.

Chapter 5: ANALYTICAL DETERMINATION OF MESH PHASE RELATIONS IN GENERAL COMPOUND PLANETARY GEARS

5.1 Introduction

Previous research shows that for a simple planetary gear different mesh phases between the multiple sun-planet and ring-planet meshes significantly influence the dynamic response [5, 48, 56, 61, 75, 77, 86, 87, 94, 97]. From these studies, one would expect that proper selection of mesh phases will also reduce the vibration and noise of compound planetary gears. In order to properly optimize mesh phases in the design stage, a complete understanding of all the mesh phase relations in general compound planetary gears is needed. Any static or dynamic model must accurately represent the mesh phases. This study presents these mesh phase relations.

A rotational-translational model for general compound planetary gears was developed by Kiracofe and Parker [53] to characterize modal properties. In this model, each component has one rotational and two translational degrees of freedom. Bearings and shaft connections are modeled by one torsional and two translational stiffnesses. Gear meshes are modeled by linear stiffnesses. Because the number of teeth in contact changes as the system rotates, the mesh stiffnesses vary, exciting the system vibration. To introduce time-varying mesh stiffness or static transmission error excitation

to Kiracofe and Parker's model or any similar one, it is crucial to know the relative phases between all gear meshes in the system as the gears rotate. Such calculations require the mesh phase relations in this study.

Parker and Lin [77] clarified the mesh phase relations for simple planetary gears. The mesh phase relations of general compound planetary gears have not been studied in the published literature except that Guo and Parker presented their preliminary investigation on compound planetary gear mesh phasing in [54]. The difficulty is that the variety of compound configurations and the large number of gear meshes make description of the mesh phase relations difficult. In addition, the gear meshes in a compound planetary gear may have different mesh periods. The purpose of this study is to systematically define all the relative mesh phases in a general compound planetary gear, to define the relative phase relations between the meshes with different mesh periods, and to give a comprehensive approach to calculate these relative phases and the relations between them.

The derived results are required for any simulation that does not track the actual tooth contact conditions of geometrically precise gears and teeth as the gears rotate. Most commercial gear software does *not* track this contact; instead they use lumped stiffness representations of the tooth mesh. The same is true for conventional lumped-parameter gear models used in the literature. The results herein provide all needed results to calculate the required phases.

5.2 Relative Phases for Meshes with Different Mesh Periods

5.2.1 Definition of Relative Phases

The mesh phase relations in this study are described by the relative phases between mesh tooth variation functions. Mesh tooth variation functions track the number of teeth in contact at each gear mesh as the gears rotate. These functions take only integer values. Actual mesh stiffness and static transmission error variations are continuous functions whose mesh phase relations are identical to those of mesh tooth variation functions [77], even though the shape of those periodic quantities are not the rectangular functions studied here. The shapes of any of these quantities is immaterial here. Our purpose is to examine only the phases between these quantities.

To accurately describe relative mesh phases in compound planetary gears, it is necessary to define the following terms: *referred mesh*, *referring mesh* and *reference point*. A *referred mesh* is the gear mesh that serves as the reference for other gear meshes. A gear mesh that refers to the referred mesh in a certain relative phase is called the *referring mesh*. For example, in Figure 5.1 gear meshes A and B are the referred and referring mesh, respectively, for the relative phase γ_A^B. *Reference points* are the matching points in the mesh cycle of the referred and referring meshes. The reference point in the referred mesh can be any point in the mesh cycle. The reference point in the referring mesh must be the point that uniquely matches the reference point in the associated referred mesh. In this study the pitch points of the referring and referred meshes serve as the reference points for all relative phases. One could also choose, for example, the highest point of single tooth contact. The choice of reference point is arbitrary and does not affect the results that follow.

The definition of a relative phase between two meshes with different mesh periods

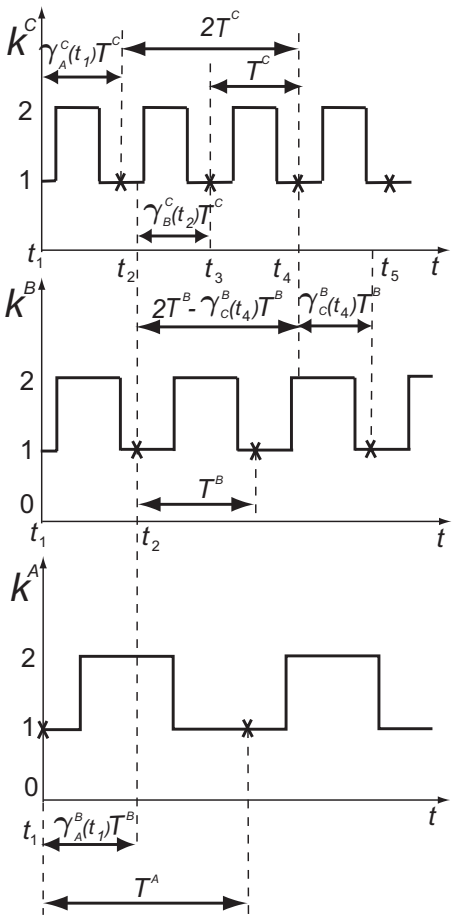

Figure 5.1: Mesh tooth variation functions for $k^A(t)$, $k^B(t)$, and $k^C(t)$. The relative phases among these meshes are marked. The symbol $\times$ denotes the time when the pitch point of the associated gear mesh is in contact.

is described in Figure 5.1. The mesh periods of meshes A and B are T^A and T^B, respectively. Mesh A is the referred mesh, and mesh B is the referring mesh for the relative phase γ_A^B. The mesh tooth variation function of mesh A is $k^A(t)$ with the pitch point in contact at $t = t_1$. The mesh tooth variation function of mesh B is $k^B(t)$. The pitch point of mesh B is in contact for the first time at t_2 ($t_2 > t_1$). Then the relative phase of $k^B(t)$ referring to $k^A(t)$ is $\gamma_A^B(t_1) = \frac{t_2 - t_1}{T^B}$, where t_1 is called the *referring time* of this relative phase. Therefore, the value of $\gamma_A^B(t_1)$ is between 0 and 1, and $\gamma_A^B(t_1)T^B$ is a portion of the referring mesh period T^B. The referring time of a relative phase is the time when the reference point (i.e., the pitch point) of the referred mesh is in contact. The referring time between gear mesh A and B in Figure 5.1 can also be at $t_1 + nT^A$, where n is any integer.

According to the above definition of relative phases, when mesh A and mesh B have the same mesh periods, the relative phase between gear mesh A and B remains the same for any choice of reference point (or referring time). There is no need to specify the referring time in this case, and $\gamma_A^B(t_1)$ simplifies to γ_A^B. Otherwise, the referring time must be specified.

The above definition of relative phase provides a way to determine the relative phase between any two gear meshes that have different mesh periods. For the example shown in Figure 5.1, the mesh tooth variation function of mesh B is $k^B(t)$, and the pitch point of mesh B is in contact at $t = t_2$. $\kappa^B(\tau)$ is a time-shifted mesh tooth variation function of mesh B. Its shape is identical to $k^B(t)$ but its origin ($\tau = 0$) is shifted to be mesh B's reference or pitch point. The absolute time is t; τ is a relative time coordinate with $\tau = 0$ being when mesh B is at its reference point. Because the pitch point of mesh B is in contact at $t = t_2$ in Figure 5.1, the time-shifting

relationships between $k^B(t)$ and $\kappa^B(\tau)$ are

$$\begin{aligned} \kappa^B(\tau) &= k^B(t + t_2) \\ \tau &= t + t_2 \end{aligned} \tag{5.1}$$

Applying the definition of $\gamma_A^B(t_1)$, t_2 in term of $\gamma_A^B(t_1)$ is

$$t_2 = \gamma_A^B(t_1)T^B + t_1 \tag{5.2}$$

The mesh tooth variation functions $\kappa^B(\tau)$ for all the mating gear pairs are typically generated by straightforward gear geometry analysis or gear design software, with each mesh having its own $\tau = 0$ corresponding to a particular reference point in that mesh's mesh period. These functions do not depend on the system configuration. Changing back to t as the absolute time and applying the relationships in equations (5.1) and (5.2), the mesh tooth variation of mesh B as a function of absolute time, which is the crucial quantity, is

$$k^B(t) = \kappa^B\left(t - \gamma_A^B(t_1)T^B - t_1\right) \tag{5.3}$$

Equation (5.3) shows the important role of relative phases in the correct representations of mesh tooth, stiffness, or static transmission error variation functions. Because the correctness of any static or dynamic compound planetary gear analysis relies on the correct representations of these functions at each gear mesh, the relative phases are critical.

5.2.2 Special Algorithm for Relative Phase Calculations

Figure 5.1 shows the relative phases among meshes $k^A(t)$, $k^B(t)$, and $k^C(t)$. Gear meshes A and B are at their pitch points at t_1 and t_2, where $t_2 = t_1 + \gamma_A^B(t_1)T^B$. Suppose $\gamma_A^B(t_1)$ and $\gamma_B^C(t_2)$ are known relative phases. Because meshes A, B, and C

may have different mesh periods, the direct addition of $\gamma_A^B(t_1)$ and $\gamma_B^C(t_2)$ does not yield $\gamma_A^C(t_1)$. The following algorithm is needed to find $\gamma_A^C(t_1)$.

According to the definition of $\gamma_B^C(t_2)$, $t_3 = t_2 + \gamma_B^C(t_2)T^C$ is the time when mesh C is at its pitch point for the first time after t_2. As shown in Figure 5.1, mesh C experiences multiple mesh periods from t_1 to t_3. Therefore, $\frac{t_3-t_1}{T^C}$ might be greater than 1 and can not be used directly as the value of $\gamma_A^C(t_1)$. The operator $dec(\ )$ is needed to force $\frac{t_3-t_1}{T^C}$ to be within the range of $[0, 1]$. When the argument of $dec(\ )$ is positive, the operator drops the whole number part and keeps the decimal part, for example, $dec(1.2) = 0.2$. When the argument is negative, its output is the decimal part of the argument plus 1, for instance, $dec(-1.2) = 0.8$. Thus, $\gamma_A^C(t_1)$ is calculated as

$$\begin{aligned}\gamma_A^C(t_1) &= dec\left(\frac{t_3 - t_1}{T^C}\right) \\ &= dec\left(\frac{\gamma_B^C(t_2)T^C + t_2 - t_1}{T^C}\right) \\ &= dec\left(\frac{\gamma_B^C(t_2)T^C + \gamma_A^B(t_1)T^B}{T^C}\right)\end{aligned} \tag{5.4}$$

When $T^A = T^B = T^C$, no referring time is needed, and equation (5.4) simplifies to

$$\gamma_A^C = dec\left(\gamma_A^B + \gamma_B^C\right) \tag{5.5}$$

Likewise, when $\gamma_A^B(t_1)$ and $\gamma_A^C(t_1)$ are known, the relative phase of mesh B referring to mesh C is determined as follows. The times $t_3 = t_1+\gamma_A^C(t_1)T^C+T^C$ and $t_4 = t_3+T^C$ are the times when mesh C is at its pitch point. Each one of them can serve as the

referring time for γ_C^B. Choosing the referring time t_4 as the example, $\gamma_C^B(t_4)$ is

$$\begin{aligned}\gamma_C^B(t_4) &= dec\left(\frac{t_5 - t_4}{T^B}\right) = dec\left(\frac{t_2 - t_4}{T^B}\right) \\ &= dec\left(\frac{\gamma_A^B(t_1)T^B + t_1 - t_4}{T^B}\right) \\ &= dec\left(\frac{\gamma_A^B(t_1)T^B - \gamma_A^C(t_1)T^C - 2T^C}{T^B}\right)\end{aligned} \tag{5.6}$$

where t_5 is the time when the pitch point of mesh B is in contact for the first time after t_4, and $t_2 = t_5 - 2T^B$. When $T^A = T^B = T^C$, equation (5.6) simplifies to

$$\gamma_C^B = dec(\gamma_A^B - \gamma_A^C) \tag{5.7}$$

5.3 Mesh Phase Relations of General Compound Planetary Gears

5.3.1 Numbering of the Components in Compound Planetary Gears

Precise numbering of each component is necessary due to the complex structures of compound planetary gears. Suppose there are a stages numbered as $1, 2, \cdots, a$. It is convenient to sequentially number the stages from input stage to output stage. The total number of central gears (i.e., sun and ring gears) of the system is b, and these central gears are numbered as $1, 2, \cdots, b$. For *typical* compound planetary gears (there is only one sun gear and one ring gear in each stage), s^i and r^i represent the central gear number of the sun gear and ring gear of stage i, respectively. For *non-typical* compound planetary gears, $s^{i,x}$ and $r^{i,y}$ represent the central gear number of the xth sun gear and the yth ring gear of stage i. The discussion in the rest of this investigation focuses on typical compound planetary gears because the only difference in the derivation of the mesh phase relations between typical and non-typical compound planetary gears is the numbering of the central gears.

The concept of a planet train is illustrated in Figure 5.2. The number of planet trains in planet set i is c^i. Train 1 is chosen arbitrarily within the planet set. All other planet trains in planet set i are numbered sequentially in the counter-clockwise direction. Each planet train has d^i planets. The numbering of the planets in any planet train is as follows: the planet in mesh with its associated sun gear is numbered as planet 1 of the planet train; the planet next to it in the train is numbered as planet 2; the rule continues until planet d^i is numbered.

5.3.2 Definitions of Relative Phases in Compound Planetary Gears

All gear meshes in a compound planetary gear are classified into meshes between a central gear and a planet (gear-planet meshes) or meshes between two planets (planet-planet meshes). $k_{gp}^{jilm}(t)$ represents the mesh tooth variation functions of the mesh between central gear j and planet m in train l of planet set i. $k_{pp}^{ilmq}(t)$ is the mesh tooth variation between planet m and planet q in train l of planet set i. The associated mesh periods are T_{gp}^{jilm} and T_{pp}^{ilmq}. With the previously defined numbering convention, k_{gp}^{jilm} is either $k_{gp}^{s^i il1}$ or $k_{gp}^{r^i ild^i}$, and k_{pp}^{ilmq} is actually $k_{pp}^{ilm(m+1)}$.

The relative phase for k_{gp}^{jilm} and k_{pp}^{ilmq} being the referred and referring meshes, respectively, is denoted $\gamma_{jilm,gp}^{ilmq,pp}(t_1)$, where t_1 is the referring time. All other relative phases are written in the same way.

It is not practical or necessary to calculate all the relative phases between any two gear meshes. Equations (5.4)-(5.7) indicate that if the relative phases of all gear meshes referring to the same referred mesh with the same referring time are calculated, the relative phase between any two gear meshes is known. Such a referred

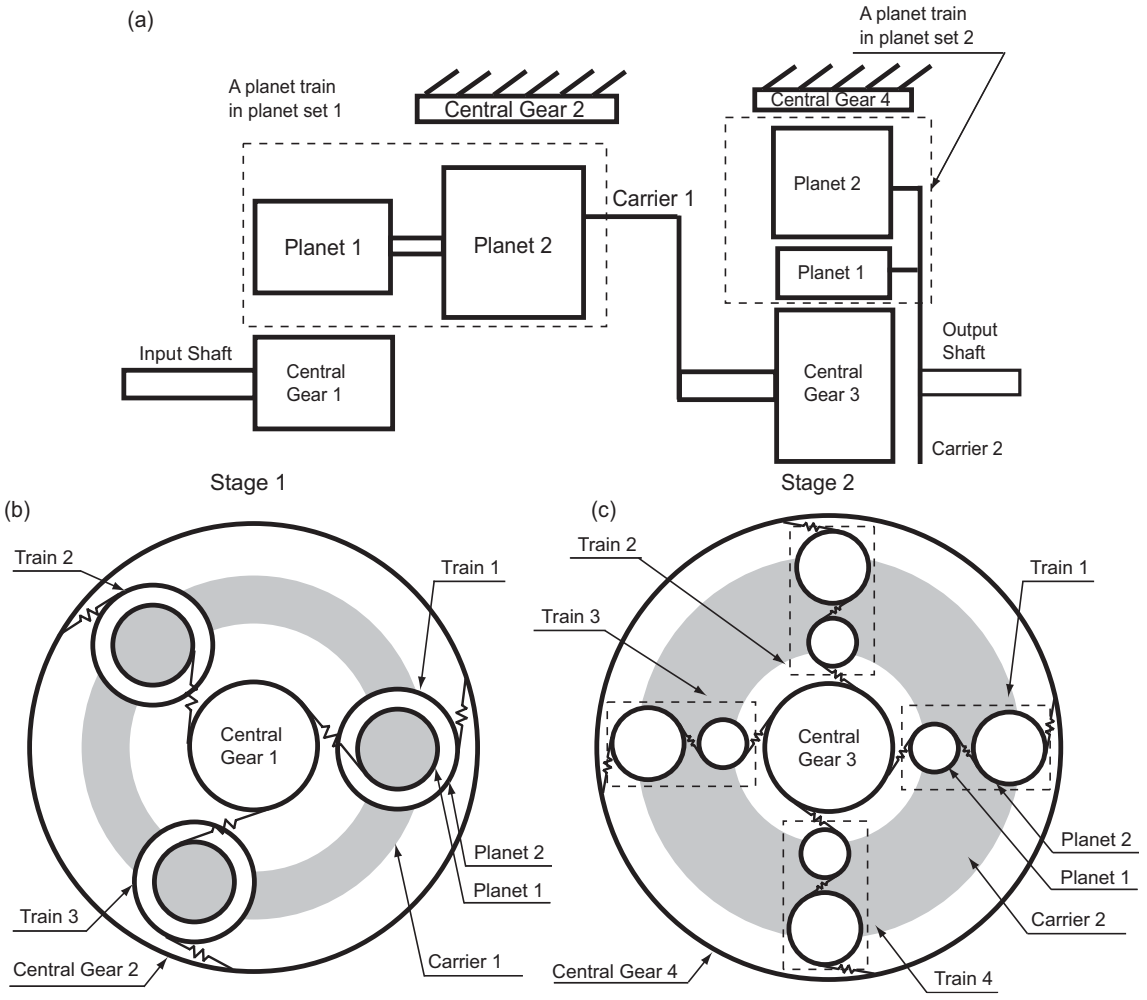

Figure 5.2: The example system. All gear meshes are represented by the springs in red color.

mesh is called the *base referred mesh* of the system.

A. System-level Relative Phases

All the relative phases having the base referred mesh as their referred mesh are called *system-level relative phases*. As mentioned above, if all the system-level relative phases are calculated, the relative phases between any two gear meshes are known. Therefore, the main objective is to calculate the system-level relative phase of each gear mesh in the system.

The mesh between the sun gear associated with stage 1 and planet 1 of train 1 in planet set 1 ($k_{gp}^{s^1111}$) is chosen to be *the base referred mesh* in this study, although this selection is arbitrary. $\hat{\gamma}^{jilm,gp}(t_1)$ and $\hat{\gamma}^{ilmq,pp}(t_1)$ represent the system-level relative phases of k_{gp}^{jilm} and k_{pp}^{ilmq} referring to the base referred mesh with referring time t_1, respectively. These are the important quantities, and they are needed for every mesh.

B. Stage-level Relative Phases

If a certain gear mesh in stage i serves as the referred mesh for all other gear meshes in the same stage, such a referred mesh is called the *stage i referred mesh*. All relative phases that use this gear mesh as their referred mesh are stage-level relative phases. In this study, the gear mesh between the stage i sun gear and planet 1 of train 1 in planet set i ($k_{gp}^{s^ii11}$) is always chosen as the stage i referred mesh. $\tilde{\gamma}^{jilm,gp}(t_1^i)$ and $\tilde{\gamma}^{ilmq,pp}(t_1^i)$ are the stage-level relative phases of k_{gp}^{jilm} and k_{pp}^{ilmq}, respectively, referring to the stage i referred mesh with referring time t_1^i. The referring time $t_1^i = t_1 + \hat{\gamma}^{s^ii11,gp}(t_1)T_{gp}^{s^ii11}$ is the time when the pitch point of mesh $k_{gp}^{s^ii11}$ is in contact for the first time after t_1.

C. Train-level Relative Phases

The relative phases of the gear meshes in train l (k_{gp}^{jilm} and k_{pp}^{ilmq}) referring to the matching gear meshes in train 1 (k_{gp}^{ji1m} and k_{pp}^{i1mq}) are also desired. Such relative

phases are called *train-level relative phases*. Train 1 of stage i in each stage is called the *base train in stage i*, and the gear meshes in train 1 of stage i are called the *base-train referred meshes in stage i*. They serve as the referred meshes for train-level relative phases. $\bar{\gamma}^{jilm,gp}(t_1^{ji1m,gp})$ and $\bar{\gamma}^{ilmq,pp}(t_1^{i1mq,pp})$ are the train-level relative phases of k_{gp}^{jilm} and k_{pp}^{i1mq} referring to their base-train referred meshes in stage i with referring times $t_1^{ji1m,gp} = t_1 + \hat{\gamma}^{s^i i11,gp}(t_1)T_{gp}^{s^i i11} + \tilde{\gamma}^{ji1m,gp}(t_1^i)T_{gp}^{ji1m}$ and $t_1^{i1mq,pp} = t_1 + \hat{\gamma}^{s^i i11,gp}(t_1)T_{gp}^{s^i i11} + \tilde{\gamma}^{i1mq,pp}(t_1^i)T_{pp}^{i1mq}$, respectively.

Dividing the problem into this structure of system-level, stage-level, and train-level, relative phases is convenient. One can analyze the simpler stage and train-level relative phases first. Then, by applying equation (5.4), the important system-level relative phase of any gear mesh is one of

$$\begin{aligned}\hat{\gamma}^{jilm,gp}(t_1) =& \gamma_{1111,gp}^{jilm,gp}(t_1) \\ =& dec\left\{\left[\bar{\gamma}^{jilm,gp}(t_1^{ji1m,gp})T_{gp}^{jilm} + \tilde{\gamma}^{ji1m,gp}(t_1^i)T_{gp}^{ji1m}\right.\right. \\ &\left.\left. + \hat{\gamma}^{s^i i11,gp}(t_1)T_{gp}^{s^i i11}\right]/T_{gp}^{jilm}\right\}\end{aligned} \tag{5.8}$$

$$\begin{aligned}\hat{\gamma}^{ilmq,pp}(t_1) =& \gamma_{1111,gp}^{ilmq,pp}(t_1) \\ =& dec\left\{\left[\bar{\gamma}^{ilmq,pp}(t_1^{i1mq,pp})T_{pp}^{ilmq} + \tilde{\gamma}^{i1mq,pp}(t_1^i)T_{pp}^{i1mq}\right.\right. \\ &\left.\left. + \hat{\gamma}^{s^i i11,gp}(t_1)T_{gp}^{s^i i11}\right]/T_{pp}^{ilmq}\right\}\end{aligned} \tag{5.9}$$

where $i = 1, \cdots, a$, $j = 1, \cdots, b$, $l = 1, \cdots, c^i$, $m, q = 1, \cdots, d^i$, and $q \neq m$.

The definitions of system, stage, and train-level relative phases and equations (5.8)-(5.9) apply to both spur and helical compound planetary gears with any gear tooth shape, including profile and lead modifications. Neither of the helix angle or the detailed gear tooth shape is used in the above definitions or derivations.

5.3.3 Calculation of Relative Phases in Compound Planetary Gears

Equations (5.8)-(5.9) show that $\hat{\gamma}^{s^i i11,gp}$, $\tilde{\gamma}^{ji1m,gp}$, $\tilde{\gamma}^{i1mq,pp}(t_1^i)$, $\bar{\gamma}^{jilm,gp}(t_1^{ji1m,gp})$, and $\bar{\gamma}^{ilmq,pp}(t_1^{i1mq,pp})$ are the only phases needed to determine any system-level relative phases. We focus on the calculation of these relative phases.

A. Calculation of $\hat{\gamma}^{s^i i11,gp}(t_1)$

$\hat{\gamma}^{s^i i11,gp}(t_1)$ is the system-level relative phase between $k_{gp}^{s^i i11}$ and the base referred mesh with the referring time t_1. Its appearance in equations (5.8) and (5.9) indicates that it impacts all the system-level relative phases in stage i. It can not be derived analytically because it depends on manufacturing, assembly, and configuration of the compound planetary gear. The definition of relative phases shows how to determine it by experiment or simulation. Suppose the base referred mesh $k_{gp}^{s^1 111}$ is at its pitch point at $t = t_1$. By locating the time t_2^i when $k_{gp}^{s^i i11}$ is at its pitch point, the relative phase is

$$\hat{\gamma}^{s^i i11,gp}(t_1) = dec\left(\frac{t_2^i - t_1}{T_{gp}^{s^i i11}}\right) \tag{5.10}$$

where $T_{gp}^{s^i i11}$ is the mesh period of $k_{gp}^{s^i i11}$.

In practice one might choose $\hat{\gamma}^{s^i i11,gp}(t_1)$ to achieve certain behavior based on static or dynamic simulations. One can then design the hardware (e.g., the relative clocking angle between two central gears on a single shaft) to achieve the desired phase.

B. Calculation of stage-level relative phases

$\tilde{\gamma}^{ji1m,gp}(t_1^i)$ and $\tilde{\gamma}^{i1mq,pp}(t_1^i)$ are stage-level relative phases. Applying the numbering convention, $\tilde{\gamma}^{ji1m,gp}(t_1^i)$ is either $\tilde{\gamma}^{s^i i11,gp}(t_1^i)$ or $\tilde{\gamma}^{r^i i1d^i,gp}(t_1^i)$, and $\tilde{\gamma}^{i1mq,pp}(t_1^i)$ is actually $\tilde{\gamma}^{i1m(m+1),pp}(t_1^i)$, where $1 \leqslant m \leqslant d^i - 1$. According to the definition of stage-level relative phases, $\tilde{\gamma}^{s^i i11,gp}(t_1^i)$ is zero. $\tilde{\gamma}^{r^i i1d^i,gp}(t_1^i)$ and $\tilde{\gamma}^{i1m(m+1),pp}(t_1^i)$ are calculated

below.

If there is no stepped-planet structure in planet set i, all the gear meshes in stage i have the same mesh period. Hence, no referring time is needed for such stage-level relative phases. By applying (5.5) and (5.7) in this case, $\tilde{\gamma}^{r^i i1 d^i,gp}$ and $\tilde{\gamma}^{i1m(m+1),pp}$ are

$$\tilde{\gamma}^{r^i i1 d^i,gp} = \begin{cases} \gamma_{s^i i11,gp}^{r^i i11,gp} & d^i = 1 \\ dec(\gamma_{s^i i11,gp}^{i112,pp} + \gamma_{i112,pp}^{r^i i12,gp}) & d^i = 2 \\ dec\left(\gamma_{s^i i11,gp}^{i112,pp} + \sum_{u=1}^{d^i-2} \gamma_{i1u(u+1),pp}^{i1(u+1)(u+2),pp} + \gamma_{i1(d^i-1)d^i,pp}^{r^i i1 d^i,gp}\right) & d^i > 2 \end{cases} \tag{5.11}$$

$$\tilde{\gamma}^{i1m(m+1),pp} = \begin{cases} \text{Does not exist.} & d^i = 1 \\ \gamma_{s^i i11,gp}^{i112,pp} & d^i = 2 \\ dec\left(\gamma_{s^i i11,gp}^{i112,pp} + \sum_{u=1}^{m-1} \gamma_{i1u(u+1),pp}^{i1(u+1)(u+2),pp}\right) & d^i > 1 \end{cases} \tag{5.12}$$

where all needed quantities in (5.11) and (5.12) are analytically determined in terms of gear parameters by the procedure described in [77] based on gear geometry.

Now we introduce a stepped-planet structure between planet $v-1$ and planet v ($1 < v \leqslant d^i$ and $d^i \geqslant 2$). The gear mesh conditions require that the mesh periods of all the gear meshes before the stepped-planet structure are equal ($k_{gp}^{s^i 111}$ and $k_{pp}^{i1m(m+1)}$, where $1 \leqslant m \leqslant v-2$), and all the mesh periods after the stepped-planet structure are equal ($k_{gp}^{r^i 11 d^i}$ and $k_{pp}^{i1m(m+1)}$, where $v-1 \leqslant m \leqslant d^i-1$). The relative phases whose referring and referred meshes have the same mesh period are independent of

the referring time. $\tilde{\gamma}^{r^i i1 d^i,gp}(t_1^i)$ and $\tilde{\gamma}^{i1m(m+1),pp}(t_1^i)$ are

$$\tilde{\gamma}^{r^i i1 d^i,gp}(t_1^i) = \begin{cases} \gamma_{s^i i11,gp}^{r^i i12,gp}(t_1^i) & d^i = 2 \\ dec\left(\gamma_{s^i i11,gp}^{i123,pp}(t_1^i)\frac{T_{pp}^{i123,pp}}{T_{gp}^{r^i i1 d^i}} + \gamma_{i123,pp}^{r^i i1 d^i,gp}\right) & d^i = 3,\ v = 2 \\ dec\left(\gamma_{s^i i11,gp}^{i112,pp}\frac{T_{pp}^{i112,pp}}{T_{gp}^{r^i i1 d^i}} + \gamma_{i112,pp}^{r^i i1 d^i,gp}(t_1^i)\right) & d^i = 3,\ v = 3 \\ dec\Bigg(\gamma_{s^i i11,gp}^{i112,pp}\frac{T_{pp}^{i112,pp}}{T_{gp}^{r^i i1 d^i}} + \sum_{u=1}^{v-3}\gamma_{i1u(u+1),pp}^{i1(u+1)(u+2),pp}\frac{T_{pp}^{i112,pp}}{T_{gp}^{r^i i1 d^i}} \\ \quad +\gamma_{i1(v-2)(v-1),pp}^{i1v(v+1),pp}(t_1^{i1(v-2)(v-1),pp}) + \\ \quad \sum_{w=v}^{d^i-2}\gamma_{i1w(w+1),pp}^{i1(w+1)(w+2),pp} + \gamma_{i1(d^i-1)d^i,pp}^{r^i i1 d^i,gp}\Bigg) & d^i \geqslant 4 \end{cases} \tag{5.13}$$

$$\tilde{\gamma}^{i1m(m+1),pp}(t_1^i) = \begin{cases} \text{Do not exist.} & d^i = 2 \\ \text{Eq.(5.12)} & d^i > 2,\ \text{and } 1 \leqslant m \leqslant v-2 \\ dec\Bigg(\gamma_{s^i i11,gp}^{i112,pp}\frac{T_{pp}^{i112,pp}}{T_{gp}^{r^i i1 d^i}} + \sum_{u=1}^{v-3}\gamma_{i1u(u+1),pp}^{i1(u+1)(u+2),pp}\frac{T_{pp}^{i112,pp}}{T_{gp}^{r^i i1 d^i}} + \\ \quad \gamma_{i1(v-2)(v-1),pp}^{i1v(v+1),pp}(t_1^{i1(v-2)(v-1),pp}) + \\ \quad \sum_{w=v}^{m-1}\gamma_{i1w(w+1),pp}^{i1(w+1)(w+2),pp}\Bigg) & d^i > 2,\ \text{and } v-2 \leqslant m \leqslant d^i-1 \end{cases} \tag{5.14}$$

where $t_1^i = t_1 + \hat{\gamma}^{s^i i11,gp}(t_1)T_{gp}^{s^i i11}$ and $t_1^{i1(v-2)(v-1),pp}$ is the time when the pitch point of $k_{pp}^{i1(v-2)(v-1)}$ is in contact for the first time after t_1^i. All quantities needed in (5.13) and (5.14) except $\gamma_{i1(v-2)(v-1),pp}^{i1v(v+1),pp}(t_1^{i1(v-2)(v-1),pp})$ are derivable from gear geometry using the procedure in [77]. $\gamma_{i1(v-2)(v-1),pp}^{i1v(v+1),pp}(t_1^{i1(v-2)(v-1),pp})$ can not be determined analytically because it relies on manufacturing and installation of the stepped-planet structure (i.e., the relative clocking angle between two planets on a single shaft). It is calculated from experiment or simulation.

C. Calculation of train-level relative phases

$\bar{\gamma}^{jilm,gp}(t_1^{jilm,gp})$ and $\bar{\gamma}^{ilmq,pp}(t_1^{ilmq,pp})$ are the train-level relative phases of k_{gp}^{jilm} and k_p^{ilmq} referring to their associated base-train referred meshes (k_{gp}^{ji1m} and k_p^{i1mq}) with the referring times $t_1^{ji1m,gp}$ and $t_1^{ilmq,pp}$, respectively. Because k_{gp}^{jilm} and k_{gp}^{ji1m} have

the same mesh period, $\bar{\gamma}^{jilm,gp}(t_1^{jilm,gp})$ and $\bar{\gamma}^{ilmq,pp}(t_1^{ilmq,pp})$ simplify to $\bar{\gamma}^{jilm,gp}$ and $\bar{\gamma}^{ilmq,pp}$.

With the numbering convention in this study, $\bar{\gamma}^{jilm,gp}$ is either $\bar{\gamma}^{s^iil1,gp}$ or $\bar{\gamma}^{r^iild^i,gp}$, and $\bar{\gamma}^{ilmq,pp}$ is $\bar{\gamma}^{ilm(m+1),pp}$. The expressions for $\bar{\gamma}^{s^iil1,gp}$, $\bar{\gamma}^{r^iild^i,gp}$, and $\bar{\gamma}^{ilm(m+1),pp}$ are summarized in Table 5.1. These train-level relative phases are determined by the tooth numbers of the sun, ring, or planet gears, the relative planet position angle $\hat{\psi}^{il}$ (refer to Nomenclature), the relative planet rotation angle $\hat{\theta}_p^{ilm}$ (discussed later), and the rotation direction of the sun, ring, or planet gears relative to the associated carrier. The above definitions differ from the definitions of train-level relative phases for simple planetary gears in [77] in two ways. First, the planet gear tooth numbers and the relative planet rotation angle $\hat{\theta}_p^{ilm}$ are present in Table 5.1. Second, the sign of the argument inside the operator *dec*( ) is determined by the rotation directions of the sun, ring, or planet gears relative to their associated carrier, instead of the absolute rotation direction of the planets. The first difference is caused by the need to determine the relative phases for planet-planet meshes that do not exist in simple planetary gears. The second difference is because the sign determination method in [77] only applies to a restricted set of simple planetary gear configurations. One of the sun gear, ring gear, or carrier must be fixed for the method of using the absolute planet rotation direction to determine the sign of the relative phases to work. For other configurations, such as torque-split differential configurations or compound planetary gears that contain multiple planet gears in the same train, the method in [77] fails. The method in this study has no such configuration limitations. The rotation directions of the sun, ring, or planet gears relative to their associated carrier are determined by simple kinematic analysis. The sign of the argument inside

the operator $dec(\ )$ for each train-level relative phase is uniquely determined.

In what follows, the derivation of the formulae and the sign determination method in Table 5.1 are explained. For the sun-planet meshes in stage i, $Z_g^{s^i}$ tooth meshes are completed if the sun gear finishes a complete revolution relative to its associated carrier (that is, $\theta_g^{s^i}$-$\theta_c^i = 2\pi$). Consider sun gear s^i starting from an arbitrary state. When this sun gear rotates $\hat{\psi}^{il} > 0$ relative to its associated carrier (the rotation direction is counter-clockwise due to the positive value of $\hat{\psi}^{il}$), $\frac{Z_g^{s^i}\hat{\psi}^{il}}{2\pi}$ tooth meshes are completed for the sun-planet mesh in train 1 of stage i. Let this sun gear's mesh tooth variation function be $k_{ccw}^{s^i}(t)$, where ccw in the subscript indicates counter-clockwise rotation. The current gear teeth positions of train 1 are exactly the same as those of train l before the sun gear rotated $\hat{\psi}^{il}$ relative to its carrier. Therefore, $dec(\frac{Z_g^{s^i}\hat{\psi}^{il}}{2\pi})$ yields the relative phase of the sun-planet mesh in train l referring to that in train 1 (first row of Table 5.1). When sun gear s^i rotates $-2\pi + \hat{\psi}^{il}$ relative to its associated carrier (the rotation direction is clockwise due to the negative value of $-2\pi + \hat{\psi}^{il}$), the completed tooth mesh number for the sun-planet mesh in train 1 of stage i is $-\frac{Z_g^{s^i}(-2\pi+\hat{\psi}^{il})}{2\pi}$. The present gear teeth position for the sun-planet gear mesh of train 1 is the same as that for the sun-planet gear mesh of train l before the sun gear rotated. Thus, the relative phase of the sun-planet mesh in train l referring to that in train 1 in this case becomes $dec(-\frac{Z_g^{s^i}(-2\pi+\hat{\psi}^{il})}{2\pi})$, where the negative sign before the fraction in the argument is caused by the clockwise rotation (when the sun gear rotates clockwise, its mesh tooth variation function $k_{cw}^{s^i}(t)$ is equivalent to $k_{ccw}^{s^i}(-t)$). Dropping the integer part in the train-level relative phase yields $\bar{\gamma}^{s^i il1,gp} = dec(-\frac{Z_g^{s^i}\hat{\psi}^{il}}{2\pi})$ (second row of Table 5.1). The same analytical process applies to the derivation of the train-level relative phases for ring-planet gear meshes ($\bar{\gamma}^{r^i ild^i,gp}$). The results are listed in Table

5.1.

The analytical process to derive the train-level relative phases for planet-planet gear meshes is as follows. For the case that there is no stepped-planet structure in the planet trains of stage i, Z_p^{ilm} tooth meshes are completed for the mesh between planets m and $m+1$ when planet m finishes a complete revolution relative to carrier i. The next step is to determine $\hat{\theta}_p^{ilm}$, the angle that planet m must rotate relative to carrier i such that the gear teeth position for the gear mesh between planets m and $m+1$ in train 1 after the rotation is equivalent to that in train l before the rotation. Once $\hat{\theta}_p^{ilm}$ is calculated as described below, $dec(\frac{Z_p^{ilm}\hat{\theta}_p^{ilm}}{2\pi})$ and $dec(-\frac{Z_p^{ilm}\hat{\theta}_p^{ilm}}{2\pi})$ are the relative phases of the mesh between planet m and $m+1$ in train l referring to that in train 1 when planet m rotates counter-clockwise and clockwise, respectively, relative to its associated carrier ($\bar{\gamma}^{ilm(m+1),pp}$ in Table 5.1).

According to the previous derivation of the relative phases for sun-planet meshes, the gear teeth positions in train 1 after the sun gear rotates $\hat{\psi}^{il}$ counter-clockwise or $2\pi - \hat{\psi}^{il}$ clockwise relative to carrier i are exactly those in train l before the rotation. Therefore, the problem to determine $\bar{\gamma}^{ilm(m+1),pp}$ reduces to calculation of the angle that planet m rotates relative to carrier i after the sun gear rotates $\hat{\psi}^{il}$ counter-clockwise or $2\pi - \hat{\psi}^{il}$ clockwise relative to carrier i.

Meshed-planet gear kinematics gives

$$\frac{\theta_p^{ilm} - \theta_c^i}{\theta_g^{s^i} - \theta_c^i} = (-1)^m \frac{Z_g^{s^i}}{Z_p^{ilm}} \tag{5.15}$$

where θ_p^{ilm}, $\theta_g^{s^i}$, and θ_c^i are the absolute rotations of planet m in train l of planet set i, the sun gear in stage i, and carrier i, respectively. For counter-clockwise sun gear rotation relative to its associated carrier, substitution of $\hat{\psi}^{il} = \theta_g^{s^i} - \theta_c^i$ and

$\hat{\theta}_p^{ilm} = \theta_p^{ilm} - \theta_c^i$ into equation (5.15) yields

$$\hat{\theta}_p^{ilm} = (-1)^m \frac{Z_g^{s^i} \hat{\psi}^{il}}{Z_p^{ilm}} \tag{5.16}$$

For clockwise sun gear rotation relative to its associated carrier, substitution of $2\pi - \hat{\psi}^{il} = \theta_g^{s^i} - \theta_c^i$ and $\hat{\theta}_p^{ilm} = \theta_p^{ilm} - \theta_c^i$ into equation (5.15) gives

$$\hat{\theta}_p^{ilm} = (-1)^m \frac{Z_g^{s^i} (2\pi - \hat{\psi}^{il})}{Z_p^{ilm}} \tag{5.17}$$

This study addresses the case where there is one stepped structure in a planet set because it is rare to have two or more stepped-planet structures in the same stage. When there is a stepped-planet structure between planets $v-1$ and v in stage i, one of $dec(\frac{Z_p^{ilm}\hat{\theta}_p^{ilm}}{2\pi})$ or $dec(-\frac{Z_p^{ilm}\hat{\theta}_p^{ilm}}{2\pi})$, depending on whether planet m rotates counter-clockwise or clockwise, still gives the relative phase of the mesh between planet m and $m+1$ in train l referring to that in train 1, once $\hat{\theta}_p^{ilm}$ is known. This is the same as above for meshed planets. The calculation of $\hat{\theta}_p^{ilm}$, however, needs to account for the stepped-planet structure. If $m \leq v-2$ (the planet-planet mesh is before the stepped-planet structure), the planet-planet mesh has the same mesh period as the sun-planet mesh in the same stage. Thus, compound planetary gear kinematics ensure that equations (5.15)-(5.17) still apply. If $m \geq v$ (the planet-planet mesh is after the stepped-planet structure), the mesh period of the planet-planet mesh is generally different from that of the sun-planet mesh in the same stage but the same as for the ring-planet mesh in the same stage. Therefore, the calculation of $\hat{\theta}_p^{ilm}$ in this case should be based on $(\theta_g^{r^i} - \theta_c^i)$, the rotation of the ring gear relative to its associated carrier. Planetary gear kinematics gives

$$\frac{\theta_p^{ilm} - \theta_c^i}{\theta_g^{r^i} - \theta_c^i} = (-1)^{d^i - m} \frac{Z_g^{r^i}}{Z_p^{ilm}} \tag{5.18}$$

Table 5.1: The expressions of train-level relative phases. The counter-clockwise rotation is the positive direction for all angles.

Relative Phase	Rotation Direction Relative to Carrier	Relative Phase Expression
$\bar{\gamma}^{s^i il1,gp}$	$\theta_g^{s^i}$-$\theta_c^i > 0$	$\bar{\gamma}^{s^i il1,gp} = dec\left(\frac{Z_g^{s^i}\hat{\psi}^{il}}{2\pi}\right)$
	$\theta_g^{s^i}$-$\theta_c^i < 0$	$\bar{\gamma}^{s^i il1,gp} = dec\left(-\frac{Z_g^{s^i}\hat{\psi}^{il}}{2\pi}\right)$
$\bar{\gamma}^{r^i ild^i,gp}$	$\theta_g^{r^i}$-$\theta_c^i > 0$	$\bar{\gamma}^{r^i ild^i,gp} = dec\left(\frac{Z_g^{r^i}\hat{\psi}^{il}}{2\pi}\right)$
	$\theta_g^{r^i}$-$\theta_c^i < 0$	$\bar{\gamma}^{r^i ild^i,gp} = dec\left(-\frac{Z_g^{r^i}\hat{\psi}^{il}}{2\pi}\right)$
$\bar{\gamma}^{ilm(m+1),pp}$	$\hat{\theta}_p^{ilm} > 0$	$\bar{\gamma}^{ilm(m+1),pp} = dec\left(\frac{Z_p^{ilm}\hat{\theta}_p^{ilm}}{2\pi}\right)$
	$\hat{\theta}_p^{ilm} < 0$	$\bar{\gamma}^{ilm(m+1),pp} = dec\left(-\frac{Z_p^{ilm}\hat{\theta}_p^{ilm}}{2\pi}\right)$

For counter-clockwise ring gear rotation relative to its associated carrier, substitution of $\hat{\psi}^{il} = \theta_g^{r^i} - \theta_c^i$ and $\hat{\theta}_p^{ilm} = \theta_p^{ilm} - \theta_c^i$ into equation (5.18) yields (compare to equation (5.16))

$$\hat{\theta}_p^{ilm} = (-1)^{d^i - m}\frac{Z_g^{r^i}\hat{\psi}^{il}}{Z_p^{ilm}} \tag{5.19}$$

Similarly, for clockwise ring gear rotation relative to its associated carrier, $\hat{\theta}_p^{ilm}$ is calculated from equation (5.18) as (compare to equation (5.17))

$$\hat{\theta}_p^{ilm} = (-1)^{d^i - m} \frac{Z_g^{r^i}(2\pi - \hat{\psi}^{il})}{Z_p^{ilm}} \tag{5.20}$$

Kinematic analysis of the compound planetary gear system is required to determine the rotation direction of each component, and the relative planet rotation angle $\hat{\theta}_p^{ilm}$. With such kinematic analysis, the formulae in Table 5.1 apply to any configuration of compound planetary gear and agree with Parker and Lin's results in [77] for the twelve simple planetary gear configurations.

All the above derivations are independent of the gear tooth type (spur or helical gears) and the detailed gear tooth shape. Therefore, the results apply to both spur and helical gears with arbitrary gear tooth shape.

5.3.4 Relations between Train-level Relative Phases

Because gear tooth numbers and relative planet position angles of compound planetary gears must satisfy system assembly conditions, there are specific relations between the train-level relative phases ($\bar{\gamma}^{s^i il1,gp}$, $\bar{\gamma}^{r^i ild^i,gp}$ and $\bar{\gamma}^{ilm(m+1),pp}$). These relations are important for investigations on the suppression of planetary gear dynamic response through mesh phasing [75].

Case A: No stepped-planet structure in planet set i

In this case, all the gear meshes in planet set i have the same mesh period. No referring time is needed for any relative phase within this stage. Suppose central gear s^i moves counter-clockwise relative to carrier i.

When $d^i = 1$, the assembly condition of a simple planetary gear [68, 77] gives,

$$(Z_g^{r^i} + Z_g^{s^i})\hat{\psi}^{il} = 2\pi n^{il} \tag{5.21}$$

where n^{il} is an arbitrary integer. Insertion of equation (5.21) into the results in Table 5.1 and invoking compound planetary kinematics yield

$$\begin{aligned}\bar{\gamma}^{s^i il1,gp} &= dec\left(\frac{Z_g^{s^i}\hat{\psi}^{il}}{2\pi}\right) \\ &= dec\left(\frac{2\pi n^{il} - Z_g^{r^i}\hat{\psi}^{il}}{2\pi}\right) = dec\left(-\frac{Z_g^{r^i}\hat{\psi}^{il}}{2\pi}\right) = \bar{\gamma}^{r^i ild^i,gp}\end{aligned} \tag{5.22}$$

When $d^i \geqslant 2$, insertion of (5.16) into the train-level relative phase for planet-planet meshes in Table 5.1 and application of meshed-planet gear kinematics for the rotation direction of planet m relative to carrier i yield

$$\begin{aligned}\bar{\gamma}^{ilm(m+1),pp} &= dec\left((-1)^m\frac{Z_p^{ilm}\hat{\theta}_p^{ilm}}{2\pi}\right) \\ &= dec\left((-1)^m(-1)^m\frac{Z_g^{s^i}\hat{\psi}^{il}}{2\pi}\right) = \bar{\gamma}^{s^i il1,gp}\end{aligned} \tag{5.23}$$

By applying meshed-planet kinematics for the rotation direction of the ring gear relative to carrier i, $\bar{\gamma}^{r^i ild^i,gp}$ in Table 5.1 is

$$\bar{\gamma}^{r^i ild^i,gp} = dec\left((-1)^{d^i}\frac{Z_g^{r^i}\hat{\psi}^{il}}{2\pi}\right) \tag{5.24}$$

The assembly condition of stage i [68] is

$$\hat{\psi}^{il} = \frac{2\pi n^{il}}{Z_g^{r^i} + (-1)^{d^i+1}Z_g^{s^i}} \tag{5.25}$$

where n^{il} is an arbitrary integer. Insertion of (5.25) into (5.24) gives

$$\begin{aligned}\bar{\gamma}^{r^i ild^i,gp} &= dec\left((-1)^{d^i}\frac{2\pi n^{il} - (-1)^{d^i+1}Z_g^{s^i}\hat{\psi}^{il}}{2\pi}\right) \\ &= dec\left((-1)^{2d^i}\frac{Z_g^{s^i}\hat{\psi}^{il}}{2\pi}\right) = \bar{\gamma}^{s^i il1,gp}\end{aligned} \tag{5.26}$$

Equations (5.23) and (5.26) show that $\bar{\gamma}^{s^i il1,gp}$, $\bar{\gamma}^{ilm(m+1),pp}$, and $\bar{\gamma}^{r^i ild^i,gp}$ are equal when $d^i \geqslant 2$.

Summarizing this case, if there is no stepped-planet structure in planet set i, the train-level relative phases whose referring meshes are in the same planet train equal each other.

Case B: Stepped-planet structure in planet set i

The stepped-planet structure is between planets $v-1$ and v in stage i, where $2 \leqslant v \leqslant d^i$. The relations between $\bar{\gamma}^{s^i il1,gp}$, $\bar{\gamma}^{r^i ild^i,gp}$, and $\bar{\gamma}^{ilm(m+1),pp}$ are investigated for the following two cases.

(I) When $1 \leqslant m \leqslant v-2$, the relationship between $\bar{\gamma}^{ilm(m+1),pp}$ and $\bar{\gamma}^{s^i il1,gp}$ is the same as equation (5.23) because the rotation direction of planet m relative to carrier i is determined in the same way and the same train-level relative phase formula in Table 5.1 is applied. That is to say, the train-level relative phases whose referring meshes are located between the sun gear and the stepped-planet structure are all equal.

(II) When $v \leqslant m \leqslant d^i-1$, insertion of (5.19) into the formulae of $\bar{\gamma}^{ilm(m+1),pp}$ in Table 5.1 and use of kinematics to determine the rotation direction of planet m relative to carrier i yields

$$\begin{aligned} \bar{\gamma}^{ilm(m+1),pp} &= dec\left((-1)^{m-1}(-1)^{d^i-m}\frac{Z_g^{r^i}\hat{\psi}^{il}}{2\pi}\right) \\ &= dec\left((-1)^{d^i-1}\frac{Z_g^{r^i}\hat{\psi}^{il}}{2\pi}\right) \end{aligned} \tag{5.27}$$

Applying stepped-planet kinematics for the rotation direction of the ring gear in stage i relative to carrier i, the ring-planet relative phase in Table 5.1 becomes

$$\bar{\gamma}^{r^i ild^i,gp} = dec\left((-1)^{d^i-1}\frac{Z_g^{r^i}\hat{\psi}^{il}}{2\pi}\right) \tag{5.28}$$

Equations (5.27) and (5.28) show that the train-level relative phases whose referring meshes are located between the ring gear and the stepped-planet structure are equal

to each other, similar to (I) above.

The assembly condition of a stepped planetary gear requires that [68]

$$\begin{aligned} \hat{\psi}^{il} &= n_s^{il}\delta_1^{s^i} + n_r^{il}\delta_2^{r^i} \\ \delta_1^{s^i} &= \frac{2\pi Z_p^{ilv}}{Z_g^{s^i} Z_p^{il(v-1)} + (-1)^{d^i} Z_g^{s^i} Z_p^{ilv}} \\ \delta_2^{r^i} &= \frac{2\pi Z_p^{il(v-1)}}{Z_g^{r^i} Z_p^{il(v-1)} + (-1)^{d^i} Z_g^{s^i} Z_p^{ilv}} \end{aligned} \tag{5.29}$$

where n_s^{il} and n_r^{il} are integers, $\delta_1^{s^i}$ is the angle that carrier i rotates when the ring gear r^i is fixed and the sun gear rotates one tooth counter-clockwise relative to the fixed reference frame, and $\delta_2^{r^i}$ is the angle that carrier i rotates when the sun gear s^i is fixed and the ring gear rotates one tooth counter-clockwise relative to the fixed reference frame. The above assembly condition indicates that when the sun and ring gears rotate through n_s^{il} and n_r^{il} tooth meshes (that is, the sun and ring gears rotate $\frac{2\pi n_s^{il}}{Z_g^{s^i}}$ and $\frac{2\pi n_r^{il}}{Z_g^{r^i}}$, respectively), carrier i rotates $\hat{\psi}^{il}$. Thus, planet train 1 is brought to the position of train l before the rotation. At the same time, because both the sun and ring gears rotate integer numbers of teeth, a new planet train can be installed at the position of train 1 before the rotation with exactly the same gear teeth positions as train 1.

The above process not only illustrates the installation of a new planet train in a stepped compound planetary gear but also indicates the numbers of tooth meshes that the sun and ring gears complete when train 1 moves to the position of train l. The angles that the sun and ring gears rotate relative to carrier i during the above assembly process are $(\frac{2\pi n_s^{il}}{Z_g^{s^i}} - \hat{\psi}^{il})$ and $(\frac{2\pi n_r^{il}}{Z_g^{r^i}} - \hat{\psi}^{il})$. Thus, the numbers of gear meshes that the sun and ring gears complete are $|n_s^{il} - \hat{\psi}^{il} Z_g^{s^i}/2\pi|$ and $|n_r^{il} - \hat{\psi}^{il} Z_g^{r^i}/2\pi|$, which directly reflect how many mesh cycles that the sun-planet and ring-planet meshes in

train l are ahead of or behind those in train 1. Application of the operator $dec()$ to these two numbers yields the train-level sun-planet and ring-planet relative phases between train l and train 1 as

$$\begin{aligned} \bar{\gamma}^{s^i il1,gp} &= dec(|n_s^{il} - \hat{\psi}^{il} Z_g^{s^i}/2\pi|) \\ \bar{\gamma}^{r^i ild^i,gp} &= dec(|n_r^{il} - \hat{\psi}^{il} Z_g^{r^i}/2\pi|) \end{aligned} \tag{5.30}$$

Because n_s^{il} and n_r^{il} are integers and they have infinite combinations to satisfy (5.29), the outcomes of $\bar{\gamma}^{s^i il1,gp}$ and $\bar{\gamma}^{r^i ild^i,gp}$ in (5.30) have only two possibilities: $dec(\pm\hat{\psi}^{il} Z_g^{s^i}/2\pi)$ and $dec(\pm\hat{\psi}^{il} Z_g^{r^i}/2\pi)$. For example, if $\hat{\psi}^{il} Z_g^{s^i}/2\pi = 0.8$, $dec(|n_s^{il} - 0.8|) = 0.2 = dec(-0.8)$ when $n_s^{il} = 2$ and $dec(|n_s^{il} - 0.8|) = 0.8 = dec(0.8)$ when $n_s^{il} = -1$. Thus, equation (5.30) simplifies to

$$\begin{aligned} \bar{\gamma}^{s^i il1,gp} &= dec(\pm\hat{\psi}^{il} Z_g^{s^i}/2\pi) \\ \bar{\gamma}^{r^i ild^i,gp} &= dec(\pm\hat{\psi}^{il} Z_g^{r^i}/2\pi) \end{aligned} \tag{5.31}$$

The $\pm$ sign is necessary because in the above process the rotation direction of each component is not specified and only the assembly condition is used. The rotation directions of the sun and ring gears relative to the associated carrier determine the signs for the input arguments to $dec(\ )$ in (5.31). For example, if the sun gear s^i rotates counter-clockwise relative to carrier i and the sun-planet mesh in train 1 completes $\hat{\psi}^{il} Z_g^{s^i}/2\pi$ tooth meshes, the gear teeth positions of train 1 are exactly the same as those of train l before the sun gear rotation. Thus, the positive sign is used such that $\bar{\gamma}^{s^i il1,gp} = dec(\hat{\psi}^{il} Z_g^{s^i}/2\pi)$. If the sun gear s^i rotates clockwise relative to carrier i and the sun-planet mesh in train 1 completes $\hat{\psi}^{il} Z_g^{s^i}/2\pi$ tooth meshes, the gear teeth positions of train 1 are exactly the same as those of train $c^i - l$ before the sun gear rotates. In order to make the gear teeth positions of train 1 be the same as those of train l, the sun-planet mesh in train 1 needs to complete $Z_g^{s^i} - \hat{\psi}^{il} Z_g^{s^i}/2\pi$ tooth

meshes. In this case, the negative sign is used in the input arguments to $dec(\ )$ such that $\bar{\gamma}^{s^i il1,gp} = dec(-\hat{\psi}^{il} Z_g^{s^i}/2\pi) = dec(Z_g^{s^i} - \hat{\psi}^{il} Z_g^{s^i}/2\pi)$. It is the same for $\bar{\gamma}^{r^i ild^i,gp}$. These results match the formulae in Table 5.1.

Summarizing the above discussion, the train-level relative phases whose referring meshes are located on the same side of the stepped-planet structure always share the same value. Thus, some but not all train-level relative phases are equal when planet set i has stepped-planet structure. In addition, the sun-planet and ring-planet train-level relative phase definitions for stepped planetary gears in Table 5.1 are consistent with the stepped planetary gear assembly condition.

5.4 Example Calculation of Relative Phases

The two-stage compound planetary gear shown in Figure 5.2 is used as an example. The first stage has stepped-planet structure, and the second stage has meshed-planet structure. All the gears are numbered according to the convention previously specified, as shown in Figure 5.2. The parameters are listed in Tables 5.2 and 5.3. The following illustrates the analytical procedure to calculate all the system-level relative phases with the base referred mesh $k_{gp}^{s^1 111}$ as their referred mesh.

Table 5.2: Parameters for the example system shown in Figure 5.2.

Input component		central gear 1
Connection between stage 1 and stage 2		carrier 1 connects to central gear 3
Fixed central gears or carriers		central gear 2 and central gear 4
Output component		carrier 2
Planet position angles	Stage 1	$\hat{\psi}^{11} = 0°,\ \hat{\psi}^{12} = 120°,$ $\hat{\psi}^{13} = 240°$
	Stage 2	$\hat{\psi}^{21} = 0°,\ \hat{\psi}^{22} = 90°,$ $\hat{\psi}^{23} = 180°,\ \hat{\psi}^{24} = 270°$

Table 5.3: Parameters for the example system shown in Figure 5.2. The unit for all diameters is millimeter. Planet gear (ilm) means planet m in train l of stage i.

	Stage 1				Stage 2			
	Central Gear 1	Planet gear $(1l1)$	Planet gear $(1l2)$	Central Gear 2	Central Gear 3	Planet gear $(2l1)$	Planet gear $(2l2)$	Central Gear 4
Tooth Number	35	38	62	151	29	29	33	153
Diametral Pitch	0.4	0.4	0.5	0.5	0.5	0.5	0.5	0.5
Pressure Angle	25^o	25^o	24^o	24^o	25^o	25^o	25^o	25^o
Base Diameter	79.25	86.11	113.28	275.84	52.58	52.58	59.69	277.37
Outer Diameter	88.39	100.58	124.71	319.02	61.72	61.72	69.60	324.10
Root Diameter	76.96	89.41	115.57	305.31	52.58	52.58	60.45	305.31

The numerical results throughout this example are from numerical simulation of mesh tooth variation functions calculated by Planetary2D, a multibody finite element program with precise tracking of numbers of teeth in contact at all gear meshes [95].

The software calculates the tooth variation functions based on exact gear kinematics and precise tooth geometry with no preset or user-defined mesh phase relations. Hence, the relative phases calculated from the numerical solution of mesh tooth variation functions are a reliable and independent benchmark to verify the analytical results. The simulation results of mesh tooth variation functions with all the relative phases marked are shown in Figure 5.3 and Figure 5.4.

Kinematic analysis yields all the mesh periods and the rotation directions of all components. The analytically calculated mesh periods compare well to numerical results in Table 5.4. As with all results that follow, the errors in the numerical results depend on the number of steps analyzed in a mesh cycle.

Table 5.4: Mesh periods of all gear meshes in the example system.

Stage Number	Period	Analytical	Numerical	Error range of numerical result
Stage 1	T_{gp}^{11l1}	0.6483 s	0.648 s	$\pm$0.002 s
	T_{gp}^{21l2}	0.3974 s	0.397 s	$\pm$0.002 s
Stage 2	T_{gp}^{32l1}	1.6768 s	1.677 s	$\pm$0.008 s
	T_{pp}^{2l12}	1.6768 s	1.677 s	$\pm$0.008 s
	T_{gp}^{42l2}	1.6768 s	1.677 s	$\pm$0.008 s

To begin the process, the base referred mesh of the system and the referring time of the base referred mesh are chosen. In this example, k_{gp}^{1111} is selected as the base referred mesh, and the referring time of the base referred mesh is $t_1 = 0$ at the pitch point. This defines the origin of the absolute time axis and simplifies the use of equations (5.8) and (5.9) to calculate system-level relative phases.

The key relative phases $\hat{\gamma}^{s^i i11,gp}(t_1)$, $\tilde{\gamma}^{r^i i1d^i,gp}(t_1^i)$, and $\tilde{\gamma}^{i1m(m+1),pp}(t_1^i)$ are calculated from equations (5.10)-(5.14) with the results given in Table 5.5. In this example, the system-level relative phase between the stage 2 referred mesh and the base referred mesh ($\hat{\gamma}^{3211,gp}(t_1)$), which depends on assembly conditions, is specified as zero. In real applications, equation (5.10) and simulation or experiments are needed to calculate such relative phases. In addition, the stage 1 relative phase $\tilde{\gamma}^{2112,gp}(t_1^1)$ depends not only on the gear parameters of the stage 1 sun, planet, and ring gears but also on the stepped-planet structure (the relative clocking angle between the two coaxial planets in the same train); no analytical formula is available to calculate it. Its analytical value in Table 5.5 takes the numerical result directly, which is found by recording the time when the pitch points of the referring and referred meshes are in mesh and applying equation (5.4). Whenever a system has multiple stages or stepped planets there are relative angles that depend on manufacturing or assembly. In these cases, experiments or simulation with precision contact tracking are needed as used above. If that is impractical, one can do sensitivity studies to see if these relative angles affect the response of interest in that specific system.

Kinematic analysis to find the rotation directions of each sun, ring, and planet relative to its associated carrier and the formulae in Table 5.1 yield the analytical results for $\bar{\gamma}^{jilm,gp}$ and $\bar{\gamma}^{ilmq,pp}$ that are listed in Table 5.6. The numerical results confirm the analysis.

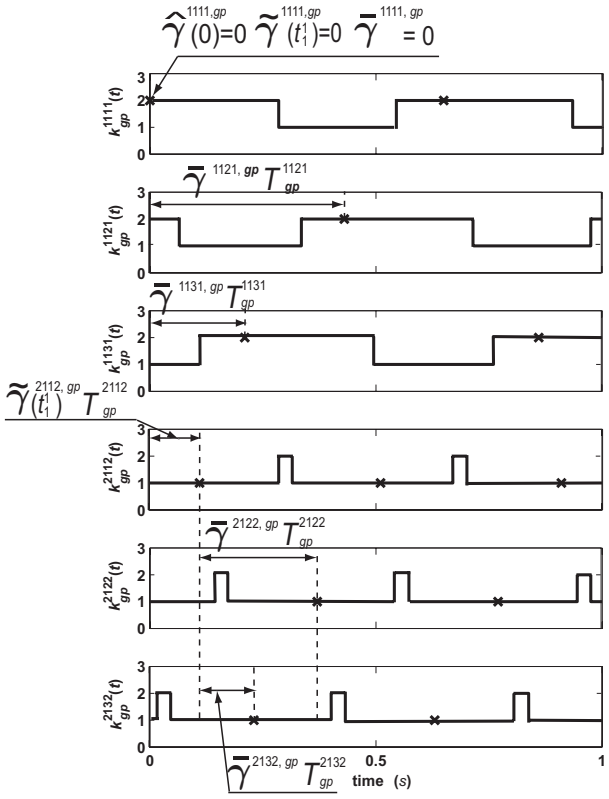

Figure 5.3: Mesh tooth variation functions of all the gear meshes in stage 1 of the example system with the related relative phases marked. The symbol × denotes the time when the pitch point of the associated gear mesh is in contact.

Table 5.5: Relative phases $\hat{\gamma}^{s^i i 1 1, gp}(t_1)$, $\tilde{\gamma}^{r^i i 1 d^i, gp}(t_1^i)$, and $\tilde{\gamma}^{i1m(m+1), pp}$. The * sign indicates the associated value in the 'Analytical' column is actually from numerical calculation.

Stage Number	Referring time	Relative phase	Analytical	Numerical	Error range of numerical result
Stage 1	$t_1 = 0$	$\hat{\gamma}^{1111,gp}(t_1)$	0	0	0
	$t_1^1 = 0$	$\tilde{\gamma}^{1111,gp}(t_1^1)$	0	0	0
	$t_1^1 = 0$	$\tilde{\gamma}^{2112,gp}(t_1^1)$	0.277*	0.277	± 0.0031
Stage 2	$t_1 = 0$	$\hat{\gamma}^{3211,gp}(t_1)$	0	0	N/A
	$t_1^2 = 0$	$\tilde{\gamma}^{3211,gp}(t_1^2)$	0	0	± 0.0048
	$t_1^2 = 0$	$\tilde{\gamma}^{4212,gp}(t_1^2)$	0.0770	0.077	± 0.0048
	$t_1^2 = 0$	$\tilde{\gamma}^{2112,pp}(t_1^2)$	0.0689	0.069	± 0.0048

Table 5.6: Train-level relative phases $\bar{\gamma}^{jilm,gp}$ and $\bar{\gamma}^{ilmq,pp}$.

Stage Number	Relative phase	Analytical	Numerical	Error range of numerical result
Stage 1	$\bar{\gamma}^{11l1,gp}$	$\bar{\gamma}^{1111,gp} = 0$ $\bar{\gamma}^{1121,gp} = 0.667$ $\bar{\gamma}^{1131,gp} = 0.333$	$\bar{\gamma}^{1111,gp} = 0$ $\bar{\gamma}^{1121,gp} = 0.663$ $\bar{\gamma}^{1131,gp} = 0.331$	± 0.0031
	$\bar{\gamma}^{21l2,gp}$	$\bar{\gamma}^{2112,gp} = 0$ $\bar{\gamma}^{2122,gp} = 0.667$ $\bar{\gamma}^{2132,gp} = 0.333$	$\bar{\gamma}^{2112,gp} = 0$ $\bar{\gamma}^{2122,gp} = 0.665$ $\bar{\gamma}^{2132,gp} = 0.335$	± 0.0031
Stage 2	$\bar{\gamma}^{32l1,gp}$	$\bar{\gamma}^{3211,gp} = 0$ $\bar{\gamma}^{3221,gp} = 0.250$ $\bar{\gamma}^{3231,gp} = 0.500$ $\bar{\gamma}^{3241,gp} = 0.750$	$\bar{\gamma}^{3211,gp} = -0.001$ $\bar{\gamma}^{3221,gp} = 0.254$ $\bar{\gamma}^{3231,gp} = 0.503$ $\bar{\gamma}^{3241,gp} = 0.753$	± 0.0048
	$\bar{\gamma}^{42l2,gp}$	$\bar{\gamma}^{4212,gp} = 0$ $\bar{\gamma}^{4222,gp} = 0.250$ $\bar{\gamma}^{4232,gp} = 0.500$ $\bar{\gamma}^{4242,gp} = 0.750$	$\bar{\gamma}^{4212,gp} = 0.002$ $\bar{\gamma}^{4222,gp} = 0.253$ $\bar{\gamma}^{4232,gp} = 0.501$ $\bar{\gamma}^{4242,gp} = 0.752$	± 0.0048
	$\bar{\gamma}^{2l12,pp}$	$\bar{\gamma}^{2112,gp} = 0$ $\bar{\gamma}^{2212,gp} = 0.250$ $\bar{\gamma}^{2312,gp} = 0.500$ $\bar{\gamma}^{2412,gp} = 0.750$	$\bar{\gamma}^{2112,gp} = 0.003$ $\bar{\gamma}^{2212,gp} = 0.252$ $\bar{\gamma}^{2312,gp} = 0.500$ $\bar{\gamma}^{2412,gp} = 0.751$	± 0.0048

Finally, all system-level relative phases $\hat{\gamma}^{jilm,gp}(t_1)$ and $\hat{\gamma}^{ilmq,pp}(t_1)$ are calculated from equations (5.8) and (5.9). The results in Table 5.7 agree with the numerical benchmark.

Thus, the relative phases of all the gear meshes referring to the base referred mesh are determined and verified with an independent numerical benchmark that can be considered exact within the given error limits resulting from discretization of the mesh cycles.

Table 5.7: System-level relative phases $\hat{\gamma}^{jilm,gp}(t_1)$ and $\hat{\gamma}^{ilmq,pp}(t_1)$.

Stage Number	Relative Phase	Analytical	Numerical	Error range of numerical result
Stage 1	$\hat{\gamma}^{11l1,gp}(t_1)$	$\hat{\gamma}^{1111,gp}(0) = 0$ $\hat{\gamma}^{1121,gp}(0) = 0.667$ $\hat{\gamma}^{1131,gp}(0) = 0.333$	$\hat{\gamma}^{1111,gp}(0) = 0$ $\hat{\gamma}^{1121,gp}(0) = 0.663$ $\hat{\gamma}^{1131,gp}(0) = 0.331$	± 0.0031
	$\hat{\gamma}^{21l2,gp}(t_1)$	$\hat{\gamma}^{2112,gp}(0) = 0.268$ $\hat{\gamma}^{2122,gp}(0) = 0.935$ $\hat{\gamma}^{2132,gp}(0) = 0.601$	$\hat{\gamma}^{2112,gp}(0) = 0.268$ $\hat{\gamma}^{2122,gp}(0) = 0.935$ $\hat{\gamma}^{2132,gp}(0) = 0.608$	± 0.0031
Stage 2	$\hat{\gamma}^{32l1,gp}(t_1)$	$\hat{\gamma}^{3211,gp}(0) = 0$ $\hat{\gamma}^{3221,gp}(0) = 0.250$ $\hat{\gamma}^{3231,gp}(0) = 0.500$ $\hat{\gamma}^{3241,gp}(0) = 0.750$	$\hat{\gamma}^{3211,gp}(0) = 0$ $\hat{\gamma}^{3221,gp}(0) = 0.250$ $\hat{\gamma}^{3231,gp}(0) = 0.502$ $\hat{\gamma}^{3241,gp}(0) = 0.751$	± 0.0048
	$\hat{\gamma}^{42l2,gp}(t_1)$	$\hat{\gamma}^{4212,gp}(0) = 0.013$ $\hat{\gamma}^{4222,gp}(0) = 0.263$ $\hat{\gamma}^{4232,gp}(0) = 0.513$ $\hat{\gamma}^{4242,gp}(0) = 0.763$	$\hat{\gamma}^{4212,gp}(0) = 0.013$ $\hat{\gamma}^{4222,gp}(0) = 0.263$ $\hat{\gamma}^{4232,gp}(0) = 0.513$ $\hat{\gamma}^{4242,gp}(0) = 0.763$	± 0.0048
	$\hat{\gamma}^{2l12,pp}(t_1)$	$\hat{\gamma}^{2112,pp}(0) = 0.069$ $\hat{\gamma}^{2212,pp}(0) = 0.319$ $\hat{\gamma}^{2312,pp}(0) = 0.569$ $\hat{\gamma}^{2412,pp}(0) = 0.819$	$\hat{\gamma}^{2112,pp}(0) = 0.070$ $\hat{\gamma}^{2212,pp}(0) = 0.318$ $\hat{\gamma}^{2312,pp}(0) = 0.570$ $\hat{\gamma}^{2412,pp}(0) = 0.819$	± 0.0048

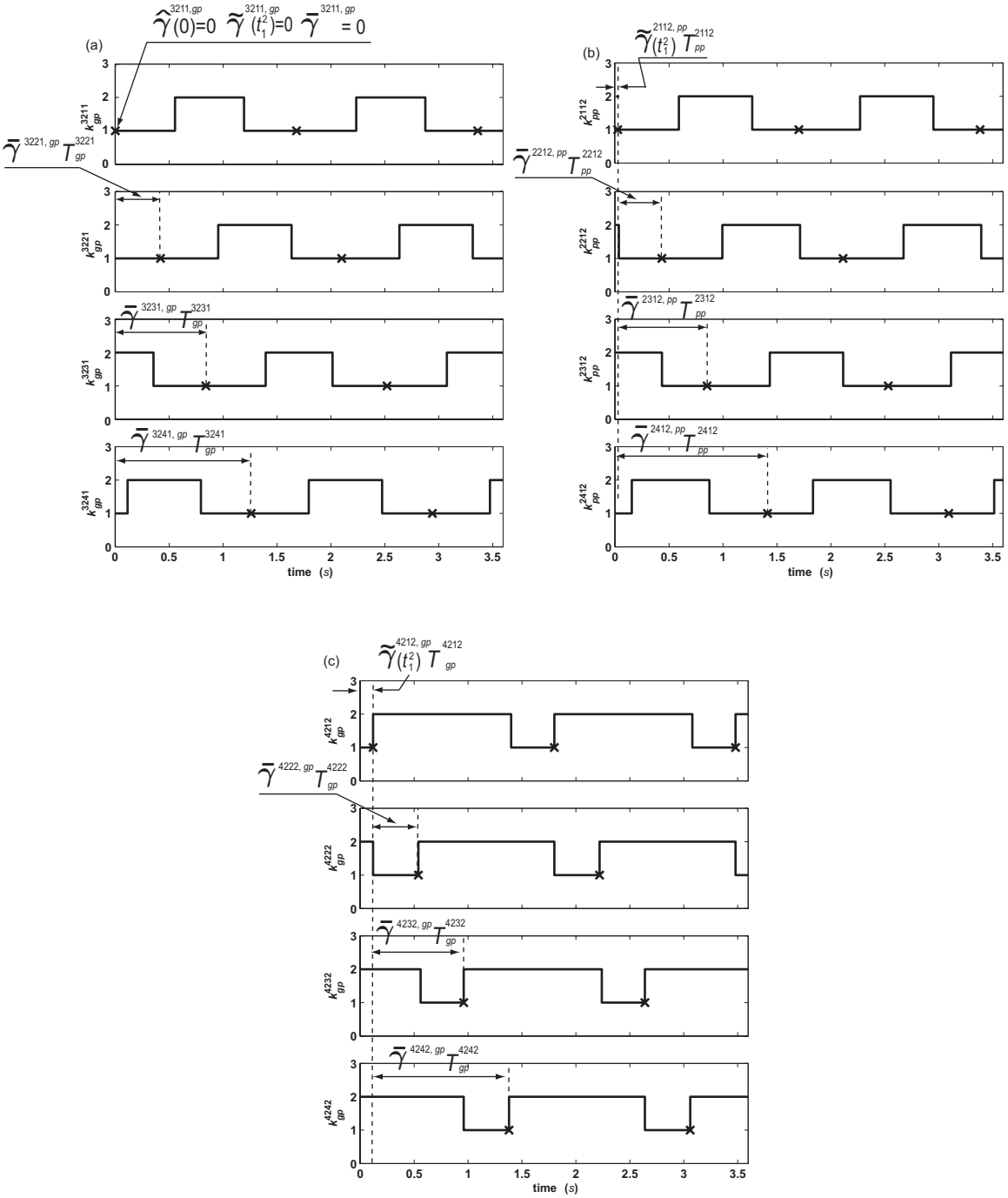

Figure 5.4: Mesh tooth variation functions of the gear meshes in stage 2 of the example system with the related relative phases marked. The symbol × denotes the time when the pitch point of the associated gear mesh is in contact.

With all the system-level relative phases calculated, analytical expressions for the mesh tooth (or mesh stiffness or static transmission error) variations of all gear meshes in the system are determined by applying equation (5.3) after straightforward calculation of $\kappa(\tau)$ for each gear pair based on basic gear geometry [77] or gear design software.

For example, the Fourier series expansion of the mesh tooth variation function for the gear mesh between the ring gear and planet 2 in train 2 of stage 2 is (the pitch point is in contact when $\tau = 0$)

$$\begin{aligned} \kappa_{gp}^{4222}(\tau) &= \sum_{u=0}^{\infty} \left[e_u \sin u\omega_{gp}^{4222}\tau + f_u \cos u\omega_{gp}^{4222}\tau \right] \\ &= \sum_{u=0}^{\infty} \left[e_u \sin u3.75\tau + f_u \cos u3.75\tau \right] \end{aligned} \tag{5.32}$$

Application of (5.3) with $\hat{\gamma}^{4222,gp}(0) = 0.263$ from Table 5.7 yields the analytical expression of the mesh tooth variation function for k_{gp}^{4222} as a function of absolute time, which is

$$k_{gp}^{4222}(t) = \sum_{u=0}^{\infty} \left[e_u \sin u3.75(t - 0.441) + f_u \cos u3.75(t - 0.441) \right] \tag{5.33}$$

The mesh tooth variation functions such as equation (5.33) are critical to study any feature of the example system's static or dynamic response that involves mesh tooth, mesh stiffness, or static transmission error variations.

5.5 Conclusions

Knowledge of all mesh phase relationships is essential for analytical or multibody computational study of compound planetary gear mechanics because the critically important mesh tooth, mesh stiffness, or static transmission error variation functions typically used in gear mechanics analysis rely on proper description of the relative

phases between all of the gear meshes. This study defines and calculates all the mesh phases for general compound planetary gears, including those with any combination of multiple mesh frequencies, multiple stages, meshed planets, and stepped planets. In addition to organizing these mesh phases into a hierarchical structure of system-level, stage-level, and train-level mesh phases to simplify the analysis, this study derives a complete and simple (other than the notation) procedure to determine all the necessary relative phases. The specific relationships between train-level relative phases that are critical for any analytical study on the suppression of compound planetary gear dynamic response through mesh phasing are derived by applying the assembly conditions of compound planetary gears. All derived results are verified through an example, where the numerical benchmark is geometrically exact and the only error is a quantifiable mesh cycle discretization error.

Chapter 6: SUPPRESSION OF VARIOUS MODAL RESPONSES IN GENERAL COMPOUND PLANETARY GEARS THROUGH MESH PHASING

6.1 Introduction

Noise and vibration problems remain major concerns for compound planetary gears [47, 53]. When planetary gears operate at speeds where the mesh frequency or an integer multiple of it is near one of the system natural frequencies, large dynamic tooth loads and loud noise are generated due to the resonant response, reducing the life of the whole transmission system. Proper design of mesh phasing by adjusting certain fundamental design parameters, such as the gear tooth number and number of planets, is able to eliminate selected resonant responses in the operating range of the system [5, 32, 75, 77].

Studies on the suppression of dynamic response through mesh phasing trace back to Schlegel and Mard's experimental measurements on the effectiveness of planet phasing on noise reduction [86] and Seager's detailed analysis using a static transmission error model [87]. Later, Palmer and Fuehrer [74], Hidaka et al. [41], Platt and Leopold [83], Kahraman [43], and Kahraman and Blankenship [48] experimentally or numerically illustrated the effectiveness of simple planetary gears mesh phasing to reduce noise and vibrations in transmission systems. Parker and Lin developed

a rotational-translational lumped-parameter model and discovered the unique vibration properties [56], identified the specific mesh phase relations [77], and analytically explained the effectiveness of planet mesh phasing to suppress certain translational and rotational mode responses [75]. The results in [75] show that the symmetry-based rules even hold when nonlinear tooth contact occurs, provided the response retains the symmetry of system geometry. Filling a gap in [75], Ambarisha and Parker [5] provided the analytical explanation for the suppression of planet mode responses in the rotational-translational model through mesh phasing and derived the rules to suppress degenerate mode responses in purely rotational planetary gear models. All these studies, however, are restricted to simple planetary gears. No published literature has examined the suppression of compound planetary gear vibration modes through mesh phasing numerically or analytically. The questions of whether the mesh phasing rules of simple planetary gears in [5, 75] can be applied to general compound planetary gears and what are the impacts of meshed-planet, stepped-planet, and multi-stage structures that are unique to compound planetary gears on the rules to suppress dynamic responses through mesh phasing are addressed in this work.

Recent progresses on compound planetary gear dynamics provide bases for this investigation. Kahraman [47] developed a purely rotational model for limited configurations of single-stage planetary gears. Kiracofe and Parker [53] developed a rotational-translational model for general compound planetary gears and proved that all the vibration modes of compound planetary gears are classified as rotational, translational, and planet modes, each having distinct properties. Guo and Parker [35] set up a purely rotational model for general compound planetary gears and analytically proved its modal properties. Guo and Parker [32] systematically defines the relative

phases in general compound planetary gears and analytically derives the mesh phase relations for all the gear meshes in the system.

This chapter utilizes the above research results on compound planetary gears to analytically examine the general rules to suppress certain dynamic responses and resonances of general compound planetary gears through planet mesh phasing for both purely rotational and rotational-translational models. Because the analytical process to derive the rules is based on the symmetry of each planet set and the periodicity of gear tooth meshes without explicit modeling of the dynamic mesh forces or system responses, the results are independent of any choice of dynamic gear mesh force model.

6.2 Rules to Suppress Selected Dynamic Responses for Rotational-translational Models

Resonance associated with a natural frequency ω_n, in general, is potentially excited when the μth harmonic of the fundamental frequency of an excitation source ω satisfies $\mu\omega = \omega_n$ in any mechanical system. For planetary gears, mesh stiffness variations with fundamental frequency being their mesh frequencies are the excitation sources. Previous studies on simple planetary gears [5, 75] show that resonances occur at some of the mesh frequency harmonics and are absent at others, and such excitation and suppression of responses at mesh frequency harmonics follow the rules that are determined by mesh phases and modal properties. Because compound planetary gears have similar modal properties as simple planetary gears and the mesh phases are systematically defined in previous chapter, it is expected that there exist certain mesh phasing rules in compound planetary gears. The main task of this investigation is to analytically derive these rules.

The structured modal properties for the rotational-translational model of general compound planetary gears [53] suggest that any vibration mode can be classified as rotational, translational, and planet modes. In rotational modes, all central gears and carriers (i.e., central components) have rotational motions only. Therefore, in the case of a rotational mode excitation, all central components only have rotational vibrations that are caused by non-zero net torques acting on these components. These non-zero net torques are the results of gear mesh forces or planet bearing forces. Once these net excitation torques (i.e, net torques) vanish, central gears and carriers no longer have rotational vibrations and this rotational mode response (i.e., rotational response) is suppressed. The net torques, hence, become the direct measurements for the excitation or suppression of rotational responses. In a similar manner, the net excitation forces (i.e., net forces) acting on central components are the direct indications for the suppression of translational mode responses (i.e., translational responses). Such criteria to determine the suppression of potentially-excited translational or rotational resonances by analyzing the net force or torque cancellation on central gears and carriers are validated in the study by Parker [75].

Due to the unique modal properties for planet modes, the net forces/torques on central components are zero in all planet modes [53]. The suppression/excitation of planet mode responses (i.e., planet responses), hence, can not be determined by evaluating the net forces or torques acting on central components. Ambarisha and Parker [5] proposed a method to analytically determine the suppression/excitation of planet responses for simple planetary gears by evaluating *the modal forces for planet modes* (i.e., planet modal forces). This study extends their method to compound planetary gears as follows. Let $\boldsymbol{\phi}_v$ be a planet mode for planet set i and the associated

planet frequency is ω_v. Multiplying the equation of motion for general compound planetary gear in (2.38) with $\boldsymbol{\phi}_v^T$ on the left and insertion of $\boldsymbol{\phi}(t) = \sum_{u=1}^{\Lambda} \varsigma_u(t)\boldsymbol{\phi}_u$ yield

$$\ddot{\varsigma}_v(t) + \boldsymbol{\phi}_v^T \mathbf{K} \sum_{u=1}^{\Lambda} \varsigma_u(t)\boldsymbol{\phi}_u = \ddot{\varsigma}_v(t) + \boldsymbol{\phi}_v^T \mathbf{f}(\boldsymbol{\phi}(t), t) = \boldsymbol{\phi}_v^T \mathbf{F}(t) \tag{6.1}$$

where ς_u is the modal coordinate for mode u. Similar to [5], $\mathbf{f}(\boldsymbol{\phi}(t), t)$ is used to denote $\mathbf{K} \sum_{u=1}^{\Lambda} \varsigma_u(t)\boldsymbol{\phi}_u$ in this study and it collects the forces caused by gear meshes, shaft connections, and bearing supports in equation (2.38). The term $\boldsymbol{\phi}_v^T \mathbf{F}(t)$ is equal to zero because of the modal property that all central components have no motion in any planet mode. The suppression of planet mode v, hence, solely depends on the vanishing of $\boldsymbol{\phi}_v^T \mathbf{f}(\boldsymbol{\phi}(t), t)$ which is denoted as

$$Q_v(t) = \boldsymbol{\phi}_v^T \mathbf{f}(\boldsymbol{\phi}(t), t) \tag{6.2}$$

where $Q_v(t)$ is the planet modal force for planet mode v) in this study.

Table 6.1 summarizes the above general criteria to suppress different types of responses in compound planetary gears.

Table 6.1: The general criteria to suppress different types of responses in general compound planetary gears. Ξ, F, and Q represent net force, net torque, and planet modal force, respectively.

Responses Types	Suppression and Excitation Criteria
Rotational Response	Excitation: $\Xi \neq 0$, Suppression: $\Xi = 0$
Translational Response	Excitation: $F \neq 0$, Suppression: $F = 0$
Planet Response	Excitation: $Q \neq 0$, Suppression: $Q = 0$

For multi-stage compound planetary gear systems, the excitation forces in each stage are transmitted throughout the system via the connections between stages. The whole system is considered to be excited if any stage of the system is excited.

The rules to suppress dynamic responses of a multi-stage system are actually the sum up of the rules from each stage. Thus, breaking the multi-stage system down into separate stages and analyzing the suppression/excitation criteria in each stage is an effective way to investigate multi-stage systems. This study, hence, focuses on a single compound planetary gear stage having one or both of meshed-planet and stepped-planet structures [32, 53]. For a single compound planetary gear stage, there are two possible cases: (a) a stage has meshed-planet structures only (i.e., meshed-planet stage), and (b) a stage has a stepped planet structure in each train and may also involve meshed-planet structures (i.e., stepped stage). The following study investigates the suppression or excitation of selected responses for both cases using the criteria in Table 6.1.

6.2.1 Suppression of Selected Responses in a Meshed-planet Stage through Mesh Phasing

An arbitrary planetary stage, numbered as stage 1, has c^1 ($c^1 \geq 3$) equally-spaced planet trains. Each planet train includes d^1 planets. These d^1 planets in each planet train have only meshed-planet structures. All planet trains are numbered from train 1 to train c^1 in the counterclockwise direction. The planet in each train that is in mesh with the sun gear is numbered as planet 1, and the planet in mesh with planet 1 is numbered as planet 2. The numbering continuous until planet d^1, which is the planet in mesh with the ring gear in each train (Figure 6.1). Same as simple planetary gears, meshed-planet stages have a single mesh frequency ω. The key stipulation to use Table 6.1 to derive the rules to suppress the selected responses through mesh phasing is that the net torques (Ξ), the net forces (F), and the planet modal forces (Q) are periodic functions with the fundamental frequency equal to the

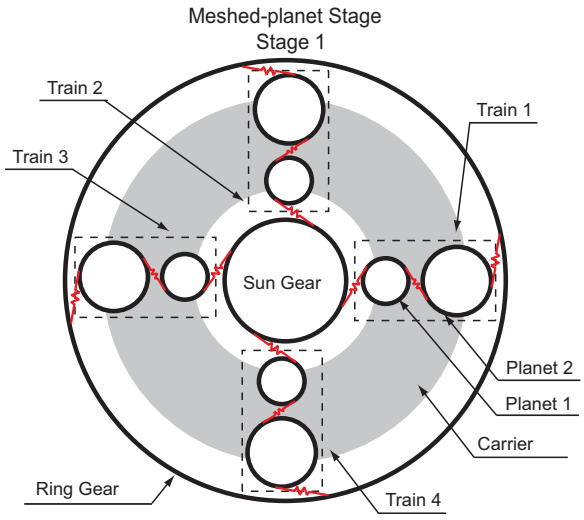

Figure 6.1: A meshed-planet stage has four planet trains. Each planet train has two planets that are in mesh with each other.

mesh frequency $\omega = \frac{1}{T}$ (T is the mesh period). Such physically plausible stipulation is consistent with the periodic mesh contact at mesh frequency and it was confirmed to be necessary for the validation of mesh phasing rules in studies on the simple planetary gear dynamics [5, 9, 34, 61, 75, 98]. This assumption implies that the rules that are derived in this study are not valid in cases of transient responses, nonlinear responses that contain sub/super-harmonic components, and vibrations driven by parametric fluctuations that are locked at the natural period [23].

Cancellation of Net Force and Torque on Central Components

The net force acting on a central component is essentially the sum of the related gear mesh forces. Taking the sun gear in a meshed-planet stage as the representative example, the sun-planet gear mesh forces are the only excitation forces acting on the sun gear. Due to cyclic symmetry, the sun-planet mesh forces in the same stage have

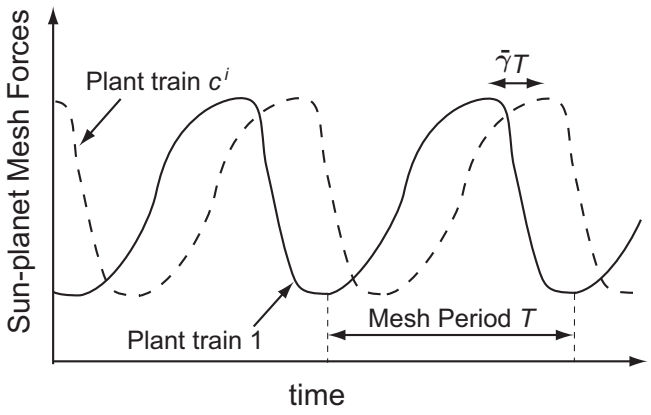

Figure 6.2: Sun-planet mesh force fluctuation showing the mesh period T and the relative phase $\bar{\gamma}$ at two arbitrarily chosen planet trains.

the same shape but differ in phases [23, 37, 75] (as shown in Figure 6.2). According to the definition of compound planetary gear mesh phases [37], the phases between sun-planet gear meshes in the same stage are train-level relative phases which are determined in Table 5.1. Without losing generality, the mesh force between the sun gear (central gear s) and planet 1 in train l of this stage (stage 1) $\mathbf{F}^{s1l1}$ is

$$\mathbf{F}^{s1l1} = F_{\xi}^{s1l1}\boldsymbol{\xi}^{1l1} + F_{\eta}^{s1l1}\boldsymbol{\eta}^{1l1} \tag{6.3}$$

where $\boldsymbol{\xi}^{1l1}$ and $\boldsymbol{\eta}^{1l1}$ are unit vectors that define the radial and tangential coordinates for planet 1 in train l of stage 1 and they retain the fixed angular separation $\hat{\psi}^{1l}$ from the carrier 1 fixed basis $\{\mathbf{i},\ \mathbf{j}\}$. Transforming the coordinate basis in (6.3)to $\{\mathbf{i},\ \mathbf{j}\}$ gives

$$\mathbf{F}^{s1l1} = \left(F_{\xi}^{s1l1}\cos\hat{\psi}^{1l} - F_{\eta}^{s1l1}\sin\hat{\psi}^{1l}\right)\mathbf{i} + \left(F_{\xi}^{s1l1}\sin\hat{\psi}^{1l} + F_{\eta}^{s1l1}\cos\hat{\psi}^{1l}\right)\mathbf{j} \tag{6.4}$$

F_{ξ}^{s1l1} and F_{η}^{s1l1} are the periodic mesh forces between the sun gear and planet 1 in train l in $\boldsymbol{\xi}$ and $\boldsymbol{\eta}$ directions and the relationship between them and the associated

mesh forces in train 1 is

$$\begin{aligned} F_{\xi}^{s1l1}(\omega t) &= F_{\xi}^{s111}(\omega t - 2\pi\bar{\gamma}^{s1l1,gp}) \\ F_{\eta}^{s1l1}(\omega t) &= F_{\eta}^{s111}(\omega t - 2\pi\bar{\gamma}^{s1l1,gp}) \end{aligned} \tag{6.5}$$

where $\bar{\gamma}^{s1l1,gp}$ is the train-level sun-planet relative phase between train l and train 1 and it is (refer to Table 5.1)

$$\bar{\gamma}^{s1l1,gp} = \pm dec\left(\frac{Z_g^s\hat{\psi}^{1l}}{2\pi}\right) \tag{6.6}$$

where the sign is determined by the positiveness of $(\theta_g^s\text{-}\theta_c^1)$. Let the Fourier series expansion for F_{ξ}^{s111} and F_{η}^{s111} be

$$\begin{aligned} F_{\xi}^{s111}(\omega t) &= \sum_{\mu=0}^{\infty}\left[e_{\mu}^{s111}\sin(\mu\omega t) + g_{\mu}^{s111}\cos(\mu\omega t)\right] \\ F_{\eta}^{s111}(\omega t) &= \sum_{\mu=0}^{\infty}\left[h_{\mu}^{s111}\sin(\mu\omega t) + j_{\mu}^{s111}\cos(\mu\omega t)\right] \end{aligned} \tag{6.7}$$

Insertion of (6.6) and (6.7) into (6.5) yields

$$\begin{aligned} F_{\xi}^{s1l1}(\omega t) &= \sum_{\mu=0}^{\infty}\left[e_{\mu}^{s111}\sin\mu\left(\omega t - 2\pi\bar{\gamma}^{s1l1,gp}\right) + g_{\mu}^{s111}\cos\mu\left(\omega t - 2\pi\bar{\gamma}^{s1l1,gp}\right)\right] = \sum_{\mu=0}^{\infty}F_{\xi,\mu}^{s1l1} \\ F_{\eta}^{s1l1}(\omega t) &= \sum_{\mu=0}^{\infty}\left[h_{\mu}^{s111}\sin\mu\left(\omega t - 2\pi\bar{\gamma}^{s1l1,gp}\right) + j_{\mu}^{s111}\cos\mu\left(\omega t - 2\pi\bar{\gamma}^{s1l1,gp}\right)\right] = \sum_{\mu=0}^{\infty}F_{\eta,\mu}^{s1l1} \end{aligned} \tag{6.8}$$

where $F_{\xi,\mu}^{s1l1} = e_{\mu}^{s111}\sin\mu\left(\omega t - 2\pi\bar{\gamma}^{s1l1,gp}\right) + g_{\mu}^{s111}\cos\mu\left(\omega t - 2\pi\bar{\gamma}^{s1l1,gp}\right)$ and $F_{\eta,\mu}^{s1l1} = h_{\mu}^{s111}\sin\mu\left(\omega t - 2\pi\bar{\gamma}^{s1l1,gp}\right) + j_{\mu}^{s111}\cos\mu\left(\omega t - 2\pi\bar{\gamma}^{s1l1,gp}\right)$ are the mesh forces between the sun gear and planet 1 in train l in $\boldsymbol{\xi}$ and $\boldsymbol{\eta}$ directions at the μth harmonic of mesh frequency. Summing up the sun-planet mesh forces (equation (6.4)) in all the trains

and insertion of (6.8) yield the net force acting on the sun gear (central gear s) as

$$\begin{aligned}
\mathbf{F}^{s1*1} &= \sum_{l=1}^{c^1} \mathbf{F}^{s1l1} \\
&= \sum_{l=1}^{c^1} \left[\left(F_{\xi}^{s1l1} \cos\hat{\psi}^{1l} - F_{\eta}^{s1l1} \sin\hat{\psi}^{1l} \right) \mathbf{i} + \left(F_{\xi}^{s1l1} \sin\hat{\psi}^{1l} + F_{\eta}^{s1l1} \cos\hat{\psi}^{1l} \right) \mathbf{j} \right] \\
&= \mathbf{i} \sum_{\mu=0}^{\infty} \sum_{l=1}^{c^1} \left(F_{\xi,\mu}^{s1l1} \cos\hat{\psi}^{1l} - F_{\eta,\mu}^{s1l1} \sin\hat{\psi}^{1l} \right) + \mathbf{j} \sum_{\mu=0}^{\infty} \sum_{l=1}^{c^1} \left(F_{\xi,\mu}^{s1l1} \sin\hat{\psi}^{1l} + F_{\eta,\mu}^{s1l1} \cos\hat{\psi}^{1l} \right) \\
&= \sum_{\mu=0}^{\infty} \mathbf{F}_{\mu}^{s1*1}
\end{aligned} \tag{6.9}$$

Once the four terms $\sum_{l=1}^{c^1} \left(F_{\xi,\mu}^{s1l1} \cos\hat{\psi}^{1l} \right)$, $\sum_{l=1}^{c^1} \left(F_{\xi,\mu}^{s1l1} \sin\hat{\psi}^{1l} \right)$, $\sum_{l=1}^{c^1} \left(F_{\eta,\mu}^{s1l1} \cos\hat{\psi}^{1l} \right)$, and $\sum_{l=1}^{c^1} \left(F_{\eta,\mu}^{s1l1} \sin\hat{\psi}^{1l} \right)$ in (6.9) are all equal to zero, $\mathbf{F}_{\mu}^{s1*1}$, the net force acting on the sun gear at μth harmonic of mesh frequency, vanishes and the associated translational responses are suppressed. In the rest part of this section, the condition to make these four terms be zero is first investigated.

When θ_g^s-$\theta_c^1 > 0$, insertion of equation (6.6) into the first term $\sum_{l=1}^{c^1} \left(F_{\xi,\mu}^{s1l1} \cos\psi^{1l1} \right)$ and application of $\sin(dec(\alpha)) = \sin\alpha$, the property of the operator $dec(\ )$, yield

$$\begin{aligned}
&\sum_{l=1}^{c^1} \left(F_{\xi,\mu}^{s1l1} \cos\hat{\psi}^{1l} \right) \\
&= \sum_{l=1}^{c^1} \left[e_{\mu}^{s111} \sin\mu \left(\omega t - 2\pi\bar{\gamma}^{s1l1,gp} \right) + g_{\mu}^{s111} \cos\mu \left(\omega t - 2\pi\bar{\gamma}^{s1l1,gp} \right) \right] \cos\hat{\psi}^{1l} \\
&= \sum_{l=1}^{c^1} \left[e_{\mu}^{s111} \sin\mu \left(\omega t - Z_g^s \hat{\psi}^{1l} \right) + g_{\mu}^{s111} \cos\mu \left(\omega t - Z_g^s \hat{\psi}^{1l} \right) \right] \cos\hat{\psi}^{1l}
\end{aligned} \tag{6.10}$$

Equally-spaced planet trains give

$$\hat{\psi}^{1l} = \frac{2\pi(l-1)}{c^1} \tag{6.11}$$

Insertion of (6.11) into (6.10) and application of the trigonometric identities yield

$$\begin{aligned}
&\sum_{l=1}^{c^1}\left(F_{\xi,\mu}^{s1l1}\cos\hat{\psi}^{1l}\right)\\
&=\sum_{l=1}^{c^1}\left[e_{\mu}^{s111}\sin\left(\mu\omega t-\frac{2\pi\mu Z_g^s(l-1)}{c^1}\right)\cos\frac{2\pi(l-1)}{c^1}+\right.\\
&\quad\left.g_{\mu}^{s111}\cos\left(\mu\omega t-\frac{2\pi\mu Z_g^s(l-1)}{c^1}\right)\cos\frac{2\pi(l-1)}{c^1}\right]\\
&=e_{\mu}^{s111}\sin\mu\omega t\sum_{l=1}^{c^1}\left[\cos\frac{2\pi\mu Z_g^s(l-1)}{c^1}\cos\frac{2\pi(l-1)}{c^1}\right]-\\
&\quad e_{\mu}^{s111}\cos\mu\omega t\sum_{l=1}^{c^1}\left[\sin\frac{2\pi\mu Z_g^s(l-1)}{c^1}\cos\frac{2\pi(l-1)}{c^1}\right]+\\
&\quad g_{\mu}^{s111}\cos\mu\omega t\sum_{l=1}^{c^1}\left[\cos\frac{2\pi\mu Z_g^s(l-1)}{c^1}\cos\frac{2\pi(l-1)}{c^1}\right]+\\
&\quad g_{\mu}^{s111}\sin\mu\omega t\sum_{l=1}^{c^1}\left[\sin\frac{2\pi\mu Z_g^s(l-1)}{c^1}\cos\frac{2\pi(l-1)}{c^1}\right]
\end{aligned}\tag{6.12}$$

Similar to [5, 75], the phasing quantity k_μ is introduced as

$$k_\mu = mod\left(\frac{\mu Z_g^s}{c^1}\right)\tag{6.13}$$

where $mod(\frac{a}{b})$ yields the integer reminder of the integer division between a and b when $\frac{a}{b}$ is positive and outputs b plus the integer reminder of $\frac{a}{b}$ when the input argument is negative (for instance, $mod(\frac{-66}{5}) = 5 + (-1) = 4$). Insertion of (6.13) into the first

two terms in (6.12) and use of the trigonometric identities give

$$\begin{aligned}
&e_\mu^{s111}\sin\mu\omega t\sum_{l=1}^{c^1}\left[\cos\frac{2\pi\mu Z_g^s(l-1)}{c^1}\cos\frac{2\pi(l-1)}{c^1}\right]- \\
&\quad e_\mu^{s111}\cos\mu\omega t\sum_{l=1}^{c^1}\left[\sin\frac{2\pi\mu Z_g^s(l-1)}{c^1}\cos\frac{2\pi(l-1)}{c^1}\right] \\
&=\frac{e_\mu^{s111}\sin\mu\omega t}{2}\sum_{l=1}^{c^1}\left[\cos\frac{2\pi(k_\mu-1)(l-1)}{c^1}+\cos\frac{2\pi(k_\mu+1)(l-1)}{c^1}\right]- \\
&\quad\frac{e_\mu^{s111}\cos\mu\omega t}{2}\sum_{l=1}^{c^1}\left[\sin\frac{2\pi(k_\mu-1)(l-1)}{c^1}+\sin\frac{2\pi(k_\mu+1)(l-1)}{c^1}\right]
\end{aligned} \tag{6.14}$$

For an arbitrary integer k, the trigonometric identities that are necessary to simplify (6.14) are

$$\begin{aligned}
&\sum_{l=1}^{c^1}\sin\left[\tfrac{2\pi(l-1)k}{c^1}\right]=0 \\
&\sum_{l=1}^{c^1}\cos\left[\tfrac{2\pi(l-1)k}{c^1}\right]=\begin{cases}0, & k/c^1\neq\text{integer}\\ c^1, & k/c^1=\text{integer}\end{cases}
\end{aligned} \tag{6.15}$$

Application of (6.15) to (6.14) gives that the first two terms in (6.12) becomes zero when $k_\mu\neq 1,\ c^1-1$ and it is the same for other terms in (6.12). $\sum_{l=1}^{c^1}\left(F_{\xi,\mu}^{s1l1}\cos\hat{\psi}^{1l}\right)$, hence, is equal to zero when $k_\mu\neq 1,\ c^1-1$. Following the same procedure, $\sum_{l=1}^{c^1}\left(F_{\xi,\mu}^{s1l1}\sin\hat{\psi}^{1l}\right)$, $\sum_{l=1}^{c^1}\left(F_{\eta,\mu}^{s1l1}\cos\hat{\psi}^{1l}\right)$, and $\sum_{l=1}^{c^1}\left(F_{\eta,\mu}^{s1l1}\sin\hat{\psi}^{1l}\right)$ in (6.9) are found to be vanished when $k_\mu\neq 1,\ c^1-1$. When θ_g^s-$\theta_c^1<0$, replacing $\bar{\gamma}^{s1l1,gp}$ with $-dec\left(\frac{Z_g^s\hat{\psi}^{1l}}{2\pi}\right)$ in the above process yields the same result. Therefore, $\mathbf{F}_\mu^{s1*1}$ is canceled out when $k_\mu\neq 1,\ c^1-1$ and the associated translational responses of the sun gear at μth harmonic of mesh frequency are suppressed.

The net torque acting on the sun gear is the sum of torques that are caused by the sun-planet mesh forces in the tangential direction $\boldsymbol{\eta}$ and it is

$$\begin{aligned}
\Xi^{s1*1} &= r_g^s \sum_{l=1}^{c^1} F_\eta^{s1l1} \\
&= r_g^s \sum_{l=1}^{c^1} \sum_{\mu=0}^{\infty} F_{\eta,\mu}^{s1l1} \\
&= r_g^s \sum_{\mu=0}^{\infty} \sum_{l=1}^{c^1} \left[h_\mu^{s111} \sin\mu\left(\omega t - 2\pi\bar{\gamma}^{s1l1,gp}\right) + j_\mu^{s111} \cos\mu\left(\omega t - 2\pi\bar{\gamma}^{s1l1,gp}\right) \right] \\
&= \sum_{\mu=0}^{\infty} \Xi_\mu^{s1*1}
\end{aligned} \tag{6.16}$$

where $\Xi_\mu^{s1*1} = r_g^s \sum_{l=1}^{c^1} \left[h_\mu^{s111} \sin\mu\left(\omega t - 2\pi\bar{\gamma}^{s1l1,gp}\right) + j_\mu^{s111} \cos\mu\left(\omega t - 2\pi\bar{\gamma}^{s1l1,gp}\right) \right]$ is the net torque acting on the sun gear at μth mesh frequency. Insertion of (6.6), (6.11), and (6.13) into the expression of Ξ_μ^{s1*1} and application of the trigonometric identities yield

$$\begin{aligned}
\Xi_\mu^{s1*1} &= r_g^s h_\mu^{s111} \sum_{l=1}^{c^1} \sin\left(\mu\omega t \pm \mu\hat{\psi}^{1l} Z_g^s\right) + r_g^s j_\mu^{s111} \sum_{l=1}^{c^1} \cos\left(\mu\omega t \pm \mu\hat{\psi}^{1l} Z_g^s\right) \\
&= r_g^s \sin\mu\omega t \left[h_\mu^{s111} \sum_{l=1}^{c^1} \cos\frac{2\pi(l-1)k_\mu}{c^1} \mp j_\mu^{s111} \sum_{l=1}^{c^1} \sin\frac{2\pi(l-1)k_\mu}{c^1} \right] \\
&\quad + r_g^s \cos\mu\omega t \left[\pm h_\mu^{s111} \sum_{l=1}^{c^1} \sin\frac{2\pi(l-1)k_\mu}{c^1} + j_\mu^{s111} \sum_{l=1}^{c^1} \cos\frac{2\pi(l-1)k_\mu}{c^1} \right]
\end{aligned} \tag{6.17}$$

where the $\pm$ sign of $\mu\hat{\psi}^{1l} Z_g^s$ comes from $\bar{\gamma}^{s1l1,gp}$ and it is determined by the positiveness of $\theta_g^s - \theta_c^1$ (Table 5.1).

Direct application of the trigonometric identities in (6.15) to (6.17) yields the relationship between Ξ_μ^{s1*1} and the phasing quantity k_μ as

$$\begin{aligned}
\Xi_\mu^{s1*1} &\neq 0, \quad k_\mu = 0 \\
\Xi_\mu^{s1*1} &= 0, \quad k_\mu \neq 0
\end{aligned} \tag{6.18}$$

Equation (6.18) reveals that the net torque acting on the sun gear at μth harmonic of mesh frequency vanishes and the associated rotational response of the sun gear is suppressed when the phasing quantity $k_\mu \neq 0$.

The net force and torque acting on other central components, the ring and the carrier, follow exactly the same rule as that for the sun gear to vanish at μth harmonic of mesh frequency. One strong argument from [5] is that the absence of any net force on the sun in the μth harmonic implies there is no sun translation and thus no response in any translational modes at this harmonic. Because translational modes are the only modes involving the translation motions of the ring or carrier, at the μth harmonic of mesh frequency the translational motions for both ring and carrier are suppressed. This implies that the μth harmonic of the net forces on these components vanish. Similar arguments based on rotational modal properties hold for the net torque cancellations of the ring and carrier.

Another way to determine the net force or torque cancellation rules for the ring gear is to apply the above analytical process to the ring gear with the exception that the sun-planet mesh phase $\bar{\gamma}^{s1l1,gp}$ should be replaced by the ring-planet mesh phase $\bar{\gamma}^{r1ld^1,gp}$. The train-level relative phase relations for meshed-planet stages in (5.22) indicate that $\bar{\gamma}^{r1ld^1,gp}$ is equal to $\bar{\gamma}^{s1l1,gp}$. The net force and torque cancellation condition for the ring gear, hence, is the same as that for the sun gear.

Because the gear mesh forces do not act on the carrier directly, the excitation forces for the carrier in a meshed-planet stage are different from those for the sun and ring and the above analytical procedure cannot be applied to carrier directly. Free body diagram analysis on the carrier indicates that the reaction forces of the planet bearing forces for the entire planet set are the excitation sources for the carrier, and the same

analysis on a single planet shows that the planet bearing force is associated with not only sun-planet and ring-planet mesh forces but also planet-planet mesh forces. Previous studies on planetary gears [5, 6, 34, 75, 90] indicate that it is reasonable to assume that the bearing force for a planet is periodic and the harmonic contents of the bearing forces are dominated by the mesh forces involving this planet. The net force and torque acting on the carrier, hence, retain the harmonic structures (i.e., mesh periods and relative phases) of the sun-planet, ring-planet, and planet-planet mesh forces. Replacing the harmonic structure associated with sun-planet mesh forces in equations (6.3)-(6.14) with the harmonic structure that sum up sun-planet, ring-planet, and planet-planet mesh forces and applying the mesh phase relations that all the train-level mesh phases are equal to each other along the same train in a meshed-planet stage (as show in equation (5.22)) produce the result that the μth harmonic of net force and torque acting on the carrier vanish in the same way as that for the sun gear.

Cancellation of Planet Modal Forces

Let mode $\boldsymbol{\phi}_v$ be a planet mode for stage 1. As introduced in the beginning of this section, the suppression of this planet mode at μth harmonic of mesh frequency depends on the vanishing of the planet modal force $Q_v(t) = \boldsymbol{\phi}_v^T \mathbf{f}(\boldsymbol{\phi}(t), t)$. $\mathbf{f}_{ps}^{\mathrm{j}}(\boldsymbol{\phi}(t), t)$ collects the elements of $\mathbf{f}(\boldsymbol{\phi}(t), t)$ in equation (6.1) that are associated with planet set 1 and it is

$$\begin{aligned}
\mathbf{f}_{ps}^{\mathrm{l}}(\boldsymbol{\phi}(t), t) &= \left[\mathbf{f}_{pt}^{\mathrm{l}1}(\boldsymbol{\phi}(t), t), \ \cdots, \ \mathbf{f}_{pt}^{\mathrm{l}c^1}(\boldsymbol{\phi}(t), t)\right]^T \\
\mathbf{f}_{pt}^{\mathrm{l}l}(\boldsymbol{\phi}(t), t) &= \left[\mathbf{f}_{p}^{\mathrm{l}l1}(\boldsymbol{\phi}(t), t), \ \cdots, \ \mathbf{f}_{p}^{\mathrm{l}ld^1}(\boldsymbol{\phi}(t), t)\right]^T \\
\mathbf{f}_{p}^{\mathrm{l}lm}(\boldsymbol{\phi}(t), t) &= \left[f_{\zeta}^{\mathrm{l}lm}(\boldsymbol{\phi}(t), t), \ f_{\eta}^{\mathrm{l}lm}(\boldsymbol{\phi}(t), t), \ f_{\theta}^{\mathrm{l}lm}(\boldsymbol{\phi}(t), t)\right]^T
\end{aligned} \tag{6.19}$$

where $m = 1, \ \cdots, \ d^1$.

Insertion of the planet modal properties in (2.48)-(2.51) and equation (6.19) into the expression of the modal force Q_v give

$$\begin{aligned} Q_v &= \sum_{l=1}^{c^1} w^l \left(\boldsymbol{\phi}_{pt,v}^{1l}\right)^T \mathbf{f}_{pt}^{11} \\ &= \underbrace{\sum_{l=1}^{c^1}\sum_{m=1}^{d^1} w^l \zeta_p^{11m} f_\zeta^{1lm}}_{Q^\zeta} + \underbrace{\sum_{l=1}^{c^1}\sum_{m=1}^{d^1} w^l \eta_p^{11m} f_\eta^{1lm}}_{Q^\eta} + \underbrace{\sum_{l=1}^{c^1}\sum_{m=1}^{d^1} w^l u_p^{11m} f_\theta^{1lm}}_{Q^\theta} \end{aligned} \tag{6.20}$$

where w^l is the scalar multiplier that satisfies (2.52). Kiracofe and Parker [53] point out the closed-form solution for w^l is

$$\mathbf{w} = \begin{bmatrix} w^1 \\ w^2 \\ \vdots \\ w^{c^1} \end{bmatrix} = \sum_n \left\{ \sigma_n \begin{bmatrix} \cos(n+1)\hat{\psi}^{11} \\ \cos(n+1)\hat{\psi}^{12} \\ \vdots \\ \cos(n+1)\hat{\psi}^{1c^1} \end{bmatrix} + \upsilon_n \begin{bmatrix} \sin(n+1)\hat{\psi}^{11} \\ \sin(n+1)\hat{\psi}^{12} \\ \vdots \\ \sin(n+1)\hat{\psi}^{1c^1} \end{bmatrix} \right\} \tag{6.21}$$

where σ_n and υ_n are arbitrary constants, and n satisfies

$$n = \begin{cases} 1, 2, \cdots, (c^1-3)/2 & \text{when } c^1 \text{ is odd} \\ 1, 2, \cdots, (c^1-2)/2 & \text{when } c^1 \text{ is even} \end{cases} \tag{6.22}$$

$\boldsymbol{\phi}_{pt,v}^{11} = \left[\zeta_v^{1lm},\ \eta_v^{1lm},\ u_v^{1lm}\right]$ is the motion of planet train 1 in stage 1 of planet mode v, and the dynamic forces $\left[f_\zeta^{1lm},\ f_\eta^{1lm},\ f_\theta^{1lm}\right]^T$ are the resultant of all mesh, shaft, and bearing forces and torques acting on planet m in train l of planet set 1 in the $[\zeta^{1lm},\ \eta^{1lm},\ \theta_p^{1lm}]$ directions (refer to Figure 2.8). Because these dynamic forces are all determined by the same sun-planet, planet-planet, or ring-planet meshes, they have similar structure (periodicity and relative phases between different trains) as the associated mesh forces and the analysis on any one of them is sufficient to capture the general behavior for others [5]. In the rest part of this section, hence, focus on $Q^\zeta = \sum_{l=1}^{c^1}\sum_{m=1}^{d^1} w^l \left[\zeta_p^{11m} f_\zeta^{1lm}\right]$, the first term in (6.20). Depending on the position of the planet in the train (the value of m), the Fourier series expansion of the dynamic

force f_ζ^{1lm} varies. When $m = 1$, f_ζ^{1l1} is impacted by a sun-planet mesh force and a planet-planet mesh force. Its Fourier series expansion, hence, is

$$f_\zeta^{1lm} = \sum_{\mu=1}^{\infty} \Bigg[\underbrace{e_\mu^{s1l1} \sin\mu\left(\omega t - 2\pi\bar{\gamma}^{s1l1,gp}\right) + g_\mu^{s1l1} \cos\mu\left(\omega t - 2\pi\bar{\gamma}^{s1l1,gp}\right)}_{\text{sun-planet mesh}} + \underbrace{h_\mu^{1l12} \sin\mu\left(\omega t - 2\pi\bar{\gamma}^{1l12,pp}\right) + j_\mu^{1l12} \cos\mu\left(\omega t - 2\pi\bar{\gamma}^{1l12,pp}\right)}_{\text{planet-planet mesh}} \Bigg] \tag{6.23}$$

Because all the train-level mesh phases along the same train equal each other in a meshed-planet stage (i.e., $\bar{\gamma}^{s^i il1,gp} = \bar{\gamma}^{r^i ild^i,gp} = \bar{\gamma}^{ilm(m+1),pp}$), replacing $\bar{\gamma}^{s1l1,gp}$ and $\bar{\gamma}^{1l12,pp}$ with $\bar{\gamma}^{1l}$ in equation (6.23) and combining the sine and cosine terms yield

$$f_\zeta^{1l1} = \sum_{\mu=1}^{\infty} \left[E_\mu^{1l1} \sin\mu\left(\omega t - 2\pi\bar{\gamma}^{1l}\right) + G_\mu^{1l1} \cos\mu\left(\omega t - 2\pi\bar{\gamma}^{1l}\right) \right] \tag{6.24}$$

Application of the same procedure to planet m in other positions of train l ($m \neq 1$) yields the general form of f_ζ^{1lm} as

$$f_\zeta^{1lm} = \sum_{\mu=1}^{\infty} \left[E_\mu^{1lm} \sin\mu\left(\omega t - 2\pi\bar{\gamma}^{1l}\right) + G_\mu^{1lm} \cos\mu\left(\omega t - 2\pi\bar{\gamma}^{1l}\right) \right] \tag{6.25}$$

Substitution of (6.25) into the expression of Q^ζ gives

$$\begin{aligned} Q^\zeta &= \sum_{l=1}^{c^1} \sum_{m=1}^{d^1} w^l \zeta_p^{11m} \sum_{\mu=1}^{\infty} \left[E_\mu^{1lm} \sin\mu\left(\omega t - 2\pi\bar{\gamma}^{1l}\right) + G_\mu^{1lm} \cos\mu\left(\omega t - 2\pi\bar{\gamma}^{1l}\right) \right] \\ &= \sum_{\mu=1}^{\infty} \underbrace{\sum_{l=1}^{c^1} \sum_{m=1}^{d^1} w^l \zeta_p^{11m} \left[E_\mu^{1lm} \sin\mu\left(\omega t - 2\pi\bar{\gamma}^{1l}\right) + G_\mu^{1lm} \cos\mu\left(\omega t - 2\pi\bar{\gamma}^{1l}\right) \right]}_{Q_\mu^\zeta} \\ &= \sum_{\mu=1}^{\infty} Q_\mu^\zeta \end{aligned} \tag{6.26}$$

where Q_μ^ζ is the μth harmonic of Q^ζ. Insertion of (6.21) and (6.6) into the expression of Q_μ^ζ gives

$$\begin{aligned} Q_\mu^\zeta =& \sum_{l=1}^{c^1}\sum_{m=1}^{d^1}\sum_n \left[\underbrace{\sigma_n \cos(n+1)\hat{\psi}^{i1}}_{I1} + \underbrace{\upsilon_n \sin(n+1)\hat{\psi}^{i1}}_{I2}\right]\times \\ & \zeta_p^{11m}\left[\underbrace{E_\mu^{1lm}\sin\left(\mu\omega t \pm \mu\hat{\psi}^{1l}Z_g^s\right)}_{I3} + \underbrace{G_\mu^{1lm}\cos\mu\left(\omega t \pm \mu\hat{\psi}^{1l}Z_g^s\right)}_{I4}\right] \\ =& \sum_{l=1}^{c^1}\sum_{m=1}^{d^1}\sum_n \zeta_p^{11m}\left(I_1I_3 + I_1I_4 + I_2I_3 + I_2I_4\right) \end{aligned} \tag{6.27}$$

Substitution of equations (6.11) and (6.13) into the expression of $\sum_{l=1}^{c^1}\sum_{m=1}^{d^1}\sum_n \zeta_p^{11m}I_1I_3$ yields

$$\begin{aligned} &\sum_{l=1}^{c^1}\sum_{m=1}^{d^1}\sum_n \zeta_p^{11m}I_1I_3 = \sum_{l=1}^{c^1}\sum_{m=1}^{d^1}\sum_n \zeta_p^{11m}E_\mu^{1lm}\sigma_n\cos(n+1)\hat{\psi}^{i1}\sin\left(\mu\omega t \pm \mu\hat{\psi}^{1l}Z_g^s\right) \\ &= \sum_{l=1}^{c^1}\sum_{m=1}^{d^1}\sum_n \frac{\zeta_p^{11m}E_\mu^{1lm}\sigma_n}{2}\left\{\sin(\mu\omega t)\left[\cos\frac{2\pi(k_\mu+n+1)(l-1)}{c^1} + \cos\frac{2\pi(k_\mu-n-1)(l-1)}{c^1}\right]\right. \\ &\left.\pm\cos(\mu\omega t)\left[\sin\frac{2\pi(k_\mu+n+1)(l-1)}{c^1} + \sin\frac{2\pi(k_\mu-n-1)(l-1)}{c^1}\right]\right\} \end{aligned} \tag{6.28}$$

Application of (6.15) to (6.28) yields $\sum_{l=1}^{c^1}\sum_{m=1}^{d^1}\sum_n \zeta_p^{11m}I_1I_3 = 0$ if $k_\mu + n + 1 \neq c^1$ and $k_\mu - n - 1 \neq 0$ for each $n = 1,\ \cdots,\ (c^1-3)/2$ when c^1 is odd, or each $n = 1,\ \cdots,\ c^1/2-1$ when c^1 is even. Summarizing the conditions for both even and odd c^1 gives $k_\mu \neq 2,\ \cdots,\ c^1-1$. Application of the same process to $\sum_{l=1}^{c^1}\sum_{m=1}^{d^1}\sum_n \zeta_p^{11m}I_1I_4$, $\sum_{l=1}^{c^1}\sum_{m=1}^{d^1}\sum_n \zeta_p^{11m}I_2I_3$, and $\sum_{l=1}^{c^1}\sum_{m=1}^{d^1}\sum_n \zeta_p^{11m}I_2I_4$ shows that the same condition make these terms be zero as well. Hence, when $k_\mu = 0,\ 1,\ c^1-1$, Q_μ^ζ becomes zero. The same result applies to Q_μ^η and Q_μ^θ, the μth harmonic of the planet modal force in η^{1lm} and θ_p^{1lm} directions. The planet responses at μth harmonic of mesh frequency, hence, are suppressed when $k_\mu = 0,\ 1,\ c^1-1$.

Table 6.2 summarizes the above results for the suppression of different responses in a meshed-planet stage. Because the train-level relative phases along the same train in a meshed-planet stage equal each other, the resultant mesh phasing rules are the same as those for a simple planetary gear in [5, 75] and the planet-planet mesh parameters, such as planet tooth numbers, has no impact on the mesh phasing rules.

Table 6.2: The conditions for the phasing quantity k_μ to suppress different responses in a meshed-planet stage.E indicates the associated responses is excited, and S means that the related responses is suppressed.

k_μ	Cancellations of F, Ξ, and Q	Translational	Rotational	Planet
$k_\mu = 0$	$F = 0,\ \Xi \neq 0,\ Q = 0$	S	E	S
$k_\mu = 1,\ c^1 - 1$	$F \neq 0,\ \Xi = 0,\ Q = 0$	E	S	S
$k_\mu \neq 0,\ 1,\ c^1 - 1$	$F = 0,\ \Xi = 0,\ Q \neq 0$	S	S	E

6.2.2 Suppression of Selected Responses in a Stepped Stage through Mesh Phasing

Different from meshed-planet stages, stepped-planet stages (Figure 6.3) generally have two different mesh frequencies exciting the stage, and the ratio of these two frequencies is determined by the tooth numbers of the two stepped planets. Without losing generality, an arbitrary stepped stage, numbered as stage 1, is studied. The two stepped planets in each train are numbered as $\nu-1$ and ν, where $2 \leq \nu \leq d^i$. The tooth numbers for these two planets are $Z_p^{1l(\nu-1)}$ and $Z_p^{1l\nu}$. Kinematics for stepped stages show that all the gear meshes that involve planets 1 to $\nu - 1$ in each train have the mesh frequency of ω and all other gear meshes have the mesh frequency of

Ω. These two mesh frequencies have the relationship as follows:

$$\Omega = \omega \frac{Z_p^{1l\nu}}{Z_p^{1l(\nu-1)}} \tag{6.29}$$

In the rest of this study, Ω is assumed to be different from ω. Resonances in a stepped stage, hence, are potentially excited when $\mu\omega = \omega_n$ or $\chi\Omega = \omega_n$. The study in previous chapter shows that the stiffness variations for the gear meshes with ω mesh frequency along the same planet train have the same train-level relative phase, and it is the same for gear meshes with Ω mesh frequency. For an arbitrary planet train l, such mesh phase relation is expressed as

$$\begin{aligned}
&\underbrace{\bar{\gamma}^{s1l1,gp}}_{\text{sun}-\text{planet 1 mesh}} = \underbrace{\bar{\gamma}^{1l12,pp}}_{\text{planet 1}-\text{planet 2 mesh}} = \cdots = \underbrace{\bar{\gamma}^{1l(\nu-2)(\nu-1),pp}}_{\text{planet } (\nu-2)-\text{planet } (\nu-1) \text{ mesh}} \\
&\qquad = \bar{\gamma}_\omega^{1l} \quad \text{(gear meshes with } \omega \text{ mesh frequency)} \\
&\underbrace{\bar{\gamma}^{1l\nu(\nu+1),pp}}_{\text{planet } \nu-\text{planet } (\nu+1) \text{ mesh}} = \cdots = \underbrace{\bar{\gamma}^{1l(d^1-1)d^1,pp}}_{\text{planet } (\mathrm{d}^1-1)-\text{planet } \mathrm{d}^\mathrm{i} \text{ mesh}} = \underbrace{\bar{\gamma}^{r1ld^1,gp}}_{\text{ring}-\text{planet } \mathrm{d}^1 \text{ mesh}} \\
&\qquad = \bar{\gamma}_\Omega^{1l} \quad \text{(gear meshes with } \Omega \text{ mesh frequency)}
\end{aligned} \tag{6.30}$$

Different from meshed-planet stages (equation (6.5)), the gear mesh forces for the gear meshes along train l in a stepped stage no longer contain just ω and its harmonics. As long as $\Omega \neq \omega$, Ω and its harmonics will participate into the harmonic structure of all the gear mesh forces along train l. Because stepped stages retain cyclic symmetry, if train l is brought to the position of a different planet train y, the mesh stiffness variations, meshes forces, and the associated responses along train l should be exactly the same as those for train y when train y is at the same position. The mesh forces along train l, hence, are periodic and have phase relations with the mesh force in other trains. Combination of equation (6.30) with the above properties for the mesh forces in a stepped stage yields the assumption on the harmonic structure of any gear mesh force in train l as follows. Any gear mesh force in train l contains ω and its harmonic

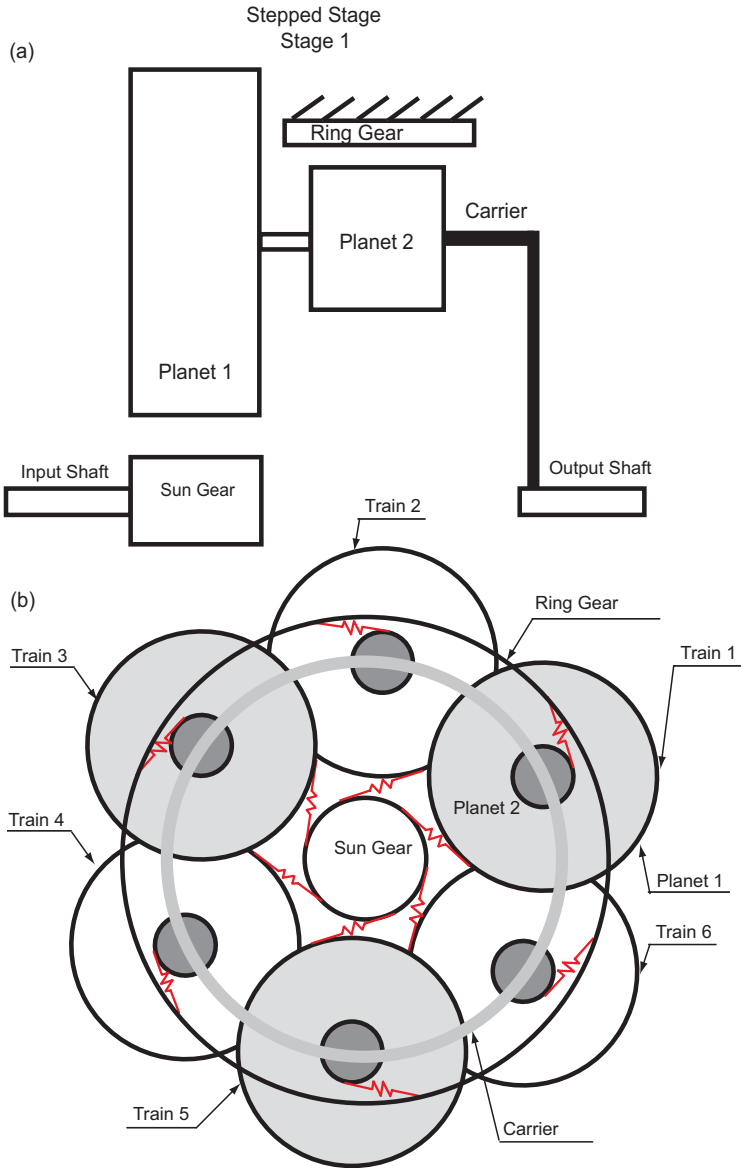

Figure 6.3: A stepped stage has six planet trains. Each planet train has two coaxial planets.

terms that are subjection to the train-level relative phase $\bar{\gamma}_{\omega}^{1l}$ and Ω and its harmonic terms that are subject to a different train-level relative $\bar{\gamma}_{\Omega}^{1l}$. The terms that contain ω and its harmonics are decoupled with those containing Ω and its harmonics. This is the key stipulation in this section to derive the mesh phasing rules for stepped stages and its validation is confirmed by the simulation results performed by Calyx [96].

The sun-planet mesh force in train l of a stepped stage is examined first. Equations (6.3) and (6.4) are still valid for the sun-planet mesh force in lth train of a stepped stage. Different from mesh planet stages, F_{ξ}^{s1l1} and F_{η}^{s1l1} in a stepped stage contain additional terms that are functions of Ωt and are subject to $\bar{\gamma}_{\Omega}^{1l}$ as follows.

$$\begin{aligned} F_{\xi}^{s1l1} &= F_{\xi,\omega}^{s111}(\omega t - 2\pi\bar{\gamma}_{\omega}^{1l}) + F_{\xi,\Omega}^{s111}(\Omega t - 2\pi\bar{\gamma}_{\Omega}^{1l}) \\ F_{\eta}^{s1l1} &= F_{\eta,\omega}^{s111}(\omega t - 2\pi\bar{\gamma}_{\omega}^{1l}) + F_{\eta,\Omega}^{s111}(\Omega t - 2\pi\bar{\gamma}_{\Omega}^{1l}) \end{aligned} \tag{6.31}$$

Expansion of $F_{\xi,\omega}^{s111}(\omega t - 2\pi\bar{\gamma}_{\omega}^{1l})$, $F_{\eta,\omega}^{s111}(\omega t - 2\pi\bar{\gamma}_{\omega}^{1l})$, $F_{\xi,\Omega}^{s111}(\Omega t - 2\pi\bar{\gamma}_{\Omega}^{1l})$, and $F_{\eta,\Omega}^{s111}(\Omega t - 2\pi\bar{\gamma}_{\Omega}^{1l})$ in (6.31) into Fourier series yields

$$\begin{aligned} F_{\xi}^{s1l1} &= \sum_{\mu=0}^{\infty}\left[e_{\omega,\mu}^{s111}\sin(\mu\omega t) + g_{\omega,\mu}^{s111}\cos(\mu\omega t)\right] + \sum_{\chi=0}^{\infty}\left[e_{\Omega,\chi}^{s111}\sin(\chi\Omega t) + g_{\Omega,\chi}^{s111}\cos(\chi\Omega t)\right] \\ &= \sum_{\mu=0}^{\infty} F_{\xi,\omega,\mu}^{s1l1} + \sum_{\chi=0}^{\infty} F_{\xi,\Omega,\chi}^{s1l1} \\ F_{\eta}^{s1l1} &= \sum_{\mu=0}^{\infty}\left[h_{\omega,\mu}^{s111}\sin(\mu\omega t) + j_{\omega,\mu}^{s111}\cos(\mu\omega t)\right] + \sum_{\chi=0}^{\infty}\left[h_{\Omega,\chi}^{s111}\sin(\chi\Omega t) + j_{\Omega,\chi}^{s111}\cos(\chi\Omega t)\right] \\ &= \sum_{\mu=0}^{\infty} F_{\eta,\omega,\mu}^{s1l1} + \sum_{\chi=0}^{\infty} F_{\eta,\Omega,\chi}^{s1l1} \end{aligned} \tag{6.32}$$

where $F_{\xi,\omega,\mu}^{s1l1}$ and $F_{\eta,\omega,\mu}^{s1l1}$ are the mesh forces between the sun gear and planet 1 in train l in $\boldsymbol{\xi}$ and $\boldsymbol{\eta}$ directions at the μth harmonic of the mesh frequency ω, and $F_{\xi,\Omega,\chi}^{s1l1}$ and $F_{\eta,\Omega,\chi}^{s1l1}$ are the mesh forces of the same gear mesh in $\boldsymbol{\xi}$ and $\boldsymbol{\eta}$ directions at the χth harmonic of the other mesh frequency Ω.

The net force acting on the sun gear in a stepped stage, hence, becomes

$$\begin{aligned}
\mathbf{F}^{s1*1} &= \sum_{l=1}^{c^1} \mathbf{F}^{s1l1} \\
&= \sum_{\mu=0}^{\infty} \underbrace{\left[\mathbf{i} \sum_{l=1}^{c^1} \left(F^{s1l1}_{\xi,\omega,\mu} \cos\hat{\psi}^{1l} - F^{s1l1}_{\eta,\omega,\mu} \sin\hat{\psi}^{1l} \right) + \mathbf{j} \sum_{l=1}^{c^1} \left(F^{s1l1}_{\xi,\omega,\mu} \sin\hat{\psi}^{1l} + F^{s1l1}_{\eta,\omega,\mu} \cos\hat{\psi}^{1l} \right) \right]}_{\mathbf{F}^{s1*1}_{\omega,\mu}} + \\
&\quad \sum_{\chi=0}^{\infty} \underbrace{\left[\mathbf{i} \sum_{l=1}^{c^1} \left(F^{s1l1}_{\xi,\Omega,\chi} \cos\hat{\psi}^{1l} - F^{s1l1}_{\eta,\Omega,\chi} \sin\hat{\psi}^{1l} \right) + \mathbf{j} \sum_{l=1}^{c^1} \left(F^{s1l1}_{\xi,\Omega,\chi} \sin\hat{\psi}^{1l} + F^{s1l1}_{\eta,\Omega,\chi} \cos\hat{\psi}^{1l} \right) \right]}_{\mathbf{F}^{s1*1}_{\Omega,\chi}} \\
&= \sum_{\mu=0}^{\infty} \mathbf{F}^{s1*1}_{\omega,\mu} + \sum_{\chi=0}^{\infty} \mathbf{F}^{s1*1}_{\Omega,\chi}
\end{aligned} \tag{6.33}$$

The cancellation of $\mathbf{F}^{s1*1}_{\omega,\mu}$ and $\mathbf{F}^{s1*1}_{\Omega,\chi}$ in (6.33) indicates that the translational responses at $\mu\omega = \omega_n$ and $\chi\Omega = \omega_n$ are suppressed, respectively. The derivation of the cancellation condition for $\mathbf{F}^{s1*1}_{\omega,\mu}$ is exactly the same as $\mathbf{F}^{s1*1}_{\mu}$ in a meshed-planet stage (from (6.10) to (6.15)) and the result is

$$\begin{aligned}
\mathbf{F}^{s1*1}_{\omega,\mu} &= 0, \text{ when } k_\mu \neq 1,\ c^1 - 1 \\
\mathbf{F}^{s1*1}_{\omega,\mu} &\neq 0, \text{ when } k_\mu = 1,\ c^1 - 1
\end{aligned} \tag{6.34}$$

where k_μ is defined in (6.13).

Similar to k_μ, the phasing quantity that is associated with $\bar{\gamma}^{1l}_{\Omega}$ and χth harmonic of Ω is defined as

$$\bar{k}_\chi = mod\left((-1)^{d^1-1} \frac{\chi Z^r_g}{c^1} \right) \tag{6.35}$$

where Z^r_g is the tooth number of the ring gear in the stepped stage. Replacing the relative phase in equation (6.10) with $\bar{\gamma}^{1l}_{\Omega} = dec\left((-1)^{d^1-1} \frac{Z^r_g \hat{\psi}^{il}}{2\pi} \right)$ [37] and application of the same process in equations (6.10)-(6.15) with the exception that (6.13) is replaced

by (6.35) produce the cancellation condition for $\mathbf{F}^{s1*1}_{\Omega,\chi}$ as

$$\begin{aligned} \mathbf{F}^{s1*1}_{\Omega,\chi} &= 0, \text{ when } \bar{k}_\chi \neq 1,\ c^1 - 1 \\ \mathbf{F}^{s1*1}_{\Omega,\chi} &\neq 0, \text{ when } \bar{k}_\chi = 1,\ c^1 - 1 \end{aligned} \tag{6.36}$$

Similar to the net torque acting on the sun gear in a meshed-planet stage, the net torque acting on the sun gear in a stepped stage is the sum of torques that are caused by the sun-planet mesh forces in the tangential direction $\boldsymbol{\eta}$. Insertion of (6.32) into $\boldsymbol{\Xi}^{s1*1} = r^s_g \sum_{l=1}^{c^1} F^{s1l1}_{\eta}$ yields

$$\begin{aligned} \boldsymbol{\Xi}^{s1*1} &= r^s_g \sum_{l=1}^{c^1} \sum_{\mu=0}^{\infty} F^{s1l1}_{\eta,\mu} \\ &= \sum_{\mu=0}^{\infty} \underbrace{r^s_g \sum_{l=1}^{c^1} \left[h^{s111}_{\omega,\mu} \sin\mu\left(\omega t - 2\pi\bar{\gamma}^{1l}_{\omega}\right) + j^{s111}_{\omega,\mu} \cos\mu\left(\omega t - 2\pi\bar{\gamma}^{1l}_{\omega}\right)\right]}_{\boldsymbol{\Xi}^{s1*1}_{\omega,\mu}} + \\ &\quad \sum_{\chi=0}^{\infty} \underbrace{r^s_g \sum_{l=1}^{c^1} \left[h^{s111}_{\Omega,\chi} \sin\chi\left(\Omega t - 2\pi\bar{\gamma}^{1l}_{\Omega}\right) + j^{s111}_{\chi} \cos\chi\left(\Omega t - 2\pi\bar{\gamma}^{1l}_{\Omega}\right)\right]}_{\boldsymbol{\Xi}^{s1*1}_{\Omega,\chi}} \\ &= \sum_{\mu=0}^{\infty} \boldsymbol{\Xi}^{s1*1}_{\omega,\mu} + \sum_{\chi=0}^{\infty} \boldsymbol{\Xi}^{s1*1}_{\Omega,\chi} \end{aligned} \tag{6.37}$$

$\boldsymbol{\Xi}^{s1*1}_{\omega,\mu}$ and $\boldsymbol{\Xi}^{s1*1}_{\Omega,\chi}$ are direct indications of the suppression of rotational responses at $\mu\omega = \omega_n$ or $\chi\Omega = \omega_n$ in a stepped stage. $\boldsymbol{\Xi}^{s1*1}_{\omega,\mu}$ has the same form as $\boldsymbol{\Xi}^{s1*1}_{\mu}$ in equation (6.16), and its suppression follows the same rule as $\boldsymbol{\Xi}^{s1*1}_{\mu}$ in (6.18). Replacing the phasing quantity k_μ with $\bar{k}_\chi$ and application of the same process as that in (6.17) give the rule to suppress $\boldsymbol{\Xi}^{s1*1}_{\Omega,\chi}$ as

$$\begin{aligned} \boldsymbol{\Xi}^{s1*1}_{\Omega,\chi} &\neq 0, \quad \bar{k}_\chi = 0 \\ \boldsymbol{\Xi}^{s1*1}_{\Omega,\chi} &= 0, \quad \bar{k}_\chi \neq 0 \end{aligned} \tag{6.38}$$

The net forces and torques acting on the ring gear and carrier have the same harmonic structures as those for the sun gear in (6.33) and (6.37). Their cancellation

conditions at $\mu\omega = \omega_n$ or $\chi\Omega = \omega_n$, hence, are the same as those for the sun gear in (6.36) and (6.38).

The general planet modal force expression in (6.20) is valid for stepped stages as well. Similar to the sun-planet mesh force in (6.31), Ω and its harmonics participate in the planet modal forces for stepped stages and they are decoupled with ω terms. Take the first term in (6.20), $Q^{\zeta} = \sum_{l=1}^{c^1} \sum_{m=1}^{d^1} w^l \left[\zeta_p^{11m} f_{\zeta}^{1lm}\right]$, as the example. In a stepped stage with ω and Ω mesh frequencies, Q^{ζ} is

$$\begin{aligned} Q^{\zeta} = & \underbrace{\sum_{\mu=1}^{\infty} \sum_{l=1}^{c^1} \sum_{m=1}^{d^1} w^l \zeta_p^{11m} \left[E_{\omega,\mu}^{1lm} \sin\mu\left(\omega t - 2\pi\bar{\gamma}_{\omega}^{1l}\right) + G_{\omega,\mu}^{1lm} \cos\mu\left(\omega t - 2\pi\bar{\gamma}_{\omega}^{1l}\right)\right]}_{Q_{\omega,\mu}^{\zeta}} + \\ & \underbrace{\sum_{\chi=1}^{\infty} \sum_{l=1}^{c^1} \sum_{m=1}^{d^1} w^l \zeta_p^{11m} \left[E_{\Omega,\chi}^{1lm} \sin\chi\left(\Omega t - 2\pi\bar{\gamma}_{\Omega}^{1l}\right) + G_{\Omega,\chi}^{1lm} \cos\chi\left(\Omega t - 2\pi\bar{\gamma}_{\Omega}^{1l}\right)\right]}_{Q_{\Omega,\chi}^{\zeta}} \\ = & \sum_{\mu=1}^{\infty} Q_{\omega,\mu}^{\zeta} + \sum_{\chi=1}^{\infty} Q_{\Omega,\chi}^{\zeta} \end{aligned} \tag{6.39}$$

The cancellation of $Q_{\omega,\mu}^{\zeta}$ suggests the suppression of Q^{ζ} at the μth harmonic of ω. Because all the terms in (6.20) have the same harmonic structure as Q^{ζ}, the modal force Q_v, as well as the associated planet mode response, is suppressed at μth harmonic of ω mesh frequency. Similarly, the cancellation of $Q_{\Omega,\chi}^{\zeta}$ indicates the suppression of the planet mode response at χth harmonic of Ω.

Because $Q_{\omega,\mu}^{\zeta}$ has the same expression as Q_{μ}^{ζ} in (6.27), the condition to suppress $Q_{\omega,\mu}^{\zeta}$ is the same as that for Q_{μ}^{ζ}. That is,

$$\begin{aligned} Q_{\omega,\mu}^{\zeta} &= 0, \text{ when } k_{\mu} = 0,\ 1,\ c^1 - 1 \\ Q_{\omega,\mu}^{\zeta} &\neq 0, \text{ when } k_{\mu} \neq 0,\ 1,\ c^1 - 1 \end{aligned} \tag{6.40}$$

Insertion of $\bar{\gamma}_{\Omega}^{1l} = dec\left((-1)^{d^1-1}\frac{Z_g^r\hat{\psi}^{il}}{2\pi}\right)$ into the expression of $Q_{\Omega,\chi}^{\zeta}$, introducing the phasing quantity for Ω mesh frequency as $\bar{k}_{\chi} = mod\left((-1)^{d^1-1}\frac{\chi Z_g^r}{c^1}\right)$, and application of the same analytical process as that for Q_{μ}^{ζ} in previous section yield the cancellation condition for $Q_{\Omega,\chi}^{\zeta}$ as

$$\begin{aligned} Q_{\Omega,\chi}^{\zeta} &= 0, \text{ when } \bar{k}_{\chi} = 0,\ 1,\ c^1 - 1 \\ Q_{\Omega,\chi}^{\zeta} &\neq 0, \text{ when } \bar{k}_{\chi} \neq 0,\ 1,\ c^1 - 1 \end{aligned} \tag{6.41}$$

Table 6.3 sums up the above rules to suppress different responses in a stepped stage. Due to the existence of two mesh frequencies, ω and Ω, in a stepped stage, two different phasing quantities, k_{μ} and $\bar{k}_{\chi}$ are needed to determine the suppression of resonant responses at $\mu\omega = \omega_n$ and $\chi\omega = \omega_n$, respectively.

Table 6.3: The conditions for the phasing quantities k_{μ} and $\bar{k}_{\chi}$ to suppress different responses in a stepped stage. E indicates the associated responses is excited, and S means that the related responses is suppressed.

k_{μ}	Cancellations of F, Ξ, and Q at $\mu\omega = \omega_n$	Translational	Rotational	Planet
$k_{\mu} = 0$	$F = 0$, $\Xi \neq 0$, $Q = 0$	S	E	S
$k_{\mu} = 1,\ c^1 - 1$	$F \neq 0$, $\Xi = 0$, $Q = 0$	E	S	S
$k_{\mu} \neq 0,\ 1,\ c^1 - 1$	$F = 0$, $\Xi = 0$, $Q \neq 0$	S	S	E
$\bar{k}_{\chi}$	Cancellations of F, Ξ, and Q at $\chi\Omega = \omega_n$	Translational	Rotational	Planet
$\bar{k}_{\chi} = 0$	$F = 0$, $\Xi \neq 0$, $Q = 0$	S	E	S
$\bar{k}_{\chi} = 1,\ c^1 - 1$	$F \neq 0$, $\Xi = 0$, $Q = 0$	E	S	S
$\bar{k}_{\chi} \neq 0,\ 1,\ c^1 - 1$	$F = 0$, $\Xi = 0$, $Q \neq 0$	S	S	E

6.3 Rules to Suppress Selected Dynamic Responses for Purely Rotational Models

All the vibration modes for purely rotational compound planetary model are classified into two types: overall modes and planet modes [35]. Similar to the rotational modes for rotational-translational models, each overall mode is associated with a distinct natural frequency, all the planet trains within the same stage have identical motions, and all the central components have rotational motions. The net torques acting on the sun, ring, and carrier, hence, are the direct measurement of the excitation/suppression of overall mode responses in a purely rotational model. Because the excitation sources are still the mesh forces in purely rotational models, the harmonic structures of these net torques are the same as those in a rotational-translational model in (6.17) and (6.38). The cancellation rules for these net torques in a purely rotational model, therefore, are the same as those in a rotational-translational model in equations (6.18) (for meshed-planet stages) and (6.39) (for stepped stages).

Equation (6.1) is generic for both rotational-translational and purely rotational models and it indicates that the excitation/suppression of planet responses can be determined by the planet modal force Q_v. Let an arbitrary meshed planet stage be numbered as stage 1. $\boldsymbol{\phi}_v$ is a planet mode for this stage. The associated planet modal force Q_v has the same form as that for a rotational-translational in equation (6.20) with the exception that w^l, the scalar multiplier for a rotational-translational model, should be replaced by v^l, the scalar multiplier for a purely rotational model that satisfies (2.37). Ambarisha and Parker [5] gives the closed-form solution for v^l

as

$$\mathbf{v} = \begin{bmatrix} v^1 \\ v^2 \\ \vdots \\ v^{c^1} \end{bmatrix} = \sum_{y=1}^{c^1-1} \left\{ \vartheta_y \begin{bmatrix} \sin y\hat{\psi}^{11} \\ \sin y\hat{\psi}^{12} \\ \vdots \\ \sin y\hat{\psi}^{1c^1} \end{bmatrix} \right\} \tag{6.42}$$

Similar to rotational-translational models, insertion of equation (6.42) and the planet modal properties in equation (2.33) into the expression of the modal force in (6.2) gives the μth harmonic of Q^θ as

$$\begin{aligned} Q_\mu^\theta =& \sum_{l=1}^{c^1} \sum_{m=1}^{d^1} \sum_{y=1}^{c^1-1} \left[\underbrace{\vartheta_y \sin y\hat{\psi}^{i1}}_{J1} \right] \times \\ & \theta_p^{11m} \left[\underbrace{E_\mu^{1lm} \sin\left(\mu\omega t \pm \mu\hat{\psi}^{1l} Z_g^s\right)}_{J2} + \underbrace{G_\mu^{1lm} \cos\mu\left(\omega t \pm \mu\hat{\psi}^{1l} Z_g^s\right)}_{J3} \right] \\ =& \sum_{l=1}^{c^1} \sum_{m=1}^{d^1} \sum_{y=1}^{c^1-1} \theta_p^{11m} \left(J_1 J_2 + J_1 J_3\right) \end{aligned} \tag{6.43}$$

Insertion of (6.11) and (6.13) into the expression of $\sum_{l=1}^{c^1} \sum_{m=1}^{d^1} \sum_{y=1}^{c^1-1} \theta_p^{11m} J_1 J_2$ gives

$$\begin{aligned} &\sum_{l=1}^{c^1} \sum_{m=1}^{d^1} \sum_{y=1}^{c^1-1} \theta_p^{11m} J_1 J_2 = \sum_{l=1}^{c^1} \sum_{m=1}^{d^1} \sum_{y=1}^{c^1-1} \theta_p^{11m} E_\mu^{1lm} \sigma_{y=1}^{c^1-1} \sin y\hat{\psi}^{i1} \sin\left(\mu\omega t \pm \mu\hat{\psi}^{1l} Z_g^s\right) \\ &= \sum_{l=1}^{c^1} \sum_{m=1}^{d^1} \sum_{y=1}^{c^1-1} \frac{\theta_p^{11m} E_\mu^{1lm} \sigma_{y=1}^{c^1-1}}{2} \left\{ \sin(\mu\omega t) \left[\sin\frac{2\pi(k_\mu + y)(l-1)}{c^1} + \sin\frac{2\pi(k_\mu - y)(l-1)}{c^1} \right] \right. \\ &\left. \pm \cos(\mu\omega t) \left[\cos\frac{2\pi(k_\mu - y)(l-1)}{c^1} - \cos\frac{2\pi(k_\mu + y)(l-1)}{c^1} \right] \right\} \end{aligned} \tag{6.44}$$

Application of the trigonometric identities in (6.15) to (6.44) yields that $\sum_{l=1}^{c^1} \sum_{m=1}^{d^1} \sum_{y=1}^{c^1-1} \theta_p^{11m} J_1 J_2 = 0$ when $k_\mu \pm y \neq 0$ for every $y = 1, \cdots, c^1 - 1$. This condition is equivalent to $k_\mu \neq 1, \cdots, c^1 - 1$ or $k_\mu = 0$. The other terms at the right hand side of (6.43) follow the same cancellation condition. Q_μ^θ, hence, cancels out when $k_\mu = 0$. That is, the

planet response at μth harmonic of mesh frequency in a purely rotational model is suppressed when $k_\mu = 0$.

Replacing ζ_p^{11m}, Q^ζ, $Q^\zeta_{\omega,\mu}$, and $Q^\zeta_{\Omega,\mu}$ in (6.40) with θ_p^{11m}, Q^θ, $Q^\theta_{\omega,\mu}$, and $Q^\theta_{\Omega,\mu}$ yields the planet modal force for a stepped stage in a rotational model as

$$\begin{aligned} Q^\theta = & \underbrace{\sum_{\mu=1}^{\infty}\sum_{l=1}^{c^1}\sum_{m=1}^{d^1} w^l\theta_p^{11m}\left[E^{1lm}_{\omega,\mu}\sin\mu\left(\omega t - 2\pi\bar{\gamma}^{1l}_{\omega}\right) + G^{1lm}_{\omega,\mu}\cos\mu\left(\omega t - 2\pi\bar{\gamma}^{1l}_{\omega}\right)\right]}_{Q^\zeta_{\omega,\mu}} + \\ & \underbrace{\sum_{\chi=1}^{\infty}\sum_{l=1}^{c^1}\sum_{m=1}^{d^1} w^l\theta_p^{11m}\left[E^{1lm}_{\Omega,\chi}\sin\chi\left(\Omega t - 2\pi\bar{\gamma}^{1l}_{\Omega}\right) + G^{1lm}_{\Omega,\chi}\cos\chi\left(\Omega t - 2\pi\bar{\gamma}^{1l}_{\Omega}\right)\right]}_{Q^\zeta_{\Omega,\chi}} \\ = & \sum_{\mu=1}^{\infty} Q^\theta_{\omega,\mu} + \sum_{\chi=1}^{\infty} Q^\theta_{\Omega,\chi} \end{aligned} \tag{6.45}$$

The cancellation of $Q^\theta_{\omega,\mu}$ in (6.45) is exactly the same as Q^θ_μ in (6.43). Substitution of $\bar{\gamma}^{1l}_{\Omega} = dec\left((-1)^{d^1-1}\frac{Z^r_g\hat{\psi}^{il}}{2\pi}\right)$ (the train-level relative phase expression in Table 5.1) into the expression of $Q^\zeta_{\Omega,\chi}$ in (6.45), insertion of $\bar{k}_\chi = mod\left((-1)^{d^1-1}\frac{\chi Z^r_g}{c^1}\right)$, and application of the same analytical process as above produce the cancellation condition for $Q^\theta_{\Omega,\chi}$ as $\bar{k}_\chi = 0$.

Table 6.4 summarizes the above results to suppress different responses in a purely rotational model for compound planetary gears. Comparing with the results for rotational-translational models in Tables 6.2 and 6.3, the condition to suppress the overall mode responses in a purely rotational model is the same as that to suppress the rotational responses in a rotational-translational model. In addition, the condition to suppress the planet responses in a purely rotational model is identical to the conditions to suppress planet and translational responses simultaneously in a rotational-translational model.

Table 6.4: The conditions for the phasing quantities k_μ and $\bar{k}_\chi$ to suppress different responses in a purely rotational model. E indicates the associated responses is excited, and S means that the related responses is suppressed.

Meshed-planet stages or stepped stages when $\mu\omega = \omega_n$			
k_μ	Cancellations of Ξ and Q	Overall	Planet
$k_\mu = 0$	$\Xi \neq 0$, $Q = 0$	E	S
$k_\mu \neq 0$	$\Xi = 0$, $Q \neq 0$	S	E
Stepped stages when $\chi\Omega = \omega_n$			
$\bar{k}_\chi$	Cancellations of Ξ and Q	Overall	Planet
$\bar{k}_\chi = 0$	$\Xi \neq 0$, $Q = 0$	E	S
$\bar{k}_\chi \neq 0$	$\Xi = 0$, $Q \neq 0$	S	E

6.4 Numerical Examples and Discussions

To numerically validate the analytical results on the phasing rules for compound planetary stages in previous section, numerical simulations are performed for compound planetary stages with different mesh phasing configurations using Plantary2D [95], a finite element software that precisely calculates dynamic responses for planetary gear systems without any preset or user-defined mesh phase relations and is proved to be the benchmark for analytical studies on planetary gear dynamics [6, 9, 75, 76].

For the meshed-planet compound stage shown in Figure 6.1, two different mesh phasing cases that are listed in Table 6.5 are simulated. The input parameters to Planetary2D are listed in Table 6.6. All gears are steel spur gears with Young's modulus equaling $207 \times 10^9 N/m^2$, density being $7595 kg/m^3$, and Poisson's ratio equaling 0.3. In both cases, the four planet trains are equally-spaced, sun gear is the

input component, ring gear is fixed, carrier is the output, and all teeth are unmodified. The finite element models for both cases are shown in Figure 6.4.

Table 6.5: Two different mesh phasing cases for the meshed-planet stage in Figure 6.1.

	Gear Tooth Numbers for Sun, Ring, and Planets	$k_\mu = mod(\mu Z_g^s/c^1)$			
		$\mu = 1$	$\mu = 2$	$\mu = 3$	$\mu = 4$
Case 1	$Z_g^s = 29,\ Z_g^r = 153$ $Z_p^{1l1} = 29,\ Z_p^{1l2} = 33$	1	2	3	0
Case 2	$Z_g^s = 30,\ Z_g^r = 154$ $Z_p^{1l1} = 29,\ Z_p^{1l2} = 33$	2	0	2	0

The changes in gear tooth numbers from Case 1 to Case 2 are minor and the kinematic properties, such as gear ratios, remain almost the same for both cases. Such little changes in gear numbers, however, have great impact on the dynamic responses of the system. The phasing quantities in Table 6.5 suggest that in Case 1 translational responses are excited at all odd orders of mesh frequency harmonics, and rotational responses are only excited every fourth harmonic of mesh frequency. For Case 2, translational responses are suppressed at *all* the harmonics of mesh frequency, and rotational responses are suppressed at odd orders of mesh frequency harmonics. The complete suppression of translational responses and the suppression of rotational responses at the first order of mesh frequency make Case 2 be the better design in the view of noise and vibration reduction. These analytical results are confirmed by the simulation results in Figures 6.5-6.6. Figure 6.5a shows the periodic sun translational response, and its first four harmonic amplitudes are listed in Figure 6.5b. The fact that the amplitudes of the first and third harmonics are much higher than those for the second and fourth harmonics matches the analytical results for Case 1 in Table 6.5 that the even order of harmonics for the sun translational response are suppressed

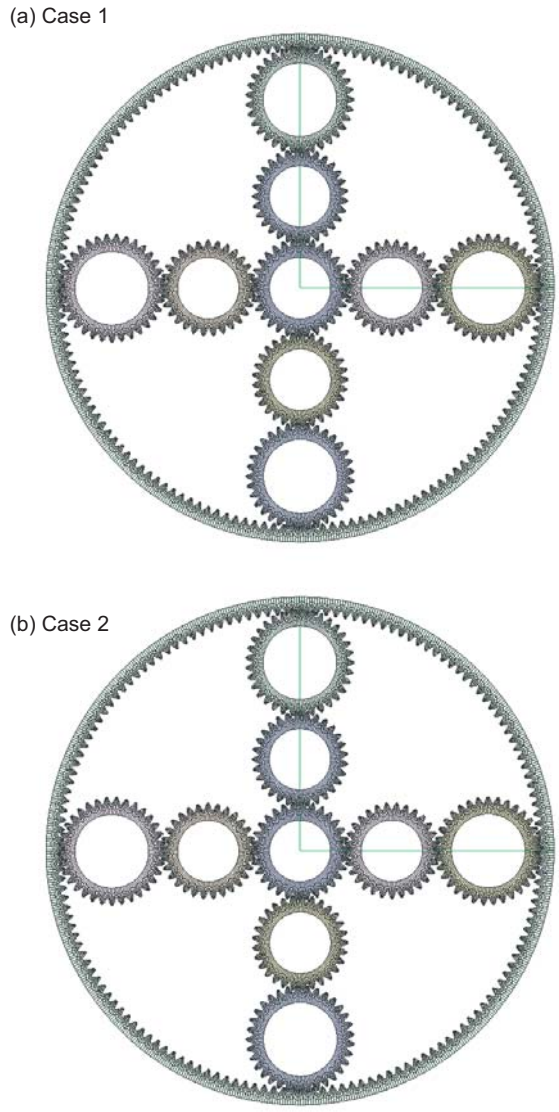

Figure 6.4: The finite element models for (a) Case 1 and (b) Case 2 in Table 6.5.

because $k_\mu \neq 1,\ 3$. To compare with Case 1, the periodic sun translational response for Case 2 is shown in Figure 6.6a, and the associated first four harmonic amplitudes are collected in Figure 6.6b. The sun translational response is completely suppressed in Figure 6.6 and this result matches with the analytical results that is based on the phasing quantity calculation in Table 6.5 (i.e., all the translational responses for Case 2 are suppressed because $k_\mu \neq 1,\ 3$ for any μ).

Table 6.6: Input parameters to Planetary2D for the two cases in Table 6.5. The unit for all diameters is millimeter. Planet gear (ilm) means planet m in train l of stage i.

	Case 1				Case 2			
	Sun Gear	Planet Gear $(1l1)$	Planet Gear $(1l2)$	Ring Gear	Sun Gear	Planet Gear $(1l1)$	Planet Gear $(1l2)$	Ring Gear
Diametral Pitch	0.5	0.5	0.5	0.5	0.5	0.5	0.5	0.5
Pressure Angle	25^o	25^o	24^o	24^o	25^o	25^o	25^o	25^o
Base Diameter	52.58	52.58	59.69	277.37	52.58	52.58	59.69	277.37
Outer Diameter	61.72	61.72	69.60	324.10	61.72	61.72	69.60	324.10
Root Diameter	52.58	52.58	60.45	305.31	52.58	52.58	60.45	305.31

The configuration (the number of planet trains and the arrangement of the two stepped planets) of the example system shown in Figure 6.3 is the similar to the practical planetary gear system in [19]. Two mesh phasing cases in Table 6.6 are simulated (all the gear parameters in Table 6.6 are completely different from the gear system in [19] with the exception of the gear tooth numbers for Case 1). All gears

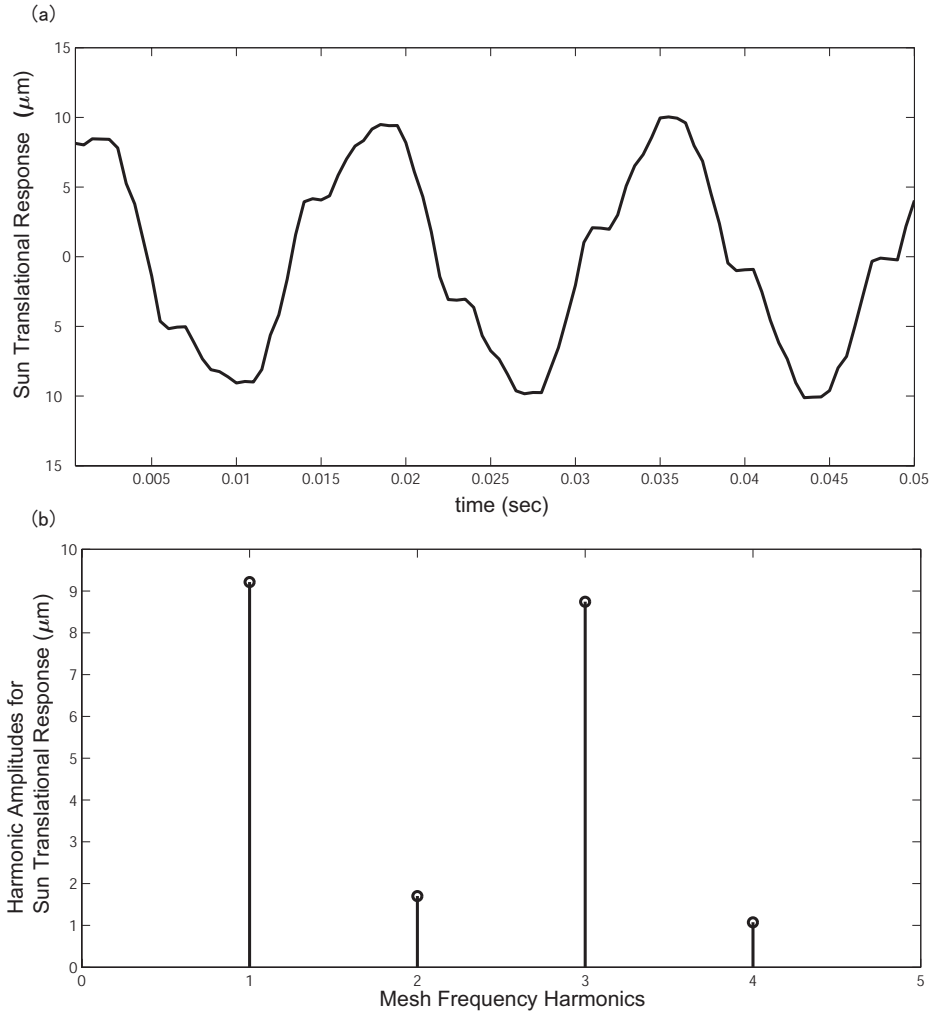

Figure 6.5: The simulated results for (a) sun translational response and (b) the associated harmonic amplitudes of Case 1 in Table 6.5. Sun gear is the input component and the input speed is 100 rpm.

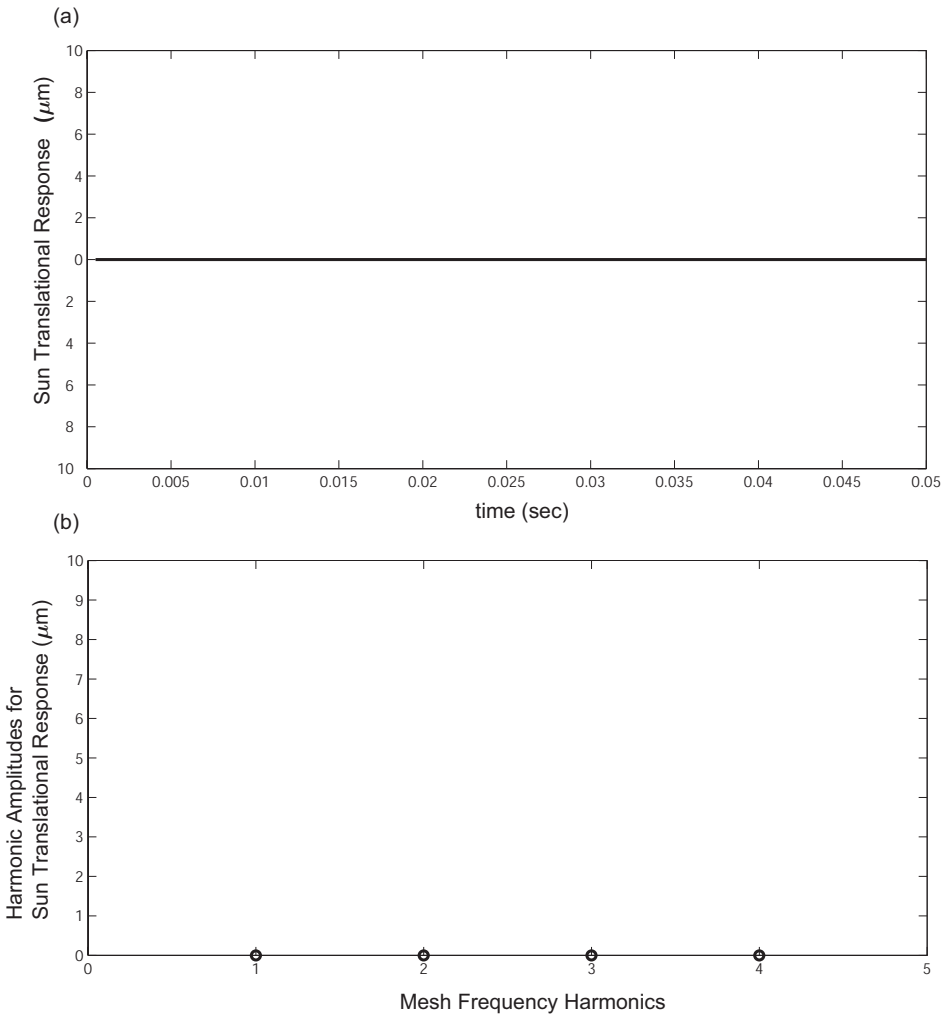

Figure 6.6: The simulated results for (a) sun translational response and (b) the associated harmonic amplitudes of Case 2 in Table 6.5. Sun gear is the input component and the input speed is 100 rpm. The input torque remains the same as that for Figure 6.5.

are spur gears in the calculation and the finite element models for these two cases are demonstrated in Figure 6.7.

Table 6.7: Two different mesh phasing cases for the stepped stage in Figure 6.3.

	Gear Tooth Numbers	Phasing Quantities			
Case 1	$Z_g^s = 24,\ Z_g^r = 108$ $Z_p^{1l1} = 66,\ Z_p^{1l2} = 18$	$k_\mu = mod(\mu Z_g^s / c^1)$			
		$\mu = 1$	$\mu = 2$	$\mu = 3$	$\mu = 4$
		0	0	0	0
		$\bar{k}_\chi = mod(\chi(-1)^{d^1-1} Z_g^r / c^1)$			
		$\chi = 1$	$\chi = 2$	$\chi = 3$	$\chi = 4$
		0	0	0	0
Case 2	$Z_g^s = 26,\ Z_g^r = 110$ $Z_p^{1l1} = 67,\ Z_p^{1l2} = 17$	$k_\mu = mod(\mu Z_g^s / c^1)$			
		$\mu = 1$	$\mu = 2$	$\mu = 3$	$\mu = 4$
		2	4	0	2
		$\bar{k}_\chi = mod(\chi(-1)^{d^1-1} Z_g^r / c^1)$			
		$\chi = 1$	$\chi = 2$	$\chi = 3$	$\chi = 4$
		4	2	0	4

Similar to the two case in Table 6.5, the differences in gear tooth numbers for the two case in Table 6.7 are slight such that the gear ratios are the almost the same for both cases. The dynamic responses for these two cases, however, differ dramatically. The phasing quantities in Table 6.7 suggest that the translational responses are suppressed at all the harmonics for both mesh frequencies (i.e, for any k_μ or $\bar{k}_\chi$) for both cases. For Case 1, the rotational responses are excited at all the harmonics for both mesh frequencies because both k_μ and $\bar{k}_\chi$ equal zero. For Case 2, the rotational responses are *only* excited at every third harmonic of both mesh frequencies. These analytical results are verified by the simulation results in Figures 6.8-6.9. The simulation results in Figure 6.8 confirms that the sun rotational response is excited at all harmonics of ω and Ω. For Case 2, due to the adjustments in mesh phasing, the sun

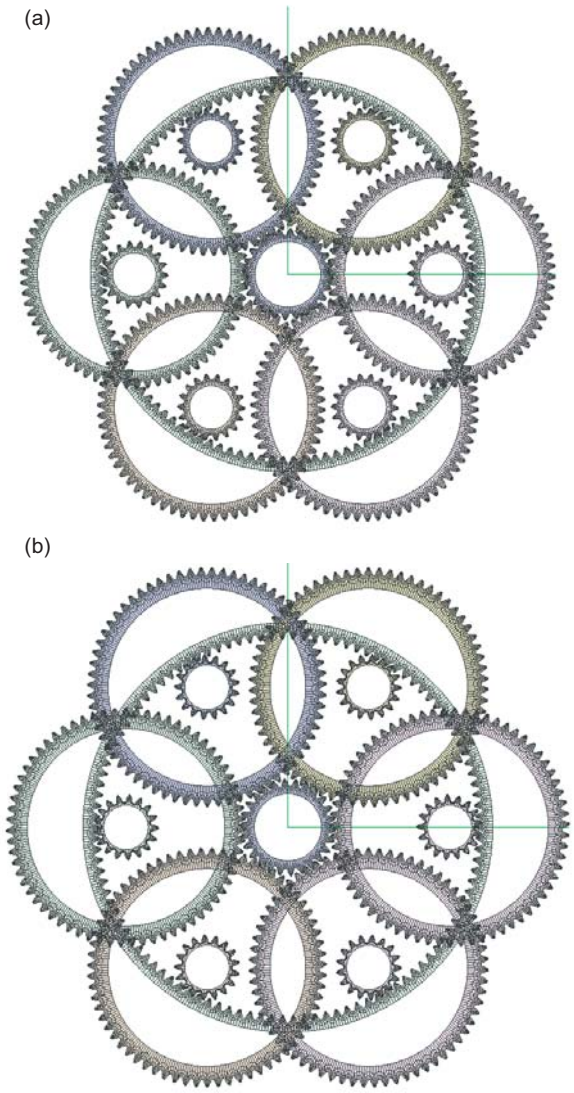

Figure 6.7: The finite element models for (a) Case 1 and (b) Case 2 in Table 6.7.

rotational response in Figure 6.9 is only excited at every third harmonics for ω and Ω. The phenomenon that the fundamental frequency of the sun rotational response in Figure 6.9a is three times of that in Figure 6.8a further confirms the analytical results that is based on the phasing quantity calculation in Table 6.7.

Making the translational bearing/shaft stiffnesses in the above cases be stiffer (at least one hundred times of their original values) and conducting the simulations to calculate the rotational responses for the sun, and planet gear for the same cases in tables 6.5 and 6.7 yield the numerical results that agree with the rules in Table 6.4. The mesh phasing rules for purely rotational models, hence, is also numerically verified.

6.5 Conclusion

The chapter analytically investigates the general rules to suppress certain dynamic responses and resonances of compound planetary gears through mesh phasing for purely rotational and rotational-translational models. For meshed-planet stages, the excitation or suppression of various modal responses at μth harmonic of mesh frequency is solely determined by the phasing quantity k_μ. The resultant rules are the same as those for simple planetary gears and the planet-planet gear meshes have no impact on the mesh phasing rules for meshed-planet stages due to the specific train-level relative phase relations that are determined by the assembly conditions. For stepped stages, due to the existence of two generally different mesh frequencies, two different phasing quantities, k_μ and $\bar{k}_\chi$, are required to determine the excitation or suppression of various modal responses at μth harmonic of one mesh frequency and χth harmonic of the other one. For multi-stage systems, the mesh phasing rules are

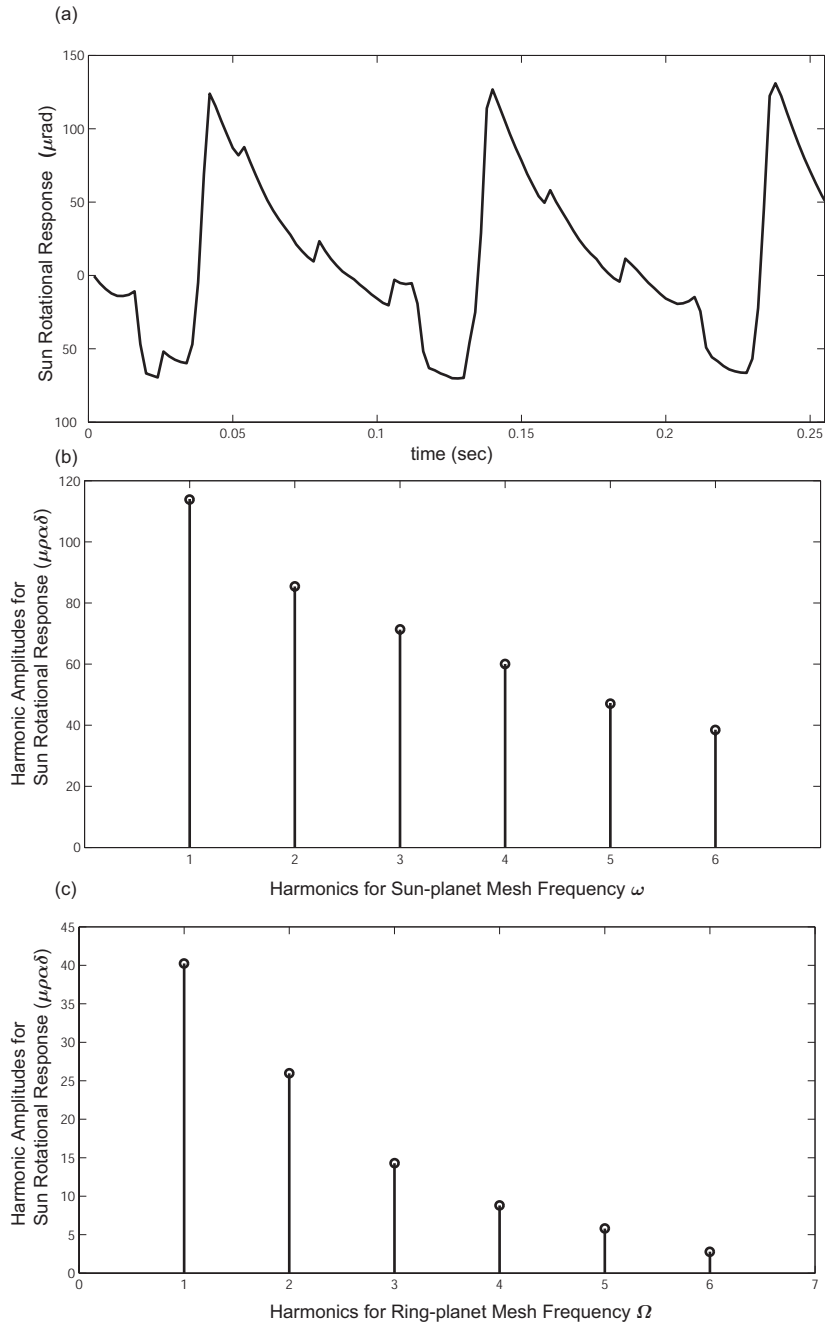

Figure 6.8: The simulated results for (a) sun translational response, (b) the amplitudes of first sixth harmonics of sun-planet mesh frequency ω, and (c) the amplitudes of first sixth harmonics of ring-planet mesh frequency Ω for Case 1 in Table 6.7. Sun gear is the input component and the input speed is 100 rpm.

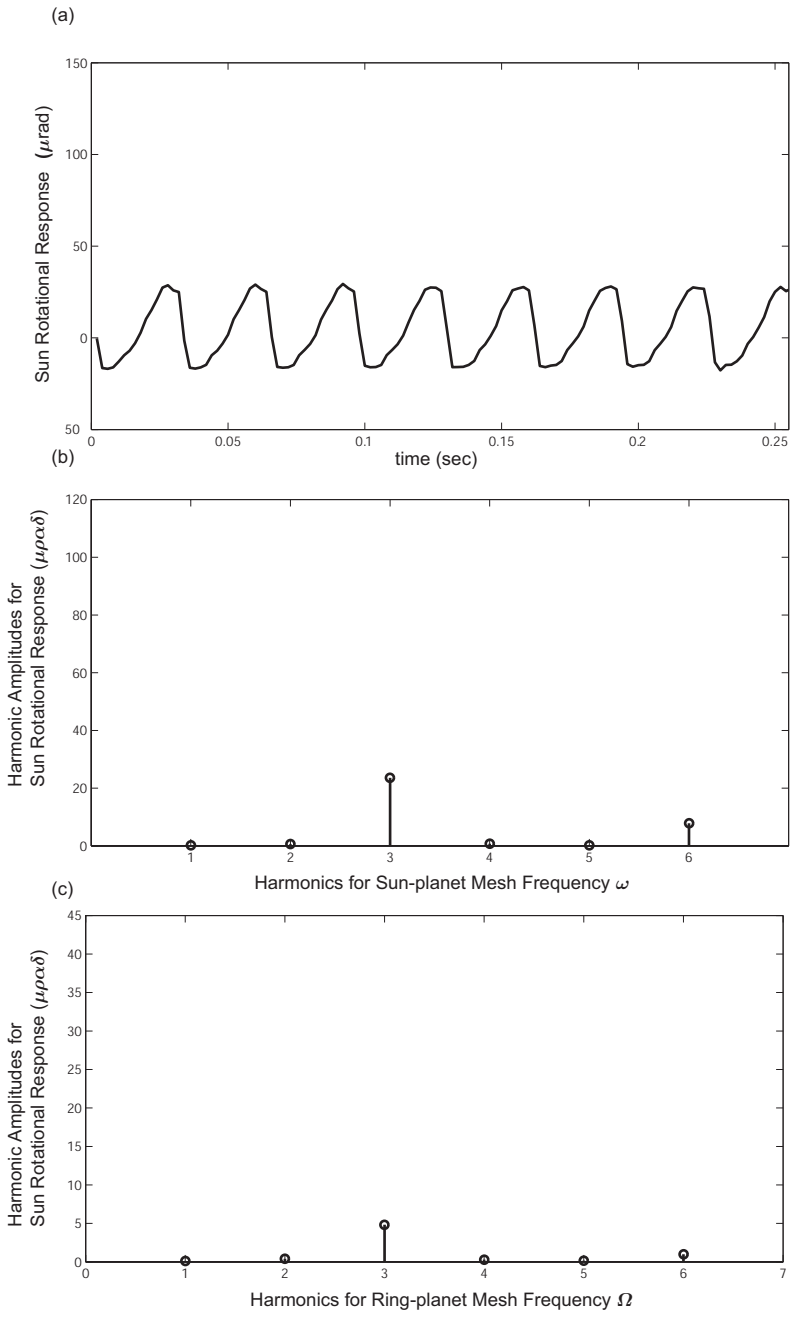

Figure 6.9: The simulated results for (a) sun translational response, (b) the amplitudes of first sixth harmonics of sun-planet mesh frequency ω, and (c) the amplitudes of first sixth harmonics of ring-planet mesh frequency Ω for Case 1 in Table 6.7. Sun gear is the input component and the input speed is 100 rpm. The input torque remains the same as that for Figure 6.8.

the sum of the rules from individual stage which is either a stage with meshed-planet structure only or a stepped stage. The results of this study are critical to the design of compound planetary gear systems and are effective in troubleshooting the vibration and noise problems in real compound planetary gear applications.

Chapter 7: PARAMETRIC INSTABILITIES OF GENERAL COMPOUND PLANETARY GEAR CAUSED BY MESH STIFFNESS VARIATIONS

7.1 Introduction

Mesh stiffness variation is a primary excitation of gear noise and vibrations [60,61, 98] and is typically represented by time-varying mesh stiffnesses that parametrically excite gear systems in analytical studies [61]. When the operating speed of the system meets certain conditions, instabilities that are caused by mesh stiffness parametric excitations will occur such that noise and vibrations are created, the dynamic load on each component of the system is dramatically increased, and the chance of hardware failure, such as the damages in gear teeth and bearings, is greatly increased [61, 98]. In order to prevent gear systems from operating in the instability regions, it is crucial to investigate the parametric instabilities caused by mesh stiffness variations and to identify the instability boundaries at the design stage of the system.

Parametric instability for a single gear pair was investigated analytically and numerically in several studies [4, 12, 14, 71]. The experimental work on the parametric instabilities in a spur gear pair was performed by Kahraman and Blankenship [49]. Nonlinear phenomena such as gear tooth contact loss, period-doubling and chaos were also observed in their study. As for the parametric instability of multi-mesh

gear systems, very limited studies were performed. The studies on the instabilities of two-stage gear systems by Tordion and Gauvin [93] and Benton and Seireg [10] gave contradictory conclusions. This was clarified by Lin and Parker's investigation [60] which provided analytical formulae to allow designers to suppress particular instabilities by changing gear mesh parameters, such as contact ratios and mesh phasing. Liu and Parker [63] examined the nonlinear resonant vibrations of idler gears that are parametrically excited by mesh stiffness variation. The study on the planetary gear parametric instability was first performed by Lin and Parker [61] who analytically investigated the parametric instability of simple planetary gear using a purely rotational model. Bahk and Parker [9] used the same purely rotational model to study the nonlinear resonant vibration of simple planetary gears parametrically excited by mesh stiffness variations. Wu and Parker [98] extended the parametric instability investigation scope to simple planetary gears having an elastic continuum ring gear.

Compound planetary gear parametric instability, however, is not investigated in any previous studies mainly due to the complexity in modeling, the complex mesh phasing relations caused by meshed-planet and stepped-planet structures, and multi-frequency excitations incurred by stepped-planet and multi-stage structures. Studies in previous chapters develop the lumped-parameter models for compound planetary gears, define and clarify the complex mesh phasing relations, and derive the rules that govern the suppression of selected dynamic responses through mesh phasing. All these provide necessary foundations for the current problem of parametric instability for compound planetary gears.

Compared to the rotational-translational compound planetary gear model in [53], the purely rotational model developed in chapter 2 greatly simplifies the analytical

work on gear dynamics while keeping the main dynamic behavior generated by mesh stiffness variations. The work in [61] confirms the effectiveness of a purely rotational model in capturing the parametric instability properties for simple planetary gears. The study in this chapter, hence, uses the purely rotational model to investigate compound planetary gear parametric instabilities. By applying the method of multiple scale, the well-defined modal properties in chapter 2, and the mesh phase relations in chapter 5, the instability boundaries are analytically obtained and the general instability existence rules are derived.

7.2 Mesh Stiffnesses Variations in Compound Planetary Gears

Meshed-planet, stepped-planet, and multi-stage structures are unique to compound planetary gears. Meshed planets introduce new planet-planet meshes to the system. Stepped-planet and multi-stage structures allow the system to have multiple mesh frequencies. $k_{gp}^{silm}(t)$ is the time varying mesh stiffness between central gear s and planet m in train l of stage i and its mesh frequency is Ω_i^1. If all other gear meshes along train l in the same stage have the same mesh frequency, stage i is either a simple stage (a stage that is equivalent to a simple planetary gear) or a meshed-planet stage. Otherwise, there exists a stepped-planet structure along train l and there is always a central gear-planet mesh having a mesh frequency different from Ω_i^1. Without losing generality, $k_{gp}^{rilq}(t)$ is the mesh stiffness between central gear r and planet q along train l in stage i and its mesh frequency is Ω_i^2. When $\Omega_i^2 = \Omega_i^1$, stage i is a simple planet gear, a meshed-planet stage, or a special stepped stage with single mesh frequency. Otherwise, stage i is a stepped stage with two different mesh frequencies. With the assumption that the mesh stiffnesses are independent of the load, the time-varying

mesh stiffness $k_{gp}^{silm}(t)$ and $k_{gp}^{rilq}(t)$ are

$$\begin{aligned} k_{gp}^{silm}(t) &= k_{gp}^{si*m} + \tilde{k}_{gp}^{silm}(t) \\ k_{gp}^{rilq}(t) &= k_{gp}^{ri*q} + \tilde{k}_{gp}^{rilq}(t) \end{aligned} \tag{7.1}$$

where k_{gp}^{si*m} and k_{gp}^{ri*q} are mean values for $k_{gp}^{silm}(t)$ and $k_{gp}^{rilq}(t)$, and $\tilde{k}_{gp}^{silm}(t)$ and $\tilde{k}_{gp}^{rilq}(t)$ are zero-mean mesh stiffness variations. Similar to [98], trapezoidal waves are used to approximate the mesh stiffness variations due to its advantage over rectangular waves in case of corner contacts. Figure 7.1 shows the trapezoidal approximations for $\tilde{k}_{gp}^{silm}(t)$ and $\tilde{k}_{gp}^{rilq}(t)$. $\hat{\gamma}^{gp,silm}(0)$ and $\hat{\gamma}^{gp,rilq}(0)$ are the system-level relative phases for $k_{gp}^{silm}(t)$ and $k_{gp}^{rilq}(t)$ and the referring time 0 indicates that the pitch point of the base referred mesh is in contact at $t = 0$. The contact ratios for these two mesh stiffnesses are c_{gp}^{si*m} and c_{gp}^{ri*q} and the mesh periods are $T_{gp}^{si*m} = \frac{2\pi}{\Omega_i^1}$ and $T_{gp}^{ri*q} = \frac{2\pi}{\Omega_i^2}$. ρ_{gp}^{si*m} and ρ_{gp}^{ri*q} are the slope coefficients for the non-parallel sides of the trapezoidal waves for $\tilde{k}_{gp}^{silm}(t)$ and $\tilde{k}_{gp}^{rilq}(t)$ and they are in the range of $[0,\ \frac{1}{4}]$ (0 and $\frac{1}{4}$ correspond to rectangular and triangle waves, respectively). $2k_{vg}^{sl*m}$ and $2k_{vg}^{rl*q}$ are the peak-to-peak amplitudes for $\tilde{k}_{gp}^{silm}(t)$ and $\tilde{k}_{gp}^{rilq}(t)$.

Fourier expansion of $\tilde{k}_{gp}^{silm}(t)$ and (b) $\tilde{k}_{gp}^{rilq}(t)$ yields

$$\begin{aligned} \tilde{k}_{gp}^{silm}(t) &= 2k_{vg}^{sl*m} \sum_{\mu=1}^{\infty} [A_{\mu}^{gp,silm} \sin \mu\Omega_i^1 t + B_{\mu}^{gp,silm} \cos \mu\Omega_i^i t] \\ \tilde{k}_{gp}^{rilq}(t) &= 2k_{vg}^{rl*q} \sum_{\mu=1}^{\infty} [A_{\mu}^{gp,rilq} \sin \mu\Omega_i^2 t + B_{\mu}^{gp,rilq} \cos \mu\Omega_i^2 t] \end{aligned} \tag{7.2}$$

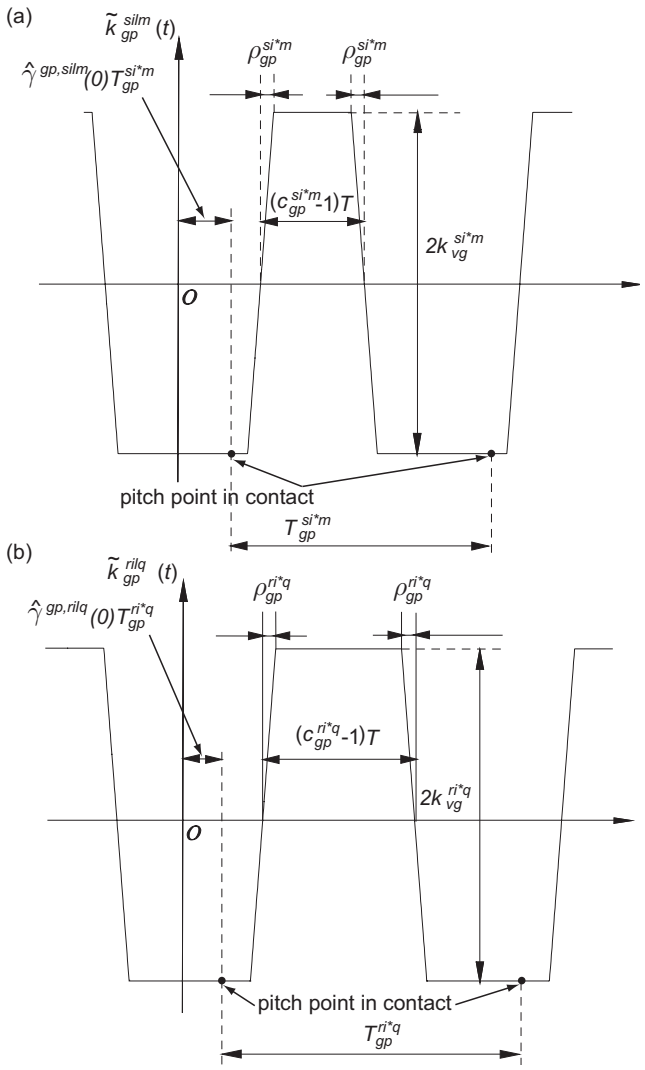

Figure 7.1: The zero-mean mesh stiffness variations (a) $\tilde{k}_{gp}^{silm}(t)$ and (b) $\tilde{k}_{gp}^{rilq}(t)$. $\hat{\gamma}^{gp,silm}(0)$ and $\hat{\gamma}^{gp,rilq}(0)$ are system-level mesh phases, c_{gp}^{si*m} and c_{gp}^{ri*q} are contact ratios, T_{gp}^{si*m} and T_{gp}^{ri*q} are mesh periods, and ρ_{gp}^{si*m} and ρ_{gp}^{ri*q} are trapezoid wave slope coefficients.

where the Fourier coefficients $A_\mu^{gp,silm}$, $B_\mu^{gp,silm}$, $A_\mu^{gp,rilq}$, and $B_\mu^{gp,rilq}$ are

$$\begin{aligned}
A_\mu^{gp,silm} &= \frac{\sin(2\mu\pi\rho_{gp}^{si*m})}{\rho_{gp}^{si*m}\mu^2\pi^2}\sin\left[\mu\pi(c_{gp}^{si*m}+2\hat{\gamma}^{gp,silm}(0))\right]\sin(\mu\pi c_{gp}^{si*m}) \\
B_\mu^{gp,silm} &= \frac{\sin(2\mu\pi\rho_{gp}^{si*m})}{\rho_{gp}^{si*m}\mu^2\pi^2}\cos\left[\mu\pi(c_{gp}^{si*m}+2\hat{\gamma}^{gp,silm}(0))\right]\sin(\mu\pi c_{gp}^{si*m}) \\
A_\mu^{gp,rilq} &= \frac{\sin(2\mu\pi\rho_{gp}^{ri*q})}{\rho_{gp}^{ri*q}\mu^2\pi^2}\sin\left[\mu\pi(c_{gp}^{ri*q}+2\hat{\gamma}^{gp,rilq}(0))\right]\sin(\mu\pi c_{gp}^{ri*q}) \\
B_\mu^{gp,rilq} &= \frac{\sin(2\mu\pi\rho_{gp}^{ri*q})}{\rho_{gp}^{ri*q}\mu^2\pi^2}\cos\left[\mu\pi(c_{gp}^{ri*q}+2\hat{\gamma}^{gp,rilq}(0))\right]\sin(\mu\pi c_{gp}^{ri*q})
\end{aligned} \tag{7.3}$$

$\epsilon_{gp}^{sl*m}=\frac{k_{vg}^{sl*m}}{k_{gp}^{si*m}}$ and $\epsilon_{gp}^{rl*q}=\frac{k_{vg}^{rl*q}}{k_{gp}^{ri*q}}$ are the relative amplitudes of mesh stiffness variations. Without losing generality, k_{gp}^{1111} is the mesh stiffness for the base referred mesh, and its relative mesh stiffness variation amplitude is $\epsilon_{gp}^{1l*1}=\epsilon$. According to [61, 98], it is reasonable to assume that ϵ_{gp}^{sl*m} and ϵ_{gp}^{rl*q} are of the same order as ϵ. That is,

$$\begin{aligned}
\epsilon_{gp}^{sl*m} &= g_{gp}^{sl*m}\epsilon \\
\epsilon_{gp}^{rl*q} &= g_{gp}^{rl*q}\epsilon
\end{aligned} \tag{7.4}$$

where $g_{gp}^{sl*m},\ g_{gp}^{rl*q}=O(1)$ are relative variation coefficients. Application of the analytical process in equations (7.1)-(7.4) to all other gear meshes in the same compound planetary gear yields the Fourier expansions for these gear meshes. Substitution of the resultant Fourier expansions for all the gear meshes into the stiffness matrix for the purely rotational model (2.23) gives

$$\begin{aligned}
\mathbf{K}(t) &= \mathbf{K}_b+\mathbf{K}_m=\mathbf{K}_b+\underbrace{\mathbf{K}_o+\mathbf{K}_v(t)}_{\mathbf{K}_m} \\
&= \mathbf{K}_{iv}+\mathbf{K}_v(t) \\
&= \mathbf{K}_{iv}+2\epsilon\sum_{\mu=1}^{\infty}\sum_{i=1}^{a}\left[\left(\mathbf{K}_{i11}^{\mu}\sin\mu\Omega_i^1 t+\mathbf{K}_{i12}^{\mu}\cos\mu\Omega_i^1 t\right)+\right. \\
&\quad \left.\left(\mathbf{K}_{i21}^{\mu}\sin\mu\Omega_i^2 t+\mathbf{K}_{i22}^{\mu}\cos\mu\Omega_i^2 t\right)\right]
\end{aligned} \tag{7.5}$$

where $\mathbf{K}_{iv}=\mathbf{K}_b+\mathbf{K}_o$ is the time-invariant part of $\mathbf{K}(t)$, $\mathbf{K}_v(t$ is the time-varying part of $\mathbf{K}(t)$, $\mathbf{K}_o$ has the same form as $\mathbf{K}_m$ with all the mesh stiffness substituted by

their mean values, and $\mathbf{K}_{i11}^{\mu}$, $\mathbf{K}_{i12}^{\mu}$, $\mathbf{K}_{i21}^{\mu}$, and $\mathbf{K}_{i22}^{\mu}$ are the Fourier coefficient matrices for stage i gear meshes with Ω_i^1 and Ω_i^2 mesh frequencies, respectively. They have the same form as $\mathbf{K}_m$ with all the mesh stiffnesses that have the mesh frequency of Ω_i^1 (for $\mathbf{K}_{i11}^{\mu}$ and $\mathbf{K}_{i12}^{\mu}$) or Ω_i^2 (for $\mathbf{K}_{i21}^{\mu}$ and $\mathbf{K}_{i22}^{\mu}$) being substituted by the production of relative variation coefficients, their mean values, and the associated Fourier coefficients (for example, $k_{gp}^{silm}(t)$ in $\mathbf{K}_{i11}^{\mu}$ is replaced by $g_{gp}^{si*m}k_{gp}^{si*m}A_{\mu}^{gp,silm}$ and $k_{gp}^{silm}(t)$ in $\mathbf{K}_{i12}\mu$ is replaced by $g_{gp}^{si*m}k_{gp}^{si*m}A_{\mu}^{gp,silm}$), and all other terms in these two matrices are zeros.

7.3 Derivation of General Instability Boundaries for Compound Planetary Gears

Parametric instabilities occur when harmonics of the mesh frequency are close to particular combinations of the natural frequencies [60, 61, 98], that is,

$$\mu\Omega \approx \omega_e + \omega_f \tag{7.6}$$

where Ω is an arbitrary mesh frequency, μ is an arbitrary integer, and ω_e and ω_f are two natural frequencies of the system. Because the rigid-body mode (the mode associated with zero natural frequency) is a special overall mode that does not impact the instabilities of the system, the overall modes that were discussed in the rest of this chapter exclude the rigid-body mode. According to equations of motion in (2.15)-(2.17), the free vibration equation of a purely rotational compound planetary gear is

$$\mathbf{M}\ddot{\boldsymbol{\theta}} + \mathbf{K}(\mathbf{t})\boldsymbol{\theta} = \mathbf{0} \Longrightarrow \mathbf{M}\ddot{\boldsymbol{\theta}} + \mathbf{K}_{\mathbf{iv}}\boldsymbol{\theta} + \mathbf{K}_{\mathbf{v}}(\mathbf{t})\boldsymbol{\theta} = \mathbf{0} \tag{7.7}$$

where the time-invariant mass and stiffness matrices, $\mathbf{M}$ and $\mathbf{K_{iv}}$, are the same as those in (2.18), and the time-varying stiffness matrix $\mathbf{K_v(t)}$ is the same as that in

(7.5). Let $\boldsymbol{\Theta} = [\boldsymbol{\theta}_1, \ \cdots, \ \boldsymbol{\theta}_\Gamma]$ ($\Gamma = a + b + \sum_{i=1}^{a} c^i d^i$ is the total degrees of freedom of the system) be a set of normalized vibration modes (i.e., $\boldsymbol{\Theta}^T \mathbf{M} \boldsymbol{\Theta} = \mathbf{I}$). Application of the modal transformation $\boldsymbol{\theta} = \boldsymbol{\Theta} \boldsymbol{z}$ to (7.7) and insertion of (7.5) into (7.7) yield

$$\ddot{z}_n + \omega_n^2 z_n + 2\epsilon \sum_{w=1}^{\Gamma} \sum_{\mu=1}^{\infty} \sum_{i=1}^{a} \left[\left(K_{i11,nw}^{\mu} \sin \mu \Omega_i^1 t + K_{i12,nw}^{\mu} \cos \mu \Omega_i^1 t \right) + \left(K_{i21,nw}^{\mu} \sin \mu \Omega_i^2 t + K_{i22,nw}^{\mu} \cos \mu \Omega_i^2 t \right) \right] z_w = 0 \tag{7.8}$$

where $n = 1, \ \cdots, \ \Gamma$ (if the first mode is a rigid-body mode, n starts from 2. It is the same for the rest of this chapter), and $K_{i11,nw}^{\mu}$, $K_{i12,nw}^{\mu}$, $K_{i21,nw}^{\mu}$, and $K_{i22,nw}^{\mu}$ are $\boldsymbol{\theta}_n^T \mathbf{K}_{i11}^{\mu} \boldsymbol{\theta}_w$, $\boldsymbol{\theta}_n^T \mathbf{K}_{i21}^{\mu} \boldsymbol{\theta}_w$, $\boldsymbol{\theta}_n^T \mathbf{K}_{i12}^{\mu} \boldsymbol{\theta}_w$, and $\boldsymbol{\theta}_n^T \mathbf{K}_{i22}^{\mu} \boldsymbol{\theta}_w$, respectively. Application of the method of multiple scales gives the form of the solution for (7.8) as

$$z_n = z_{n0}(t, \tau) + \epsilon z_{n1}(t, \tau) + \cdots \tag{7.9}$$

where $\tau = \epsilon t$ and $d/dt \Longrightarrow \partial/\partial t + \epsilon \partial/\partial t$. Insertion of 7.9 into 7.8 gives

$$\frac{\partial^2 z_{n0}}{\partial t^2} + \omega_n^2 z_{n0} = 0 \tag{7.10}$$

$$\frac{\partial^2 z_{n1}}{\partial t^2} + \omega_n^2 z_{n1} = -2 \frac{\partial^2 z_{n0}}{\partial t \partial \tau} - 2 \sum_{w=1}^{\Gamma} \sum_{\mu=1}^{\infty} \sum_{i=1}^{a} \left[\left(K_{i11,nw}^{\mu} \sin \mu \Omega_i^1 t + K_{i12,nw}^{\mu} \cos \mu \Omega_i^1 t \right) + \left(K_{i21,nw}^{\mu} \sin \mu \Omega_i^2 t + K_{i22,nw}^{\mu} \cos \mu \Omega_i^2 t \right) \right] z_{w1} \tag{7.11}$$

where $n = 1, \ \cdots, \ \Gamma$. The solution for (7.10) is

$$z_{n0} = C_n(\tau) e^{j \omega_n t} + cc, \quad n = 1, \ \cdots, \ \Gamma \tag{7.12}$$

where j is the imaginary unit and cc means the complex conjugate of preceding terms. Substitution of (7.12) into (7.11) gives

$$\begin{aligned}\frac{\partial^2 z_{n1}}{\partial t^2} + \omega_n^2 z_{n1} = & -2j\omega_n e^{j\omega_n t}\frac{\partial C_n}{\partial \tau} \\ & - \sum_{w=1}^{\Gamma}\sum_{\mu=1}^{\infty}\sum_{i=1}^{a}\Big[\left(-jK_{i11,nw}^{\mu} + K_{i12,nw}^{\mu}\right)e^{j(\omega_n+\mu\Omega_i^1)t} + \left(jK_{i11,nw}^{\mu} + K_{i12,nw}^{\mu}\right)e^{j(\omega_n-\mu\Omega_i^1)t} \\ & + \left(-jK_{i21,nw}^{\mu} + K_{i22,nw}^{\mu}\right)e^{j(\omega_n+\mu\Omega_i^2)t} + \left(jK_{i21,nw}^{\mu} + K_{i22,nw}^{\mu}\right)e^{j(\omega_n-\mu\Omega_i^2)t}\Big]C_w \\ & + cc \quad n = 1, \ \cdots, \ \Gamma\end{aligned} \tag{7.13}$$

The equations matching with (7.13) in [60, 61, 98] are inconsistent and this study confirms that the discrepancies are caused by the typos in [60, 61]. The resultant equation (7.13) agrees with that in [98].

Without losing generality, when a harmonic of Ω_i^1 is close to the sum of two natural frequencies $\omega_e + \omega_f$ and the harmonics of other mesh frequencies do *not* approach $\omega_e + \omega_f$, secular terms present in (7.13) and parametric instability happens. Such parametric instability that is caused by a individual mesh frequency is classified as *individual-excitation type* of instability in this study, and the condition is

$$\mu\Omega_i^1 = \omega_e + \omega_f + \epsilon\sigma \tag{7.14}$$

where σ is the detuning parameter to be determined.

Multiple mesh frequencies present in compound planetary gears involving stepped-planet or multi-stage structures. It is, hence, possible that the harmonics of two or more mesh frequencies is close to the sum of two natural frequencies $\omega_e + \omega_f$. For this case, secular terms exist in 7.13 and parametric instability also occurs. This kind of instability is caused by multiple mesh frequencies, and it is called *mutual-excitation type* of instability in this chapter. In the rest of this section, the instability boundaries for both types of instabilities are investigated.

7.3.1 Parametric Instability Boundaries for Individual-excitation Type of Instabilities

Depending on the degeneracy of ω_e and ω_f, the solvability conditions for 7.13 are classified into three cases: (A) two distinct eigenvalues (distinct-distinct), (B) one distinct eigenvalue and one degenerate eigenvalue (distinct-degenerate), and (C) two degenerate eigenvalues (degenerate-degenerate). Similar to previous studies [61, 98], to derive the boundaries for single mode and combination instabilities is focus for each cases. The definition of the single mode instability for compound planetary gears is different from that in [98]. In addition to the requirement of $\omega_e = \omega_f$, ω_e and ω_f have to be the same type of natural frequencies. All other cases belong to combination instabilities. That is, if ω_e is an overall frequency and ω_f is a planet frequency, the instability at $\omega_f + \omega_e$ is always a combination one regardless the equality of these two frequencies. Such definition of single mode has no mathematical impact on the following derivation of instabilities but prevents the confusions in terminology.

Case (A): distinct-distinct

When both ω_e and ω_f are distinct, elimination of the secular terms in (7.13) requires [60]

$$\begin{aligned} 2j\omega_e \frac{\partial C_e}{\partial \tau} + \bar{C}_f(-jK^{\mu}_{i11,ef} + K^{\mu}_{i12,ef})e^{\mu\sigma\tau} = 0 \\ 2j\omega_f \frac{\partial C_f}{\partial \tau} + \bar{C}_e(-jK^{\mu}_{i11,fe} + K^{\mu}_{i12,fe})e^{\mu\sigma\tau} = 0 \end{aligned} \tag{7.15}$$

According to [60], the form of the solutions for (7.15) are

$$\begin{aligned} C_e = (R_e + jI_e)e^{-j\varsigma\tau} \\ C_f = (R_f + jI_f)e^{-j(\varsigma+\sigma)\tau} \end{aligned} \tag{7.16}$$

where R_e, I_e, R_f, and I_f are real coefficients independent of τ. ς in (7.16) is the root of the associated characteristic equation that is derived from the eigenvalue problem

by insertion of (7.16) into (7.15) and it is

$$\begin{aligned} \varsigma &= -\frac{1}{2}[\sigma \pm (\sigma^2 - \Lambda^{\mu}_{ef}/(\omega_e\omega_f))^{1/2}] \\ \Lambda^{\mu}_{ef} &= (K^{\mu}_{i11,ef})^2 + (K^{\mu}_{i12,ef})^2 \end{aligned} \tag{7.17}$$

Equations (7.15)-(7.17) suggest that C_e and C_f are unbounded if $\sigma^2 < \Lambda^{\mu}_{ef}/(\omega_e\omega_f)$. Hence, $\sigma = \pm\sqrt{\Lambda^{\mu}_{ef}/(\omega_e\omega_f)}$ separates the stable and unstable regions. The parametric instability boundaries for $\mu\Omega^1_i \approx \omega_e + \omega_f$, hence, are

$$\Omega^1_i = \frac{1}{\mu}[\omega_e + \omega_f \pm \epsilon\sqrt{\Lambda^{\mu}_{ef}/(\omega_e\omega_f)}] \tag{7.18}$$

where Λ^{μ}_{ef} is the instability indicator of the width for the instability region. If $\Lambda^{\mu}_{e(f+x-1)}$ vanishes, the width for the instability region is zero and the instability at $\mu\Omega^1_i = \omega_e + \omega_f$ vanishes. For single mode instability, equation (7.16) can be further simplified as

$$\Omega^1_i = \frac{1}{\mu}[2\omega_e \pm \epsilon\sqrt{\Lambda^{\mu}_{ee}}/\omega_e] \tag{7.19}$$

where $\Lambda^{\mu}_{ee} = (K^{\mu}_{i11,ee})^2 + (K^{\mu}_{i12,ee})^2$ is the instability indicator.

Case (B): distinct-degenerate

When ω_e is a distinct natural frequency and $\omega_f = \cdots = \omega_{f+u-1}$ is a degenerate one with multiplicity u ($u \geq 2$), single mode instability is not possible because ω_e and $\omega_{f,\cdots,f+u-1}$ are always different types of natural frequencies. The elimination of the secular terms in (7.13) leads to $u+1$ equations as

$$\begin{aligned} 2j\omega_e\frac{\partial C_e}{\partial\tau} + \sum_{x=1}^{u}\bar{C}_{f+x-1}(-jK^{\mu}_{i11,e(f+x-1)} + K^{\mu}_{i12,e(f+x-1)})e^{\mu\sigma\tau} = 0 \\ 2j\omega_{f+x-1}\frac{\partial C_{f+x-1}}{\partial\tau} + \bar{C}_e(-jK^{\mu}_{i11,(f+x-1)e} + K^{\mu}_{i12,(f+x-1)e})e^{\mu\sigma\tau} = 0, \quad x = 1,\ \cdots,\ u \end{aligned} \tag{7.20}$$

The solutions for (7.20) have the same form as (7.16). With similar algebraic process of the associated $2(u+1)\times 2(u+1)$ eigenvalue problem as that in (7.17)-(7.19), the

instability boundaries for this case are obtained in closed-form as

$$\Omega_i^1 = \frac{1}{\mu}[\omega_e + \omega_f \pm \epsilon\sqrt{\sum_{x=1}^{u} \Lambda^{\mu}_{e(f+x-1)}/(\omega_e\omega_f)}] \tag{7.21}$$

where $\Lambda^{\mu}_{e(f+x-1)} = (K^{\mu}_{i11,e(f+x-1)})^2 + (K^{\mu}_{i12,e(f+x-1)})^2$ and $\sum_{x=1}^{u} \Lambda^{\mu}_{e(f+x-1)}$ is the instability indicator. Single mode instabilities do not exist for this case because ω_e and $\omega_{f+x-1},\ x = 1,\ \cdots,\ u$ are always different types of natural frequencies.

Case (C): degenerate-degenerate

When $\omega_e = \cdots = \omega_{e+v-1}$ $(v \geq 2)$ and $\omega_f = \cdots = \omega_{f+u-1}$ $(u \geq 2)$ are two degenerate natural frequencies, the solvability conditions of (7.13) yield $v+u$ equations as

$$\begin{aligned} 2j\omega_{e+y-1}\frac{\partial C_{e+y-1}}{\partial \tau} + \sum_{x=1}^{u} \bar{C}_{f+x-1}(-jK^{\mu}_{i11,(e+y-1)(f+x-1)} + K^{\mu}_{i12,(e+y-1)(f+x-1)})e^{\mu\sigma\tau} = 0 \\ y = 1,\ \cdots, v \\ 2j\omega_{f+x-1}\frac{\partial C_{f+x-1}}{\partial \tau} + \sum_{y=1}^{n} \bar{C}_{e+y-1}(-jK^{\mu}_{i11,(f+x-1)(e+y-1)} + K^{\mu}_{i12,(f+x-1)(e+y-1)})e^{\mu\sigma\tau} = 0 \\ x = 1,\ \cdots, u \end{aligned} \tag{7.22}$$

The solutions of (7.22) have the same form as (7.16), producing a $2(v+u) \times 2(v+u)$ eigenvalue problem. Previous studies on simple planetary gears indicate that it is difficult to derive the instability boundaries from such a large size coefficient matrix directly. Provided with modal and mesh phasing conditions, this type of instability is possible to be determined analytically and such analysis is performed in the later part of this study.

Single model instability is possible for this case in compound planetary gears because any degenerate planet frequency belongs to this type. Let $\omega_e = \cdots = \omega_{e+v-1}$. Similar to the distinct-distinct case, the vanishing of the unbounded responses in

(7.13) gives

$$2j\omega_{e+y-1}\frac{\partial C_{e+y-1}}{\partial \tau}+\sum_{x=1}^{v}\bar{C}_{e+x-1}(-jK^{\mu}_{i11,(e+y-1)(e+x-1)}+K^{\mu}_{i12,(e+y-1)(e+x-1)})e^{\mu\sigma\tau}=0$$
$$y=1,\ \cdots,\ v \tag{7.23}$$

The associated coefficient matrix for (7.23) is a $2v\times 2v$ one. Similar to the combination instability, analytical solution can not be derived directly from the coefficient matrix unless $K^{\mu}_{i11,(e+y-1)(e+x-1)}$ and $K^{\mu}_{i12,(e+y-1)(e+x-1)}$ have specific features to further simplified the coefficient matrix. Numerical evaluation can still determine the instability boundaries.

7.3.2 Parametric Instability Boundaries for Mutual-excitation Type of Instabilities

Mutual-excitation type of instabilities happen when the harmonics of two or more mesh frequencies approach the sum of two natural frequencies. Take Ω^1_i and Ω^2_i ($\Omega^1_i\neq\Omega^2_i$) as the representative example. Let $\mu\Omega^1_i=\chi\Omega^2_i=\omega_e+\omega_f+\epsilon\sigma$. Similar to individual-excitation type of instabilities, three cases are studied here: (a) distinct-distinct, (b)distinct-degenerate, and (c) degenerate-degenerate. Application of the same process as that for individual-excitation type of instabilities yields the instability boundaries for case (a) and case (b) as

$$\begin{aligned}\Omega^1_i=\frac{\chi}{\mu}\Omega^2_i&=\frac{1}{\mu}[\omega_e+\omega_f\pm\epsilon\sqrt{\Pi^{\mu}_{ef}/(\omega_e\omega_f)}]\quad\text{case (a)}\\ \Omega^1_i=\frac{\chi}{\mu}\Omega^2_i&=\frac{1}{\mu}[\omega_e+\omega_f\pm\epsilon\sqrt{\sum_{x=1}^{u}\Pi^{\mu}_{e(f+x-1)}/(\omega_e\omega_f)}]\quad\text{case (b)}\end{aligned} \tag{7.24}$$

where $\Pi^{\mu}_{e(f+x-1)}=(K^{\mu}_{i11,e(f+x-1)}+K^{\chi}_{i21,e(f+x-1)})^2+(K^{\mu}_{i12,e(f+x-1)}+K^{\chi}_{i22,e(f+x-1)})^2$ ($x=1,\ \cdots,\ u$) and $\sum_{x=1}^{u}\Pi^{\mu}_{e(f+x-1)}$ is the instability indicator. The forcing of $\omega_e=\omega_f$ in (7.24) gives the single mode instability boundaries for case (a).

For case (c), the solvability conditions of (7.13) produce $v+u$ equations for combination instabilities as

$$\begin{aligned}
&2j\omega_{e+y-1}\frac{\partial C_{e+y-1}}{\partial \tau}+\sum_{x=1}^{u}\bar{C}_{f+x-1}\Big[(-jK^{\mu}_{i11,(e+y-1)(f+x-1)}+K^{\mu}_{i12,(e+y-1)(f+x-1)})\\
&\quad+(-jK^{\chi}_{i21,(e+y-1)(f+x-1)}+K^{\chi}_{i22,(e+y-1)(f+x-1)})\Big]e^{\mu\sigma\tau}=0,\quad y=1,\ \cdots,v\\
&2j\omega_{f+x-1}\frac{\partial C_{f+x-1}}{\partial \tau}+\sum_{y=1}^{n}\bar{C}_{e+y-1}\Big[(-jK^{\mu}_{i11,(f+x-1)(e+y-1)}+K^{\mu}_{i12,(f+x-1)(e+y-1)})\\
&\quad+(-jK^{\chi}_{i21,(f+x-1)(e+y-1)}+K^{\chi}_{i22,(f+x-1)(e+y-1)})\Big]e^{\mu\sigma\tau}=0,\quad x=1,\ \cdots,u
\end{aligned}\tag{7.25}$$

For single mode instabilities, the associated solvability conditions are simplified as

$$\begin{aligned}
&2j\omega_{e+y-1}\frac{\partial C_{e+y-1}}{\partial \tau}+\sum_{x=1}^{v}\bar{C}_{e+x-1}\Big[(-jK^{\mu}_{i11,(e+y-1)(e+x-1)}+K^{\mu}_{i12,(e+y-1)(e+x-1)})\\
&\quad+(-jK^{\chi}_{i21,(e+y-1)(e+x-1)}+K^{\chi}_{i22,(e+y-1)(e+x-1)})\Big]e^{\mu\sigma\tau}=0,\quad y=1,\ \cdots,v
\end{aligned}\tag{7.26}$$

Compared with (7.22) and (7.23), the additional terms in (7.25) and (7.26) are caused by the excitation from χth harmonic of Ω_i^2. Same as the individual-excitation type, the instability boundaries cannot be analytically determined from the coefficient matrix of (7.25) and (7.26).

The above analytical expressions for instability boundaries indicate that $K^{\mu}_{i11,ef}$, $K^{\mu}_{i12,ef}$, $K^{\chi}_{i21,ef}$, and $K^{\chi}_{i22,ef}$ are critical for the determination of the instability boundaries and they are called *key instability terms* in this investigation. Algebraic manipulation of equations (7.5), (7.7), and (7.8) yields the analytical expression for these

key instability terms as

$$
\begin{aligned}
K^{\mu}_{i11,ef} = \boldsymbol{\theta}_e^T \mathbf{K}^{\mu}_{i11} \boldsymbol{\theta}_f = & \sum_{s,m} \underbrace{g_{gp}^{si*m} k_{gp}^{si*m} \sum_{l}^{c^i} A_{\mu}^{gp,silm} \delta_{gp,e}^{silm} \delta_{gp,f}^{silm}}_{\text{central gear}-\text{planet meshes with } \Omega_{\text{i}}^1 \text{ mesh frequency}} \\
& + \sum_{m,q} \underbrace{g_{pp}^{i*mq} k_{pp}^{i*mq} \sum_{l}^{c^i} A_{\mu}^{pp,ilmq} \delta_{pp,e}^{ilmq} \delta_{pp,f}^{ilmq}}_{\text{planet}-\text{planet meshes with } \Omega_{\text{i}}^1 \text{ mesh frequency}} \\
K^{\mu}_{i12,ef} = \boldsymbol{\theta}_e^T \mathbf{K}^{\mu}_{i12} \boldsymbol{\theta}_f = & \sum_{s,m} \underbrace{g_{gp}^{si*m} k_{gp}^{si*m} \sum_{l}^{c^i} B_{\mu}^{gp,silm} \delta_{gp,e}^{silm} \delta_{gp,f}^{silm}}_{\text{central gear}-\text{planet meshes with } \Omega_{\text{i}}^1 \text{ mesh frequency}} \\
& + \sum_{m,q} \underbrace{g_{pp}^{i*mq} k_{pp}^{i*mq} \sum_{l}^{c^i} B_{\mu}^{pp,ilmq} \delta_{pp,e}^{ilmq} \delta_{pp,f}^{ilmq}}_{\text{planet}-\text{planet meshes with } \Omega_{\text{i}}^1 \text{ mesh frequency}} \\
K^{\chi}_{i21,ef} = \boldsymbol{\theta}_e^T \mathbf{K}^{\chi}_{i21} \boldsymbol{\theta}_f = & \sum_{r,q} \underbrace{g_{gp}^{ri*q} k_{gp}^{ri*q} \sum_{l}^{c^i} A_{\chi}^{gp,rilq} \delta_{gp,e}^{rilq} \delta_{gp,f}^{rilq}}_{\text{central gear}-\text{planet meshes with } \Omega_{\text{i}}^2 \text{ mesh frequency}} \\
& + \sum_{t,w} \underbrace{g_{pp}^{i*tw} k_{pp}^{i*tw} \sum_{l}^{c^i} A_{\mu}^{pp,iltw} \delta_{pp,e}^{iltw} \delta_{pp,f}^{iltw}}_{\text{planet}-\text{planet meshes with } \Omega_{\text{i}}^2 \text{ mesh frequency}} \\
K^{\chi}_{i22,ef} = \boldsymbol{\theta}_e^T \mathbf{K}^{\chi}_{i22} \boldsymbol{\theta}_f = & \sum_{r,q} \underbrace{g_{gp}^{ri*q} k_{gp}^{ri*q} \sum_{l}^{c^i} B_{\chi}^{gp,rilq} \delta_{gp,e}^{rilq} \delta_{gp,f}^{rilq}}_{\text{central gear}-\text{planet meshes with } \Omega_{\text{i}}^2 \text{ mesh frequency}} \\
& + \sum_{t,w} \underbrace{g_{pp}^{i*tw} k_{pp}^{i*tw} \sum_{l}^{c^i} B_{\chi}^{pp,iltw} \delta_{pp,e}^{iltw} \delta_{pp,f}^{iltw}}_{\text{planet}-\text{planet meshes with } \Omega_{\text{i}}^2 \text{ mesh frequency}}
\end{aligned}
\tag{7.27}
$$

where $\delta_{gp,e}^{silm}$ (gear mesh deflection between central gear s and planet m in train l of planet set i in vibration mode e) and $\delta_{pp,e}^{ilmq}$ (gear mesh deflection between planets m and q in train l of planet set i in vibration mode e) are given in (2.6) and (2.9), respectively. Equation (7.27) shows that key instability terms depend on modal gear

mesh deflections and the Fourier coefficients in terms of mesh parameters (contact ratios, peak-to-peak amplitudes of mesh stiffness variation, and etc.). Insertion of (7.3) and (7.27) into (7.18), (7.21), (7.22), (7.23), (7.24), (7.25), and (7.26) yields the expressions for the instability boundaries or associated governing equations in terms of mesh parameters, and the impacts of mesh parameters on the instability regions can be predicted parametrically.

7.4 Impacts of Modal Properties and Mesh Phasing Conditions on Compound Planetary Gear Instabilities

Studies in previous chapters show that compound planetary gears, similar to simple planetary gears, have well-defined modal properties and unique dynamic response excitation/suppression patterns depending on different mesh phasing conditions. Because different modal properties and mesh phasing conditions impact modal gear mesh deflections which determines the key instability terms in (7.27), it is important to understand how compound planetary gear parametric instability boundaries are affected by different modal properties and mesh phasing conditions. To simplify the modal structure of the following discussions, the investigation scope is limited to the systems with three or more planet trains in each stage (i.e., $c^i \geq 3$) such that any distinct frequency is associated a overall mode and any degenerate frequency is a planet frequency. The results of chapters 5 and 6 show that there are two mesh phasing conditions for stage i phasing quantities k_μ (i.e., $k_\mu = 0$ and $k_\mu \neq 0$) and $\bar{k}_\chi$ (i.e., $\bar{k}_\chi = 0$ and $\bar{k}_\chi \neq 0$), respectively. Combining these mesh phasing conditions with the parametric instabilities types for compound planetary gears, the following situations are studied: (i) individual excitation with zero phasing quantity ($k_\mu = 0$), (ii) individual excitation with nonzero phasing quantity ($k_\mu \neq 0$), (iii) mutual excitation

with zero phasing quantities ($k_\mu,\ \bar{k}_\chi = 0$), (iv) mutual excitation with nonzero phasing quantities ($k_\mu \neq= 0$ and $\bar{k}_\chi \neq 0$), and (v) mutual excitation with mixed phasing quantities ($k_\mu = 0$ and $\bar{k}_\chi \neq 0$, or vice versa).

7.4.1 Individual and Mutual Excitations with Zero Phasing Quantities

Due to the high similarity, the investigations on situations (i) and (iii) are combined in this section. The individual excitation with zero phasing quantity is first investigated and the three cases of instabilities, (1) distinct-distinct, (2) distinct-degenerate, and (3) degenerate-degenerate, are addressed as follows.

Case (1): distinct-distinct

The distinct natural frequencies in this study can only be overall frequencies. For two arbitrary distinct natural frequencies, ω_e and ω_f, the overall mode properties lead to

$$\begin{aligned} \delta_{gp,e}^{silm} &= \delta_{gp,e}^{si*m} \\ \delta_{gp,f}^{silm} &= \delta_{gp,f}^{si*m} \\ \delta_{pp,e}^{ilmq} &= \delta_{pp,e}^{i*mq} \\ \delta_{pp,f}^{ilmq} &= \delta_{pp,f}^{i*mq} \end{aligned} \tag{7.28}$$

where $l = 1,\ \cdots,\ c^i$. The zero-phasing-quantity condition ensures that the Fourier coefficients $A_\mu^{gp,silm}$, $B_\mu^{gp,silm}$, $A_\mu^{pp,ilmq}$, and $B_\mu^{pp,ilmq}$ are independent of planet trains. Replacing l with $*$ for these Fourier coefficients, moving them out of the summations

in (7.27), and insertion of (7.28) into (7.27) give

$$\begin{aligned} K^{\mu}_{i11,ef} = \boldsymbol{\theta}_e^T \mathbf{K}^{\mu}_{i11} \boldsymbol{\theta}_f &= \sum_{s,m} c^i g^{si*m}_{gp} k^{si*m}_{gp} A^{gp,si*m}_{\mu} \delta^{si*m}_{gp,e} \delta^{si*m}_{gp,f} \\ &\quad + \sum_{m,q} c^i g^{i*mq}_{pp} k^{i*mq}_{pp} A^{pp,i*mq}_{\mu} \delta^{i*mq}_{pp,e} \delta^{i*mq}_{pp,f} \\ K^{\mu}_{i12,ef} = \boldsymbol{\theta}_e^T \mathbf{K}^{\mu}_{i12} \boldsymbol{\theta}_f &= \sum_{s,m} c^i g^{si*m}_{gp} k^{si*m}_{gp} B^{gp,si*m}_{\mu} \delta^{si*m}_{gp,e} \delta^{si*m}_{gp,f} \\ &\quad + \sum_{m,q} c^i g^{i*mq}_{pp} k^{i*mq}_{pp} B^{pp,i*mq}_{\mu} \delta^{i*mq}_{pp,e} \delta^{i*mq}_{pp,f} \end{aligned} \tag{7.29}$$

Substitution of (7.29) into the expression of the associated instability indicator, Λ^{μ}_{ef}, gives

$$\begin{aligned} \Lambda^{\mu}_{ef} &= (K^{\mu}_{i11,ef})^2 + (K^{\mu}_{i12,ef})^2 \\ &= \left[\sum_{s,m} c^i g^{si*m}_{gp} k^{si*m}_{gp} A^{gp,si*m}_{\mu} \delta^{si*m}_{gp,e} \delta^{si*m}_{gp,f} + \sum_{m,q} c^i g^{i*mq}_{pp} k^{i*mq}_{pp} A^{pp,i*mq}_{\mu} \delta^{i*mq}_{pp,e} \delta^{i*mq}_{pp,f} \right]^2 \\ &\quad + \left[\sum_{s,m} c^i g^{si*m}_{gp} k^{si*m}_{gp} B^{gp,si*m}_{\mu} \delta^{si*m}_{gp,e} \delta^{si*m}_{gp,f} + \sum_{m,q} c^i g^{i*mq}_{pp} k^{i*mq}_{pp} B^{pp,i*mq}_{\mu} \delta^{i*mq}_{pp,e} \delta^{i*mq}_{pp,f} \right]^2 \end{aligned} \tag{7.30}$$

Because $\delta^{si*m}_{gp,e} \delta^{si*m}_{gp,f}$ and $\delta^{i*mq}_{pp,e} \delta^{i*mq}_{pp,f}$ are not zero for any overall modes except the rigid-body mode, Λ^{μ}_{ef} is not equal to zero in general. The instability boundary, hence, does not vanish for most of the cases. Under certain circumstances, however, Λ^{μ}_{ef} in (7.30) may be canceled out. For example, the condition that $\sin(\mu\pi c^{si*m}_{gp}) = 0$ for all central gear-planet meshes with Ω^1_i mesh frequency and $\sin(\mu\pi c^{i*mq}_{pp}) = 0$ for all planet-planet meshes with Ω^1_i mesh frequency is sufficient to force all the Fourier coefficients $A^{gp,si*m}_{\mu}$, $B^{gp,si*m}_{\mu}$, $A^{pp,i*mq}_{\mu}$, and $B^{pp,i*mq}_{\mu}$ to be zero. For such a particular case, the instability at $\mu\Omega^1_i = \omega_e + \omega_f$ vanishes. The same conclusion applies to distinct-distinct single mode instabilities.

Case (2): distinct-degenerate

When ω_e is a overall frequency and $\omega_f = \cdots = \omega_{f+u-1}$ is a planet frequency with multiplicity u, the modal properties for overall and planet modes yield

$$\sum_{l=1}^{c^i} \delta_{gp,e}^{silm} \delta_{gp,(f+x-1)}^{silm} = 0, \quad x = 1, \ \cdots, \ u \tag{7.31}$$

Therefore, $K_{i11,e(f+x-1)}^{\mu}$ and $K_{i12,e(f+x-1)}^{\mu}$ $(x = 1, \ \cdots, \ u)$ are zero and the instability indicator is canceled out. That is, the instability at $\mu\Omega_i^1 = \omega_e + \omega_f$ disappears if ω_e is a overall frequency, and ω_f is a planet frequency with multiplicity $u \geq 2$.

Case (3): degenerate-degenerate

If $\omega_e = \cdots = \omega_{e+v-1}$ and $\omega_f = \cdots = \omega_{f+u-1}$ are two degenerate natural frequencies with multiplicities v $(v \geq 2)$ and u $(u \geq 2)$ and they are planet frequencies for different stages, the planet mode properties (2.33) ensure that $\delta_{gp,e}^{si*m}\delta_{gp,f}^{si*m}$ and $\delta_{pp,e}^{i*mq}\delta_{pp,f}^{i*mq}$ are zero because only the components in one stage have motions in any planet mode. Equation (7.25), hence, is simplified as

$$\begin{aligned} 2j\omega_{e+y-1}\frac{\partial C_{e+y-1}}{\partial \tau} &= 0, \quad y = 1, \ \cdots, \ v \\ 2j\omega_{f+x-1}\frac{\partial C_{f+x-1}}{\partial \tau} &= 0, \quad x = 1, \ \cdots, \ u \end{aligned} \tag{7.32}$$

C_{e+y-1} and C_{f+x-1} are bounded in equation (7.32) and it suggests that the instability at $\mu\Omega_i^1 = \omega_e + \omega_f$ vanishes when the two planet frequencies are for two different stages.

When the two planet frequencies are for the same stage, u has to equal to v for this case. Let $\omega_e = \cdots = \omega_{e+u-1}$, $\omega_f = \cdots = \omega_{f+u-1}$ $(u \geq 2)$, and $\omega_e \neq \omega_f$. Application of the planet mode properties (2.33), insertion of the Fourier coefficients in (7.3) and the closed-form solutions for v^l in (6.42) into (2.6) and (2.9), and use of the trigonometric

identities in (6.15) yield

$$\begin{aligned}
\sum_{l=1}^{c^i} \delta_{gp,e}^{silm} \delta_{gp,f}^{silm} &= 0 \\
\sum_{l=1}^{c^i} \delta_{gp,e}^{silm} \delta_{gp,e}^{silm} &= \Delta_{gp,e}^{si*m} \\
\sum_{l=1}^{c^i} \delta_{pp,e}^{ilmq} \delta_{pp,f}^{ilmq} &= 0 \\
\sum_{l=1}^{c^i} \delta_{pp,e}^{ilmq} \delta_{pp,e}^{ilmq} &= \Delta_{pp,e}^{i*mq}
\end{aligned} \tag{7.33}$$

where $\Delta_{gp,e}^{silm}$ and $\Delta_{pp,e}^{ilmq}$ are not equal to zero. Insertion of (7.33) into (7.22) directly gives the same equation as (7.32). The instability boundaries, hence, vanish for this case. This result agrees with the mesh phasing rules in chapter 6 that planet mode responses are suppressed when $k_\mu \neq= 0$.

For single mode instability, however, the instability may exist. Insertion of (7.33) into (7.23) gives

$$\begin{aligned}
2j\omega_{e+y-1}\frac{\partial C_{e+y-1}}{\partial \tau} + \bar{C}_{e+y-1}\Bigg[-j\left(\sum_{s,m} A_\mu^{gp,si*m} X_{gp,e+y-1}^{si*m} + \sum_{m,q} A_\mu^{pp,i*mq} Y_{pp,e+y-1}^{i*mq}\right) \\
+ \left(\sum_{s,m} B_\mu^{gp,si*m} X_{gp,e+y-1}^{si*m} + \sum_{m,q} B_\mu^{pp,i*mq} Y_{pp,e+y-1}^{i*mq}\right)\Bigg] e^{\mu\sigma\tau} = 0 \\
y = 1, \ \cdots, \ v
\end{aligned} \tag{7.34}$$

where $X_{gp,e+y-1}^{si*m} = g_{gp}^{si*m} k_{gp}^{si*m} \Delta_{gp}^{si*m}$, and $Y_{pp,e+y-1}^{i*mq} = g_{pp}^{i*mq} k_{pp}^{i*mq} \Delta_{pp}^{i*mq}$. Equation (7.34) indicates that all C_{e+y-1} $(y = 1, \ \cdots, \ v)$ are decoupled. Application of the same process as that in case (A) in section 7.3.1 yields the instability indicators for single

mode instabilities of planet frequencies as

$$\begin{aligned}\Lambda^{\mu}_{(e+y-1)(e+y-1)} &= \left(\sum_{s,m} A^{gp,si*m}_{\mu} X^{si*m}_{gp,e+y-1} + \sum_{m,q} A^{pp,i*mq}_{\mu} Y^{i*mq}_{pp,e+y-1}\right)^2 \\ &+ \left(\sum_{s,m} B^{gp,si*m}_{\mu} X^{si*m}_{gp,e+y-1} + \sum_{m,q} B^{pp,i*mq}_{\mu} Y^{i*mq}_{pp,e+y-1}\right)^2, \quad y = 1, \ \cdots, \ v \\ \Omega^1_i &= \frac{1}{\mu}[2\omega_e \pm \epsilon\sqrt{\max_{y=1, \ \cdots, \ v}(\Lambda^{\mu}_{(e+y-1)(e+y-1)})}/\omega_e]\end{aligned} \tag{7.35}$$

Because $\Lambda^{\mu}_{(e+y-1)(e+y-1)}$ in equation (7.35) is not equal to zero for any planet mode, single mode instabilities always exist for planet frequencies as long as the Fourier coefficients are not equal zero. In another word, the mesh phasing rules in chapter 6 that planet responses are suppressed when $k_\mu = 0$ is no longer hold in case of the single mode instabilities for planet frequencies. This result agrees with the findings in previous studies on simple planetary gears [61, 98].

For mutual excitations with zero phasing quantities($k_\mu, \ \bar{k}_\chi = 0$, and $\mu\Omega^1_i = \chi\Omega^2_i = \omega_e + \omega_f$), the same analytical process as above applies and the results are the same with the exception that $K^{\chi}_{i21,ef}$ and $K^{\chi}_{i22,ef}$ participate in all the instability expressions and $\Pi^{\mu}_{e(f+x-1)}$ replaces $\Lambda^{\mu}_{e(f+x-1)}$ ($x = 1, \ \cdots, \ u$).

7.4.2 Individual and Mutual Excitations with Nonzero Phasing Quantities

When stage i phasing quantities ($k_\mu, \ \bar{k}_\chi$) are not zero, application of the trigonometric identities in (6.15) to the Fourier coefficients $A^{gp,silm}_{\mu}$, $B^{gp,silm}_{\mu}$, $A^{pp,ilmq}_{\mu}$, and $B^{pp,ilmq}_{\mu}$ yields

$$A^{gp,silm}_{\mu} = B^{gp,silm}_{\mu} = A^{pp,ilmq}_{\mu} = B^{pp,ilmq}_{\mu} = 0 \tag{7.36}$$

Equation (7.36) is valid for any individual or mutual excitations with nonzero phasing quantities.

Similar to previous section, individual excitation with nonzero phasing quantity is investigated for three cases (I) distinct-distinct, (II) distinct-degenerate, and (III) degenerate-degenerate. For case (I), insertion of (7.36) into (7.27) produces

$$\begin{aligned} K^{\mu}_{i11,ef} &= 0 \\ K^{\mu}_{i12,ef} &= 0 \end{aligned} \tag{7.37}$$

The associated instability indicator $\Lambda^{\mu}_{ef} = (K^{\mu}_{i11,ef})^2 + (K^{\mu}_{i12,ef})^2$, hence, is zero. That is, the instability for case (I) vanishes for nonzero phasing quantity. It is the same for single mode instabilities. Such result indicates that the mesh phasing rule that overall mode responses are always suppressed when $k_{\mu} \neq 0$ still holds for distinct-distinct type of instabilities.

For cases (II) and (III), it is difficult to obtain simple expressions for the instability boundaries and the instability conditions have to calculated from equations (7.20), (7.22), and (7.23). As long as $K^{\mu}_{i11,ef}$ and $K^{\mu}_{i12,ef}$ in these equations equal zero (such as two planet frequencies of different stages), the instability boundaries vanish.

The same analytical process applies to mutual excitation with nonzero phasing quantity and the results are the same except that $K^{\chi}_{i21,ef}$ and $K^{\chi}_{i22,ef}$ participate in all the instability expressions and equations (7.24), (7.25), and (7.26 are used for cases (II) and (III).

7.4.3 Mutual Excitation with Mixed Phasing Quantities

The situation of mixed phasing quantities is only possible for mutual-excitation type of instability. Without losing generality, k_{μ} is zero and $\bar{k}_{\chi}$ is not equal to zero. Three cases of instabilities, (α) distinct-distinct, (β) distinct-degenerate, and (γ) degenerate-degenerate, are investigated. For case (α), the phasing condition of $k_{\mu} = 0$ ensures that the Fourier coefficients $A^{gp,silm}_{\mu}$, $B^{gp,silm}_{\mu}$, $A^{pp,ilmq}_{\mu}$, and $B^{pp,ilmq}_{\mu}$ are

independent of planet trains and $K^{\mu}_{i11,ef}$ and $K^{\mu}_{i12,ef}$ satisfies (7.29). The phasing condition of $\bar{k}_{\chi} \neq 0$ leads to

$$\begin{aligned} K^{\chi}_{i21,ef} &= 0 \\ K^{\chi}_{i22,ef} &= 0 \end{aligned} \tag{7.38}$$

Insertion of (7.29) and (7.38) into the expression of the associated instability indicator in (7.24) gives

$$\begin{aligned} \Pi^{\mu}_{ef} &= (K^{\mu}_{i11,ef})^2 + (K^{\mu}_{i12,ef})^2 \\ &= \left[\sum_{s,m} c^i g^{si*m}_{gp} k^{si*m}_{gp} A^{gp,si*m}_{\mu} \delta^{si*m}_{gp,e} \delta^{si*m}_{gp,f} + \sum_{m,q} c^i g^{i*mq}_{pp} k^{i*mq}_{pp} A^{pp,i*mq}_{\mu} \delta^{i*mq}_{pp,e} \delta^{i*mq}_{pp,f} \right]^2 \\ &+ \left[\sum_{s,m} c^i g^{si*m}_{gp} k^{si*m}_{gp} B^{gp,si*m}_{\mu} \delta^{si*m}_{gp,e} \delta^{si*m}_{gp,f} + \sum_{m,q} c^i g^{i*mq}_{pp} k^{i*mq}_{pp} B^{pp,i*mq}_{\mu} \delta^{i*mq}_{pp,e} \delta^{i*mq}_{pp,f} \right]^2 \end{aligned} \tag{7.39}$$

The right-hand side of equation (7.39) is identical to that (7.30) and it is the result of the mutual effects of the cancellation of $K^{\chi}_{i21,ef}$ and $K^{\chi}_{i22,ef}$ (caused by $\bar{k}_{\chi} \neq 0$) and planet-train independent Fourier coefficients $A^{gp,silm}_{\mu}$, $B^{gp,silm}_{\mu}$, $A^{pp,ilmq}_{\mu}$, and $B^{pp,ilmq}_{\mu}$ (cased by $k_{\mu} = 0$). The instability boundaries for this case of mutual excitation with mixed phasing quantities, hence, do not vanish in general and follow the same rule as that for case (A) of individual excitation with zero phasing quantity.

For cases (β) and (γ), simple expressions cannot be derived and equations (7.24), (7.25), and (7.26) have to used to determine the associated instability boundaries. The vanishing of the instability boundaries is still possible for these cases, if $K^{\mu}_{i11,ef}$, $K^{\mu}_{i12,ef}$, $K^{\chi}_{i21,ef}$, and $K^{\chi}_{i22,ef}$ are all zeros.

Table 7.1 summarizes the above analysis results on compound planetary gear parametric instability boundaries with different modal and phasing conditions.

Table 7.1: Compound planetary gear parametric instability boundaries for different modal and phasing conditions.

	Individual excitations: $\mu\Omega_i^1 = \omega_e + \omega_f$				
	Distinct-distinct (combination)	Distinct-distinct (single mode)	Distinct-degenerate	Degenerate-degenerate (combination)	Degenerate-degenerate (single mode)
$k_\mu = 0$	exist in general (equation (7.30))	exist in general (equation (7.30))	always vanish	always vanish	exist in general (equations (7.34) and (7.35))
$k_\mu \neq 0$	always vanish	always vanish	equation (7.20)	equation (7.22)	equation (7.23)

	Mutual excitations: $\mu\Omega_i^1 = \chi\Omega_i^2 = \omega_e + \omega_f$				
	Distinct-distinct (combination)	Distinct-distinct (single mode)	Distinct-degenerate	Degenerate-degenerate (combination)	Degenerate-degenerate (single mode)
$k_\mu = 0$, $\bar{k}_\chi = 0$	exist in general (equation (7.24))	exist in general (equation (7.24))	always vanish	always vanish	exist in general (equation (7.26))
$k_\mu \neq 0$, $\bar{k}_\chi \neq 0$	always vanish	always vanish	equation (7.24)	equation (7.25)	equation (7.26))
$k_\mu = 0$, $\bar{k}_\chi \neq 0$	exist in general (equation (7.39))	equation (7.24)	equation (7.24)	equation (7.25)	equations (7.26)

7.5 Conclusions

This chapter analytically investigates the parametric instabilities caused by mesh stiffness variations in compound planetary gears. The instability boundaries are analytically derived for purely rotational systems. Both individual and mutual (unique to compound planetary gears) types of excitations are investigated and the instability

boundaries are analytically determined in terms of mesh parameters. Application of the well-defined modal properties and specific mesh phasing conditions reduces the instability boundary expressions to simple, closed-form formulae. Under particular phasing conditions, some parametric instabilities vanish while other do not. Overall frequency instabilities, regardless they are combination or single mode instabilities, always vanish when the associated phasing quantities are not equal to zero. Planet frequency instabilities, however, violate the mesh phasing rules when they are single mode instabilities. For combination planet frequency instabilities, the mesh phasing rules still hold. The conclusions from this study are consistent with all previous studies on simple planetary gears.

Chapter 8: BACK-SIDE CONTACT GEAR MESH STIFFNESS

8.1 Introduction

Back-side contact in a gear mesh contact refers to the contact at the back side of gear teeth. Recent studies on gear dynamics [34,39,54,84] show that it is possible for tooth wedging (or tight mesh), the simultaneous drive-side and back-side contacts, to happen in real applications, such as wind turbine gearboxes. Tooth wedging is the combined effect of gravity and bearing clearance nonlinearity, and it is a major source of gearbox failures, especially the bearing fails. For better understanding of the impact of tooth wedging on gearbox failures, it is important to develop a model that includes the accurate description of the back-side contact mesh stiffness.

Besides tooth wedging, the anti-backlash gear is another case for back-side contact to occur. To minimize the undesirable characteristics which are caused by backlash, anti-backlash gears typically eliminate the backlash by using certain preloaded springs to force the fixed part of the driving gear to be in contact with the drive side of the driven gear teeth and simultaneously the free part of the driving gear to be in contact with the back side of the driven gear teeth [18]. Analytical studies on anti-backlash gear dynamics are necessary to prevent excessive vibration and noise in anti-backlash

gears and optimize the design for such systems. The accurate modeling of back-side contact mesh stiffness is important to support such analytical studies.

Mesh stiffness variation and its impact on gear dynamics were extensively investigated in previous studies. Parametric excitation caused by mesh stiffness variation along with clearance nonlinearity for a single mesh gear was studied in [49]. Lin and Parker systematically analyzed the mesh stiffness variation instabilities in two-stage gear systems [60], as well as in simple planetary gear systems [61]. Their studies showed that the parametric excitation from the time-varying mesh stiffness causes instability and severe vibration under certain operating conditions. They applied a perturbation method to analytically determine the instability conditions. Wu and Parker [98] extended the study on parametric instability to planetary gears with elastic continuum ring Gears. Sun and Hu [90] investigated the mesh stiffness parametric excitation and clearance nonlinearity for simple planetary gears. Bahk and Parker [9] derived closed-form solutions for the dynamic response of planetary gears with time-varying mesh stiffness and tooth separation nonlinearity based on a purely torsional planetary gear model. Guo and Parker [34] modeled and analyzed a simple planetary gear with time-varying mesh stiffness, tooth wedging, and bearing clearance nonlinearity. Although the back-side contact is included in their model, the average value of the periodic mesh stiffness on the drive-side is used to approximate the back-side mesh stiffness which is not an accurate description of the back-side mesh stiffness.

Despite the abundance of the literature on mesh stiffness variation and gear dynamics, no studies have tried to derive the back-side mesh stiffness in their analytical model. One possible reason is that the symmetry of gear tooth ensures that the contact ratios, mesh periods, and average mesh stiffnesses over the mesh period are the

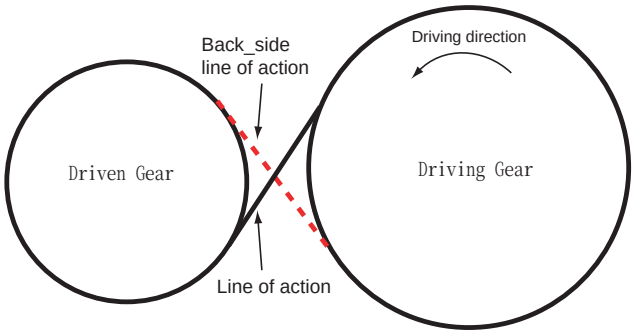

Figure 8.1: Drive-side gear contact model (solid line) and back-side gear contact model (dashed line)

same for both the drive- and back-side contacts. This may mislead some researchers to assume that the back-side mesh stiffness is the same as the drive-side one. The back-side mesh stiffness, however, is not equivalent to the drive-side one, because the back-side contact is along the back-side line of action (the dashed line in Figure 8.1) and the number of gear teeth in contact along the back-side line of action is not always equal to that along the line of action (the solid line in Figure 8.1). Figure 8.2 (the simulation results from Calyx [96], a multi-body finite element program with precise gear mesh contact) illustrates one such case. There are two pairs of gear teeth in contact along the back-side line of action, while only one pair of teeth in contact along the line of action. Therefore, the back-side mesh stiffness differs from the drive-side mesh stiffness at this moment. If the variation of the back-side mesh stiffness is not modeled correctly, the results from the model is questionable. Therefore, it is important to have a clear understanding of back-side mesh stiffness. In addition, how the backlash impacts the phase lag of the back-side mesh stiffness is not studied in previous literature and it is investigated in this work as well.

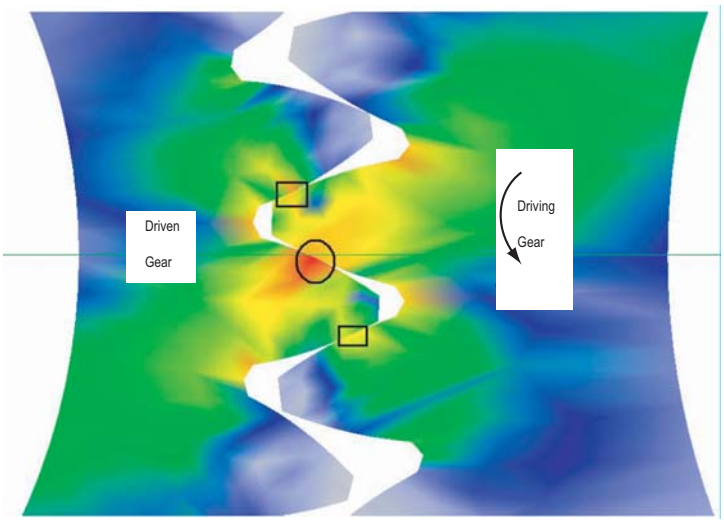

Figure 8.2: Numerical simulation of Calyx on an ideal gear pair with both drive-side and back-side gear contacts. One pair of teeth (marked by a circle) is in contact along the drive-side line of action, and two pairs of teeth (marked by two rectangles) are in contact along the back-side line of action.

8.2 Derivation of Back-side Mesh Stiffness

The drive-side mesh stiffness refers to the stiffness that reflects the compliance of the nominally contacting teeth at a mesh. It varies as the number of teeth in contact fluctuates during the rotation of the gear system. The stiffness acts along the line of action and its variation function's period is known for a given rotation speed. Mesh stiffness variation functions are often approximated by Fourier series in analytically studies and they can also be accurately calculated by Finite Element Method (FEM) software. The drive-side mesh stiffness function is critical to the analytical studies on gear dynamics [6, 7, 9, 76, 78].

Similar to the drive-side mesh stiffness, the back-side mesh stiffness in this study is the stiffness that reflects the change of the in-contact gear tooth number along the

back-side line of action. It is not straightforward to determine or calculate because the back-side contact does not occur until tooth wedging happens due to the existence of backlash. In order to get simultaneous drive-side and back-side contacts at all times, in the following sections an ideal gear pair (a gear pair which operates at the nominal center distance and has zero backlash tooth thickness) is first investigated. Then the results of the ideal gear pair is extended to arbitrary gear pairs with backlash and anti-backlash gears.

Back-side Mesh Stiffness for an Ideal Gear Pair

Figure 8.3 illustrates the drive-side and back-side contacts for an arbitrary ideal gear pair. Z_{dr} and Z_{dn} are the tooth numbers of the driving and driven gears, respectively. T is the mesh period of this gear pair. At $t = 0$, the pitch point at the drive side of the driving gear is in mesh (Figure 8.3a). The dashed line in the middle of each sub-figure is the center line between the two gears. After one mesh period T, the driving gear tooth moves one driving gear circular pitch $p_{dr} = \frac{2\pi r_{dr}}{Z_{dr}}$, and the driven gear tooth moves $p_{dn} = \frac{2\pi r_{dn}}{Z_{dn}}$ (r_{dr} and r_{dn} are the pitch radii). After one fourth of the mesh period ($t = \frac{T}{4}$), the driving gear tooth moves one fourth of its circular pitch. Because there is no backlash along the pitch circle, the circular tooth thickness of the driving gear q_{dr} is equal to

$$q_{dr} = \frac{1}{2} p_{dr} \tag{8.1}$$

The movement of the driving gear is equivalent to half of its circular tooth thickness $\frac{1}{2} q_{dr}$. Thus, at $t = \frac{T}{4}$ the center line passes through the middle of the tooth tip of the driving gear (Figure 8.3b). At this moment both gears are symmetric about the center line and the number of gear teeth in contact along the drive-side line of

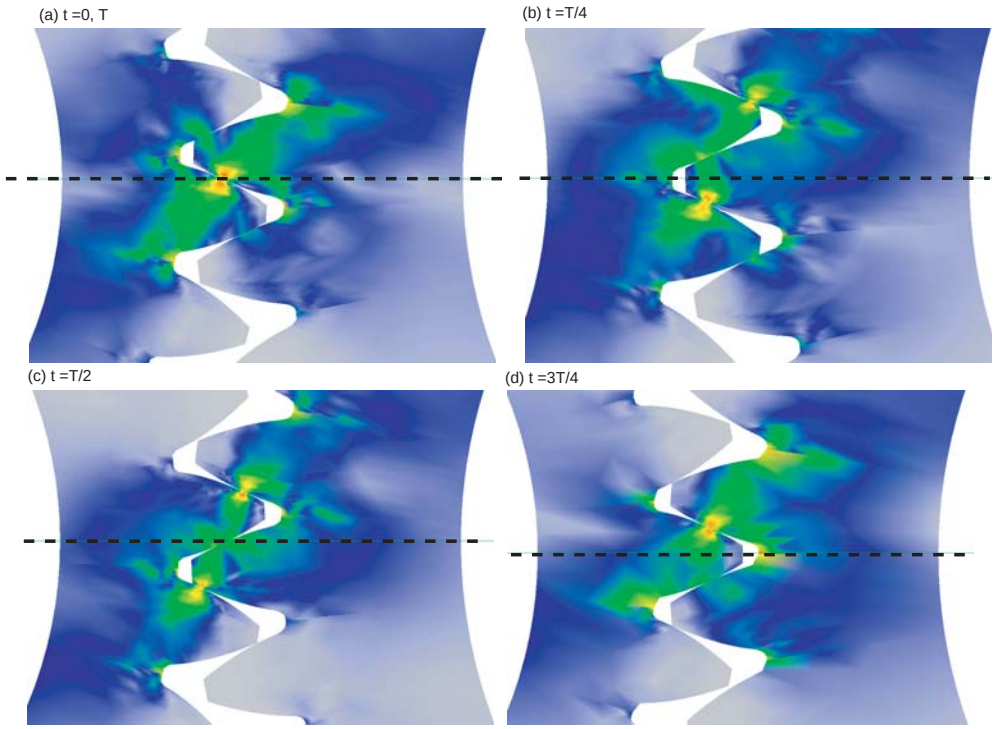

Figure 8.3: The gear mesh contacts for an arbitrary external ideal gear pair. The dashed line in the middle of each sub-figure is the center line. The driving gear is at the right hand side of each subplot and the driving direction is counter-clockwise.

action equals that along the back-side line of action. The back-side and drive-side mesh stiffnesses are equal at this moment.

At $t = \frac{T}{2}$, the driving gear tooth moves q_{dr} which is equal to its circular tooth thickness, and the center line passes right through the pitch point at the back-side of the driving gear tooth (Figure 8.3c). At $t = \frac{3T}{4}$, the driving gear moves $\frac{3}{2}q_{dr}$ and the driven gear moves $\frac{3}{2}q_{dn}$ (q_{dn} is the circular tooth thickness of the driven gear). At this moment, the center line passes through the middle point of the tooth tip of the driven gear, and both gears are symmetric about the center line. Therefore, the back-side and drive-side mesh stiffnesses are equal at $t = \frac{3T}{4}$.

The varying drive-side mesh stiffness is $k^I(t)$, and the matching back-side mesh stiffness is $k_b^I(t)$. Without losing generality, at $t = 0$ the pitch point at the drive side of the driving gear is in mesh. $g^I(\tau) = k^I(t - \frac{T}{4})$ is a phase-shifted function of $k^I(t)$, and at its origin $\tau = 0$ or $t = \frac{T}{4}$ (as shown in Figure 8.3b), the back-side and drive-side mesh stiffnesses are equal. $h^I(\tau)$ is defined as the back-side mesh stiffness function that matches with $g^I(\tau)$. Due to the symmetry of the gear pair at $\tau = 0$, the driving-side mesh stiffness at the moment of τ is equivalent to the back-side mesh stiffness at the moment of $-\tau$. Thus, $h^I(\tau)$ and $g^I(\tau)$ have the relation

$$h^I(\tau) = g^I(-\tau) \tag{8.2}$$

Insertion of $g^I(\tau) = k^I(t - \frac{T}{4})$ into (8.2) yields

$$h^I(\tau) = k^I(-t + \frac{T}{4}) \tag{8.3}$$

Similar to the relation between $g^I(\tau)$ and the drive-side mesh stiffness $k^I(t)$, $h^I(\tau)$ is a phase-shifted function of the back-side mesh stiffness $k_b^I(t)$, and it is

$$h^I(\tau) = k_b^I(t - \frac{T}{4}) \tag{8.4}$$

Substitution of $h^I(\tau)$ with $k_b^I(t - \frac{T}{4})$ in (8.3) gives

$$\begin{aligned} k_b^I(t - \frac{T}{4}) &= k^I(-t + \frac{T}{4}) \\ \Rightarrow k_b^I(t) = k^I(-t + \frac{T}{2}) &= k^I(-t - \frac{T}{2}) \end{aligned} \tag{8.5}$$

Equation (8.5) reveals that $k_b^I(t)$ is uniquely determined once the drive-side mesh stiffness function $k^I(t)$ is known, and it is the symmetrical function of $k^I(t)$ with $\frac{T}{2}$ phase shift. According to equation (8.5), the number of gear teeth in contact at the back side at $t = 0$ equals the number of gear teeth in contact at the drive side at

$t = \frac{T}{2}$. It is confirmed by the simulation results in Figure 8.3. There are two pairs of teeth in contact at the back side in Figure 8.3a ($t = 0$), and there are exactly two pairs of teeth in contact at the drive side in Figure 8.3c ($t = \frac{T}{2}$).

Summarizing the above discussion, the back-side mesh stiffness varying function for an ideal gear pair is the symmetrical function of the drive-side mesh stiffness function with a phase shift of half of the mesh period.

8.2.1 Back-side Mesh Stiffness for a Gear Pair with Nominal Backlash

Real gear applications, however, always include backlash to allow lubrication, manufacturing errors, deflection under load, and thermal expansion. It is typically created by slightly increasing the center distance of the gear pair or reducing the circular tooth thickness.

Figure 8.4 illustrates the backlash for an external gear pair. The nominal backlash for the gear pair is $2b$ (the backlash remains at $2b$ for this case), the circular pitch is p, and the mesh period is T. The case that the center distance of the gear pair remains unchanged and there is no relative radial motion between the gears is investigated first (to simplify the results, the assumption that there is no relative tangential motions between the gears is imposed throughout the rest of this study). The impacts of the center distance change and relative radial motion are studied subsequently.

Once a gear pair is installed with an unchanged center distance (the nominal center distance), the backlash remains at its nominal value $2b$ if there is no relative radial motion between the gears. The thick dashed line in Figure 8.4 represents the case of back-side contact. If the varying drive-side mesh stiffness is $k(t)$, equation (8.5) does not give the desired back-side mesh stiffness varying function. Instead, it

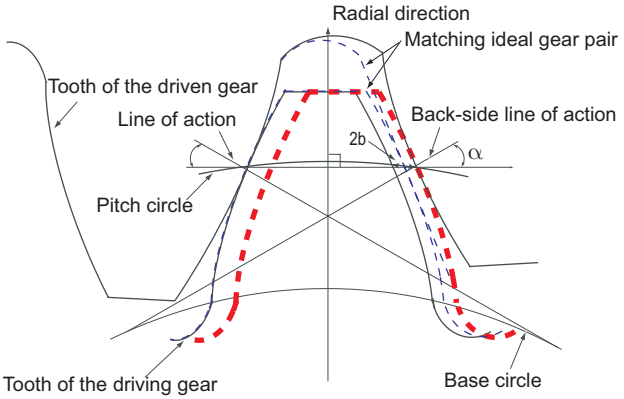

Figure 8.4: The drive-side and back-side gear mesh contacts for a gear pair with $2b$ backlash and its matching ideal gear pair.

gives $k_b^I(t)$ the back-side mesh stiffness varying function for the matching ideal gear pair (the thin dashed line in Figure 8.4) who have the same center distance and pitch circle as the original gear pair in Figure 8.4 but different tooth thicknesses. To ensure zero backlash, the tooth thickness of the matching ideal gear pair is equal to b plus the thickness of the original gear pair in Figure 8.4.

If the matching ideal gear pair moves b along the pitch circle in the reverse driving direction in Figure 8.4, the back-side contact of the ideal gear mesh in the thin dashed line will coincide with the actual back-side contact in the thick dashed line. The phase lag between the back-side mesh stiffness functions of the matching ideal gear pair and the original gear pair for the above process is $\frac{b}{p}T$. In other words, the actual back-side mesh stiffness varying function $k_b(t)$ of a gear pair is the back-side mesh stiffness varying function for the matching ideal gear $k_b^I(t)$ with $\frac{b}{p}T$ phase lag, that is,

$$k_b(t) = k_b^I(t - \frac{b}{p}T) \tag{8.6}$$

Insertion of $k_b^I(t) = k^I(-t - \frac{T}{2})$ (from equation (8.5)) into equation (8.6) and application of the condition that the drive-side mesh stiffness function of the matching ideal gear pair is equivalent to that of the original gear pair (Figure 8.4) yields

$$k_b(t) = k(-t - \frac{T}{2} + \frac{b}{p}T) \tag{8.7}$$

8.2.2 Back-side Mesh Stiffness for an Arbitrary Gear Pair with Changing Backlash

In real applications, the actual operating center distance of a gear pair always differs from the nominal one due to manufacturing errors of the axes, axes deflections under load, and axial misalignments during installation. In addition, vibration of the gears in the relative radial direction changes the actual center distance [34]. Figure 8.5a shows the change of center distance Δ_c (the positive sign of Δ_c indicates the reduction of center distance) causes the actual backlash to be reduced by the amount of $2\Delta_c \tan\alpha$, where α is the pressure angle. Figures 8.5b and 8.5c explain this relation geometrically. When the driving gear moves Δ_c toward the driven gear (i.e., Δ_c change in center distance), the gaps between the two gears along drive- and back-side of lines of action are to be reduced by $\Delta_c \sin\alpha$ (Figure 8.5b), respectively. Because the driving gear is pressed against the driven gear along the line of action and there is no room for the driving gear to move toward the driven gear along the line of action, the total gap reduction along the back-side line of action becomes $2\Delta_c \sin\alpha$. The gap change along the pitch circle is approximated by the associated cord length shown in Figure 8.5c. By applying the trigonometric relations in the triangle shown in Figure 8.5c, the length of the cord that approximates the gap change along the pitch circle is calculated as: $\frac{2\Delta_c \sin\alpha}{\cos\alpha} = 2\Delta_c \tan\alpha$. When Δ_c reaches $\frac{b}{\tan\alpha}$ such that $2\Delta_c \tan\alpha = 2b$

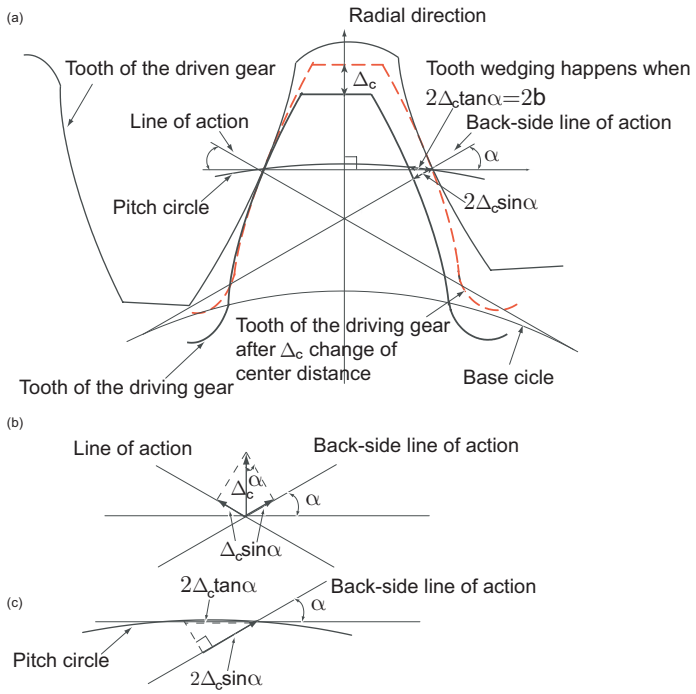

Figure 8.5: Back-side tooth contact for the case of tooth wedging when $2\Delta_c \tan\alpha = 2b$. b is half of the backlash along the pitch circle, Δ_c is the change of the central distance, and α is the pressure angle.

($2b$ is the nominal backlash), the back side of the driving gear (the dashed line in Figure 8.5a) is in contact with the back side of the driven gear and the tooth wedging happens.

When $\Delta_c < \frac{b}{\tan\alpha}$, the actual backlash of the gear pair $2b'$ is $2(b - \Delta_c \tan\alpha)$. This case is equivalent to the case in Figure 8.4 with the exception that the backlash is $2b'$ instead of the nominal value $2b$. Replacing b with b' in (8.7) gives

$$\begin{aligned} k_b(t) &= k(-t - \frac{T}{2} + \frac{b'}{p}T) \\ &= k(-t - \frac{T}{2} + \frac{b - \Delta_c \tan\alpha}{p}T) \end{aligned} \tag{8.8}$$

Equation (8.8) is the back-side mesh stiffness for a general external gear pair with $2b$ nominal backlash and Δ_c center distance change.

In most applications, the backlash and the change of center distance of a gear pair is much smaller than the circular pitch p. Therefore, the phase lag term $\frac{b-\Delta_c \tan\alpha}{p}T$ in equation (8.8) is small and equation (8.5) may be sufficient to estimate the back-side mesh stiffness of a gear pair with small backlash and center distance change.

8.2.3 Back-side Tooth Number Variation Function for an Anti-backlash Gear Pair with Changing Backlash

For an anti-backlash gear pair, the drive-side mesh stiffness is not only determined by the number of teeth in contact, but also by other design parameters, such as the face width in contact and the the modulus of elasticity. To exclude the impacts from the parameters other than the in-contact number of teeth at the drive and back sides, the in-contact tooth number variation functions of the drive ($n(t)$) and back ($n_b(t)$) sides are used to investigate the back-side mesh stiffness of anti-backlash gears. Because the derivation of equations (8.5-8.8) relies only on the in-contact tooth number variations and the phase relations between the drive and back sides, replacing the mesh stiffness functions $k(t)$ and $k_b(t)$ with the in-contact tooth number variation functions $n(t)$ and $n_b(t)$ and application of the same analytical process in the above three sub-sections yield

$$n_b(t) = n(-t - \frac{T}{2} + \frac{b - \Delta_c \tan\alpha}{p}T) \tag{8.9}$$

Equation (8.9) is the back-side tooth number variation function for an arbitrary anti-backlash gear or a general external gear pair with $2b$ nominal backlash and Δ_c center distance change.

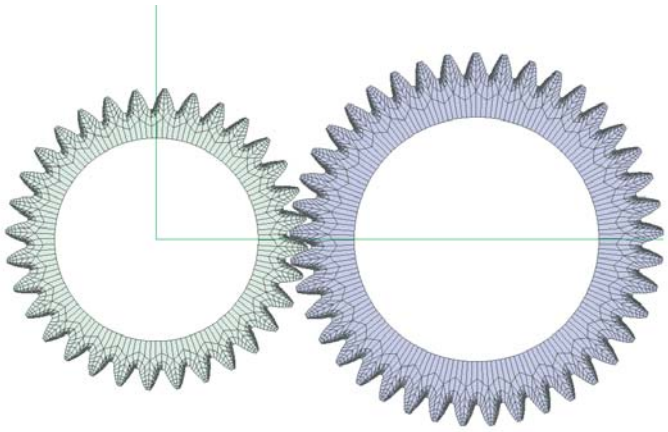

Figure 8.6: Calyx FEM model of the example ideal gear pair.

8.3 Numerical Verification of Back-side Mesh Stiffness

The drive-side and back-side mesh stiffness relation in (8.5) is the key to the general back-side mesh stiffness in (8.8) or back-side tooth variation function in (8.9). Therefore, equation (8.5) is verified first. The verification is achieved with a Calyx [96] finite element model of an ideal external gear pair (Figure 8.6). Calyx has very precise tracking of tooth contact for precise tooth geometry. In the simulations that follow Calyx tracks the contact for specified gear kinematics under unloaded conditions. The gear parameters are listed in Table 1.

Figure 8.7 shows the in-contact tooth number variations at the drive and back sides by tracking the numbers of gear teeth along the drive- and back-side lines of action using the above Calyx model. At $t = 0$, the pitch point at the drive side of the driving gear is in contact. O and O' are the points on the drive- (O) and back-side

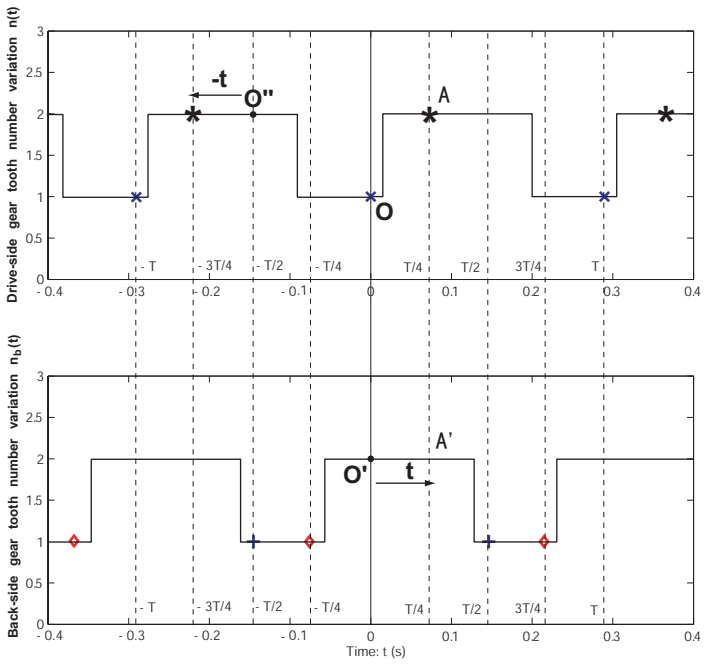

Figure 8.7: The drive- and back-side gear tooth number variation functions for the example ideal gear pair in Figure 6. 'x' indicates the time that the pitch point of the drive side of the driving gear is in contact, 'A' indicates the time that the middle point of the drive gear tooth tip is aligned with the center line, '+' indicates the time that the pitch point of a driven gear tooth is in contact, and '*' indicates the time that the middle point of a driven gear tooth tip is aligned with the center line.

(O') tooth number variation functions at $t = 0$. Figure 8.3a illustrates the drive-side and back-side tooth contacts at $t = 0$.

At $t = \frac{T}{4}$, the middle point of the driving gear tooth tip is aligned with the center line (Figure 8.3b). A and A' are the points on the drive- (A) and back-side (A') tooth number variation functions at $t = \frac{T}{4}$. For better illustration, the drive-side tooth number variation function before point A and the back-side tooth number variation function after point A' are shown in Figure 8.8. They are symmetrical about the solid vertical line (that is, $\tau = 0$, where $\tau = t - \frac{T}{4}$). This matches the expression in equation (8.2). O'' in Figure 8.7 and Figure 8.9 is the point on the drive-side

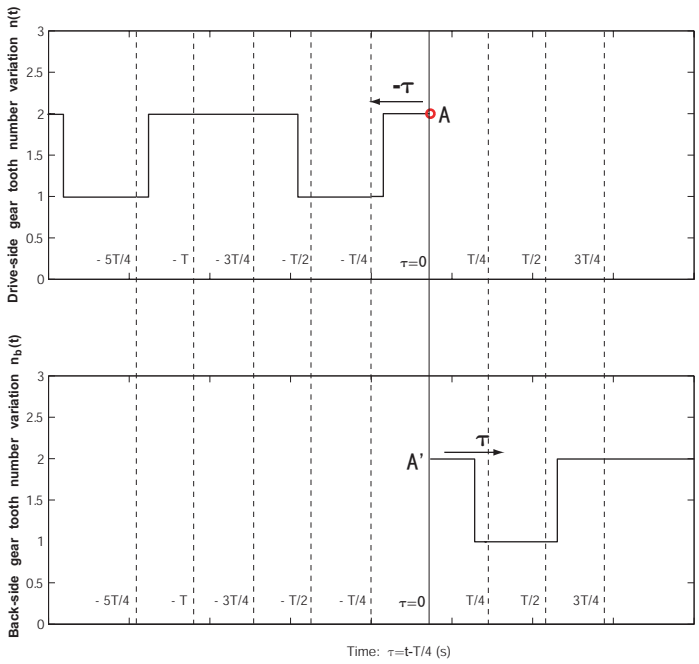

Figure 8.8: The drive-side gear tooth number variation function before point A and the back-side gear tooth number variation function after point A'.

tooth number variation function at $t = \frac{T}{2}$. Figure 8.9 shows that the drive-side tooth number variation function before point O'' is symmetrical to the back-side gear tooth number variation function after point O'. This provides numerical validation of equation (8.5).

The next step is to verify the back-side mesh stiffness varying function for the gear pairs with $2b$ nominal backlash in equation (8.7). To do so, the tooth thickness of the gear pair in Figure 8.6 is reduced by 10% such that $\frac{b}{p} = 0.05$. The tracking results of the drive-side and back-side tooth number variations from Calyx are shown in Figure 8.10. $\bar{O}$ in Figure 8.10 is the point on the drive-side gear tooth number variation function at $t = -\frac{T}{2} + \frac{b}{p}T$. The drive-side gear tooth number variation function before

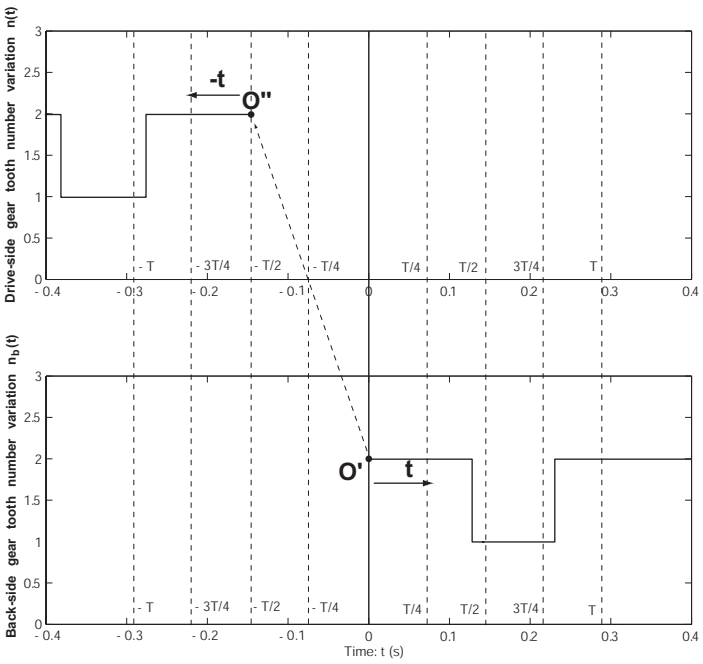

Figure 8.9: The drive-side gear tooth number variation function before point O'' and the back-side gear tooth number variation function after point O'.

point $\bar{O}$ is symmetrical to the back-side gear tooth number variation function after point O'. Thus, the results in Figure 8.10 agree with equation (8.7).

In order to verify the general back-side tooth variation function in equation (8.9), the center distance between the two gears in Figure 8.6 is reduced such that $\frac{\Delta_c \tan\alpha}{p} = 0.025$. The tracking results for the drive-side and back-side tooth number variation functions are shown in Figure 8.11. $\tilde{O}$ in Figure 8.11 is the point on the drive-side gear tooth number variation function at $t = -\frac{T}{2} + \frac{b-\Delta_c \tan\alpha}{p}T$. The drive-side gear tooth number variation function before point $\tilde{O}$ is symmetrical to the back-side gear tooth number variation function after point $\tilde{O}$. Comparing with Figure 8.10, the phase lag of the back-side tooth number variation function in Figure 8.11 is reduced

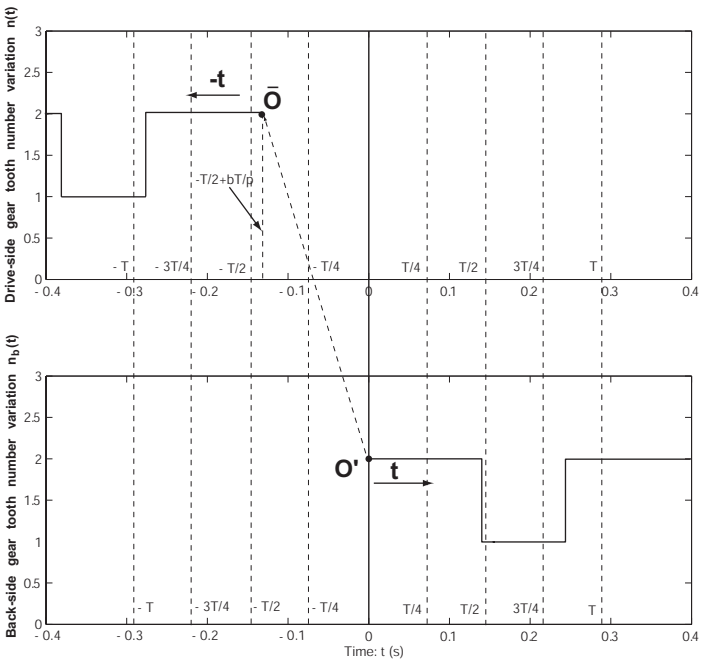

Figure 8.10: Back-side and drive-side gear tooth number variation functions the example gear pairs with zero center distance change and $2b$ nominal backlash (b satisfies $\frac{b}{q} = 0.05$).

by $0.025T$. This phase lag reduction is caused by the reduction of the center distance and this result matches equation (8.9).

8.4 Conclusion

This study investigates the drive-side mesh stiffness for arbitrary gear pairs and anti-backlash gear pairs. The results reveal the inherent relation between the back-side and drive-side mesh stiffnesses or gear tooth variation functions. The impact of backlash on the phase lag in the back-side mesh stiffness variation function is also quantified in this study. The resultant formulae are important for the correct

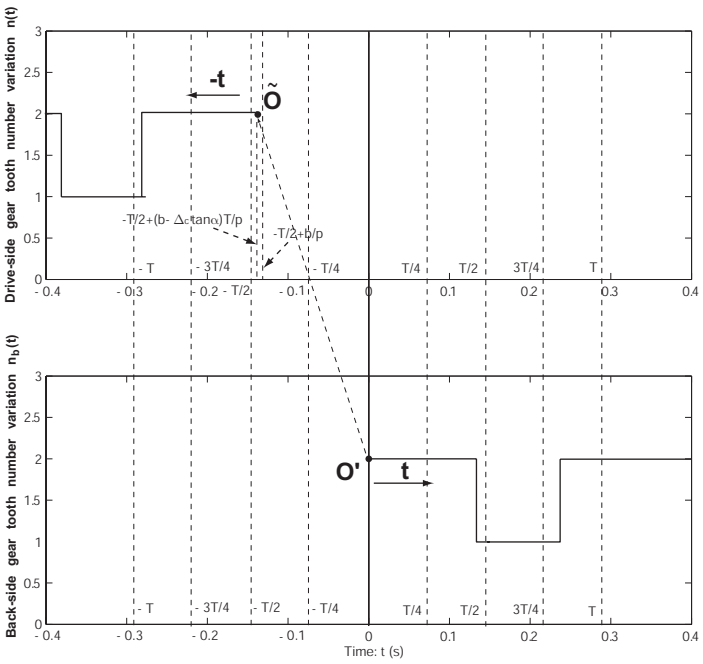

Figure 8.11: Back-side and drive-side gear tooth number variation functions the example gear pairs with $2b$ nominal backlash (b satisfies $\frac{b}{q} = 0.05$) and Δ_c change in the center distance ($\frac{\Delta_c \tan\alpha}{p} = 0.025$).

modeling and further dynamic analysis on the gear systems that involve back-side gear tooth contacts, such as anti-backlash gears.

Table 8.1: Gear parameters for the example system shown in Figure 8.6.

	Driving Gear	Driven Gear
Number of Teeth	41	32
Diametral Pitch	10.34	10.34
Pressure Angle (deg)	25	25
Outer Diameter (in)	4.12	3.33
Root Diameter (in)	3.54	2.87
Mesh Period (sec)	0.293	0.293

Chapter 9: CONCLUSIONS AND FUTURE WORK

9.1 Conclusions

9.1.1 Compound Planetary Gear Models and Associated Modal Properties

A purely rotational model for general compound planetary gears is developed. This model clarifies discrepancies in gear mesh deflection expressions and corrects errors in previously published models. The distinct modal properties for this purely rotational model are presented and analytically proved. All the vibration modes for the purely rotational model can be classified into two groups: overall and planet modes. In an overall mode, all planet trains in the same planet set have identical motions and each mode is associated with a distinct natural frequency. Planet modes exist when the system has a stage with two or more planet trains. In any planet mode, only the planets in one stage have motion and all other components have no motion. This purely rotational model simplifies the subsequent analyses on parametric instability caused by mesh stiffness variations while keeping the main dynamic behavior generated by mesh stiffness variations.

9.1.2 Sensitivity of General Compound Planetary Gear Natural Frequencies and Vibration Modes to Model Parameters

The systematic study on general compound planetary gear eigensensitivities are performed by using the rotational-translational compound planetary gear model. Application of the well-defined modal properties of general compound planetary gears simplifies the eigensensitivity expressions to simple, closed-form expressions. For both tuned and mistuned systems, the modal strain/kinetic energy distribution plots provide effective and straightforward means to identify which system parameters have the greatest impact on tuning the related natural frequency.

Rotational modes are independent of translational support/shaft stiffnesses and masses of central gears/carriers. Translational modes are independent of torsional support/shaft stiffnesses and moments of inertia of central gears/carriers. Planet modes of a certain planet set are independent of any system parameters associated with other planet sets. They are also independent of the mass/moment of inertia parameters and support/shaft stiffness parameters of all central gears/carriers.

When a system is perturbed by a mistuned parameter, a degenerate translational mode natural frequency of the unperturbed system splits into two distinct frequencies. A mistuned planet bearing stiffness, translational shaft stiffness between two planets in a stepped planet arrangement, or planet mass impacts both modes associated with the two frequencies, while any other mistuned parameter affects only one of the modes despite the apparent disruption of system symmetry. Parameter mistuning always splits degenerate planet mode frequencies of the stage associated with the mistuned parameter into two frequencies. One frequency keeps its original value

and its associated modes retain the well-defined planet mode properties; the other frequency is distinct and its associated mode loses the planet mode properties.

The results of this study provide important information for tuning resonances away from operating speeds and minimizing dynamic response for general compound planetary gears.

9.1.3 Natural Frequency Veering and Crossing Patterns for General Compound Planetary Gears

Natural frequency veering and crossing phenomena are systematically investigated for general compound planetary gears. By checking whether the axisymmetry in all stages are retained, all system parameters are divided into tuned and mistuned parameters. Tuned parameters are further classified as rotational, translational, and planet tuned parameters based on their eigensensitivities. The veering/crossing patterns with respect to each group of tuned parameters are determined by examining the analytical expressions of the associated coupling factors. The veering/crossing patterns for mistuned parameters are determined in a similar way. Compared with the patterns for tuned parameters, more occurrences of veering are found in the veering/crossing pattern for any mistuned parameter.

9.1.4 Mesh Phase Relations of General Compound Planetary Gears

This investigation systematically defines and calculates all the mesh phases for general compound planetary gears. Grouping compound planetary gear mesh phases into a hierarchical structure of system-level, stage-level, and train-level mesh phases to simplify the analysis, this study derives a complete procedure to determine all

the necessary relative phases. The specific relationships between train-level relative phases that are critical for any analytical study on the suppression of compound planetary gear dynamic response through mesh phasing are derived by applying the assembly conditions of compound planetary gears. All derived results are verified through an example, where the numerical benchmark is geometrically exact and the only error is a quantifiable mesh cycle discretization error.

9.1.5 Suppression of Various Modal Responses in General Compound Planetary Gears through Mesh Phasing

This chapter analytically investigates the general rules to suppress certain dynamic responses and resonances of general compound planetary gears through planet mesh phasing for both the purely rotational and rotational-translational models.

For meshed-planet stages, the excitation or suppression of various modal responses at μth harmonic of mesh frequency is solely determined by the phasing quantity k_μ. The resultant rules suggest that the planet-planet gear meshes have no impact on the mesh phasing rules for meshed-planet stages due to the specific train-level relative phase relations. For stepped stages, due to the existence of two generally different mesh frequencies, two different phasing quantities, k_μ and $\bar{k}_\chi$, are required to determine the excitation or suppression of various modal responses at μth harmonic of one mesh frequency and χth harmonic of the other one. For multi-stage systems, the mesh phasing rules are the sum of the rules from each of the individual stages, where these may be meshed-planet or stepped-planet stages. The mesh phasing rules are numerically verified.

9.1.6 Parametric Instabilities of General Compound Planetary Gear Caused by Mesh Stiffness Variations

Analytical investigation on compound planetary gear parametric instabilities caused by mesh stiffness variations are performed in this chapter. The instability boundaries are analytically derived for two different types of parametric excitations: individual and mutual (unique to compound planetary gears) excitations.

Applying the structured modal properties for rotational models and using specific phasing conditions, the analytical expressions of instability boundaries are simplified to compact, closed-form formulae. The results indicate that overall frequency instabilities always vanish as long as the associated phasing quantities are not zero. Combination planet frequency instabilities also obey the mesh phasing rules while single mode planet frequency instabilities violate the mesh phasing rules. The resultant parametric expressions of instability boundaries are essential for the tuning of the instability regions away from the operating range at the design stage of compound planetary gears.

9.1.7 Back-side Contact Gear Mesh Stiffness

Driven by the needs of advanced planetary gear modeling and anti-backlash gear modeling, the contact at the back side of a gear mesh is examined and the inherent relationships between the back-side and drive-side mesh stiffnesses or gear tooth variation functions are discovered. The impact of backlash on back-side mesh stiffness variations is also quantified. The resultant formulae are important for planetary gear vibration models that consider tooth wedging or anti-backlash gears.

9.2 Future Work

This research addressed a series of key issues in compound planetary gear dynamic and it builds solid foundations for further analyses. The future work is recommended for the following areas.

9.2.1 Analytical Study on Anti-backlash Gear Dynamics

Backlash presents in most involute gear applications to allow lubrication, manufacturing errors, deflection under load, and thermal expansion. It is typically created by slightly increasing the center distance of the gear pair or reducing the circular tooth thickness. To minimize the undesirable characteristics which are caused by backlash, anti-backlash gears (or scissors gears) are used. The most common way for anti-backlash gears to eliminate backlash is to use certain preloaded springs to force the driving gear to be in continuous contact with the driven gear (Figure 9.1). In spite of the abundant studies on single-mesh, multi-mesh, and planetary gear dynamics, the investigation on anti-backlash gear dynamics is very few and limited to the finite element approach [18]. No literature ever analytically addressed the anti-backlash gear dynamics. To understand the dynamic behavior of anti-backlash gears and to optimize the design of such systems, it is necessary to conduct a series of analytical investigations.

Figure 9.1 shows a lumped parameter model for anti-backlash gears. The anti-backlash assembly consists of two parts: fixed and free parts. The fixed part is fixed to the input shaft and its contact with the driven gear is the drive-side contact. The free part can rotate freely relative to the input shaft and its contact with the driven gear is on the back side. The fixed and free parts are connected by a preloaded

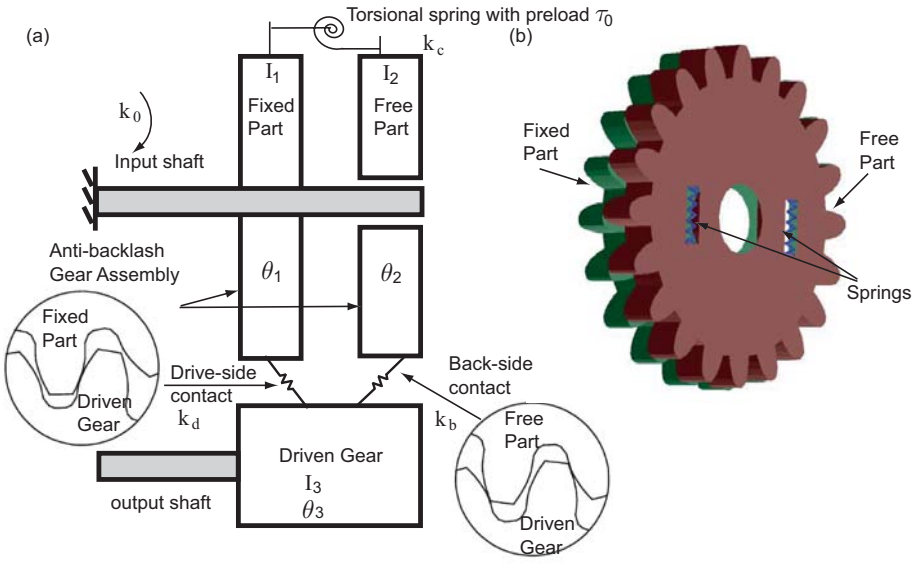

Figure 9.1: A lumped parameter model for anti-backlash gears: (a) front view of the whole system (b) side view of the anti-backlash assembly.

torsional spring. As a preliminary investigation, only rotational degrees of freedom is considered for the model shown in Figure 9.1. The equations of motions are

$$\begin{aligned} I_1\ddot{\theta}_1 + k_0\theta_1 + k_d(t)(\theta_1 r_1 + \theta_3 r_3) + k_c(\theta_1 - \theta_2) &= \tau_0 \\ I_2\ddot{\theta}_2 - k_b(t)(\theta_2 r_2 + \theta_3 r_3) + k_c(\theta_2 - \theta_1) &= -\tau_0 \\ I_3\ddot{\theta}_3 + k_d(t)(\theta_1 r_1 + \theta_3 r_3) - k_b(t)(\theta_2 + \theta_3) &= 0 \end{aligned} \tag{9.1}$$

where $(I_1,\, \theta_1,\, r_1)$, $(I_2,\, \theta_2,\, r_2)$, and $(I_3,\, \theta_3,\, r_3)$ are the moments of inertia, rotations, and base radii for the fixed part, free part, and the driven gear, respectively. k_0 is the torsional shaft stiffness of the input shaft. k_c is the torsional coupling stiffness between the fixed and free parts of the anti-backlash assembly and τ_0 is the preload torque for this coupling stiffness. $k_d(t)$ is the time-varying mesh stiffness between the fixed part and the driven gear and the associated contact happens at the drive-side of the driven gear tooth. $k_b(t)$ is the mesh stiffness between the free part and the

driven gear and the contact is at the back-side of the driven gear. Let H be the mesh stiffness per unit face width. If ι_1 and ι_2 are the effective face widthes for the drive- and back-side meshes, $k_d(t)$ and $k_b(t)$ can be simplified as

$$\begin{aligned} \bar{k}_d(t) &= H\iota_1 n_d(t) \\ \bar{k}_b(t) &= H\iota_2 n_b(t) \end{aligned} \tag{9.2}$$

where $n_d(t)$ and $n_b(t)$ are tooth number variation functions for the drive and back sides, respectively. Insertion of (9.2) into (8.9) yield the relation between $k_d(t)$ and $k_b(t)$ as

$$k_b(t) = \frac{\iota_2}{\iota_1} k_d(-t + -\frac{T}{2} + \frac{b}{p}T) \tag{9.3}$$

where p is the circular pitch of the mesh between the fixed part and the driven gear and T is the mesh period.

With the model in Figure 9.1 and the specific relation between $k_d(t)$ and $k_b(t)$ in (9.3), the recommended investigations are

1. to understand the free vibration problem of anti-backlash gears, such as the modal properties,

2. to evaluate the eigensensitivities in order to understand the impacts of key parameters on natural frequencies and vibration modes,

3. to investigate the parametric instabilities caused by the variations of $k_d(t)$ and $k_b(t)$,

4. to inspect the nonlinear behaviors of anti-backlash gears.

9.2.2 Investigations on 3-D Helical Compound Planetary Gears

In real transmission applications, helical compound planetary gears are more popular than spur compound planetary gears due to the advantage of lower fluctuation

in static transmission error ([23]). In order to understand the effects of design parameters on dynamic behaviors of helical compound planetary gears and optimize the system parameters during the design stage, it is desirable to extend the 2-D rotational-translational model to a 3-D one. The elaborate investigations on compound planetary gears in this study, together with Eritenel and Parker's studies on 3-D simple helical planetary gear [25, 26], provide necessary foundations for the inspection on 3-D helical compound planetary gears. The suggested investigations are

1. to develop an lumped-parameter 3-D helical compound planetary gear model,
2. to examine the modal properties of 3-D helical compound planetary gears,
3. to evaluate the impacts of system parameters on natural frequencies and vibration modes,
4. to inspect the existence of mesh phasing rules for helical compound planetary gears.

9.2.3 Extended Investigation on Parametric Instabilities of Compound Planetary Gears

The analytical study in chapter 7 can be extended to the refined rotational-translational model in [53]. The analytical process and the general formulae for distinct-distinct, distinct-degenerate, and degenerate-degenerate instabilities in (7.15)-(7.27) apply to the rotational-translational model if the free vibration equation of compound planetary gear in (7.7) is replaced by the one associated with the rotational-translational model in (2.38) and the stiffness matrix in (7.5) is replaced by the one for the rotational-translational model in the appendix of [53].

Because the rotational-translational model, compared with the purely rotational model, has more sophiscated modal structures in (2.40)-(2.52) and more complex mesh phasing rules in tables (6.2) and (6.3), the analytical results in Section 7.4 can not be applied to the rotational-translational model directly and thorough investigations on the impacts of rotational-translational modal properties and mesh phasing conditions on instability boundaries are suggested. The instabilities that are related to translational frequencies (unique to the rotational-translational model) is expected to be the focus of this extended investigation. In addition, it is desirable to compare the analytical results with the numerical solutions from Floquet theory or finite element method.

9.2.4 Nonlinear Dynamics of Compound Planetary Gears

Nonlinearities in gear systems, mainly the gear mesh contact loss, have great impacts on dynamic responses, load sharing among planets, bearing loads, tooth fatigue, and gear noise [50, 88, 90]. The nonlinear dynamics for single-mesh [50, 78, 91] and multi-mesh gears [1,2,63] are already extensively studied. The effects of nonlinearities on simple planetary gears also receive some attention in recent years. Ambarisha and Parker [6] calculated the nonlinear response of planetary gears by using both lumped-parameter and finite element models. Mesh phasing rules are confirmed except for chaotic and period-doubling regions. In addition, Bahk and Parker [9] studied the nonlinear dynamics for a purely rotational simple planetary gear model. Perturbation, harmonic balance/arclength continuation, and numerical integration methods were used in their study and the frequency-response functions were presented in closed-form expressions. Guo and Parker [34] investigates a simple planetary gear

model with not only contact loss nonlinearity, but also tooth wedging and bearing clearance nonlinearity. No studies, however, ever addressed the nonlinear dynamics for compound planetary gears. To provide improved design guidance for compound planetary gears based on dynamic responses with different nonlinearities considered, the recommended studies on compound planetary gear nonlinear dynamics are

1. to improve the rotational-translational compound planetary gear model to make it incorporate with different nonlinearities, such as contact loss and bearing clearance,

2. to add the back-side gear mesh contacts to the model by applying the results from chapter 8 in this work,

3. to investigate the nonlinear effects caused by these nonlinearities by using different methods to find the solutions for the nonlinear problems analytically or numerically, such as the method of multiple scales, harmonic, balance method, and arclength continuation method,

4. to evaluate the impacts of the nonlinearities on the validation of the mesh phasing rules in chapter 6 of this study.

Appendix A: APPENDIX FOR CHAPTER 2

The sub-matrices of $\mathbf{M}$ in (2.22) are

$$\begin{array}{l}
\mathbf{I}_c = diag\left(I_{ce}^1, \cdots, I_{ce}^a\right);\ \mathbf{I}_g = diag\left(I_g^1, \cdots, I_g^b\right) \\
\mathbf{I}_{c,ps} = diag\left(\left(\mathbf{I}_{c,ps}^1\right)^T, \cdots, \left(\mathbf{I}_{c,ps}^a\right)^T\right) \\
\mathbf{I}_{c,ps}^i = \left[\left(\mathbf{I}_{c,pt}^{i1}\right)^T, \cdots, \left(\mathbf{I}_{c,pt}^{ic^i}\right)^T\right]^T;\ \mathbf{I}_{c,pt}^{il} = \left[I_p^{il1}, \cdots, I_p^{ild^i}\right]^T \\
\mathbf{I}_{ps} = diag\left(\mathbf{I}_{ps}^1, \cdots \mathbf{I}_{ps}^a\right);\ \mathbf{I}_{ps}^i = diag\left(\mathbf{I}_{pt}^{i1}, \cdots \mathbf{I}_{pt}^{ic^i}\right) \\
\mathbf{I}_{pt}^{il} = diag\left(I_p^{il1}, \cdots I_p^{ild^i}\right)
\end{array} \tag{A.1}$$

The sub-matrices of $\mathbf{K}_m$ in (2.25) are

$$\mathbf{K}_c = \begin{bmatrix} k_c^{11} & \cdots & k_c^{1a} \\ \vdots & \ddots & \vdots \\ k_c^{a1} & \cdots & k_c^{aa} \end{bmatrix} \tag{A.2}$$

$$k_c^{ih} = \begin{cases} \sum_{j=1}^{b} \sum_{l=1}^{c^i} \sum_{m=1}^{d^i} \left(r_g^j\right)^2 k_{gp}^{jilm} + \sum_{n=1, n\neq i}^{a} k_{cc,\theta\theta}^{in} + \sum_{j=1}^{b} k_{cg,\theta\theta}^{ij} & i = h \\ -k_{cc,\theta\theta}^{ih} & i \neq h \end{cases}$$

$$\mathbf{K}_{c,g} = \begin{bmatrix} k_{c,g}^{11} & \cdots & k_{c,g}^{1b} \\ \vdots & \ddots & \vdots \\ k_{c,g}^{a1} & \cdots & k_{c,g}^{ab} \end{bmatrix};\ k_{c,g}^{ij} = -\sum_{l=1}^{c^i} \sum_{m=1}^{d^i} \left(r_g^j\right)^2 k_{gp}^{jilm} - k_{cg,\theta\theta}^{ij} \tag{A.3}$$

$$\mathbf{K}_{c,ps} = \begin{bmatrix} \left(\mathbf{k}_{c,ps}^{1}\right)^T & \cdots & \mathbf{0} \\ \vdots & \ddots & \vdots \\ \mathbf{0} & \cdots & \left(\mathbf{k}_{c,ps}^{a}\right)^T \end{bmatrix};\ \mathbf{k}_{c,ps}^{i} = \left[\mathbf{k}_{c,pt}^{i1}, \cdots \mathbf{k}_{c,pt}^{ic^i}\right]^T$$

$$\mathbf{k}_{c,pt}^{il} = \left[k_{c,p}^{il1}, \cdots, k_{c,pt}^{ild^i}\right]^T;\ k_{c,p}^{ilm} = \sum_{j=1}^{b} \sigma^j k_{gp}^{jilm} r_g^j r_p^{ilm}$$

$$\mathbf{K}_g = \begin{bmatrix} k_g^{11} & \cdots & k_g^{1b} \\ \vdots & \ddots & \vdots \\ k_g^{b1} & \cdots & k_g^{bb} \end{bmatrix} \tag{A.4}$$

$$k_g^{jn} = \begin{cases} \sum_{i=1}^{a} \sum_{l=1}^{c^i} \sum_{m=1}^{d^i} \left(r_g^j\right)^2 k_{gp}^{jilm} + \sum_{h=1,h\neq j}^{b} k_{gg,\theta\theta}^{jh} + \sum_{i}^{a} k_{cg,\theta\theta}^{ij} & j = n \\ -k_{gg,\theta\theta}^{jn} & j \neq n \end{cases}$$

$$\mathbf{K}_{g,ps} = \begin{bmatrix} \left(\mathbf{k}_{g,ps}^{11}\right)^T & \cdots & \left(\mathbf{k}_{g,ps}^{1a}\right)^T \\ \vdots & \ddots & \vdots \\ \left(\mathbf{k}_{g,ps}^{b1}\right)^T & \cdots & \left(\mathbf{k}_{g,ps}^{ba}\right)^T \end{bmatrix};\ \mathbf{k}_{g,ps}^{ji} = \left[\mathbf{k}_{g,pt}^{ji1}, \cdots, \mathbf{k}_{g,pt}^{jic^i}\right]^T$$

$$\mathbf{k}_{g,pt}^{jil} = \left[-\sigma^j k_{gp}^{jil1} r_g^j r_p^{il1}, \cdots, -\sigma^j k_{gp}^{jild^i} r_g^j r_p^{ild^i}\right]^T$$

$$\mathbf{K}_{ps} = \begin{bmatrix} \mathbf{K}_{ps}^{1} & \cdots & \mathbf{0} \\ \vdots & \ddots & \vdots \\ \mathbf{0} & \cdots & \mathbf{K}_{ps}^{a} \end{bmatrix};\ \mathbf{K}_{ps}^{i} = diag\left(\mathbf{K}_{pt}^{i1}, \cdots, \mathbf{K}_{pt}^{ic^i}\right) \tag{A.5}$$

$$\mathbf{K}_{pt}^{il} = \begin{bmatrix} k_p^{il11} & \cdots & k_p^{il1d^i} \\ \vdots & \ddots & \vdots \\ k_p^{ild^i1} & \cdots & k_p^{ild^id^i} \end{bmatrix}$$

$$k_p^{ilmn} = \begin{cases} \sum_{j=1}^{b} k_{gp}^{jilm} \left(r_p^{ilm}\right)^2 + \sum_{q=1,q\neq m}^{d^i} \left[k_{pp}^{ilmq} \left(r_p^{ilm}\right)^2 + k_{p-p,\theta\theta}^{ilmq}\right] & m = n \\ -k_{p-p,\theta\theta}^{ilmn} + k_{pp}^{ilmn} r_p^{ilm} r_p^{iln} & m \neq n \end{cases} \tag{A.6}$$

Appendix B: APPENDIX FOR CHAPTER 3

B.1 Expressions of Eigensensitivities for Tuned Compound Planetary Gears

The following notation is applied in this appendix: $i, h = 1, \cdots, a$; $j, n = 1, \cdots, b$; $l = 1, \cdots, c^i$; $m, q = 1, \cdots, d^i$. For a degenerate eigenvalue $\lambda_u = \lambda_{u+1} = \cdots = \lambda_{u+w-1}$ with multiplicity $w \geq 2$, the associated first order eigenvector derivatives can not be determined. The expressions of $\boldsymbol{\phi}'_u$ and λ'' for a rotational mode or a distinct planet mode are

$$\frac{\partial \boldsymbol{\phi}_u}{\partial k^i_{cb,\theta\theta}} = \sum_{v=1, v\neq u}^{\Lambda} \frac{\theta^i_{c,v}\theta^i_{c,u}}{\lambda_u - \lambda_v}\boldsymbol{\phi}_v \tag{B.1}$$

$$\frac{\partial^2 \lambda_u}{\partial k^2_{cb}} = \sum_{v=1, v\neq u}^{\Lambda} \frac{2(x^i_{c,v}x^i_{c,u} + y^i_{c,v}y^i_{c,u})^2}{\lambda_u - \lambda_v} \tag{B.2}$$

$$\frac{\partial \boldsymbol{\phi}_u}{\partial k^j_{gb,\theta\theta}} = \sum_{v=1, v\neq u}^{\Lambda} \frac{\theta^j_{g,v}\theta^j_{g,u}}{\lambda_u - \lambda_v}\boldsymbol{\phi}_v \tag{B.3}$$

$$\frac{\partial^2 \lambda_u}{\partial k^2_{gb}} = \sum_{v=1, v\neq u}^{\Lambda} \frac{2(x^j_{g,v}x^j_{g,u} + y^j_{g,v}y^j_{g,u})^2}{\lambda_u - \lambda_v} \tag{B.4}$$

$$\frac{\partial \boldsymbol{\phi}_u}{\partial k^{ij}_{cg,\theta\theta}} = \sum_{v=1, v\neq u}^{\Lambda} \frac{(\theta^i_{c,v} - \theta^j_{g,v})(\theta^i_{c,u} - \theta^j_{g,u})}{\lambda_u - \lambda_v}\boldsymbol{\phi}_v \tag{B.5}$$

$$\frac{\partial^2 \lambda_u}{(\partial k^{ij}_{cg,\theta\theta})^2} = \sum_{v=1,v\neq u}^{\Lambda} \frac{2[(\theta^i_{c,v} - \theta^j_{g,v})(\theta^i_{c,u} - \theta^j_{g,u})]^2}{\lambda_u - \lambda_v} \tag{B.6}$$

$$\frac{\partial \boldsymbol{\phi}_u}{\partial k^{ih}_{cc,\theta\theta}} = \sum_{v=1,v\neq u}^{\Lambda} \frac{(\theta^i_{c,v} - \theta^h_{c,v})(\theta^i_{c,u} - \theta^h_{c,u})}{\lambda_u - \lambda_v} \boldsymbol{\phi}_v \tag{B.7}$$

$$\frac{\partial^2 \lambda_u}{(\partial k^{ih}_{cc,\theta\theta})^2} = \sum_{v=1,v\neq u}^{\Lambda} \frac{2[(\theta^i_{c,v} - \theta^h_{c,v})(\theta^i_{c,u} - \theta^h_{c,u})]^2}{\lambda_u - \lambda_v} \tag{B.8}$$

$$\frac{\partial \boldsymbol{\phi}_u}{\partial k^{jn}_{gg,\theta\theta}} = \sum_{v=1,v\neq u}^{\Lambda} \frac{(\theta^j_{g,v} - \theta^n_{g,v})(\theta^j_{g,u} - \theta^n_{g,u})}{\lambda_u - \lambda_v} \boldsymbol{\phi}_v \tag{B.9}$$

$$\frac{\partial^2 \lambda_u}{(\partial k^{jn}_{gg,\theta\theta})^2} = \sum_{v=1,v\neq u}^{\Lambda} \frac{2[(\theta^j_{g,v} - \theta^n_{g,v})(\theta^j_{g,u} - \theta^n_{g,u})]^2}{\lambda_u - \lambda_v} \tag{B.10}$$

$$\frac{\partial \boldsymbol{\phi}_u}{\partial k^{i*m}_{p}} = \sum_{v=1,v\neq u}^{\Lambda} \sum_{l=1}^{c^i} \frac{(\delta^{ilm}_{\zeta,v})(\delta^{ilm}_{\zeta,u}) + (\delta^{ilm}_{\eta,v})(\delta^{ilm}_{\eta,u})}{\lambda_u - \lambda_v} \boldsymbol{\phi}_v \tag{B.11}$$

$$\frac{\partial^2 \lambda_u}{(\partial k^{i*m}_{p})^2} = \sum_{v=1,v\neq u}^{\Lambda} \frac{2}{\lambda_u - \lambda_v} \left\{ \sum_{l}^{c^i} [(\delta^{ilm}_{\zeta,v})(\delta^{ilm}_{\zeta,u}) + (\delta^{ilm}_{\eta,v})(\delta^{ilm}_{\eta,u})] \right\}^2 \tag{B.12}$$

$$\frac{\partial \boldsymbol{\phi}_u}{\partial k^{i*mq}_{pp}} = \sum_{v=1,v\neq u}^{\Lambda} \sum_{l=1}^{c^i} \frac{\delta^{ilmq}_{p,v}\delta^{ilmq}_{p,u}}{\lambda_u - \lambda_v} \boldsymbol{\phi}_v \tag{B.13}$$

$$\frac{\partial^2 \lambda_u}{(\partial k^{i*mq}_{pp})^2} = \sum_{v=1,v\neq u}^{\Lambda} \frac{2}{\lambda_u - \lambda_v} \left(\sum_{l=1}^{c^i} \delta^{ilmq}_{p,v}\delta^{ilmq}_{p,u} \right)^2 \tag{B.14}$$

$$\frac{\partial \boldsymbol{\phi}_u}{\partial k^{i*mq}_{p-p}} = \sum_{v=1,v\neq u}^{\Lambda} \sum_{l=1}^{c^i} \frac{(\zeta^{ilm}_{p,v} - \zeta^{ilq}_{p,v})(\zeta^{ilm}_{p,u} - \zeta^{ilq}_{p,u}) + (\eta^{ilm}_{p,v} - \eta^{ilq}_{p,v})(\eta^{ilm}_{p,u} - \eta^{ilq}_{p,u})}{\lambda_u - \lambda_v} \boldsymbol{\phi}_v \tag{B.15}$$

$$\frac{\partial^2 \lambda_u}{(\partial k_{p-p}^{i*mq})^2} =$$
$$\sum_{v=1,v\neq u}^{\Lambda} \frac{2}{\lambda_u - \lambda_v} \left\{ \sum_{l=1}^{c^i} [(\zeta_{p,v}^{ilm} - \zeta_{p,v}^{ilq})(\zeta_{p,u}^{ilm} - \zeta_{p,u}^{ilq}) + (\eta_{p,v}^{ilm} - \eta_{p,v}^{ilq})(\eta_{p,u}^{ilm} - \eta_{p,u}^{ilq})] \right\}^2 \tag{B.16}$$

$$\frac{\partial \boldsymbol{\phi}_u}{\partial k_{p-p,\theta\theta}^{i*mq}} = \sum_{v=1,v\neq u}^{\Lambda} \sum_{l=1}^{c^i} \frac{(u_{p,v}^{ilm}/r_p^{ilm} - u_{p,v}^{ilq}/r_p^{ilq})(u_{p,u}^{ilm}/r_p^{ilm} - u_{p,u}^{ilq}/r_p^{ilq})}{\lambda_u - \lambda_v} \boldsymbol{\phi}_v \tag{B.17}$$

$$\frac{\partial^2 \lambda_u}{(\partial k_{p-p,\theta\theta}^{i*mq})^2} = \sum_{v=1,v\neq u}^{\Lambda} \frac{2}{\lambda_u - \lambda_v} \left[\sum_{l=1}^{c^i} (u_{p,v}^{ilm}/r_p^{ilm} - u_{p,v}^{ilq}/r_p^{ilq})(u_{p,u}^{ilm}/r_p^{ilm} - u_{p,u}^{ilq}/r_p^{ilq}) \right]^2 \tag{B.18}$$

$$\frac{\partial \boldsymbol{\phi}_u}{\partial m_c^i} = \sum_{v=1,v\neq u}^{\Lambda} \frac{-\lambda_u (x_{c,v}^i x_{c,u}^i + y_{c,v}^i y_{c,u}^i)}{\lambda_u - \lambda_v} \boldsymbol{\phi}_v - \frac{\boldsymbol{\phi}_u}{2} [(x_{c,u}^i)^2 + (y_{c,u}^i)^2] \tag{B.19}$$

$$\frac{\partial^2 \lambda_u}{(\partial m_c^i)^2} = \sum_{v=1,v\neq u}^{\Lambda} \frac{2\lambda_u^2 (x_{c,v}^i x_{c,u}^i + y_{c,v}^i y_{c,u}^i)^2}{\lambda_u - \lambda_v} + 2\lambda_u [(x_{c,u}^i)^2 + (y_{c,u}^i)^2]^2 \tag{B.20}$$

$$\frac{\partial \boldsymbol{\phi}_u}{\partial I_c^i} = \sum_{v=1,v\neq u}^{\Lambda} \frac{-\lambda_u \theta_{c,v}^i \theta_{c,u}^i}{\lambda_u - \lambda_v} \boldsymbol{\phi}_v - \frac{\boldsymbol{\phi}_u}{2} (\theta_{c,u}^i)^2 \tag{B.21}$$

$$\frac{\partial^2 \lambda_u}{(\partial I_c^i)^2} = \sum_{v=1,v\neq u}^{\Lambda} \frac{2\lambda_u^2 (\theta_{c,v}^i \theta_{c,u}^i)^2}{\lambda_u - \lambda_v} + 2\lambda_u (\theta_{c,u}^i)^4 \tag{B.22}$$

$$\frac{\partial \boldsymbol{\phi}_u}{\partial m_g^j} = \sum_{v=1,v\neq u}^{\Lambda} \frac{-\lambda_u (x_{g,v}^j x_{c,u}^i + y_{g,v}^j y_{g,u}^j)}{\lambda_u - \lambda_v} \boldsymbol{\phi}_v - \frac{\boldsymbol{\phi}_u}{2} [(x_{g,u}^j)^2 + (y_{g,u}^j)^2] \tag{B.23}$$

$$\frac{\partial^2 \lambda_u}{(\partial I_g^j)^2} = \sum_{v=1, v\neq u}^{\Lambda} \frac{2\lambda_u^2 (\theta_{g,v}^j \theta_{g,u}^j)^2}{\lambda_u - \lambda_v} + 2\lambda_u (\theta_{g,u}^j)^4 \tag{B.24}$$

$$\frac{\partial \boldsymbol{\phi}_u}{\partial I_g^j} = \sum_{v=1, v\neq u}^{\Lambda} \frac{-\lambda_u \theta_{g,v}^j \theta_{g,u}^j}{\lambda_u - \lambda_v} \boldsymbol{\phi}_v - \frac{\boldsymbol{\phi}_u}{2} (\theta_{g,u}^j)^2 \tag{B.25}$$

$$\frac{\partial^2 \lambda_u}{(\partial I_g^j)^2} = \sum_{v=1, v\neq u}^{\Lambda} \frac{2\lambda_u^2 (\theta_{g,v}^j \theta_{g,u}^j)^2}{\lambda_u - \lambda_v} + 2\lambda_u (\theta_{g,u}^j)^4 \tag{B.26}$$

$$\frac{\partial \boldsymbol{\phi}_u}{\partial m_p^{i*m}} = \sum_{v=1, v\neq u}^{\Lambda} \sum_{l=1}^{c^i} \frac{-\lambda_u (\zeta_{p,v}^{ilm} \zeta_{p,u}^{ilm} + \eta_{p,v}^{ilm} \eta_{p,u}^{ilm})}{\lambda_u - \lambda_v} \boldsymbol{\phi}_v - \frac{\boldsymbol{\phi}_u}{2} \sum_{l=1}^{c^i} [(\zeta_{p,u}^{ilm})^2 + (\eta_{p,u}^{ilm})^2] \tag{B.27}$$

$$\frac{\partial^2 \lambda_u}{(\partial m_p^{i*m})^2} = \sum_{v=1, v\neq u}^{\Lambda} \frac{2\lambda_u^2}{\lambda_u - \lambda_v} [\sum_{l=1}^{c^i} (\zeta_{p,v}^{ilm} \zeta_{p,u}^{ilm} + \eta_{p,v}^{ilm} \eta_{p,u}^{ilm})]^2 + 2\lambda_u \left\{ \sum_{l=1}^{c^i} [(\zeta_{p,u}^{ilm})^2 + (\eta_{p,u}^{ilm})^2] \right\}^2 \tag{B.28}$$

$$\frac{\partial \boldsymbol{\phi}_u}{\partial I_p^{i*m}} = \sum_{v=1, v\neq u}^{\Lambda} \sum_{l=1}^{c^i} \frac{-\lambda_u u_{p,v}^{ilm} u_{p,u}^{ilm}}{(r_p^{ilm})^2 (\lambda_u - \lambda_v)} \boldsymbol{\phi}_v - \frac{\boldsymbol{\phi}_u}{2} \sum_{l=1}^{c^i} (\frac{u_{p,u}^{ilm}}{r_p^{ilm}})^2 \tag{B.29}$$

$$\frac{\partial^2 \lambda_u}{(\partial I_p^{i*m})^2} = \sum_{v=1, v\neq u}^{\Lambda} \frac{2\lambda_u^2}{\lambda_u - \lambda_v} (\sum_{l=1}^{c^i} \frac{u_{p,v}^{ilm} u_{p,u}^{ilm}}{(r_p^{ilm})^2})^2 + 2\lambda_u \left[\sum_{l=1}^{c^i} \left(\frac{u_{p,u}^{ilm}}{r_p^{ilm}} \right)^2 \right]^2 \tag{B.30}$$

Translational bearing/shaft stiffnesses of central gears and carriers (k_{cb}^i, k_{gb}^j, k_{cg}^{ij}, k_{cc}^{in}, k_{gg}^{jh}) have no impact on any rotational mode or distinct planet mode.

B.2 Eigensensitivities of Mistuned Compound Planetary Gears With a Single Mistuned Parameter

The following notation is used in this appendix:$i, h = 1, \cdots, a$; $j, n = 1, \cdots, b$; $l = 1, \cdots, c^i$; $m, q = 1, \cdots, d^i$. R means rotational mode, and T means translational mode. 1P, 2P, and 3P indicate planet modes with multiplicity one, two and

three or more, respectively. The eigensensitivities for any natural frequency with multiplicity $w \geq 1$ ($\lambda_u = \cdots = \lambda_{u+w-1}$) with its associated preferred set of planet modes $\boldsymbol{\phi}_u,\ \cdots,\ \boldsymbol{\phi}_{u+w-1}$ (a preferred set of planet modes diagonalizes $\mathbf{D}$ in (3.5) if $w \geq 2$) to a mistuned parameter are

$$\begin{aligned}
&\tfrac{\partial \lambda_u}{\partial k_p^{ilm}} = \tfrac{2}{k_p^{ilm}} U_{pb,u}^{ilm} && \text{(R/T/1P/2P/3P)} \\
&\tfrac{\partial \lambda_{u+1}}{\partial k_p^{ilm}} = \begin{cases} \tfrac{2}{k_p^{ilm}} U_{pb,u+1}^{ilm} & \text{(T)} \\ 0 & \text{(2P)} \end{cases} \\
&\tfrac{\partial \lambda_{u+t}}{\partial k_p^{ilm}} = 0,\ t = 2, \cdots, w-1 && \text{(3P)}
\end{aligned} \tag{B.31}$$

$$\begin{aligned}
&\tfrac{\partial \boldsymbol{\phi}_u}{\partial k_p^{ilm}} = \sum_{v=1, v\neq u, \cdots, u+w-1}^{\Lambda} \tfrac{(\delta_{\zeta,v}^{ilm})(\delta_{\zeta,u}^{ilm}) + (\delta_{\eta,v}^{ilm})(\delta_{\eta,u}^{ilm})}{\lambda_u - \lambda_v} \left[\boldsymbol{\phi}_v + \sum_{z=u+1}^{u+w-1} \tfrac{(\delta_{\zeta,z}^{ilm})(\delta_{\zeta,u}^{ilm}) + (\delta_{\eta,z}^{ilm})(\delta_{\eta,u}^{ilm})}{\lambda_u' - \lambda_z'} \boldsymbol{\phi}_z \right] \\
&\quad \text{(R/T/1P/2P)} \\
&\tfrac{\partial \boldsymbol{\phi}_{u+1}}{\partial k_p^{ilm}} = \begin{cases} \displaystyle\sum_{v=1, v\neq u, \cdots, u+w-1}^{\Lambda} \tfrac{(\delta_{\zeta,v}^{ilm})(\delta_{\zeta,u}^{ilm}) + (\delta_{\eta,v}^{ilm})(\delta_{\eta,u}^{ilm})}{\lambda_u - \lambda_v} \left[\boldsymbol{\phi}_v + \displaystyle\sum_{z=u, z\neq u+1}^{u+w-1} \tfrac{(\delta_{\zeta,z}^{ilm})(\delta_{\zeta,u}^{ilm}) + (\delta_{\eta,z}^{ilm})(\delta_{\eta,u}^{ilm})}{\lambda_u' - \lambda_z'} \boldsymbol{\phi}_z \right] & \text{(T)} \\ \mathbf{0} & \text{(2P)} \end{cases} \\
&\tfrac{\partial \boldsymbol{\phi}_{u+s}}{\partial k_p^{ilm}} \text{ can not be determined, where } s = 0,\ \cdots,\ w-1. && \text{(3P)}
\end{aligned} \tag{B.32}$$

$$\begin{aligned}
&\tfrac{\partial^2 \lambda_u}{(\partial k_p^{ilm})^2} = \sum_{v=1, v\neq u}^{\Lambda} \tfrac{2}{\lambda_u - \lambda_v} [(\delta_{\zeta,v}^{ilm})(\delta_{\zeta,u}^{ilm}) + (\delta_{\eta,v}^{ilm})(\delta_{\eta,u}^{ilm})]^2 && \text{(R/T/1P/2P/3P)} \\
&\tfrac{\partial^2 \lambda_{u+1}}{(\partial k_p^{ilm})^2} = \begin{cases} \displaystyle\sum_{v=1, v\neq u+1}^{\Lambda} \tfrac{2}{\lambda_{u+1} - \lambda_v} [(\delta_{\zeta,v}^{ilm})(\delta_{\zeta,u+1}^{ilm}) + (\delta_{\eta,v}^{ilm})(\delta_{\eta,u+1}^{ilm})]^2 & \text{(T)} \\ 0 & \text{(2P)} \end{cases} \\
&\tfrac{\partial^2 \lambda_{u+t}}{(\partial k_p^{ilm})^2} = 0,\ t = 2, \cdots, w-1 && \text{(3P)}
\end{aligned} \tag{B.33}$$

$$\begin{aligned}
&\tfrac{\partial \lambda_u}{\partial k_{pp}^{ilmq}} = \tfrac{2}{k_{pp}^{ilmq}} U_{pp,u}^{ilm,q} && \text{(R/T/1P/2P/3P)} \\
&\tfrac{\partial \lambda_{u+t}}{\partial k_{pp}^{ilmq}} = 0, \text{ where } t = 1,\ \cdots,\ w-1. && \text{(T/2P/3P)}
\end{aligned} \tag{B.34}$$

$$
\begin{aligned}
&\frac{\partial \boldsymbol{\phi}_u}{\partial k_{pp}^{ilmq}} = \sum_{v=1,v\neq u,\cdots,u+w-1}^{\Lambda} \frac{\delta_{p,v}^{ilmq}\delta_{p,u}^{ilmq}}{\lambda_u-\lambda_v}\boldsymbol{\phi}_v && \text{(R/T/1P/2P)}\\
&\frac{\partial \boldsymbol{\phi}_{u+1}}{\partial k_{pp}^{ilmq}} = \mathbf{0} && \text{(T/2P)}\\
&\frac{\partial \boldsymbol{\phi}_{u+s}}{\partial k_{pp}^{ilmq}} \text{ can not be determined, where } s=0,\ \cdots,\ w-1. && \text{(3P)}
\end{aligned}
\tag{B.35}
$$

$$
\begin{aligned}
&\frac{\partial^2 \lambda_u}{(\partial k_{pp}^{ilmq})^2} = \sum_{v=1,v\neq u}^{\Lambda} \frac{2}{\lambda_u-\lambda_v}\left(\delta_{p,v}^{ilmq}\delta_{p,u}^{ilmq}\right)^2 && \text{(R/T/1P/2P/3P)}\\
&\frac{\partial^2 \lambda_{u+t}}{(\partial k_{pp}^{ilmq})^2} = 0, \text{ where } t=1,\ \cdots,\ w-1. && \text{(T/2P/3P)}
\end{aligned}
\tag{B.36}
$$

$$
\begin{aligned}
&\frac{\partial \lambda_u}{\partial k_{p-p}^{ilmq}} = \frac{2}{k_{pp}^{ilmq}}U_{p-p,u}^{ilmq} && \text{(R/T/1P/2P/3P)}\\
&\frac{\partial \lambda_{u+1}}{\partial k_{p-p}^{ilmq}} = \begin{cases} \frac{2}{k_{pp}^{ilmq}}U_{p-p,u+1}^{ilmq} & \text{(T)}\\ 0 & \text{(2P)}\end{cases}\\
&\frac{\partial \lambda_{u+t}}{\partial k_{p-p}^{ilmq}} = 0, \text{ where } t=2,\ \cdots,\ w-1. && \text{(3P)}
\end{aligned}
\tag{B.37}
$$

$$
\begin{aligned}
&\frac{\partial \boldsymbol{\phi}_u}{\partial k_{p-p}^{ilmq}} = \sum_{v=1,v\neq u,\cdots,u+w-1}^{\Lambda} \frac{(\zeta_{p,v}^{ilm}-\zeta_{p,v}^{ilq})(\zeta_{p,u}^{ilm}-\zeta_{p,u}^{ilq})+(\eta_{p,v}^{ilm}-\eta_{p,v}^{ilq})(\eta_{p,u}^{ilm}-\eta_{p,u}^{ilq})}{\lambda_u-\lambda_v}[\boldsymbol{\phi}_v+\\
&\qquad \sum_{z=u+1}^{u+w-1} \frac{(\zeta_{p,z}^{ilm}-\zeta_{p,z}^{ilq})(\zeta_{p,u}^{ilm}-\zeta_{p,u}^{ilq})+(\eta_{p,z}^{ilm}-\eta_{p,z}^{ilq})(\eta_{p,u}^{ilm}-\eta_{p,u}^{ilq})}{\lambda_u'-\lambda_z'}\boldsymbol{\phi}_z] && \text{(R/T/1P/2P)}\\
&\frac{\partial \boldsymbol{\phi}_{u+1}}{\partial k_{p-p}^{ilmq}} = \begin{cases} \sum\limits_{v=1,v\neq u,\cdots,u+w-1}^{\Lambda} \frac{(\zeta_{p,v}^{ilm}-\zeta_{p,v}^{ilq})(\zeta_{p,u}^{ilm}-\zeta_{p,u}^{ilq})+(\eta_{p,v}^{ilm}-\eta_{p,v}^{ilq})(\eta_{p,u}^{ilm}-\eta_{p,u}^{ilq})}{\lambda_u-\lambda_v}[\boldsymbol{\phi}_v+ \\ \qquad \sum\limits_{z=u,z\neq u+1}^{u+w-1} \frac{(\zeta_{p,z}^{ilm}-\zeta_{p,z}^{ilq})(\zeta_{p,u}^{ilm}-\zeta_{p,u}^{ilq})+(\eta_{p,z}^{ilm}-\eta_{p,z}^{ilq})(\eta_{p,u}^{ilm}-\eta_{p,u}^{ilq})}{\lambda_u'-\lambda_z'}\boldsymbol{\phi}_z] & \text{(T)}\\ \mathbf{0} & \text{(2P)}\end{cases}\\
&\frac{\partial \boldsymbol{\phi}_{u+t}}{\partial k_{p-p}^{ilmq}} \text{ can not be determined, where } t=0,\ \cdots,\ w-1. && \text{(3P)}
\end{aligned}
\tag{B.38}
$$

$$
\begin{aligned}
&\frac{\partial^2 \lambda_u}{(\partial k_{pp}^{ilm-p})^2} = \sum_{v=1,v\neq u}^{\Lambda} \frac{2}{\lambda_u-\lambda_v}\left[(\zeta_{p,v}^{ilm}-\zeta_{p,v}^{ilp})(\zeta_{p,u}^{ilm}-\zeta_{p,u}^{ilp})+(\eta_{p,v}^{ilm}-\eta_{p,v}^{ilp})(\eta_{p,u}^{ilm}-\eta_{p,u}^{ilp})\right]^2\\
&\quad \text{(R/T/1P/2P/3P)}\\
&\frac{\partial^2 \lambda_{u+1}}{(\partial k_{pp}^{ilm-p})^2} = \begin{cases} \sum\limits_{v=1,v\neq u+1}^{\Lambda} \frac{2}{\lambda_{u+1}-\lambda_v}\Big[(\zeta_{p,v}^{ilm}-\zeta_{p,v}^{ilp})(\zeta_{p,u+1}^{ilm}-\zeta_{p,u+1}^{ilp})+ \\ (\eta_{p,v}^{ilm}-\eta_{p,v}^{ilp})(\eta_{p,u+1}^{ilm}-\eta_{p,u+1}^{ilp})\Big]^2 & \text{(T)}\\ 0 & \text{(2P)}\end{cases}\\
&\frac{\partial^2 \lambda_{u+t}}{(\partial k_{pp}^{ilm-p})^2} = 0, \text{ where } t=2,\ \cdots,\ w-1. && \text{(3P)}
\end{aligned}
\tag{B.39}
$$

$$\begin{aligned}
&\frac{\partial\lambda_u}{\partial k^{ilmq}_{p-p,\theta\theta}} = \frac{2}{k^{ilmq}_{p-p,\theta\theta}} U^{ilmq}_{p-p,\theta\theta,u} \qquad \text{(R/T/1P/2P/3P)} \\
&\frac{\partial\lambda_{u+t}}{\partial k^{ilmq}_{p-p,\theta\theta}} = 0, \text{ where } t = 1, \cdots, w-1. \text{ (T/2P/3P)}
\end{aligned} \tag{B.40}$$

$$\begin{aligned}
\frac{\partial\boldsymbol{\phi}_u}{\partial k^{ilmq}_{p-p,\theta\theta}} = &\sum_{v=1,v\neq u,\cdots,u+w-1}^{\Lambda} \frac{(u^{ilm}_{p,v}/r^{ilm}_p - u^{ilq}_{p,v}/r^{ilq}_p)(u^{ilm}_{p,u}/r^{ilm}_p - u^{ilq}_{p,u}/r^{ilq}_p)}{\lambda_u-\lambda_v}(\boldsymbol{\phi}_v + \\
&\sum_{z=u+1}^{u+w-1} \frac{(u^{ilm}_{p,z}/r^{ilm}_p - u^{ilq}_{p,z}/r^{ilq}_p)(u^{ilm}_{p,u}/r^{ilm}_p - u^{ilq}_{p,u}/r^{ilq}_p)}{\lambda'_u-\lambda'_z}\boldsymbol{\phi}_z) \quad \text{(R/T/1P/2P)} \\
\frac{\partial\boldsymbol{\phi}_{u+1}}{\partial k^{ilmq}_{p-p,\theta\theta}} = &\mathbf{0} \qquad \text{(T/2P)} \\
\frac{\partial\boldsymbol{\phi}_{u+s}}{\partial k^{ilmq}_{p-p,\theta\theta}} &\text{ can not be determined, where } s = 0, \cdots, w-1. \text{ (3P)}
\end{aligned} \tag{B.41}$$

$$\begin{aligned}
&\frac{\partial^2\lambda_u}{(\partial k^{ilmq}_{p-p,\theta\theta})^2} = \sum_{v=1,v\neq u}^{\Lambda} \frac{2}{\lambda_u-\lambda_v}\left[(u^{ilm}_{p,v}/r^{ilm}_p - u^{ilp}_{p,v}/r^{ilp}_p)(u^{ilm}_{p,u}/r^{ilm}_p - u^{ilp}_{p,u}/r^{ilp}_p)\right]^2 \\
&\text{(R/T/1P/2P/3P)} \\
&\frac{\partial^2\lambda_{u+t}}{(\partial k^{ilmq}_{p-p,\theta\theta})^2} = 0, \text{ where } t = 1, \cdots, w-1. \qquad \text{(T/2P/3P)}
\end{aligned} \tag{B.42}$$

$$\begin{aligned}
&\frac{\partial\lambda_u}{\partial m^{ilm}_p} = -\frac{2}{m^{ilm}_p} T^{ilm}_{p,u} \qquad \text{(R/T/1P/2P/3P)} \\
&\frac{\partial\lambda_{u+1}}{\partial m^{ilm}_p} = \begin{cases} -\frac{2}{m^{ilm}_p} T^{ilm}_{p,u+1} & \text{(T)} \\ 0 & \text{(2P)} \end{cases} \\
&\frac{\partial\lambda_{u+t}}{\partial m^{ilm}_p} = 0, \text{ where } t = 2, \cdots, w-1. \text{ (3P)}
\end{aligned} \tag{B.43}$$

$$\begin{aligned}
\frac{\partial\boldsymbol{\phi}_u}{\partial m^{ilm}_p} = &\sum_{v=1,v\neq u,\cdots,u+w-1}^{\Lambda} \frac{\zeta^{ilm}_{p,v}\zeta^{ilm}_{p,u} + \eta^{ilm}_{p,v}\eta^{ilm}_{p,u}}{\lambda_u-\lambda_v}\left[-\lambda_u\boldsymbol{\phi}_v + \sum_{z=u+1}^{u+w-1} \frac{\lambda^2_u(\zeta^{ilm}_{p,z}\zeta^{ilm}_{p,u} + \eta^{ilm}_{p,z}\eta^{ilm}_{p,u})}{\lambda'_u-\lambda'_z}\boldsymbol{\phi}_z\right] \\
&- \frac{\boldsymbol{\phi}_u}{2}[(\zeta^{ilm}_{p,u})^2 + (\eta^{ilm}_{p,u})^2] \qquad \text{(R/T/1P/2P)} \\
\frac{\partial\boldsymbol{\phi}_{u+1}}{\partial m^{ilm}_p} = &\begin{cases} \sum\limits_{v=1,v\neq u,\cdots,u+w-1}^{\Lambda} \frac{\zeta^{ilm}_{p,v}\zeta^{ilm}_{p,u} + \eta^{ilm}_{p,v}\eta^{ilm}_{p,u}}{\lambda_u-\lambda_v}\left[-\lambda_u\boldsymbol{\phi}_v + \sum\limits_{z=u,z\neq u+1}^{u+w-1} \frac{\lambda^2_u(\zeta^{ilm}_{p,z}\zeta^{ilm}_{p,u} + \eta^{ilm}_{p,z}\eta^{ilm}_{p,u})}{\lambda'_u-\lambda'_z}\boldsymbol{\phi}_z\right] \\ \quad - \frac{\boldsymbol{\phi}_u}{2}[(\zeta^{ilm}_{p,u})^2 + (\eta^{ilm}_{p,u})^2] \qquad \text{(T)} \\ \mathbf{0} \qquad \text{(2P)} \end{cases} \\
\frac{\partial\boldsymbol{\phi}_{u+s}}{\partial m^{ilm}_p} &\text{ can not be determined, where } s = 0, \cdots, w-1. \text{ (3P)}
\end{aligned} \tag{B.44}$$

$$
\begin{aligned}
&\frac{\partial^2\lambda_u}{(\partial m_p^{ilm})^2} = \sum_{v=1,v\neq u}^{\Lambda} \frac{2\lambda_u^2}{\lambda_u-\lambda_v}(\zeta_{p,v}^{ilm}\zeta_{p,u}^{ilm}+\eta_{p,v}^{ilm}\eta_{p,u}^{ilm})^2 + 2\lambda_u[(\zeta_{p,u}^{ilm})^2+(\eta_{p,u}^{ilm})^2]^2 \\
&\quad \text{(R/T/1P/2P/3P)} \\
&\frac{\partial^2\lambda_{u+1}}{(\partial m_p^{ilm})^2} = \begin{cases} \sum\limits_{v=1,v\neq u+1}^{\Lambda} \frac{2\lambda_{u+1}^2}{\lambda_{u+1}-\lambda_v}(\zeta_{p,v}^{ilm}\zeta_{p,u+1}^{ilm}+\eta_{p,v}^{ilm}\eta_{p,u+1}^{ilm})^2 + 2\lambda_{u+1}[(\zeta_{p,u+1}^{ilm})^2+(\eta_{p,u+1}^{ilm})^2]^2 \\ \quad \text{(T)} \\ 0 \qquad\qquad\qquad\qquad\qquad \text{(2P)} \end{cases} \\
&\frac{\partial^2\lambda_{u+t}}{(\partial m_p^{ilm})^2} = 0, \text{ where } t = 2, \cdots, w-1. \text{ (3P)}
\end{aligned}
\tag{B.45}
$$

$$
\begin{aligned}
&\frac{\partial\lambda_u}{\partial I_p^{ilm}} = -\frac{2}{I_p^{ilm}} T_{p,\theta\theta,u}^{ilm} \qquad\qquad \text{(R/T/1P/2P/3P)} \\
&\frac{\partial\lambda_{u+t}}{\partial I_p^{ilm}} = 0, \text{ where } t = 1, \cdots, w-1. \text{ (T/2P/3P)}
\end{aligned}
\tag{B.46}
$$

$$
\begin{aligned}
&\frac{\partial\boldsymbol{\phi}_u}{\partial I_p^{ilm}} = \sum_{v=1,v\neq u,\cdots,u+w-1}^{\Lambda} \frac{-\lambda_u u_{p,v}^{ilm} u_{p,u}^{ilm}}{(r_p^{ilm})^2(\lambda_u-\lambda_v)}\boldsymbol{\phi}_v - \frac{\boldsymbol{\phi}_u}{2}(\frac{u_{p,u}^{ilm}}{r_p^{ilm}})^2 \qquad \text{(R/T/1P/2P)} \\
&\frac{\partial\boldsymbol{\phi}_{u+1}}{\partial I_p^{ilm}} = \mathbf{0} \qquad\qquad \text{(T/2P)} \\
&\frac{\partial\boldsymbol{\phi}_s}{\partial I_p^{ilm}} \text{ can not be determined, where } s = 0, \cdots, w-1. \text{ (3P)}
\end{aligned}
\tag{B.47}
$$

$$
\begin{aligned}
&\frac{\partial^2\lambda_u}{(\partial I_p^{ilm})^2} = \sum_{v=1,v\neq u}^{\Lambda} \frac{2\lambda_u^2}{\lambda_u-\lambda_v}\left[\frac{u_{p,v}^{ilm}u_{p,u}^{ilm}}{(r_p^{ilm})^2}\right]^2 + 2\lambda_u\left(\frac{u_{p,u}^{ilm}}{r_p^{ilm}}\right)^2 \text{ (R/T/1P/2P/3P)} \\
&\frac{\partial^2\lambda_{u+t}}{(\partial I_p^{ilm})^2} = 0, \text{ where } t = 1, \cdots, w-1. \qquad \text{(T/2P/3P)}
\end{aligned}
\tag{B.48}
$$

Bibliography

[1] A. Al-shyyab and A. Kahraman. Non-linear dynamic analysis of a multi-mesh gear train using multi-term harmonic balance method: period-one motions. *Journal of Sound and Vibration*, 284(1-2):151–172, June 2005.

[2] A. Al-shyyab and A. Kahraman. Non-linear dynamic analysis of a multi-mesh gear train using multi-term harmonic balance method: subharmonic motions. *Journal of Sound and Vibration*, 279(1-2):417–451, January 2005.

[3] M. Amabili and A. Rivola. Dynamic analysis of spur gear pairs: Steady-state response and stability of the sdof model with time-varying meshing damping. *Mechanical Systems and Signal Processing*, 11:375–390, 1997.

[4] M. Amabili and A. Rivola. Dynamic analysis of spur gear pairs: Steady-state response and stability of the sdof model with time-varying meshing damping. *Mechanical Systems and Signal Processing*, 11:375–390, 1997.

[5] V. K. Ambarisha and R. G. Parker. Suppression of planet mode response in planetary gear dynamics through mesh phasing. *Journal of Vibration and Acoustics*, 128(2):133–142, 2006.

[6] V. K. Ambarisha and R. G. Parker. Nonlinear dynamics of planetary gears using analytical and finite element models. *Journal of Sound and Vibration*, 203:577–595, 2007.

[7] R. August. *Dynamics of Planetary Gear Trains*. PhD thesis, Cleveland State University, 1983.

[8] R. August and R. Kasuba. Torsional vibrations and dynamic loads in a basic planetary gear system. *Journal of Vibration, Acoustics, Stress, and Reliability in Design*, 108(3):348–353, July 1986.

[9] C. J. Bahk and R. G. Parker. Analytical solution for the nonlinear dynamics of planetary gears. *ASME Journal of Computational and Nonlinear Dynamics*, 6, April 2011.

[10] M. Benton and A. Seireg. Normal mode uncoupling of systems with time varying stiffness. *Journal of Mechanical Design*, 102:379–383, 1980.

[11] M. Benton and A. Seireg. Factors influencing instability and resonances in geared systems. *Journal of Mechanical Design*, 103(2):372–378, April 1981.

[12] M. Benton and A. Seireg. Factors influencing instability and resonances in geared systems. *Journal of Mechanical Design*, 103:372–378, 1981.

[13] J. G. Bollinger and R. J. Harker. Instability potential of high speed gearing. *Journal of the Industrial Mathematics*, 17:39–55, 1967.

[14] J.G. Bollinger and R.J. Harker. Instability potential of high speed gearing. *Journal of the Industrial Mathematics,*, 17:39–55, 1967.

[15] M. Botman. Dynamic tooth loads in epicyclic gears. *Journal of Engineering for Industry*, pages 811–815, August 1976.

[16] M. Botman. Epicyclic gear vibations. *Journal of Engineering for Industry*, 97:811–815, 1976.

[17] M. Botman. Vibration measurement on planetary gears of aircraft turbine engines. *J. Aircraft*, (5), May 1980.

[18] J. Brauer. *Investigation of Transmission Error, Friction, and Wear in Anti-backlash Gear Transmissions: A Finite Element Approach*. PhD thesis, Royal Institute of Technology, Sweden, 2003.

[19] F. Brown, M. Robuck, and M. Kozachyn. Design, fabrication, assembly and test of a double helical planetary gear system for helicopter applications. Technical report, The Boeing Company, 2008.

[20] P. Chen and J. H. Ginsberg. On the relationship between veering of eigenvalue loci and parameter sensitivity of eigenfunctions. *Journal of Vibration and Acoustics*, 114:141–148, 1992.

[21] R. Courant and D. Hilbert. *Methods of Mathematical Physics*, volume 1. Interscience Publishers, six edition, May 1966.

[22] F. Cunliffe, J. D. Smith, and D. B. Welbourn. Dynamic tooth loads in epicyclic gears. *Journal of Engineering for Industry*, 5(95):578–584, May 1974.

[23] T. Eritenel. *Three-Dimensional Nonlinear Dynamics and Vibration Reduction of Gear Pairs and Planetary Gears*. PhD thesis, The Ohio State University, 2011.

[24] T. Eritenel and R. G. Parker. A static and dynamic model for three-dimensional multi-mesh gear systems. In *International Design Engineering Technical Conferences*, Long Beach, CA, Sep. 2005. Proceedings of ASME.

[25] T. Eritenel and R. G. Parker. Modal properties of three-dimensional helical planetary gears. *Journal of Sound and Vibration*, 325:397–420, 2009.

[26] T. Eritenel and R. G. Parker. Vibration suppression rules for 3-d helical planetary gears using mesh phasing. *In preparation*, 2011.

[27] R. L. Fox and M. P. Kapoor. Rates of change of eigenvalues and eigenvectors. *AIAA Journal*, 6:2426–2429, 1968.

[28] J. Frater, R. August, and F. Oswald. Vibation in planetary gear systems with unequal planet stiffness. *NASA*, (TM-83428), 1983.

[29] M. I. Friswell. The derivatives of repeated eigenvalues and their associated eigenvectors. *Journal of Vibration and Acoustics*, 188:390–397, 1996.

[30] R. W. Greogory, S. L. Harris, and R. G. Munro. Dynamic behavior of spur gears. *Proceedings of the institution of mechanical engineers*, 178:261–266, 1963.

[31] Y. Guo and R. G. Parker. Sensitivity of tuned general compound planetary gears natural frequencies and vibration modes to model parameters. In *Proceedings of 2006 International Mechanical Engineering Congress and Exposition (IMECE2006-14978)*, Chicago, IL, 2006.

[32] Y. Guo and R. G. Parker. Mesh phase relations of general compound planetary gears. In *Proceedings of 10th International ASME Power Transmission and Gearing Conference (IDETC2007-35799)*, Las Vegas, NV, 2007.

[33] Y. Guo and R. G. Parker. Sensitivity of general compound planetary gears natural frequencies and vibration modes to model parameters. In *Proceedings of 10th International ASME Power Transmission and Gearing Conference (IDETC2007-35802)*, Las Vegas, NV, 2007.

[34] Y. Guo and R. G. Parker. Dynamic modeling and analysis of a spur planetary gear involving tooth wedging and bearing clearance nonlinearity. In *European Journal of Mechanics A/Solids* [68], pages 1022–1033.

[35] Y. Guo and R. G. Parker. Purely rotational model and vibration modes of compound planetary gears. *Mechanism and Machine Theory*, 45:365–377, 2010.

[36] Y. Guo and R. G. Parker. Sensitivity of general compound planetary gears natural frequencies and vibration modes to model parameters. *Journal of Vibration and Acoustics*, 132(1):1–13, 2010.

[37] Y. Guo and R. G. Parker. Analytical determiantion of mesh phase relations in general compound planetary gears. *Mechanism and Machine Theory*, 2011. accepted.

[38] Y. Guo and R. G. Parker. Back-side contact gear mesh stiffness. In *Proceedings of 12th International ASME Power Transmission and Gearing Conference (IDETC2011-48055)*, 2011.

[39] A.M. Hansen, F. Rasmussen, and T.J. Larsen. Gearbox loads caused by double contact simulated with hawc2. In *European Wind Energy Conference and Exhibition, Poland*, 2010.

[40] S. L. Harris. Dynamic loads on the teeth of spur gears. *Inst. Mech. Eng.*, 172:87–100, 1958.

[41] T. Hidaka, Y. Terauchi, and K. Nagamura. Dynamic behavior of planetary gear (6th report, influence of meshing-phase). *Bulletin of JSME*, 22(169):1026–1033, July 1979.

[42] K. Jeong. Mode localization and veering of natural frequency loci in two circular plates coupled with a fluid. *Structural Engineering and Mechanics*, 22:719–740, 2006.

[43] A. Kahraman. Planetary gear train dynamics. *Journal of Mechanical Design*, 116(3):713–720, September 1993.

[44] A. Kahraman. Load sharing characteristics of planetary transmissions. *Mechanism and Machine Theory*, 29(8):1151–1165, November 1994.

[45] A. Kahraman. Natural modes of planetary gear trains. *Journal of Sound and Vibration*, 173(1):125–130, 1994.

[46] A. Kahraman. Natural modes of planetary gear trains (letters to the editor). *Journal of Sound and Vibration*, 173(1):125–130, 1994.

[47] A. Kahraman. Free torsional vibration characteristics of compound planetary gear sets. *Mechanism and Machine Theory*, 36:953–971, 2001.

[48] A. Kahraman and G. W. Blankenship. Planet mesh phasing in epicyclic gear sets. In *International Gearing Conference*, pages 99–104, Newcastle, UK, 1994.

[49] A. Kahraman and G. W. Blankenship. Experiments on nonlinear dynamic behavior of an oscillator with clearance and periodically time-varying parameters. *Journal of Applied Mechanics*, 64(1):217–226, March 1997.

[50] A. Kahraman and R. Singh. Non-linear dynamics of a spur gear pair. *Journal of Sound and Vibration*, 142(1):49–75, October 1990.

[51] A. Kahraman and R. Singh. Interactions between time-varying mesh stiffness and clearance non-linearities in a geared system. *Journal of Sound and Vibration*, 146(1):135–156, April 1991.

[52] M. Kim, J. Moon, and J. A. Wickert. Spatial modulation of repeated vibration modes in rotationally periodic structures. *Journal of Vibration and Acoustics*, 122(1):62–68, January 2000.

[53] D. R. Kiracofe and R. G. Parker. Structured vibration modes of general compound planetary gear systems. *Journal of Vibration and Acoustics*, 129(1):1–16, February 2007.

[54] T.J. Larsen, K. Thomsen, and F. Rasmussen. Dynamics of a wind turbine planetary gear stage. Technical report risoe-i-2112 (en), Risoe National Laboratory, Denmark, 2003.

[55] A. W. Leissa. On a curve veering aberration. *J. Appl. Math. Phys.*, 25:98–111, 1974.

[56] J. Lin and R. G. Parker. Analytical characterization of the unique properties of planetary gear free vibration. *Journal of Vibration and Acoustics*, 121(3):319–321, July 1999.

[57] J. Lin and R. G. Parker. Sensitivity of planetary gear natural frequencies and vibration modes to model parameters. *Journal of Sound and Vibration*, 228(1):109–128, November 1999.

[58] J. Lin and R. G. Parker. Structured vibration characteristics of planetary gears with unequally spaced planets. *Journal of Sound and Vibration*, 233(5):921–928, June 2000.

[59] J. Lin and R. G. Parker. Natural frequency veering in planetary gears. *Mechanics of Structures and Machines*, 29(4):411–429, 2001.

[60] J. Lin and R. G. Parker. Mesh stiffness variation instabilities in two-stage gear systems. *Journal of Vibration and Acoustics*, 124(1):68–76, January 2002.

[61] J. Lin and R. G. Parker. Planetary gear parametric instability caused by mesh stiffness variation. *Journal of Sound and Vibration*, 249(3):1, January 2002.

[62] G. Liu and R. G. Parker. Dynamic modeling and analysis of tooth profile modification of multi-mesh gears. *ASME Journal of Mechanical Design*, 130:121402–1–13, 2008.

[63] G. Liu and R. G. Parker. Nonlinear dynamics of idler gearsets. *Nonlinear Dynamics*, 53:345–367, 2008.

[64] G. Liu and R. G. Parker. Impact of tooth friction and its bending effect on gear dynamics. *Journal of Sound and Vibration*, 320:1039–1063, 2009.

[65] P. Lynwander. *Gear Drive Systems: Design and Applications*. CRC Press, Florida, 1983.

[66] P. Ma and M. Botman. Load sharing in a planetary gear stage in the presence of errors and misalignment. *ASME Journal of Mechanisms, Transmissions and Automation in Design*, 107, March 1985.

[67] W. C. Mills-Curran. Calculation of eigenvector derivatives for structures with repeated eigenvalues. *AIAA Journal*, 26:867–871, 1988.

[68] H. W. Muller. *Epicyclic Drive Trains: Analysis, Synthesis, and Applications*. Wayne State University Press, Detroit, 1982.

[69] P. S. Nair and S. Durvasula. On quasi-degeneracies in plate vibration problems. *Int. J. Mech. Sci.*, 15:975–986, 1973.

[70] C. Nataraj and A. M. Whitman. Parameter excitation effects in gear dynamics. In *American Society for Mechanical Engineers Design Engineering Technical Conferences*, Sacramento, CA, 1997.

[71] C. Nataraj and A.M. Whitman. Parameter excitation effects in gear dynamics. In *ASME Design Engineering Technical Conferences*, Las Vegas, NV, 1997. DETC99/VIB-8110.

[72] S. Natsiavas. Mode localization and frequency veering in a non-conservative mechanical system with dissimilar components. *Journal of Sound and Vibration*, 165:137–147, 1993.

[73] R. B. Nelson. Simplified calculation of eigenvector derivatives. *AIAA Journal*, 4:1201–1205, 1976.

[74] W. E. Palmer and R.R. Fuehrer. Noise control in planetary transmissions. In *Earth Moving Industry Conference, SAE*, Peoria, 1977.

[75] R. G. Parker. A physical explanation for the effectiveness of planet phasing to suppress planetary gear vibration. *Journal of Sound and Vibration*, 236(4):561–573, 2000.

[76] R. G. Parker, V. Agashe, and S. M. Vijayakar. Dynamic response of a planetary gear system using a finite element/contact mechanics model. *Journal of Mechanical Design*, 122(3):304–310, September 2000.

[77] R. G. Parker and J. Lin. Mesh phasing relationships in planetary and epicyclic gears. *Journal of Mechanical Design*, 126:365–370, 2004.

[78] R. G. Parker, S. M. Vijayakar, and T. Imajo. Non-linear dynamic response of a spur gear pair: Modelling and experimental comparisons. *Journal of Sound and Vibration*, 237(3):435–455, October 2000.

[79] R. G. Parker and X. Wu. Vibration modes of planetary gears with unequally spaced planets and an elastic ring gear. *Journal of Sound and Vibration*, 329:2265–2275, 2010.

[80] N. C. Perkins and Jr. Mote, C. D. Comments on curve veering in eigenvalue problems. *Journal of Sound Vibration*, 106:451–463, 1986.

[81] C. Pierre. Mode localization and eigenvalue loci veering phenomena in disordered structures. *Journal of Sound and Vibration*, 126:485–502, 1988.

[82] C. Pierre and R. H. Plaut. Curve veering and mode localization in a buckling problem. *Journal of Applied Mathematics and Physics*, 40:758–761, 1989.

[83] R. L. Platt and R. D. Leoplod. A study on helical gear planetary phasing effects on transmission noise. *VDI-Ber*, pages 793–807, 1996.

[84] F. Rasmussen, K. Thomsen, and T.J. Larsen. The gearbox problem revisited. Risoe fact sheet aed-rb-17 (en), Risoe National Laboratory, Denmark.

[85] A. Saada and P. Velex. An extended model for the analysis of the dynamic behavior of planetary trains. *Journal of Mechanical Design*, 117(2):241–247, June 1995.

[86] R. G. Schlegel and K. C. Mard. Transmission noise control approaches in helicopter design. In *ASME Design Engineering Conference (67-DE-58)*, New York, US, 1967.

[87] D. L. Seager. Conditions for the neutralization of excitation by the teeth in epicyclic gearing. *Journal of Mechanical Engineering Science*, 17(5):293–298, 1975.

[88] R. Singh, D. R. Houser, and A. Kahraman. Non-linear dynamic analysis of geared systems. *NASA Technical Report*, Final Report, Part II, February 1990.

[89] N. G. Stephen. On veering of eigenvalue loci. *Journal of Vibration and Acoustics*, 131:054501–054505, 2009.

[90] T. Sun and H. Hu. Nonlinear dynamics of a planetary gear system with multiple clearances. *Mechanism and Machine Theory*, 38(12):1371–1390, December 2003.

[91] S. Theodossiades and S. Natsiavas. Non-linear dynamics of gear-pair systems with periodic stiffness and backlash. *Journal of Sound and Vibration*, 229(2):287–310, January 2000.

[92] G. V. Tordion and R. Gauvin. Dynamic stability of a two-stage gear train under the influence of variable meshing stiffnesses. *Journal of Engineering for Industry*, 99:785–791, 1977.

[93] G.V. Tordion and R. Gauvin. Dynamic stability of a two-stage gear train under the influence of variable meshing stiffnesses. *Journal of Engineering for Industry*, 99:785–791, 1977.

[94] P. Velex and L. Flamand. Dynamic response of planetary trains to mesh parametric excitations. *Journal of Mechanical Design*, 118(1):7–14, March 1996.

[95] S. M. Vijayakar. *Planetary2D User's Manual*. Advanced Numerical Solutions, www.ansol.us, 2006.

[96] S.M. Vijayakar. *Calyx Programmers Manual*. Advanced Numerical Solutions, www.ansol.us, 2006.

[97] X. Wu and R. G. Parker. Modal properties of planetary gears with an elastic continuum ring gear. *Journal of Applied Mechanics*, 75(3):1–12, 2008.

[98] X. Wu and R. G. Parker. Parametric instability of planetary gears with elastic continuum ring gears. *ASME Journal of Vibration and Acoustics*, page submitted, 2010.